

Lawrence Berkeley National Laboratory

Recent Work

Title

CHEMISTRY DIVISION ANNUAL REPORT, 1963

Permalink

<https://escholarship.org/uc/item/53z716g9>

Authors

Perlman, I. (Director).
Hollander, J.M. Chemistry Division Editors:
Reynolds, F.L.
et al.

Publication Date

1964-02-01

UCRL-11213

C.2

University of California
Ernest O. Lawrence
Radiation Laboratory

TWO-WEEK LOAN COPY

*This is a Library Circulating Copy
which may be borrowed for two weeks.
For a personal retention copy, call
Tech. Info. Division, Ext. 5545*

CHEMISTRY DIVISION ANNUAL REPORT

1963

Berkeley, California

UCRL-11213
C.2

DISCLAIMER

This document was prepared as an account of work sponsored by the United States Government. While this document is believed to contain correct information, neither the United States Government nor any agency thereof, nor the Regents of the University of California, nor any of their employees, makes any warranty, express or implied, or assumes any legal responsibility for the accuracy, completeness, or usefulness of any information, apparatus, product, or process disclosed, or represents that its use would not infringe privately owned rights. Reference herein to any specific commercial product, process, or service by its trade name, trademark, manufacturer, or otherwise, does not necessarily constitute or imply its endorsement, recommendation, or favoring by the United States Government or any agency thereof, or the Regents of the University of California. The views and opinions of authors expressed herein do not necessarily state or reflect those of the United States Government or any agency thereof or the Regents of the University of California.

Research and Development

-i-

UCRL-11213
UC-4 Chemistry
TID-4500 (24th Ed.)

UNIVERSITY OF CALIFORNIA
Lawrence Radiation Laboratory
Berkeley, California

AEC Contract No. W-7405-eng-48

CHEMISTRY DIVISION ANNUAL REPORT, 1963

February 1964

I. Perlman, Director, Chemistry Division
Editors: J. M. Hollander, F. L. Reynolds, and J. C. Wallmann

Work done under the auspices of the
U. S. Atomic Energy Commission

Printed in USA. Price \$3.00. Available from the
Office of Technical Services
U. S. Department of Commerce
Washington 25, D.C.

CHEMISTRY DIVISION ANNUAL REPORT, 1963

Contents

A. RADIOACTIVITY AND NUCLEAR STRUCTURE

1.	In-Beam Nuclear Spectroscopy (Stephens, Lark, and Diamond)	1
2.	An Electrostatic Method for the Recoil Measurement of Subnanosecond Nuclear Lifetimes (Novakov, Hollander, and Graham)	2
3.	A Study of the Energy Levels of ${}_{97}\text{Bk}^{249}$ (Hollander, Holtz, Novakov, and Graham)	4
4.	Determination of the Atomic Electron Binding Energies in Element 97 (Hollander, Holtz, Novakov, and Graham)	7
5.	L-Subshell Ratios of Mixed M1-E2 Transitions (Novakov and Hollander)	9
6.	Lifetime and Multipolarity Measurements in Cs^{131} (Horen, Hollander, and Graham)	11
7.	Properties of the 57- and 351-keV Excited States in ${}_{59}\text{Pr}^{143}$ (Graham, Hollander, and Kleinheinz)	14
8.	The Decay Scheme of E^{254} (McHarris, Stephens, Asaro, and Perlman)	14
9.	Concerning Isomers of At^{208} , At^{206} , and At^{204} (Thoresen, Asaro, and Perlman)	16
10.	The Decay Scheme of Fm^{255} (Asaro, Björnholm, and Perlman)	17
11.	Ground-State Alpha Group of Protactinium-229 (Subrahmanyam, Asaro, and Perlman)	17
12.	Alpha Decay of Actinium-223 (Subrahmanyam, Mosier, Asaro, and Perlman)	19
13.	Nuclear Spins of Gd^{153} and Pm^{148} (Ali and Marrus)	19
14.	Antimony-131 Gamma Spectrum (Cooper, Gatti, Rasmussen, and Thompson)	20
15.	Theoretical Alpha Decay Rates of Odd-Mass Nuclei (Mang, Poggenburg, and Rasmussen)	20
16.	Energy Levels of Tl^{208} and Bi^{208} (Kim and Rasmussen)	23
17.	A Broad Survey of Tensor Force Effects on Spectra of Spherical Odd-Odd Nuclei (Rasmussen and Kim)	25
18.	Quasi-Particle Interactions in Even-Even Spherical Nuclei (Rho and Rasmussen)	28
19.	Comparison of Exact and BCS Solutions in Pairing-Force Problems (Rasmussen and Rho)	33
20.	Theoretical α -Decay Rate Calculations for Spherical Nuclei (Rasmussen, Macfarlane, and Rho)	39
21.	Effect of Quasi-Particle Interactions on the Quadrupole Moment of Odd-A Spherical Nuclei (Rho)	39
22.	Self-Consistent Calculations of Nuclear Deformations (Dietrich, Mang, and Pradal)	40
23.	Conserved Particle Number in the Nuclear Pairing Model (Dietrich, Mang, and Pradal)	43
24.	Digital Computer Calculation of 3-j, 6-j, and 9-j Symbols with Multiple-Precision Arithmetic (Baer and Redlich)	46

25.	Note on the Y_{40} Deformation in Heavy Nuclei (Harada)	46
B. FISSION		
1.	Gamma-Ray Spectra from Spontaneous Fission of Cf^{252} (Bowman, Thompson, and Rasmussen)	49
2.	Hilac Operations and Improvements (Ghiorso and Main)	52
3.	Ratio of Cd^{115} Isomers Produced in Heavy-Ion-Induced Fission (Sikkeland and Choppin)	53
4.	Kinetic Energy and Mass Distributions for Nuclear Fission at Moderate Excitation Energy (Burnett and Thompson)	56
5.	Energy-Mass Distributions and Angular Momentum Effects in Heavy-Ion-Induced Fission (Plasil and Thompson)	58
6.	Fission Barrier of Thallium-201 (Burnett, Gatti, Plasil, Price, Swiatecki, and Thompson)	60
7.	Fission Barrier of Mercury-198 (Gatti, Khodai-Joopary, and Thompson)	63
C. NUCLEAR REACTIONS		
1.	Polarization in Elastic Scattering of 22-MeV Protons from Deuterons (Conzett, Igo, and Knox)	64
2.	Optical-Model Analysis for 48-MeV Alpha Particles on Carbon (Pehl and Wilkins)	65
3.	Proton-Induced Two-Nucleon Pickup Reactions on O^{16} (Cerny and Pehl)	68
4.	Scattering of 65-MeV Helium Ions by O^{16} (Harvey, Rivet, Springer, Meriwether, Jones, Elliott, and Darriulat)	70
5.	The Formation of Strongly Populated High Spin Levels in (α , d) Reactions (Rivet, Cerny, Harvey, Pehl, and Haag)	71
6.	Muon Capture in O^{16} and C^{12} (Gillet and Jenkins)	72
7.	The Scattering of 64.3-MeV Alpha Particles from Nickel-58 and Iron-58 (Darriulat, Igo, Pugh, Meriwether, and Yamabe)	73
8.	The Scattering of Alpha Particles from Cu^{63} and Ni^{62} (Harvey, Horen, and Meriwether)	77
9.	Neutron and Photon Emission from Dy and Tb Compound Nuclei: Range Distributions (Alexander, Gilat, and Sisson)	79
10.	Stopping of Dy and Tb Ions in Gases and Aluminum (Gilat and Alexander)	80
11.	Inelastic Scattering of 166-MeV O^{16} Ions by Ta^{181} (Isoya, Conzett, Hadjimichael, and Shield)	83
12.	Phase-Shift Analysis of Heavy-Ion Scattering (Conzett, Isoya, and Hadjimichael)	83
13.	Production of Be^7 in He^3 - and He^4 -Induced Nuclear Reactions (Pape and Markowitz)	84
14.	Nuclear Reactions Induced by π Mesons. The $C^{12}(\pi^-, \pi^-n)C^{11}$ Reaction (Reeder and Markowitz)	86
D. PHYSICAL CHEMISTRY		
1.	Activation Analysis for Carbon and Nitrogen by He^3 -Induced Nuclear Reactions (Mahony, Parsa, and Markowitz)	87
2.	Crystal Structure and Melting Point of Curium Metal (Cunningham and Wallmann)	90
3.	The Crystal Structure of Thorium Tetraiodide (Zalkin, Forrester, and Templeton)	92

4.	Crystal Structure of Terbium Trichloride (Forrester, Zalkin, Templeton, and Wallmann)	94
5.	Refinement of the Crystal Structure of Mercuric Sulfate Monohydrate (Templeton, Templeton, and Zalkin)	97
6.	The Crystal Structure of Manganese Dichloride Tetrahydrate (Zalkin, Forrester, and Templeton)	99
7.	Determination of the Crystal Structure of Xenon Trioxide (Templeton, Zalkin, Forrester, and Williamson)	102
8.	Sodium Perxenate Hexahydrate (Zalkin, Forrester, Templeton, Williamson, and Koch)	104
9.	Chemistry of XeO ₃ in Aqueous Solution (Williamson and Koch)	106
10.	The Reaction of XeO ₃ (aq) with Bromide and Iodide Anion: A Kinetic Study (Koch and Williamson)	107
11.	Xenon Tetrafluoride: Reaction with Aqueous Solutions (Williamson and Koch)	108
12.	Ion-Exchange Studies in Concentrated Solutions. III. The Alkaline Earth Cations with a Sulfonic Acid Resin (Whitney and Diamond)	109
13.	The Extraction of Acids by Basic Organic Solvents. IV. Tributyl Phosphate and Trioctyl Phosphine Oxide--HaUCl ₄ and HAuBr ₄ (Tocher, Whitney, and Diamond)	110
14.	The Extraction of Tetraalkyl Ammonium Hydroxides and the Solvation of the Hydroxide Ion (Agarwal and Diamond)	110
15.	The Aqueous Solution Behavior of Large Univalent Ions: A New Type of Ion Pairing (Diamond)	111
16.	Radiation Chemistry of Peptides: γ -Ray-Induced Oxidation of Poly-L-Glutamic Acid in Aqueous Solution (Sokol, Bennett, and Garrison)	112
17.	Reactions of Organo-Nitrogen Compounds with the Oxidizing and Reducing Species Formed in Water Radiolysis: Reactions of Alanine (Weeks, Cole, and Garrison)	112
18.	A Metastable State of the Doubly Charged Carbon Dioxide Ion (Newton and Sciamanna)	115
19.	Excess-Kinetic-Energy Ions in Organic Mass Spectra (Olmsted, Street, and Newton)	117
20.	Triple Ionization in Small Molecules (Newton)	121
21.	Molecular Beam Electric Resonance Experiments on LiF, LiBr, LiI, and NaF (Hebert, Breivogel, Hollowell, and Street)	121
22.	Energy Levels of AmIV in LaCl ₃ (Conway)	123
23.	Self-Luminescence Spectrum of Bk ³⁺ (5f ⁸) (Gutmacher, Hulet, Worden, and Conway)	125
24.	Use of Electrodeless Discharge Lamps in the Analysis of Atomic Spectra (Conway, Worden, and Gutmacher)	125
25.	Configuration Interaction Effects in l ^N Configurations (Rajnak and Wybourne)	128
26.	Electrostatically Correlated Spin-Orbit Interactions in l ^N -type Configurations (Rajnak and Wybourne)	129
27.	Quadrupole Antishielding in the Rare Earths (Blok and Shirley)	130
28.	Interpretation of Isomer Shifts (Shirley)	132
29.	Angular Distribution of Conversion Electrons from Oriented Ce ^{137m} (Stone, Frankel, and Shirley)	133
30.	Polarization of Silver Nuclei in Iron and Nickel (Westenbarger and Shirley)	136

31.	Hyperfine Structure of ${}_{68}\text{Er}^{171}$ (Maleh)	138
32.	Chemical Effects Following the ${}^{34}\text{S}(n,\gamma){}^{35}\text{S}$ Reaction in Gaseous Sulfur Compounds (Hyder and Markowitz)	138
E. INSTRUMENTATION		
1.	Cyclotron Development Experience (Grunder and Selph)	139
2.	High-Resolution γ -Ray Spectroscopy with Lithium-Drifted Germanium Detectors (Shirley)	144
3.	Mass Spectroscopy (Reynolds)	145
4.	Decay Energy of $\text{U}^{235\text{m}}$ (Bailey and Robinson)	147
5.	Semiconductor Radiation Detectors (Goulding and Hansen)	148
6.	A Linear Amplifier and Gating System (Goulding and Landis)	148
7.	A Method for Phototube Noise Rejection in Low-Energy x-Ray Scintillation Spectrometry (Landis and Goulding)	149
8.	An Improved Particle Identifier Technique (Goulding and Cerny)	149
9.	Automatic Recording of Information from Spectrograms (DeHaro, Nakamura, and Ward)	151
10.	Iron-Free Spectrometer Power Supply and Current-Stepping System (Salz, McClure, and Hollander)	151
11.	A. Digital Gain-Stabilization System (Nakamura and LaPierre)	152
12.	Mössbauer Effect Instrumentation (Zane)	153
13.	Analog Gain Stabilizer (DeHaro)	153
14.	Hilac Operations and Improvements (Ghiorso and Main)	153
F. CHEMICAL ENGINEERING		
1.	Sulfate Reduction by Bacteria (Leban and Wilke)	154
2.	Turbulent Exchange of Momentum, Mass, and Heat Between Fluid Streams and Pipe Wall (Wasan and Wilke)	155
3.	The Addition of Individual Phase Resistances in Mass-Transfer Processes (King)	156
4.	Mechanical and Chemical Properties of Nonequilibrium Liquid-Liquid Interfaces--Studies with the Oscillating Jet (Vandegrift and Vermeulen)	157
5.	Kinetic Studies of Super-Acid Catalysis (Gmitro, Miller, and Vermeulen)	158
6.	Liquid-Liquid and Gas-Liquid Agitation (Clark, Coughlen, and Vermeulen)	159
7.	Axial Mixing (Longitudinal Dispersion) in Packed Extraction and Absorption Columns (Hennico, Moon, and Vermeulen)	160
G. THESIS ABSTRACTS		
1.	Richard N. Chanda (Ph. D.)	163
2.	Alan Emanuel (Ph. D.)	164
3.	Ronald W. Grant (Ph. D.)	165
4.	Edward Anthony Grens II (Ph. D.)	166
5.	Robert Gordon Hickman (Ph. D.)	167
6.	Richard Leslie Kiefer (Ph. D.)	169
7.	Charles Michael Lederer (Ph. D.)	170
8.	James Anthony McHugh, Jr. (Ph. D.)	171
9.	David W. Seegmiller (Ph. D.)	172

10.	Bruce D. Wilkins (Ph. D.)	174
11.	Albert D. Epstein (M. S.)	175
12.	Alfred William Peterson (M. S.)	176
13.	Graham F. Somerville (M. S.)	177
H. AUTHOR INDEX		
1.	Papers Published and UCRL Reports Issued, 1963	178
2.	Contributors to this Report	193

CHEMISTRY DIVISION ANNUAL REPORT, 1963

Lawrence Radiation Laboratory
University of California
Berkeley, California

February 1964

A. RADIOACTIVITY AND NUCLEAR STRUCTURE

1. IN-BEAM NUCLEAR SPECTROSCOPY

F. S. Stephens, Neil Lark, and Richard M. Diamond

Last year's report discussed an investigation of isomeric transitions in odd-mass thallium isotopes studied by γ -ray and conversion electron spectroscopy in the intervals between the 3-msec beam bursts of the Berkeley Hilac. This type of spectroscopic work has been extended to in-beam investigation of the final γ -ray cascade depopulating the excited nucleus after an (HI, xn) reaction. In these first studies, attention has been focused on the transitions in neutron-deficient even-even nuclei in the band of deformed nuclei centering in the heavy rare earths. As in the previous study, the electron spectrometer has been most used because of its higher resolution.

From the conversion electron spectra [an example, from the reaction $\text{Tb}^{159}(\text{B}^{11}, 4n)\text{Yb}^{166}$, is shown in Fig. A. 1-1], it can be seen that certain low- and moderate-energy transitions

stand out very clearly over the background. This is particularly true if the projectile bombarding energy and target thickness are chosen for optimum results. From the K-L conversion electron spacings and from crude excitation functions, elemental and mass assignments, respectively, could be made for the transitions observed. The dominant transitions found in the light Yb, Hf, and W nuclei could readily be assigned to the ground-state rotational band of the resulting even-even nucleus; a partial level scheme deduced for Yb^{166} is shown in Fig. A. 1-2. The rotational band is seen up to the spin 14 member. The observation of so many members of this rotational band with the determination of their transition energies to ± 1 keV allows for a stringent test of current hypotheses on the energy-level structure of such rotating deformed nuclei, and permits certain choices to be made. A detailed analysis of these data is in progress.

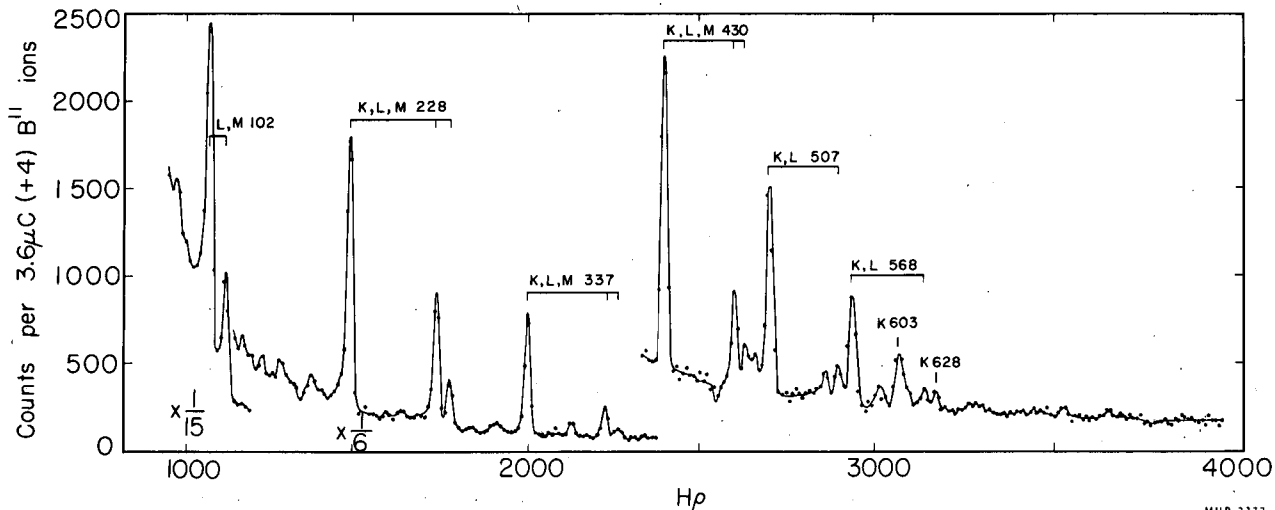
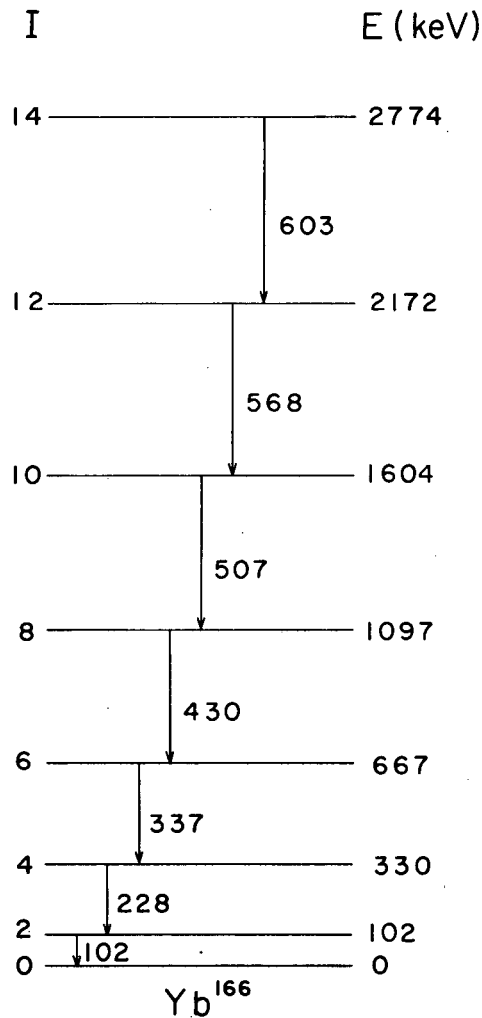


Fig. A. 1-1. Conversion electron spectrum of Yb^{166} .



MU-33612

Fig. A.1-2. Energy-level scheme for Yb^{166} .

2. AN ELECTROSTATIC METHOD FOR THE RECOIL MEASUREMENT OF SUBNANOSECOND NUCLEAR LIFETIMES*

Tihomir Novakov, J. M. Hollander, and Robert L. Graham

The Berkeley iron-free $\pi\sqrt{2}$ beta spectrometer ($\Delta p/p \leq 0.1\%$) has been adapted to measure the lifetimes of excited nuclei recoiling from alpha decay. The method involves the use of an electrostatic device which allows measurement to be made of the distance traveled by the recoil

* Material condensed from T. Novakov, J. M. Hollander, and R. L. Graham, An Electrostatic Method for the Recoil Measurement of Subnanosecond Nuclear Lifetimes, UCRL-10875, July 1963, to be published in Nuclear Instruments and Methods.

atom in the spectrometer before the emission of an internal-conversion electron. A two-grid electrode system, placed close to the source position in the spectrometer, decelerates and then re-accelerates electrons emerging in the spectrometer direction and gives a net acceleration to the electrons that is proportional to the distance traveled by the recoil atom before electron emission. By analysis of the line shapes resulting from application of an electric field in the grid system, one can deduce the distance distribution of the decaying recoils, and from this the time distribution, since the recoil velocity v_r

is known. The method is quantitative and readily applicable to lifetimes $< 10^{-9}$ second.

The shape recorded in the spectrometer of the L_{III} line emitted from the 42.9-keV excited state of Pu^{240} following a decay of Cm^{244} is shown in Fig. A.2-1. The Doppler "shoulder" on the high-energy side of the line, resulting from electrons emitted from moving recoil atoms, is evident. The electric field is arranged so as to affect only the electron distribution in the shoulder.

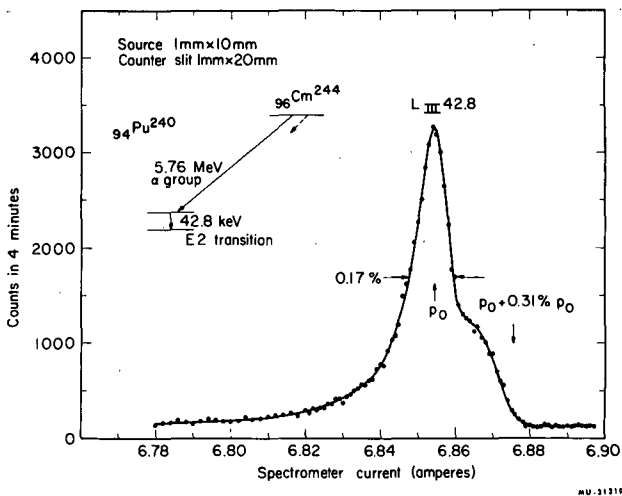


Fig. A.2-1. Shape of the L_{III} 42.8 conversion line in Pu^{240} as observed from an uncovered source of Cm^{244} in an iron-free double-focusing spectrometer.

A diagrammatic view of the grid system is shown in Fig. A.2-2. On application of an electric field V_0/L to the first grid (with second grid and source at ground potential), the energy gain given to a conversion electron emitted from a forward-directed recoil atom is

$$E = l(V_0/L)$$

where l is the distance traveled by the recoil atom before decay. The number of electrons that receive an energy increment is proportional to the number of recoil nuclei decaying (in a

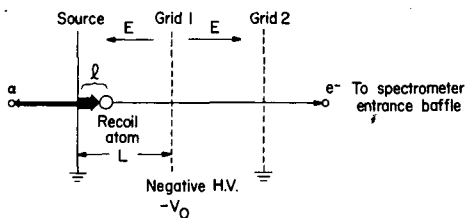


Fig. A.2-2. Basic features of the electrostatic preaccelerator system used in this work.

plane parallel to the source plane) at a distance l . Since the time distribution of recoil atom decays is exponential, so also will be the energy (or momentum) distribution of the electrons emitted from in front of the source ($l > 0$). The effect of applying a voltage to the preaccelerator system is to change the steep high-energy side of the conversion line into an exponential high-energy tail. The slope of this exponential tail, $\epsilon_{1/2}$, is proportional to the half-life of the excited nuclear level $T_{1/2}$. For electrons emitted from atoms recoiling forward ($\cos \theta = 1$), $E_{1/2}$ is related quantitatively to the half-life by the expression

$$T_{1/2} = \frac{\epsilon_{1/2}}{(V_0/L) v_r}$$

Experimentally, electrons emitted from forward-directed recoils are identified in the spectrometer by being observed in coincidence with a particles emitted in the backwards direction.

The effect of an electric field of 39 500 V/cm on the Cm^{244} L_{III} 42.8-keV line in the system described above is shown in Fig. A.2-3. Analysis of the observed exponential slope of the high-energy tail yields the value for the half-life of the 42.9-keV state: $T_{1/2} = 1.6 \times 10^{-10}$ second. This half-life has also been determined electronically by Bell et al. ¹ as $(1.73 \pm 0.15) \times 10^{-10}$ sec-

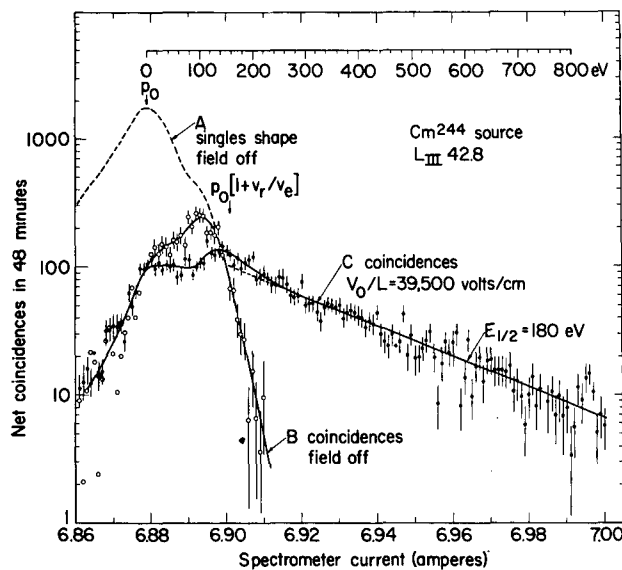


Fig. A.2-3. L_{III} 42.8 conversion line in Pu^{240} as observed in coincidence with a particles at the highest preaccelerator electric field used in this work.

1. R. E. Bell, S. Bjørnholm, and J. C. Severiens, Kgl. Danske Videnskab. Selskab Mat.-Fys. Medd. 32, No. 12 (1960).

ond. It is also possible to determine half-lives by the electrostatic technique described here without the use of coincidence measurements, that is, without selection of recoil direction. The analysis of the resulting line shapes is then slightly more complicated because one must take account of the isotropic emission of recoils, but

essentially identical results are obtained.

The method is expected to have application to the accurate determination of half-lives of excited states as short as $\approx 3 \times 10^{-12}$ sec following a decay and as short as $\approx 3 \times 10^{-13}$ sec following heavy-ion reactions.

3. A STUDY OF THE ENERGY LEVELS OF ${}_{97}\text{Bk}^{249}$

J. M. Hollander, M. D. Holtz, T. Novakov, and R. L. Graham

The availability of high-intensity sources of ${}_{99}\text{Es}^{253}$ has made possible a reinvestigation of the decay scheme of this interesting 20-day isotope by means of the high-precision iron-free beta spectrometer. The preparation of milli-curie-strength sources of Es^{253} was accomplished by long-duration neutron irradiations of appropriate target materials (e. g., Cm^{244}) as part of a continuing program of heavy-isotope production being carried out at this Laboratory by a group under the direction of Dr. Sherman Fried.

The energy levels of ${}_{97}\text{Bk}^{249}$, populated by the α decay of ${}_{99}\text{Es}^{253}$, had previously been studied by means of α , electron, and γ -ray spectroscopic techniques.¹ In the work reported here, the internal conversion electron spectrum was re-examined with the iron-free spectrometer,^{2, 3} and the improved precision of the data has made it possible to undertake a more complete theoretical analysis of the data.

Eighty lines from 23 transitions have been measured and their relative intensities determined in this study. A partial summary of these results is given in Fig. A. 3-1 and Table A. 3-I.⁴ The conversion-electron line widths were 0.2 to 0.3% in momentum, and the transition energies were measured with a precision of a few parts in 10^4 .

The energy levels of Bk^{249} have been divided¹ into three rotational bands based on the single-particle Nilsson orbitals $7/2+ [633]$, $5/2+ [642]$, and $3/2- [521]$. Four previously

uncertain rotational states have been verified in this work, and a new rotational level in the $5/2+$ band has been tentatively identified.

Stephens has calculated energies of the rotational levels in the $5/2+$ and $7/2+$ bands by considering the effects of the Coriolis interaction and particle pairing among the various levels of these bands.⁵ Although qualitative agreement with the data was obtained, the experimental energies were not sufficiently accurate for a really quantitative test of the model.

The calculations have now been extended, and a reasonably good quantitative fit with the present data has been made.

The presence of a large Coriolis interaction in the positive-parity bands is easily demon-

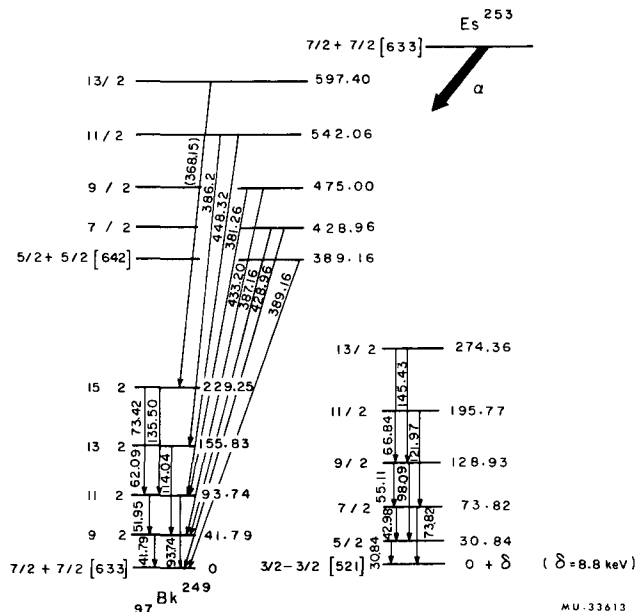


Fig. A. 3-1. Decay scheme of ${}_{99}\text{Es}^{253}$.

5. Frank S. Stephens, unpublished data.

strated. The rotational constant, $\hbar^2/2I$, of the $3/2^-$ band is 6.1 keV, which is similar to the values usually found in odd-mass nuclei of this region, whereas in the $7/2^+$ band it is only 4.5 keV and in the $5/2^+$ band only 5.4 keV. Furthermore there are irregular positive deviations

Table A. 3-I. Some properties of transitions from decay of Es^{253} , as measured with a 50-cm $\pi\sqrt{2}$ iron-free spectrometer.

$I_i \rightarrow I_f$	Transition energy (keV)	Subshell line observed	Approximate line intensity (arbitrary scale)	Multipolarity
Intraband Transitions				
$K\pi = 7/2^+$				
$9/2 \rightarrow 7/2$	41.79	L_I	100,000	M1-E2
		L_{II}	29,000	($\approx 1.7\% E2$)
		L_{III}	12,000	
$11/2 \rightarrow 9/2$	51.95	L_I	12,000	M1-E2
		L_{II}	2,780	($\approx 2.0\% E2$)
		L_{III}	1,080	
$13/2 \rightarrow 11/2$	62.09	M_I	330	M1-E2
		M_{II}	100	
$15/2 \rightarrow 13/2$	73.42	L_I	235	
$11/2 \rightarrow 7/2$	93.74	L_{II}	405	E2
		L_{III}	252	
$13/2 \rightarrow 9/2$	114.04	L_{II}	70	E2
		L_{III}	44	
$15/2 \rightarrow 11/2$	135.50	L_{II}	140	E2
$K\pi = 3/2^-$				
$5/2 \rightarrow 3/2$	30.84	M_I	7,530	M1-E2
		M_{II}	2,180	
$7/2 \rightarrow 5/2$	42.98	L_I	13,600	M1-E2
		L_{II}	2,900	
$9/2 \rightarrow 7/2$	55.11	L_I	3,830	M1-E2
		L_{II}	855	
$11/2 \rightarrow 9/2$	66.84	M_I	330	
$7/2 \rightarrow 3/2$	73.82	L_{II}	900	E2
		L_{III}	570	
		L_I	320	
$9/2 \rightarrow 5/2$	98.09	L_{II}	450	E2
		L_{III}	320	
$11/2 \rightarrow 7/2$	124.97	L_{II}	150	E2
		L_{III}	59	
$13/2 \rightarrow 9/2$	145.43	L_{II}	≈ 1	
Interband Transitions				
$K = 5/2^+ \rightarrow K = 7/2^+$				
$5/2 \rightarrow 7/2$	389.16	K	410	
		L_I	59	
$7/2 \rightarrow 7/2$	428.96	K	64	
		L_I	86	
$7/2 \rightarrow 9/2$	387.16	K	299	
		L_I	86	
$9/2 \rightarrow 9/2$	433.20	K	24	
$9/2 \rightarrow 11/2$	381.26	K	79	
$11/2 \rightarrow 11/2$	448.32	K	5.3	
$11/2 \rightarrow 13/2$	386.2	K	18	
$13/2 \rightarrow 15/2$	368.2	K	≈ 4	

from the $I(I+1)$ formula in the $7/2^+$ band, and large alternating positive and negative deviations in the $5/2^+$ band. These deviations can be understood in terms of mixing of states in different rotational bands via the Coriolis interaction. This interaction couples states that have the same spin and parity but are different by one unit in K (the projection of the spin on the nuclear symmetry axis). Berkelium-249 is a particularly favorable case because in the 82-126 proton shell the only positive parity levels are the seven doubly degenerate states from the $i_{13/2}$ single-particle orbital, and the effect of each of these is included in the calculations. The $7/2^+$ [633] band lies lowest in Bk^{249} , and is affected in first order by the states of the $9/2^+$ [624] and $5/2^+$ [642] bands, in second order by the $11/2^+$ [615] and $3/2^+$ [651] states, and in third order by the $13/2^+$ [606] and $1/2^+$ [660] states. The third-order effect of the $1/2^+$ [660] band on the $7/2^+$ [633] band, although small, can be seen because the alternating structure of the $1/2^+$ band causes the $9/2^+$ and $13/2^+$ levels of the $7/2^+$ band to be depressed more than the other levels. This alternation is shown in Fig. A. 3-2. The effect of the $1/2^+$

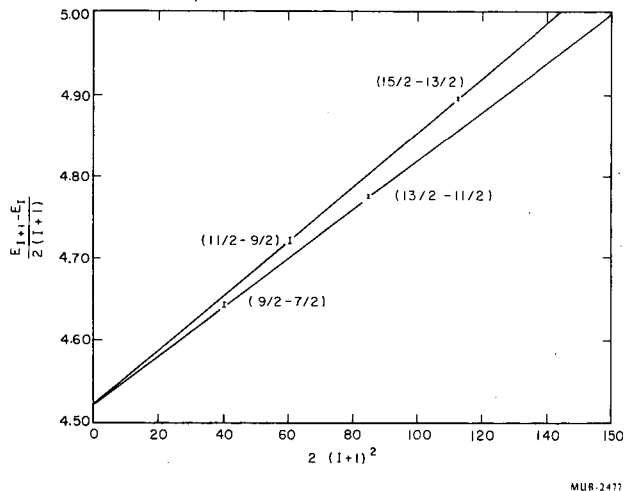


Fig. A. 3-2. Illustration of the influence of the $K = 1/2^+$ band on the $K = 7/2^+$ band in Bk^{249} . Without this influence the above plot should give one straight line, according to the rotational formula $E_{I+1/2} - E_{I/2} = A + 2B(I+1)^2$. Because of the alternating effect of the $1/2^+$ band two sets of points are obtained which for low values of I can be approximated by two straight lines.

I	E_{γ}	$E_{\sqrt{2(I+1)}}$
$7/2$	41.79	4.643
$9/2$		
$11/2$	51.95	4.723
$13/2$		
$15/2$	62.09	4.776
	73.42	4.895

A = 4.522 keV
B = 0.00316 keV

band on the 5/2+ band is much larger, since here the interaction is in second order.

Calculation of the energy shifts caused by the mixing has been done by solving a secular determinant for each I value, in which the diagonal elements E_{IK} are the unperturbed energies of the state I in the various rotational bands and the elements one off the diagonal are the Coriolis matrix elements. (All other matrix elements are set equal to zero.) The lowest two eigenvalues of the determinant correspond to the perturbed energies of the state of spin I in the 7/2+ and 5/2+ bands respectively.

Of the excited positive parity Nilsson levels, only the energy of the 5/2 [642] state is known experimentally. However, approximate values of the energies of the other states have been calculated by Rasmussen et al.⁶ We have used their values together with the constant $\hbar^2/2I = 7$ in order to construct all the rotational bands.

The Coriolis matrix elements were determined from the formula

$$H_{K, K+1}^I = -\frac{\hbar^2}{2I} \sqrt{(I \pm K)(I \pm K + 1)} \sqrt{(j \pm r)(j \pm r + 1)} \quad (1)$$

with the use of Nilsson's eigenfunctions.⁷ As an example, the following determinant was used for the calculation of the perturbed energies of the various states of spin 7/2:

$$\begin{vmatrix} E_{7/2, 1/2}^{-\epsilon} & H_{1/2, 3/2} & 0 & 0 \\ H_{1/2, 3/2} & E_{7/2, 3/2}^{-\epsilon} & H_{3/2, 5/2} & 0 \\ 0 & H_{3/2, 5/2} & E_{7/2, 5/2}^{-\epsilon} & H_{5/2, 7/2} \\ 0 & 0 & H_{5/2, 7/2} & E_{7/2, 7/2}^{-\epsilon} \end{vmatrix} = 0$$

An IBM 7090 computer was programmed to obtain a least-squares fit to the experimental level energies by allowing a selected combination of single-particle energies and Coriolis matrix elements to vary. A good fit can be obtained by allowing variation of only the Coriolis interactions between the 7/2+ and 5/2+ bands and between the 7/2+ and 9/2+ bands, and by simultaneously adjusting the energy of the unperturbed 5/2+ [642] state. Thus a total of three parameters is used to fit nine level ener-

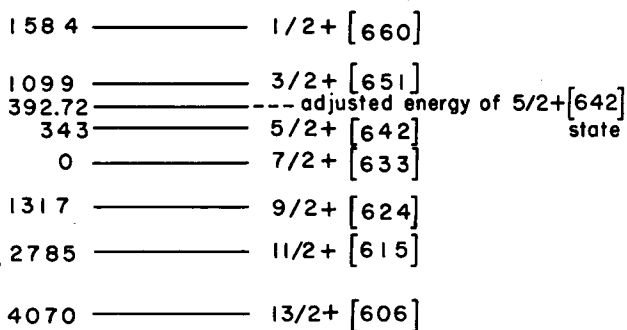
6. J. O. Rasmussen, H. Mang, K. Poggenburg, J. Pradal, and V. Gillet, in Chemistry Division Annual Report, UCRL-9566, Feb. 1961, and private communication.

7. S. G. Nilsson, Kgl. Danske Videnskab, Selskab Mat. - Fys. Medd. 29, No. 161 (1955).

gies. It is interesting to note that it was found necessary to reduce both Coriolis matrix elements appreciably, a fact also noted by Stephens.⁵ Some details of the calculations are shown in Fig. A. 3-3 and Table A. 3-II, and the comparison between experimental and calculated level energies is shown in Fig. A. 3-4.

It may also be worth noting that the fit between calculated and experimental level energies could be improved by further adjusting the energy of the 1/2+ band downward so that this band lies very close to the 3/2+ band. There seems, however, to be no physical basis for this adjustment.

Branching ratios of M1 transitions proceeding between the members of 5/2+ and 7/2+ bands were also calculated, as well as M1-E2 mixing ratios in transitions within the ground-



MU-33604

Fig. A. 3-3. Single-particle energies of Nilsson states derived from the $i_{13/2}$ orbital used in the calculations reported here. The unadjusted values were taken from work of Rasmussen et al., reference 6.

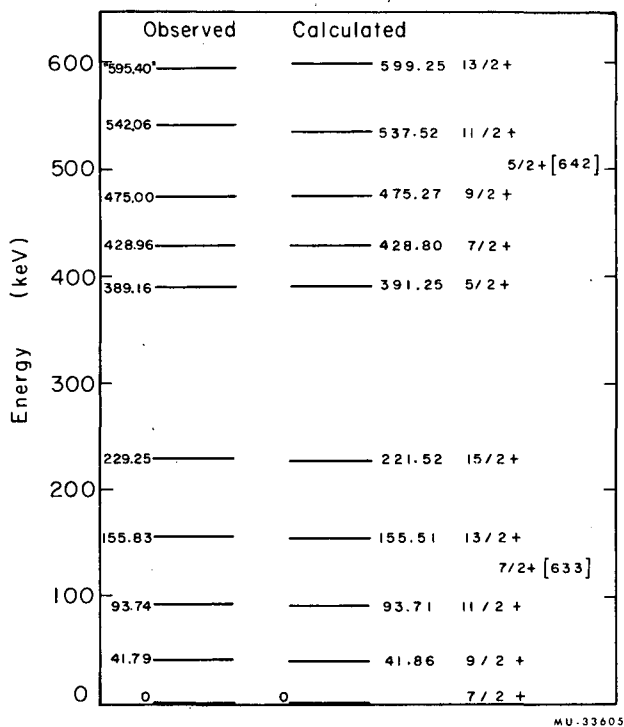
Table A. 3-II. Values of Coriolis matrix elements used in Bk²⁴⁹ energy-level calculations (in keV).

	a.	b.	c.
A _{1/2, 3/2}	44.8	44.8	
A _{3/2, 5/2}	43.5	43.3	
A _{5/2, 7/2}	42.2	34.2	26.4
A _{7/2, 9/2}	43.5	36.3	31.2
A _{9/2, 11/2}	33.9	33.7	
A _{11/2, 13/2}	25.1	25.1	

a. Unadjusted value.

b. After reduction due to pairing force.

c. After adjustment for best fit.



state band, but there are at present insufficient experimental intensity data to allow a meaningful comparison to be made.

Fig. A.3-4. Comparison of observed and calculated level energies in ${}_{97}\text{Bk}^{249}$.

4. DETERMINATION OF THE ATOMIC ELECTRON BINDING ENERGIES IN ELEMENT 97

J. M. Hollander, M. D. Holtz, T. Novakov, and R. L. Graham

The atomic electron binding energy is a quantity of importance in nuclear spectroscopy because of its use in calculating nuclear transition energies from internal conversion electron energy data. Values of atomic binding energies of the various electron shells have usually been obtained from x-ray spectroscopic data, and several tables of atomic electron binding energies are in use.^{1, 2}

Because of the lack of x-ray data for the very heavy elements, the quoted values of the binding energies have necessarily been extrapolations from lower Z. The heaviest element for which direct x-ray measurements have been made is americium (Z = 95); the L-x-ray spectra of this element have been studied by Merrill.³

In some cases it is possible to make use of a high-precision electron spectrometer to determine atomic electron binding energies in a man-

ner independent of x-ray spectroscopy. One such case is illustrated by the partial-level scheme in Fig. A.4-1. In this simple cascade-crossover situation, the absolute transition energy of transition A may be found from the energy difference between any two like (i. e., same subshell) con-

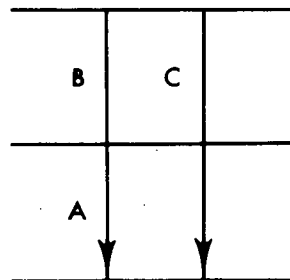


Fig. A.4-1. Cascade-crossover relationship used to obtain absolute transition energy of transition A.

1. Hill, Church, and Mihelich, Rev. Sci. Instr. 23, 523 (1952).

2. E. K. Hyde, Some Useful Tables for Nuclear Spectroscopy in Transmercury Group of Elements: Electron Binding Energies, x-Ray Energies, Auger Electron Energies, and Fluorescent

Yields, UCRL-9642, May 1961.

3. J. J. Merrill, Precision Measurement of x-Ray Spectra with Application to the L x-Ray Spectra of Uranium, Neptunium, and Americium, (Ph.D. Thesis), California Institute of Technology, 1960.

version lines from transitions B and C; because, in taking the difference, the binding energy cancels. Having obtained the absolute energy of transition A, one can then compute the binding energies of the various subshells by subtracting the measured energies of the corresponding subshell conversion electron lines from the transition energy.

The decay of ${}^{253}\text{Es}$ provides opportunity for the direct determination of the atomic binding energies of element 97, which are now known only as extrapolated values. In the decay scheme (Fig. A. 3-1 of Paper A.3 of this report), several cascade-crossover sequences are prominent and may be used for this purpose. These are:

$$E_{\gamma}(51.9) = E_{ic}(93.7) - E_{ic}(41.8).$$

$$E_{\gamma}(43.0) = E_{ic}(73.8) - E_{ic}(30.8).$$

The relative momenta of the subshell internal lines from Es^{253} were measured in the 50-cm iron-free spectrometer with use of a Leeds and Northrup Type K-2 potentiometer. Results of the absolute transition-energy determinations are given in Table A.4-I, and the binding energy calculations are summarized in Table A.4-II.

It was not possible to determine the K binding energy in the same manner as the others because the cascade-crossover sequences used for the determinations were all of such low energy that their transitions do not produce K lines. In-

Table A.4-I. Determination of absolute transition energies of 51.9- and 43.0-keV transitions from Es^{253} decay

A. $E_{\gamma}(51.9) = E_i(93.8) - E_i(41.8)$			
Subshell i	$E_i(93.8)$	$E_i(41.8)$	Difference
L_{II}	69.358 ± 0.022	17.402 ± 0.004	51.956 ± 0.022
L_{III}	74.294 ± 0.022	22.337 ± 0.007	51.957 ± 0.023
M_{II}	87.575 ± 0.031	35.634 ± 0.009	51.941 ± 0.032
M_{III}	88.747 ± 0.031	36.803 ± 0.009	51.944 ± 0.032
			$E_{\gamma} = 51.950 \pm 0.028$
B. $E_{\gamma}(43.0) = E_i(73.8) - E_i(30.8)$			
Subshell i	$E_i(73.8)$	$E_i(30.8)$	Difference
M_{II}	67.650 ± 0.022	24.685 ± 0.007	42.965 ± 0.023
M_{III}	68.831 ± 0.023	25.848 ± 0.007	42.983 ± 0.024
			$E_{\gamma} = 42.974 \pm 0.024$

stead, use was made of the K- L_I energy difference measured for the 387.1- and 389.2-keV transitions, which are fairly strong in the scheme. These data are also included in Table A.4-II. It is interesting to note that the absolute value of the K binding energy so obtained differs by more than 200 eV from the extrapolated value given in the table of Hyde.²

Because of the recent acquisition of a very-high-precision potentiometer (Guildline No. 9144) and because of increased stability of the spectrometer current control system, it will be possible in forthcoming experiments to improve the accuracy of these measurements.

Table A.4-II. Determination of electron binding energies in element 97 (berkelium).

Shell	Transition energy (keV)	Conversion line energy (keV)	Difference (keV)	Selected value	
L_I	51.950 ± 0.028	26.679 ± 0.008	25.271 ± 0.028	L_I	25.272 ± 0.027
	42.974 ± 0.024	17.702 ± 0.006	25.272 ± 0.025		
L_{II}	51.950	27.571 ± 0.008	24.379 ± 0.028	L_{II}	24.382 ± 0.027
	42.974	18.590 ± 0.006	24.384 ± 0.025		
L_{III}	51.950	32.502 ± 0.008	19.448 ± 0.028	L_{III}	19.450 ± 0.027
	42.974	23.522 ± 0.007	19.452 ± 0.025		
M_I	51.950	45.394 ± 0.010	6.556 ± 0.029	M_I	6.555 ± 0.028
	42.974	36.420 ± 0.009	6.554 ± 0.026		
M_{II}	51.950	45.804 ± 0.009	6.146 ± 0.028	M_{II}	6.146 ± 0.028
M_{III}	51.950	46.974 ± 0.010	4.976 ± 0.029	M_{III}	4.976 ± 0.029
N_I	51.950	50.187 ± 0.010	1.763 ± 0.029	N_I	1.755 ± 0.028
	42.974	41.227 ± 0.009	1.747 ± 0.026		
O_I	51.950	51.565 ± 0.010	0.385 ± 0.029	O_I	0.398 ± 0.028
	42.974	42.563 ± 0.009	0.411 ± 0.026		
K	387.1	$K-L_I = 106.25 \pm 0.10$		$K-L_I$	106.29 ± 0.10
	389.2				

5. L-SUBSHELL RATIOS OF MIXED M1-E2 TRANSITIONS

T. Novakov and J. M. Hollander

I. INTRODUCTION

Much experimental and theoretical study has been devoted to the influence of nuclear structure on the internal conversion process. In general two distinct classes of transitions have been examined:

(1) Highly retarded transitions. In these cases the normal (extranuclear) conversion matrix elements are suppressed and the usually small contribution to internal conversion from the penetrating electrons may become significant

In very slow electric dipole transitions, the penetration effects often dominate, and anomalies of as much as a factor of 20 have been observed in the L_I and L_{II} subshells.^{1, 2}

There is also considerable evidence, from conversion coefficient measurements and electron-gamma angular correlation studies, of the effects of nuclear structure on internal conversion of moderately retarded 1-forbidden M1 transitions.³

Some evidence on the influence of the nuclear structure effect on L subshell conversion ratios has been also reported.⁴

(2) Fast transitions. Much effort has gone into the measurement of the K-internal conversion coefficients of E2 transitions, which are generally "fast."^{5, 6, 7} There appears to be good agreement, in most cases, between theory and experiment for K-conversion of E2 transitions, which has been taken as evidence of the essential correctness of the Sliv and Rose theoretical calculations.^{8, 9}

It is interesting to examine the situation between these two extremes, to look for anomalies in internal-conversion coefficients of transitions neither very slow nor very fast. In this paper we report the results of a preliminary study of the L-subshell conversion coefficients of some mixed M1-E2 transitions, carried out with the Berkeley high-resolution 50-cm iron-free $\pi\sqrt{2}$ spectrometer.

Careful study of M1-E2 mixed transitions is also motivated by the practical need to have accurate values of the smaller component (usually a few percent E2) for use in transition-probability correlations with nuclear models, as for example the E2 branching ratio between cascade and cross-over transitions within a rotational band. Also, as interpretation of γ - γ angular distribution data with mixed M1-E2 transitions may depend quite sensitively on the percentage of E2 admixture, it is important to know this quantity as well as possible.

II. RESULTS

When the three L-subshell internal conversion lines are resolved, the M1-E2 mixing ratio is overdetermined because a unique value of $\delta^2(E2/M1)$ is given by any one of the ratios L_I/L_{II} , L_I/L_{III} , or L_{II}/L_{III} . (Only two of these ratios are algebraically independent, of course.) Thus, if all three ratios are measured experimentally, the same value of δ^2 should in principle be obtained.

In fact, this does not appear to be the case.

1. Asaro, Stephens, Hollander, and Perlman, Phys. Rev. 117, 492 (1960).

2. C. J. Herrlander and G. T. Ewan, Anomalous L Subshell Conversion of Some Hindered E1 Transitions in the Rare Earth Region, talk given at the conference: "Role of Atomic Electrons in Nuclear Transformations," Warsaw, Sept. 1963.

3. See, for example, T. R. Gerholm, B. G. Pettersson, V. Van Noijen, and Z. Grabowski, Nucl. Phys. 24, 177 (1964).

4. T. Novakov and R. Stepic, Phys. Letters 3, 82 (1962).

5. See, for example, K. E. Bergqvist and S. Hultberg, Arkiv for Fysik, to be published (1963); S. Hultberg, A Precision Measurement of $(\alpha)_K$ of the 412-keV Transition in Hg^{198} and a High-Resolution Study of the 412-keV Angular Distri-

bution of Gold K-Shell Photoelectrons, talk given at the conference: "Role of Atomic Electrons in Nuclear Transformations," Warsaw, Sept. 1963.

6. J. H. Hamilton, E2 Conversion Coefficients in Sm^{152} , Gd^{154} , and Xe^{132} talk given at the conference: "Role of Atomic Electrons in Nuclear Transformations," Warsaw, Sept. 1963.

7. B. V. Thosar, K-Shell Conversion Coefficients for Pure E2 Transitions in Some Deformed Nuclei, talk given at the conference: "Role of Atomic Electrons in Nuclear Transformations," Warsaw, Sept. 1963.

8. M. E. Rose, Internal Conversion Coefficients (North-Holland Publishing Co., Amsterdam, 1958).

9. L. A. Sliv and I. M. Band, Koefficienti nutrenee konverzii gamma lucei, I, II (Akademia Nauk SSSR, Leningrad 1956, 1958).

Of the six transitions already investigated, agreement within experimental error is obtained in only one case. The experimental situation is illustrated by Figs. A.5-1 and A.5-2, where the results are shown for the 103-keV M1-E2 transition in Eu^{153} , as analyzed with both the Sliv and Rose theoretical coefficients. Table A.5-I summarizes the results obtained to date.

From Table A.5-I it is seen that the E2 admixtures calculated from the three subshell ratios deviate outside the experimental errors in all measured cases when the calculations are made with use of Rose's theoretical coefficients. If instead the theoretical coefficients of Sliv and Band are used, one finds reasonable consistency in the 58-keV rotational transition in Tb^{159} and in the 69-keV rotational transition in Eu^{153} , but not in the other four cases. It is interesting to

note that the two transitions for which there is "agreement" are relatively fast (M1 photon hindrance factors < 50), whereas the transition that gives the largest deviations (the 103-keV interband transition in Eu^{153}) has an M1 photon hindrance factor of ≈ 1000 . If a correlation of this type were in fact substantiated by further experimental data, it would constitute evidence for a nuclear structure effect on the internal conversion of these predominantly M1 transitions. Nuclear structure effects, if present, should affect differently the different electron shells.¹⁰ It is therefore possible that the measurement of L-subshell conversion coefficients or intensity ratios to high accuracy might be a very sensitive tool with which to study such effects in moderately fast transitions.

10. E. L. Church and J. Weneser, *Bull. Am. Phys. Soc.* **7**, 490 (1962), and private communication.

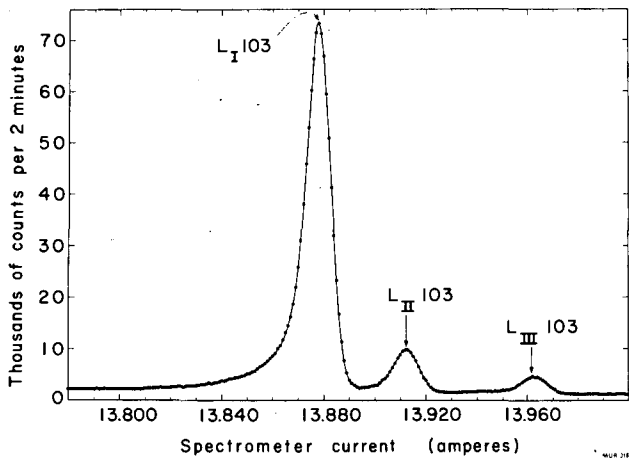


Fig. A.5-1. The L-conversion spectrum of the 103-keV M1-E2 transition in Eu^{153} , recorded by a 50-cm iron-free $\pi\sqrt{2}$ beta spectrometer.

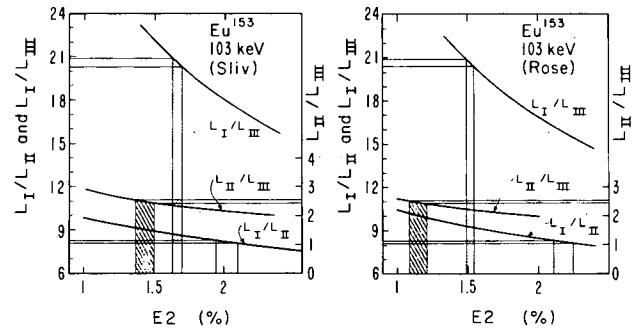


Fig. A.5-2. Analysis of the L-conversion electron intensities with use of both the Sliv and Rose theoretical coefficients. The solid lines represent the theoretical subshell intensity ratios as a function of percentage E2 admixture, and the shaded bands represent the experimental data.

Table A.5-I. Summary of E2 admixtures obtained from Sliv and Rose theoretical tables, in mixed M1-E2 transitions.

Nucleus	Transition energy (keV)	Exp. L subshell ratios			E2 admixture (%) from L subshell ratios					
		$L_I:L_{II}$	$L_I:L_{III}$	$L_{II}:L_{III}$	Rose ^a			Sliv ^b		
		$L_I:L_{II}$	$L_I:L_{III}$	$L_{II}:L_{III}$	$L_I:L_{II}$	$L_I:L_{III}$	$L_{II}:L_{III}$	$L_I:L_{II}$	$L_I:L_{III}$	$L_{II}:L_{III}$
Eu^{153}	69	$6.35 \pm .13$	$9.85 \pm .03$	$1.55 \pm .03$	$1.88 \pm .07$	$1.73 \pm .03$	$1.56 \pm .10$	$1.81 \pm .10$	$1.87 \pm .03$	$2.00 \pm .12$
		$6.22 \pm .08$	$9.87 \pm .10$	$1.59 \pm .03^c$						
Eu^{153}	103	$8.22 \pm .10$	$20.65 \pm .28$	$2.51 \pm .05$	$2.18 \pm .07$	$1.52 \pm .03$	$1.15 \pm .06$	$2.02 \pm .08$	$1.66 \pm .03$	$1.44 \pm .06$
		$8.42 \pm .09$	$20.86 \pm .37$	$2.47 \pm .05^c$						
Tb^{159}	58	$5.96 \pm .21$	$9.47 \pm .29$	$1.59 \pm .07$	$1.52 \pm .08$	$1.29 \pm .04$	$1.02 \pm .12$	$1.43 \pm .12$	$1.40 \pm .05$	$1.37 \pm .13$
Lu^{175}	114	$2.46 \pm .03$	$3.24 \pm .03$	$1.32 \pm .02$	$16.70 \pm .15$	$16.55 \pm .10$	$15.65 \pm .35$	$17.15 \pm .15$	$18.25 \pm .05$	$21.6 \pm .50$
Bk^{249}	42	$3.47 \pm .03$	$8.36 \pm .13$	$2.41 \pm .04$	--	--	--	$1.97 \pm .06$	$1.76 \pm .03$	$1.48 \pm .07$
Bk^{249}	52	$4.35 \pm .03$	$11.33 \pm .16$	$2.60 \pm .04$	--	--	--	$1.79 \pm .05$	$1.98 \pm .03$	$2.23 \pm .09$

a. Reference 8
 b. Reference 9
 c. Measured with the Chalk River $\pi\sqrt{2}$ spectrometer

On the other hand, the present situation appears highly unsatisfactory from a theoretical point of view, because of gross deviations between the Rose theoretical coefficients and those of Sliv and Band, which naturally complicate the interpretation of experimental results. These deviations can be as much as 50% between the values from the two theoretical tables, as illustrated by Fig. A.5-3. This picture shows the ratio of the Sliv theoretical L-subshell values to those of Rose as a function of atomic number for M1 and E2 transitions of energy $0.1 m_0 c^2$.

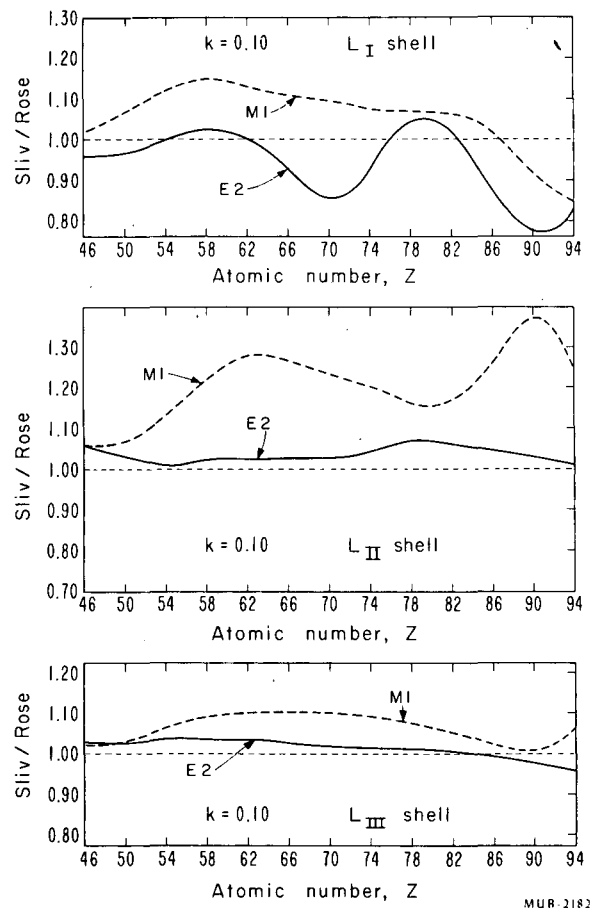


Fig. A.5-3. Graphs of the ratios of Sliv's theoretical conversion coefficients to those of Rose, for the L subshells. The energy plotted here is $k = 0.1$ (≈ 50 keV).

6. LIFETIME AND MULTIPLICITY MEASUREMENTS IN Cs^{131}

D. J. Horen,[†] J. M. Hollander, and R. L. Graham[‡]

Recently, the decay of 11.5-d Ba^{131} was investigated at this Laboratory¹ and a tentative level scheme was proposed that embodied most of the known experimental data. In addition, it was suggested that the 78.6-keV and ground states in Cs^{131} might be the analogies of the ground and 80.99-keV states in Cs^{133} . To investigate this possibility, we have measured the half-life of the 78.6-keV level in Cs^{131} and have determined the multipolarity of the transition originating from this state. In the course of this work, we have also measured (a) the lifetimes of a number of other levels in Cs^{131} ,

(b) the multiplicities of a number of transitions, and (c) the energies of most of the transitions to a higher accuracy than has been done previously.

The apparatus consisted of the Berkeley 50-cm $\pi\sqrt{2}$ iron-free spectrometer,^{2,3} and fast coincidence circuitry which has been described elsewhere.⁴ The lifetime measure-

2. K. Siegbahn, C. L. Nordling, and J. M. Hollander, in Chemistry Division Annual Report, UCRL-10023, Jan. 1962, p. 232.

3. J. M. Hollander and R. L. Graham, in Chemistry Division Annual Report, UCRL-10624, Jan. 1963, p. 273.

4. R. L. Graham, J. M. Hollander, and P. Kleinheinz, Properties of the 57- and 351-keV Excited States in ^{143}Pr , UCRL-10792, June 1963.

[†]Permanent address: Naval Radiological Defense Laboratory, San Francisco, California.

[‡]Permanent address: Physics Division, Atomic Energy of Canada, Ltd., Chalk River, Ontario.

1. W. H. Kelly and D. J. Horen, Nuclear Phys. **47**, 454 (1963).

ments were performed with the spectrometer baffle aperture set for $\approx 0.5\%$ resolution in momentum. The electron detector consisted of a sheet of Naton 136 plastic phosphor, 10 mm wide by 25 mm high by 1 mm thick, optically coupled to a 14-stage CBS 1090 photomultiplier. A larger plastic phosphor mounted on a 14-stage RCA 6810A was placed behind the source to detect K x rays.

The lifetime of the 123.73-keV state was measured by recording coincidences between K 123.73 electrons and K x rays. From a least-squares fit to the slope of the delay curve so obtained, a best value is found for the half-life of the 123.73-keV state:

$$T_{1/2} = 3.7 \pm 0.1 \text{ nsec.}$$

This is in good agreement with the values reported by other workers.^{1, 5}

To measure the lifetime of the 133.54-keV state, the spectrometer current was set to detect the K 133.54 line. Shown in Fig. A.6-1 is the K 133.54 electron-K x-ray delay curve, from which the half-life of the 133.54-keV state was determined as

$$T_{1/2} = 9.3 \pm 0.3 \text{ nsec.}$$

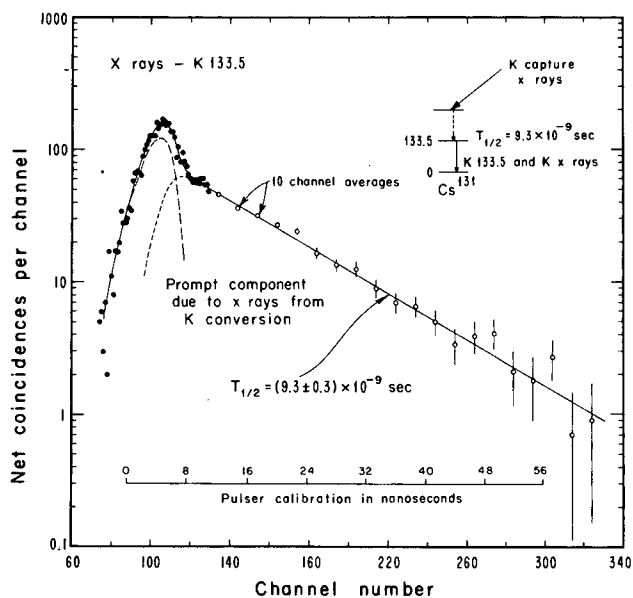


Fig. A.6-1. K 133.54-K x-ray delayed coincidence spectrum (background subtracted). Increasing pulse height above the prompt position represents electrons delayed relative to x rays.

5. Nuclear Data Sheets, National Academy of Sciences, National Research Council (U. S. Government Printing Office, Washington 25, D. C.)

This value is about 30% lower than those previously reported by Bodenstedt et al.⁶ and Kelly and Horen.¹ This difference is probably attributable to the fact that these authors used scintillation detectors for their determinations, in which the width of the energy-selecting channels was such as to measure the lifetimes of the 123.73- and 133.54-keV states simultaneously. Hence, they obtained a compound decay curve with the 13-nsec component much weaker than the 3.7-nsec component. In this work, the higher resolution of the spectrometer allowed us to select in one channel the radiation from only the 133.54-keV state, and a single decay curve with an improved true-to-chance ratio was obtained.

The L 54.84-K x ray delayed coincidence spectrum is shown in Fig. A.6-2. Since the spectrometer was set to detect L electrons there is no prompt contribution to this spectrum. In this figure, increasing pulse height to the right of the prompt position (\approx channel 205) corresponds to the delay of electrons with respect to x rays. Delay to the left (decreasing pulse height) corresponds to coincidences in which x rays follow electrons, and from this portion of the curve the half-life of the 78.69-keV state was measured as

$$T_{1/2} = 9.6 \pm 0.3 \text{ nsec.}$$

A K 216.01-K x ray time spectrum was also

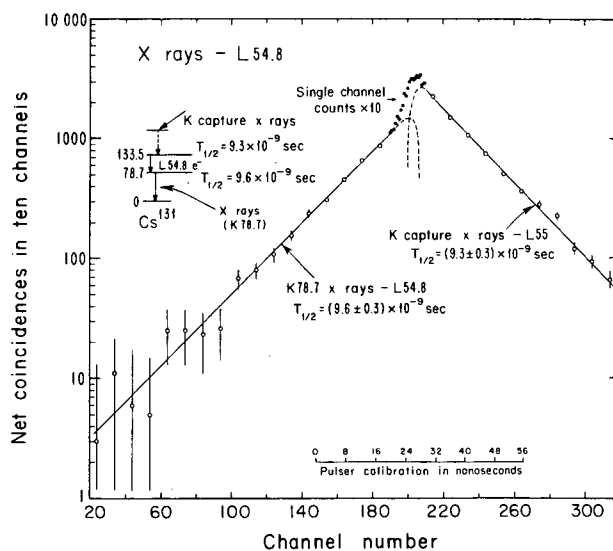


Fig. A.6-2. L 54.84-K x-ray delayed coincidence spectrum (background subtracted). Increasing pulse height above the prompt position represents electrons delayed relative to x rays.

6. E. Bodenstedt, H. J. Körner, C. Günter, D. Hovestadt, and J. Radeloff, Nuclear Phys. 20, 557 (1960).

Table A.6-I. Comparison of γ -ray emission probabilities of the transitions between the first excited and ground states of Cs^{131} ($7/2+ \rightarrow 5/2+$) and Cs^{133} ($5/2+ \rightarrow 7/2+$).

Nucleus	Transition energy (keV)	Multi-polarity	Experiment (sec^{-1})		Theory (sec^{-1}) S. F. = 1		Statistical factor ^a		Expt / Theory	
			T(M1)	T(E2)	T(M1)	T(E2)	M1	E2	M1	E2
Cs^{131}	78.69	99.5% M1 0.5% E2	2.58×10^7	1.30×10^5	1.37×10^{10}	1.51×10^5	1.29	0.143	1.46×10^{-3}	6
Cs^{133}	80.99	97.4% M1	3.98×10^7	1.02×10^6	1.49×10^{10}	1.81×10^5	1.71	0.190	1.56×10^{-3}	30

a. See reference 7.

measured. From the slope of the delay curve, we can set an upper limit for the half-life of the 216.01-keV state as

$$T_{1/2} \leq 0.4 \text{ nsec.}$$

Using the lifetime and multipolarity data obtained in this work, one can compare the γ -ray emission probabilities of the 78.69-keV transition ($7/2+ \rightarrow 5/2+$) in Cs^{131} with those for the analogous transition in Cs^{133} ($5/2+ \rightarrow 7/2+$). The results are given in Table A.6-I. That the M1 emission probabilities are nearly equal (column 10) when the statistical factor (column 8) is included is interpreted as additional support for the $7/2+$ assignment to the 78.69-keV state in Cs^{131} , as well as an indication that the major compositions of the respective levels in Cs^{131} and Cs^{133} are similar.

The E2 emission probabilities, on the other hand, seem to indicate a difference in the components of the wave functions responsible for the small E2 admixtures. That the E2 enhancement in Cs^{131} is considerably smaller than that in Cs^{133} seems surprising, as Cs^{131} is thought to be more deformed than Cs^{133} . With the assumption of a statistical factor of unity, the E2 components of the emission probabilities are nearly equal to the single-particle estimates. This, coupled with the large M1 hindrances, suggests that the $7/2+$ and $5/2+$ states are nearly pure $g_{7/2}$ and $d_{5/2}$ single-particle states, respectively.

A tentative decay scheme for 11.5-d Ba^{131} is shown in Fig. A.6-3. A more detailed account of this work is in preparation.

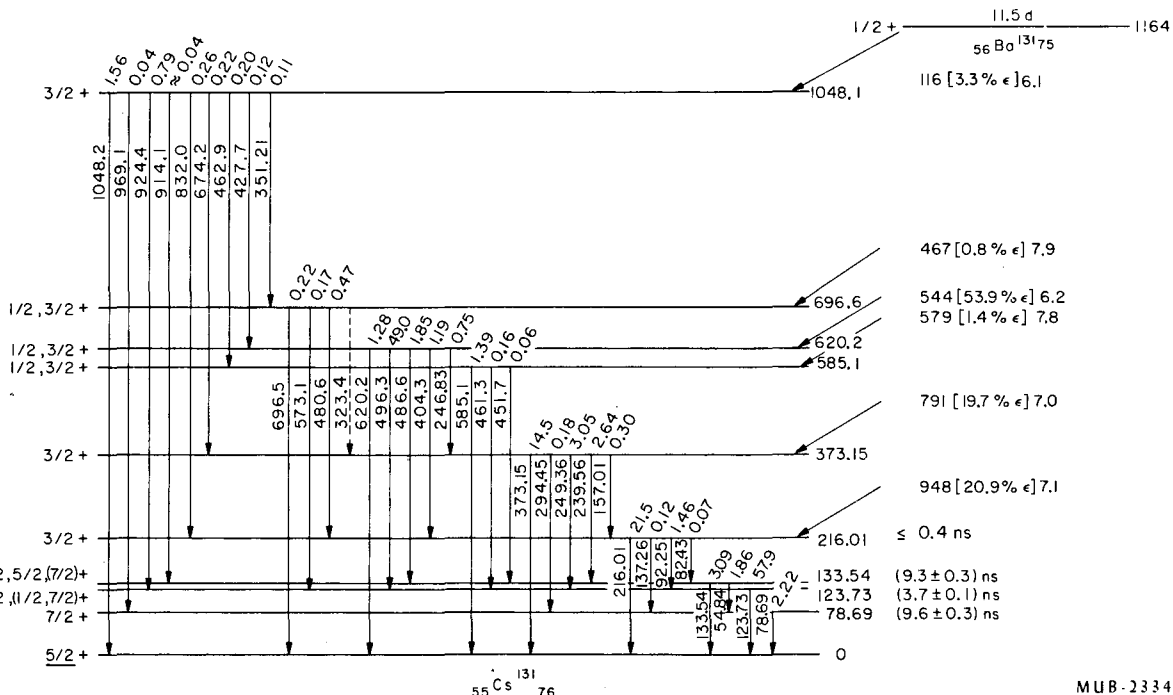


Fig. A.6-3. Tentative decay scheme for 11.5-d Ba^{131} . All energies are given in keV, the percent electron capture within the brackets, and the log ft values to the right of the percent branchings. Spins contained within parenthesis cannot be excluded but are thought improbable. See text for discussion.

7. S. A. Moszkowski, in *Beta and Gamma-Ray Spectroscopy*, edited by K. Siegbahn (North-Holland Publishing Co., Amsterdam, 1955), Ch. 13.

7. PROPERTIES OF THE 57- AND 351-keV EXCITED STATES IN ${}_{59}\text{Pr}^{143(*)}$

R. L. Graham, J. M. Hollander, and P. Kleinheinz

Some features of the decay scheme of 33-hour Ce^{143} have been studied with a 50-cm-radius iron-free beta spectrometer equipped with a nanosecond "time sorter."

From the measured L-subshell conversion ratios the 57.37 \pm 0.05-keV transition is found to be predominantly M1, with less than 0.3% E2 admixture. The half-life of the 57-keV state is measured as 4.17 \pm 0.09 nanoseconds. Similar-

* Abstract of article to be published in Nucl. Phys.

ly, the 293.3 \pm 0.1-keV M1-E2 transition, de-exciting the 350.7-keV level, is found to have a 34 \pm 16% E2 admixture and half-life \leq 0.3 nanosecond. The K line of the 350.7 \pm 0.1-keV cross-over transition has also been observed.

Analysis of these data, in combination with angular correlation results of other experimenters, supports a 5/2+ assignment for the 57.37-keV level, and suggests a 3/2+ assignment for the 350.7-keV state. The magnetic moment of the 57-keV state is discussed in terms of the presently available data.

8. THE DECAY SCHEME OF E^{254}

William C. McHarris, F. S. Stephens, Frank Asaro, and I. Perlman

The alpha and electron spectra of E^{254} were studied with high-resolution magnetic spectrographs, and the decay scheme given in Fig. A.8-1 was worked out. The α groups, their intensities, and their hindrance factors are given in Table A.8-1. It is seen that members of five rotational bands in Bk^{250} are populated. Assigning the values of K and I to the levels was aided by knowing the levels present in two of the neighboring odd-mass nuclides, Bk^{249} from E^{253} decay¹ and Cf^{251} from Fm^{255} decay.² Favored a decay takes place to a K, I π = 7, 7+ band made up of the 7/2+ [633 \uparrow] proton and the 7/2+[613 \uparrow] neutron state;³ therefore E^{254} was assigned this same configuration. This 280-day α -emitting E^{254} was found by closed-cycle calculations to be the ground state, with the 38-hour β emitter lying about 100 keV higher.

The γ -ray spectra were studied by singles, α - γ and γ - γ spectroscopy. The α particles were detected by a ZnS screen sprayed onto a photomultiplier tube, γ rays and L x rays were detected by appropriately mounted NaI crystals,

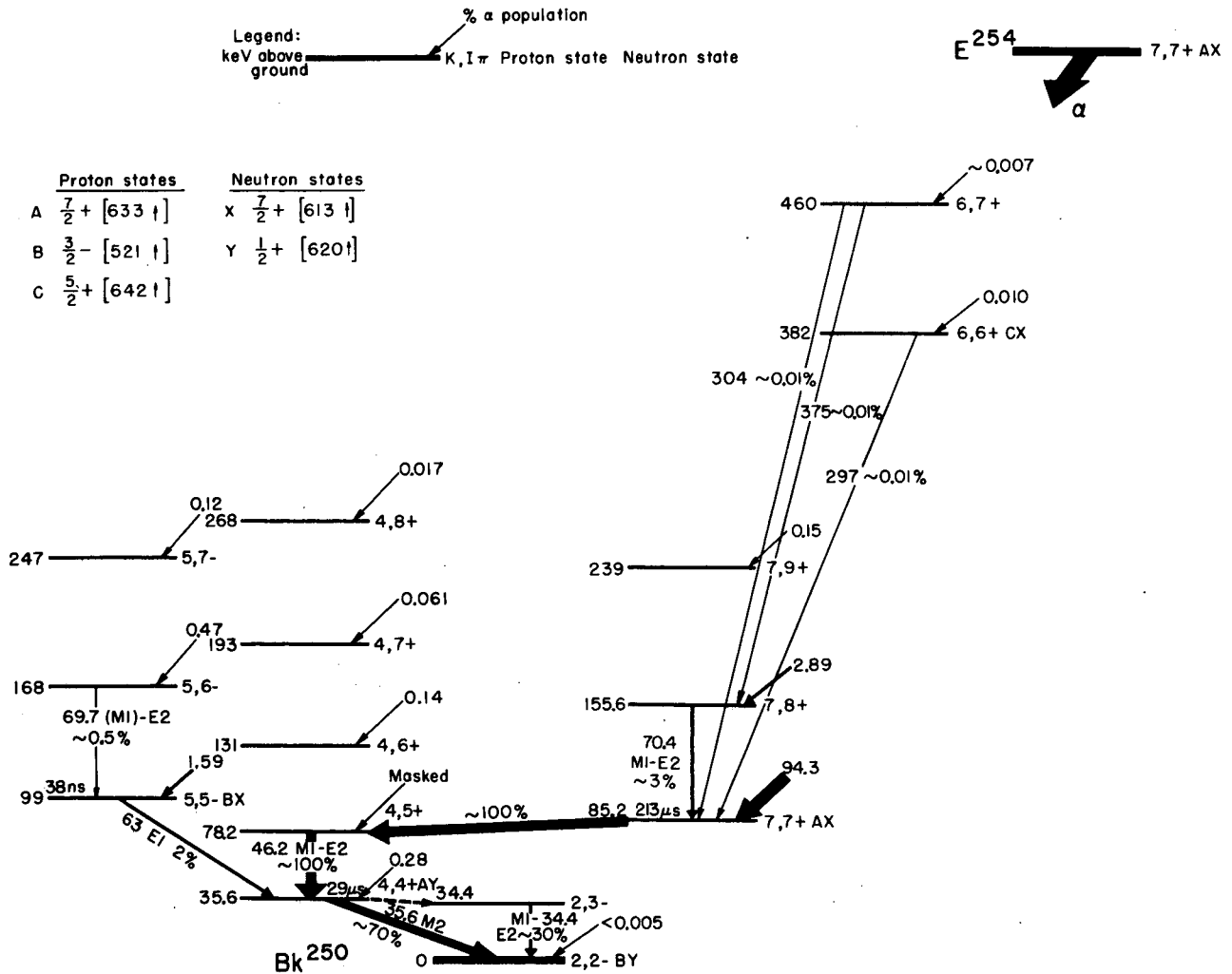
and electrons were detected in a windowless proportional counter. Prompt or delayed coincidence events were investigated by standard techniques with a time-to-height converter.

Working out the sequence of depopulation from the 7, 7+ state in Bk^{250} (which receives 94.3% of the alpha population) to the 2, 2- ground state presented some problems in delay techniques. Of the approximately 220% L vacancies found to accompany a decay, some 200% follow a 213- μ -sec delayed transition. Figure A.8-2 shows the delay curve obtained when a time-to-height converter was started with a pulses and stopped with L x-ray pulses. The "dip" immediately after the prompt edge of this curve indicates a second, shorter-delay transition in cascade with the first. L x-ray vs. L x-ray time-to-height experiments established a 29- μ sec half-life for the second delay. It was then found that the curve shown in Fig. A.8-2 fitted the shape of a theoretical curve for a 213- μ sec half-life followed by a 29- μ sec half-life, with approximately 4% of the 29- μ sec transition starting early and partially filling the "dip." This prompt 29- μ sec component is due to the 63-keV E1 cross-over transition (which was found to have a 38-nsec half-life) from the 5- band and to the rotational transitions that depopulate the upper members of the 4+ band. A delay curve obtained by starting the time-to-height converter with the 63-keV γ and stopping it with L x-ray pulses confirmed that the 29- μ sec delay (but no 213- μ sec

1. F. Asaro, S. G. Thompson, F. S. Stephens, and I. Perlman, Proc. Intern. Conf. Nucl. Structure, Kingston, 1960, p. 581.

2. F. Asaro, S. Bjørnholm, and I. Perlman, Phys. Rev., in press (also UCRL-10635, July 1963).

3. S. G. Nilsson, Kgl. Danske Videnskab. Selskab, Mat.-Fys. Medd. 29, No. 16 (1955).



MUB-2310

Fig. A. 8-1. The decay scheme of E²⁵⁴. Only those states definitely assigned to one of the five rotation bands are shown. The γ intensities and multipolarities are experimentally determined quantities independent of the decay scheme.

Table A.8-I. Alpha energies, abundances, and hindrance factors for the E²⁵⁴ alpha groups.

K, I π of final state	E (MeV)	Q (MeV)	Abundance (%)	Calc. t _{1/2} (days)	Hindrance factor
7, 7+	6.430	6.533	94.3	119.3	2.49
7, 8+	6.361	6.463	2.89	263	36.8
7, 9+	6.279	6.379	0.15	641	300
5, 5-	6.417	6.520	1.59	141	125
5, 6-	6.349	6.451	0.47	296	200
5, 7-	6.271	6.371	0.12	710	325
4, 4+	6.479	6.583	0.28	70.5	1400
4, 5+	masked	6.540	---	112	---
4, 6+	6.385	6.487	0.14	203	990
4, 7+	6.324	6.425	0.061	395	1200
4, 8+	6.250	6.350	0.017	890	1800
(2, 2-)	6.517	6.621	< 0.005	46.4	> 1.2 × 10 ⁶
6, 6+	6.138	6.236	0.010	3010	1300
6, 7+	6.062	6.159	~0.007	7200	~1000

Electron lines down through the O-shell were seen for the 35.5- and 42.6-keV transitions, and down through the N-shell for the 34.4-keV transition. They uniquely established these to be M2, M1-E2, and M1-E2, respectively. The 34.4-keV transition, taken with the decrease in intensity of the 35.5-keV lines with respect to the 42.6-keV lines, shows that the depopulation of the 4, 4+ state branches and the 29- μ sec half-life is a composite of that for the M2 transition and a ≈ 1.1 keV (probably E1) transition to the 2, 3-state. Lines were also seen for the 70.4-keV M1-E2 transition from the 7, 8+ to the 7, 7+ state and for the 69.7-keV transition (mostly E2) from the 5, 6- to the 5, 5-state.

All the levels seen involve the higher-K member of the doublets formed by coupling only the most obviously available single-particle states. None of the lower-K members of these doublets was seen; partly this is because they lie at higher energies for these particular combinations of states, but they would also involve a change in the sign of Σ , which would introduce a large hindrance factor into any a decay to them. delay) followed it. An experiment in which L x rays started the time-to-height converter and electronically delayed pulses from a windowless proportional counter stopped it contained three components in sequence: a reversed 213- μ sec delay, a prompt peak, and a normal 29- μ sec delay -- thus, the cascade that depopulates the 7, 7+ is well established.

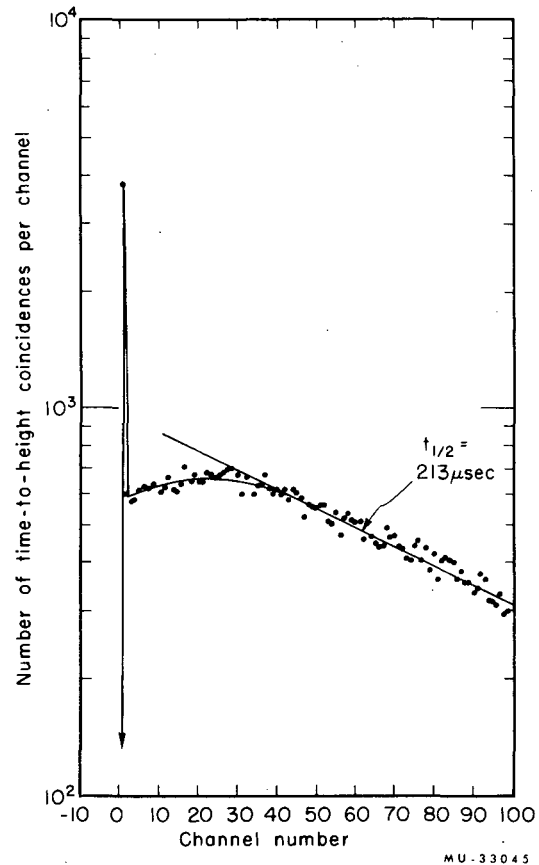


Fig. A.8-2. Delay curve obtained by starting a time-to-height converter with a pulses and stopping it with L x rays. The total ramp sweep was a possible 500 μ sec, with each channel being 3.41 μ sec. The data are shown corrected for channel width.

9. CONCERNING ISOMERS OF At^{208} , At^{206} , AND At^{204}

Per E. Thoresen, Frank Asaro, and I. Perlman

The half-lives of isomers of At^{208} , At^{206} , and At^{204} produced in α -particle bombardments of bismuth were investigated by periodically separating and analyzing the polonium daughters.

Only the shorter-lived "isomer" of each as-

tatine isotope was observed; i. e., 9-min At^{204} , 33-min At^{206} , and 1.6-h At^{208} . It was found that the previously assigned longer-lived isomers of At^{208} , At^{206} , and probably At^{204} were illusions due to chemical effects, and did not actually occur.

10. THE DECAY SCHEME OF Fm²⁵⁵

Frank Asaro, Sven Björnholm, and I. Perlman

The α -decay scheme of Fm²⁵⁵ has been investigated by α -particle, γ -ray, and electron spectroscopy.

Nine α groups were observed with α -particle energies and abundances of

7.122, (0.09 \pm 0.01)%; 7.098, (0.10 \pm 0.01)%;

7.076, (0.43 \pm 0.05)%; 7.019, (93)%;

6.977, (0.11 \pm 0.02)%; 6.960, (5.3 \pm 0.1)%;

6.887, (0.60 \pm 0.03)%; 6.803, (0.12 \pm 0.02)%;

and 6.58 MeV, (4.5 \pm 0.9) $\times 10^{-2}$ %.

The ground state of Cf²⁵¹ was assigned a spin of 1/2 and is probably the 1/2+ [620 \uparrow] Nilsson state. Five members of the rotational band based on the ground state were observed. The value of the decoupling parameter a is 0.24 \pm 0.03, and $\hbar^2/2\mathcal{J}$ has a value of 6.4 \pm 0.3. The ground state of Fm²⁵⁵ decays by an unhind-

ered α transition to a 106-keV state in Cf²⁵¹. Both these states are assigned a spin of 7/2 and are presumably the 7/2+ [613 \uparrow] Nilsson state. Four members of the rotational band based on the 106-keV state in Cf²⁵¹ were observed, and their energies correspond to a value of $\hbar^2/2\mathcal{J}$ of 6.69 \pm 0.03. The 106-keV state with the 7/2+ [613 \uparrow] assignment has a half-life of (3.7 \pm 0.2) $\times 10^{-8}$ sec. The γ rays that de-excite this state to the ground-state band are thought to originate through a multiple Coriolis interaction between two states 0.56 keV apart.

Two other intrinsic levels in Cf²⁵¹ were detected. One at 546 keV was given the assignment of 11/2- [725 \uparrow] and the other, tentatively at 425 keV, was given the assignment 9/2+ [615].

The appropriate α -transition probabilities for the decay to the various states agree well with the expectations for unhindered and hindered α decay.

11. GROUND-STATE ALPHA GROUP OF PROTACTINIUM-229

Vishnubhotla Subrahmanyam, Frank Asaro, and I. Perlman

The energy of the ground-state α particle in the decay of 1.5-d Pa²²⁹ was variously reported by different workers.^{1,2} The fine structure of the α spectrum was studied by Hill,³ who concluded that the 5.665-MeV α particles led to the ground state of Ac²²⁵; the observed but unexplained 5.69-MeV α group was not assigned to the decay of Pa²²⁹ because of the requirement of a 40-keV first excited state⁴ in Ac²²⁵.

Protactinium-229 used in the present in-

vestigations was prepared by bombarding Th²³² foils with protons from the 88-inch cyclotron. The energy of the protons was so chosen as to avoid the formation of Pa²²⁸. The γ spectrum in coincidence with 5.665-MeV α particles of Pa²²⁹ is represented in Fig. A. 11-1--a spectrum that is a combination of four separate experiments under identical conditions from which the background and accidentals are subtracted. Resolving time of the equipment was 0.25 μ sec.

The coincident γ spectrum (Fig. A. 11-1) was resolved into various γ rays by using standard peak shapes. The intensities of the γ rays were determined to be 65 keV (12 \pm 3%); 51 keV (\approx 1%); 40 keV (18 \pm 2.5%); and \approx 26 keV (\approx 0.4%) per α particle populating this state. The observed 40-keV γ ray is believed to be the same one reported by Stephens⁴ in the study of the β decay of Ra²²⁵, which has a multipolarity E1 with a total conversion coefficient of 1.1 and which comes from the depopulation of the first excited state.

1. E. K. Hyde, M. H. Studier, and R. J. Bruehlman, The Properties of Protactinium-229, Argonne National Laboratory Report ANL-4112, 1948, p. 223.

2. W. W. Meinke, A. Ghiorso, and G. T. Seaborg, Phys. Rev. **81**, 782 (1951).

3. Max W. Hill, Nuclear Decay Studies of Protactinium Isotopes (Ph. D. Thesis), UCRL-8423, August 1958.

4. F. S. Stephens, Jr., Phys. Rev. **98**, 262A (1955).

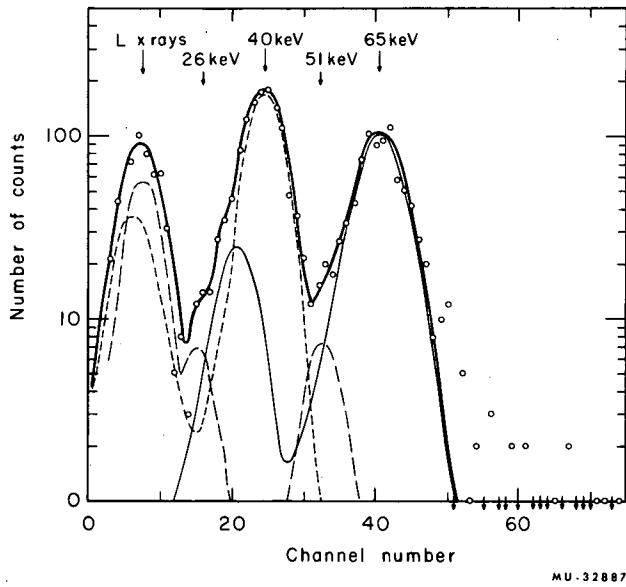


Fig. A. 11-1. Gamma spectrum in coincidence with 5.665-MeV α particles of Pa^{229} .

The two prominent γ rays of 40 and 65 keV are interpreted as parallel transitions. If these two transitions are in cascade, the 65-keV γ ray must proceed through the 40-keV first excited state. A cascade of this nature should produce by coincidence effects a peak at 105 keV that is not observed. The observed 51-keV γ ray re-

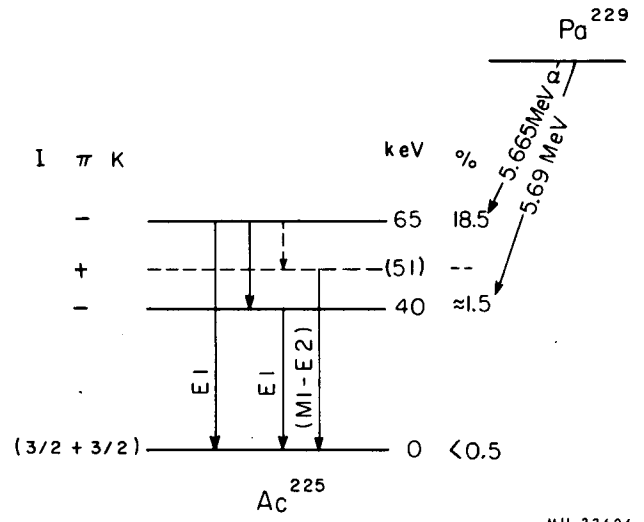


Fig. A. 11-2. Partial decay system of Pa^{229} .

quires the presence of a level at either 51 keV or 14 keV; and the existence of the former is preferred from coincidence studies with other groups of Pa^{229} . A portion of the decay scheme consistent with the above data is represented in Fig. A. 11-2, where the energy of the ground-state alpha particle is 5.73 MeV. The multipolarities of the 51- and 65-keV transitions are derived from the observed intensities of the respective γ rays.

12. ALPHA DECAY OF ACTINIUM-223

Vishnubhotla Subrahmanyam, Duane F. Mosier, Frank Asaro, and I. Perlman

The energies of the various α particles from the decay of 2.2-m Ac^{223} were determined by using surface-barrier gold-silicon solid-state detectors. Samples of Ac^{223} consisted of 3-min recoil collections from vacuum-sublimed Pa^{227} . The energies and abundances of the α particles assigned to the decay of Ac^{223} are shown in Table A. 12-I; these values were determined from a spectra (obtained on a magnetic spectrograph) of Pa^{227} samples in equilibrium with their daughters. The γ spectra determined in coincidence with specific α -particle energies (using recoil-collected samples of Ac^{223}) indicated the presence of transitions represented in the decay scheme shown in Fig. A. 12-1.

Table A. 12-I. Alpha groups of actinium-223

α Particle energy (MeV)	Excited-state energy (keV)	Abundance (%)
6.65 ₇	0	37.6
6.64 ₃	14	42.1
6.56	96	13.3
6.52	136	3.8
6.47	187	3.2

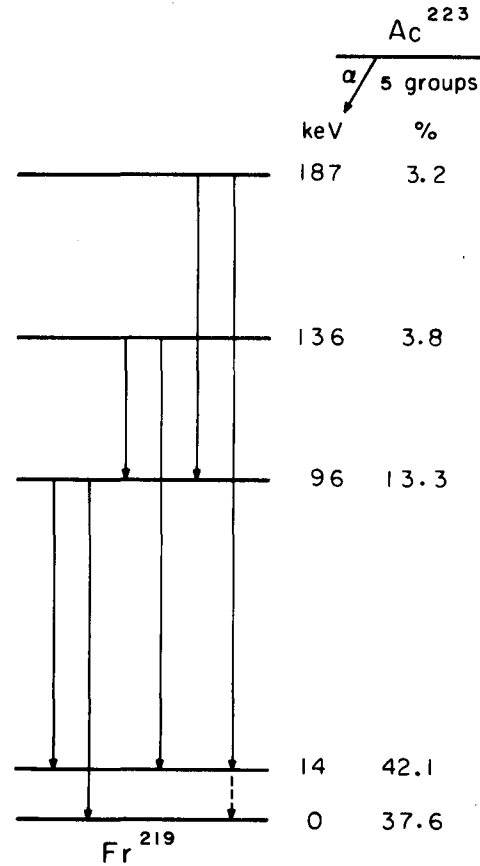


Fig. A. 12-1. Decay scheme of Ac^{223} .

MU-33607

13. NUCLEAR SPINS OF Gd^{153} AND Pm^{148}

Dolores Ali and Richard Marrus

The nuclear spins of two radioactive rare-earth isotopes have been measured by the atomic-beam magnetic-resonance "flop-in" method. They are: $I(\text{Gd}^{153}) = 3/2$ and $I(\text{Pm}^{148}) = 1$. The promethium is produced by neutron irradiation of 2.7- μ Pm^{147} ; and the gadolinium, by neutron irradiation of the natural metal. Continuous-flow β counters are used to detect atoms deposited on platinum target foils. Each isotope is i-

dentified by its measured half-life. The spin measurement of Pm^{148} confirms an earlier measurement by Grant and Shirley.¹ The result for Gd^{153} is consistent with a Nilsson-state assignment $3/2$ [651] for the 89th neutron.

1. R. W. Grant and D. A. Shirley, Phys. Rev. 130, 1100 (1963).

14. ANTIMONY-131 GAMMA SPECTRUM

John A. Cooper, Raymond Gatti, John O. Rasmussen, and Stanley G. Thompson

Nuclei near doubly closed shells are of special interest because of the applicability of shell-model calculations. In the past, nuclei in the region of doubly magic Sn^{132} have not been investigated to the same extent as those near Pb^{208} and Ca^{40} . Studies in the region of Sn^{132} have been limited by the lack of a rapid chemical separation of antimony and tin from fission fragments. With the recent development by Love and Greendale^{1,2} of a rapid separation of Sn and Sb from fission fragments, this region has now been opened to investigation.

In our studies of the neutron-excess isotopes of antimony produced in the fission of Cf^{252} , we observed two γ rays which we have

assigned to Sb^{131} on the basis of previously reported half lives^{3,4,5} and the growth of its daughter, Te^{131} . The energies and intensities are given below.

We have also observed several γ rays belonging to Sb^{132} and Sb^{133} , but because of the complexity of their spectra, more work needs to be done on these isotopes.

Sb^{131} γ rays		
Energy (MeV)	Intensity	Half-life
0.645 ± 0.015	0.39 ± 0.17	26 ± 2 min
0.950 ± 0.020	0.48 ± 0.20	25 ± 2 min

1. A. E. Greendale and D. L. Love, Rapid Radiochemical Procedure for Antimony and Arsenic, USNRDL-TR-607, 17 Jan. 1962.

2. A. E. Greendale and D. L. Love, A Rapid Radiochemical Procedure for Tin, USNRDL-TR-623, 28 Feb. 1963.

3. A. C. Pappas and D. R. Wiles, J. Inorg. Nucl. Chem. 2, 69 (1956).

4. J. Uhler et al., Arkiv Fysik, 21 (3), 46 (1961).

5. P. Del Marmol and J. Colard, Nucl. Phys. 36, 111 (1962).

15. THEORETICAL ALPHA DECAY RATES OF ODD-MASS NUCLEI

Hans Joerg Mang, J. Kenneth Poggenburg, and John O. Rasmussen

The method of Mang and Rasmussen¹ for calculating α -decay rates of spheroidal nuclei in the actinide region from Nilsson's single-particle wave functions has been extended to consider a greater number of states, and has also been applied to odd-mass nuclei. The number of states considered has been increased from ten each, to 25 proton and 40 neutron states.

The proton and neutron states are listed in Table A. 15-I with their single-particle energies, ϵ_{ν} . The energy levels have been slightly modified from those given by Nilsson in order to afford better agreement with observed experimental ground states of odd-mass nuclei. In the nuclei studied, the 76 protons and 106 neutrons in the Nilsson states below those considered do not contribute much to the formation of an alpha wave at the nuclear surface and are arbitrarily treated as an inert core. This core

is accounted for, however, in the deformed potential of the Nilsson representation.

The details of the calculation have previously been given¹ and will only be outlined here. The alpha wave function is roughly proportional to the simple overlap at the nuclear surface of the wave functions of a pair of protons and a pair of neutrons. The calculation of the "overlap integral" Γ_{Lm} for each combination of Nilsson orbitals projects out from the shell-model product wave function the wave function of a four-particle cluster with finite Gaussian internal wave function. Overlap integrals Γ_{LO} were evaluated for $L = 0, 2, 4, 6,$ and 8 for the 25×40 orbitals, giving 5 000 integrals for even-even decay. In favored decay of odd-mass nuclei, the odd-particle state is the same in both initial and final states. This implies that the alpha wave function can be formed from a pair of particles taken from any other state, Fig. A. 15-1a. Thus, only the odd state does not contribute to the alpha formation, and the Γ_{LO} involving that state do not contribute to favored decay. In hindered decay, the odd

1. H. J. Mang and J. O. Rasmussen, Kgl. Danske Videnskab. Selskab Mat.-Fys. Skrifter 4, No. 3 (1962).

Table A. 15-I. Single-particle energies (units of $\kappa \hbar \omega_0 = 331$ keV).

Protons		Neutrons			
$\Omega[Nn_z\Lambda]$	ϵ_v	$\Omega[Nn_z\Lambda]$	ϵ_v	$\Omega[Nn_z\Lambda]$	ϵ_v
1/2[501]	6.721	3/2[602]	6.868	1/2[631]	-12.960
3/2[501]	4.507	1/2[600]	6.636	5/2[622]	-13.095
5/2[503]	2.838	7/2[604]	3.260	5/2[633]	-14.561
1/2[510]	-3.330	5/2[602]	2.568	5/2[752]	-15.058
7/2[503]	-3.658	1/2[611]	-0.286	1/2[501]	-16.382
3/2[512]	-4.249	5/2[613]	-2.228	3/2[631]	-16.384
13/2[606]	-5.540	11/2[606]	-2.639	3/2[761]	-16.569
9/2[505]	-6.936	3/2[611]	-2.832	13/2[606]	-16.900
11/2[615]	-7.421	1/2[750]	-3.313	1/2[770]	-17.378
5/2[512]	-9.545	3/2[752]	-3.755	3/2[642]	-17.394
9/2[624]	-9.679	9/2[604]	-4.790	5/2[503]	-18.077
1/2[521]	-10.981	1/2[761]	-5.623	3/2[501]	-18.553
7/2[514]	-12.328	9/2[615]	-6.990	1/2[640]	-18.853
7/2[633]	-13.406	11/2[725]	-7.293	1/2[651]	-20.443
3/2[521]	-14.753	3/2[622]	-7.446	11/2[615]	-20.661
5/2[642]	-16.705	1/2[620]	-9.000	9/2[624]	-24.020
5/2[523]	-17.006	7/2[613]	-9.188	7/2[633]	-26.920
1/2[530]	-18.815	9/2[734]	-10.343	5/2[642]	-29.285
3/2[651]	-18.833	7/2[624]	-10.952	3/2[651]	-31.011
1/2[400]	-19.760	7/2[743]	-12.954	1/2[660]	-31.957
3/2[402]	-19.940				
11/2[505]	-20.000				
1/2[660]	-20.170				
3/2[532]	-20.824				
1/2[541]	-23.367				

particle is in different states initially and finally. This implies that the alpha wave must be made up from a particle taken from the odd initial state and one taken from the odd final state,

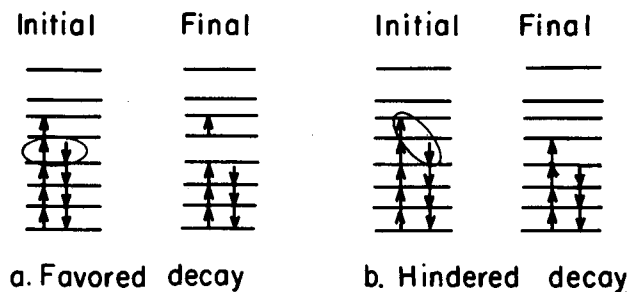


Fig. A. 15-1.

Fig. A. 15-1b. In this case, the overlap integrals must be calculated specifically for the overlap of the two odd particles with pairs of the even kind. This greatly reduces the states that can contribute to a decay and explains the large hindrance factors encountered.

The probability that the various states are occupied by a pair in initial and final states must also be calculated. This is done by using the BCS formulation with a p-p and n-n pairing force. The effect of introducing the nonconstant pairing force matrix elements has been previously reported.² The result of this calculation is a set of occupation probabilities for the various states, v_v^2 . The probability that a state v is

2. J. O. Rasmussen et al., in Chemistry Division Annual Report, 1962, UCRL-10624, Jan. 1963.

unoccupied is u_ν^2 , and the normalization condition is $u_\nu^2 + v_\nu^2 = 1$.

The probability for the formation of the α wave function at the nuclear surface is a function of the probability that proton and neutron states are occupied by pairs in the parent and are vacant in the daughter, and the corresponding Γ_{LO} coefficients for the overlap of these states. Using ν for neutron states and π for proton states, the probability for forming an α particle in an odd-neutron favored decay is proportional to

$$\sum_{\pi} v_\nu i_\nu f_\nu i_\pi f_\pi \Gamma_{LO}(\pi\nu)$$

$\nu \neq \text{odd state}$

In hindered decay, the uv factor for the odd states is unity and the summation reduces to

$$\sum_{\pi} v_\pi i_\pi f_\pi \Gamma_{Lm}(\pi\nu)$$

where the Γ_{Lm} are the specific transition. The result of this summation is a vector G_{LO} which gives the amplitude of the α L waves near the nuclear surface.

The penetration of the anisotropic barrier by the α wave is calculated by a Fröman³

3. P. O. Fröman, Kgl. Danske Videnskab. Selskab Mat.-Fys. Skrifter 1, No. 3 (1957).

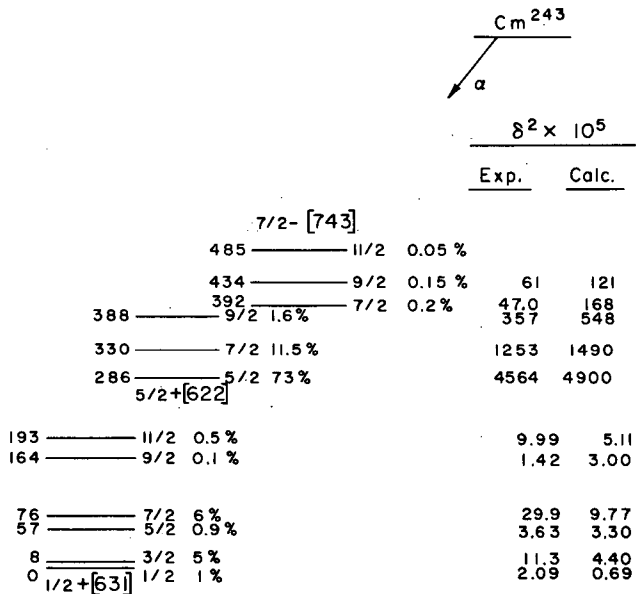
matrix treatment. The anisotropy causes mixing of the various L waves as the α wave is transmitted through the barrier. The amplitudes of the transmitted vector G_{LO} on an infinite sphere are a measure of the transition probabilities of the various α l waves that should be observed experimentally, and the square of the amplitude multiplied by the velocity of the α group is proportional to the reduced width, δ_L^2 .

In Figs. A. 15-2 and A. 15-3 the calculated values of δ^2 are compared with experimental values for transitions of Cm^{243} and Pu^{239} . The intensities were taken from Strominger et al.,⁴ Baranov et al.,⁵ and Novikova et al.⁶ A normalization factor was chosen to give the best agreement for the δ^2 values calculated for Cm^{242} even-even decay. This same factor has been used throughout. There are some systematic deviations apparent. There are several sources for error in the calculations. No allowance has been made for a p-n interaction, which is known to be significant. The barrier penetration treatment is a probable source of error. Despite these, however, the results show generally good agreement and reproduce the enhancement of the intensities of favored transitions.

4. D. Strominger, J. M. Hollander, and G. T. Seaborg, Rev. Mod. Phys. 30, 828 (1958).

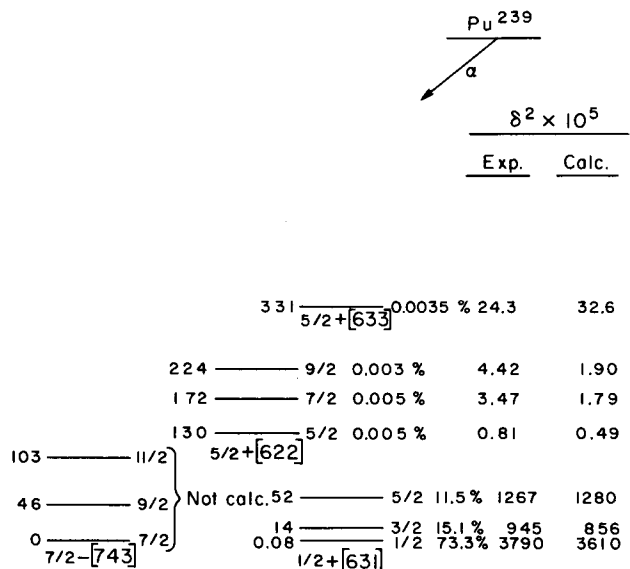
5. S. A. Baranov, V. M. Kulakov, and S. N. Belensky, Nucl. Phys. 41, 95 (1963).

6. G. I. Novikova, L. N. Kondrat'ev, Yu. P. Sobolev, and L. L. Gold'in, Soviet Phys. JETP (English transl.) 5, 832 (1958).



MU-33240

Fig. A. 15-2. Decay scheme for Cm^{243} .



MU-33241

Fig. A. 15-3. Decay scheme for Pu^{239} .

16. ENERGY LEVELS OF Tl²⁰⁸ AND Bi²⁰⁸(*)

Yeong E. Kim† and John O. Rasmussen

Recently, it was demonstrated^{1, 2} that inclusion of a tensor force in the residual nucleon-nucleon force provides a natural explanation of some low-energy nuclear properties of odd-odd spherical nuclei Y⁹⁰ and Bi²¹⁰ and even-even Po²¹⁰. In particular, nuclear spectra of the ground-state multiplet in Bi²¹⁰ and RaE beta decay parameter $i \langle \mathbf{r} \rangle / \langle \boldsymbol{\sigma} \times \mathbf{r} \rangle$ have been explained by Kim and Rasmussen using a phenomenological Gaussian potential which explicitly include the tensor force.²

It is interesting to see if one can obtain reasonable agreement with experimental data, using the same potential for other neighboring odd-odd nuclei with a particle and a hole outside the doubly closed shell. We consider two such nuclei, Tl²⁰⁸ and Bi²⁰⁸, and calculate the energy spectra of low-lying energy levels of these nuclei, using the j-j coupling odd-group model with configuration mixing.

For nuclei with the doubly closed-shell core plus one particle and one hole (Tl²⁰⁸ and Bi²⁰⁸) it is convenient to use the method of second quantization. Brink and Satchler³ showed that the occupation-number representation of Dirac⁴ leads to a simpler procedure than the conventional one for the calculation of the matrix elements of operators in the shell model. The final expression for the matrix elements of two-body interaction for the particle-hole states is given by⁵

$$\begin{aligned} & \langle \bar{j}_1 j_2 JM | V | \bar{j}_1 j_2' JM \rangle \\ &= \sum_{j_c j_c'} \frac{1}{2} \langle j_c j_c' JM | V | j_c j_c' JM \rangle \end{aligned}$$

* Short version of paper to be submitted to Phys. Rev.

† Present address: Bell Telephone Laboratories, Murray Hill, New Jersey.

1. Y. E. Kim, Phys. Rev. **131**, 1712 (1963).
2. P. A. Mello and J. Flores, Nucl. Phys. **47**, 177 (1963); Y. E. Kim and John O. Rasmussen, Nucl. Phys. **47**, 184 (1963).
3. D. M. Brink and G. R. Satchler, Nuovo Cimento **4**, 549 (1956).
4. P. A. M. Dirac, Principles of Quantum Mechanics (Oxford University Press, Oxford, 1958), Ch. X.
5. J. C. Carter, W. T. Pinkston, and W. W. True, Phys. Rev. **120**, 504 (1960).

$$\begin{aligned} & + \sum_{j_c} [- \langle j_c j_1 JM | V | j_c j_1 JM \rangle \\ & + \langle j_c j_2 JM | V | j_c j_2 JM \rangle] \\ & + \langle \bar{j}_1 j_2 JM | i_{12} | \bar{j}_1 j_2' JM \rangle \end{aligned}$$

where³

$$\begin{aligned} \langle \bar{j}_1 j_2 JM | i_{12} | \bar{j}_1 j_2' JM \rangle &= \sum_k (-1)^{j_1+j_2+j_1'+j_2'} \\ & - (2k+1) W(j_2 j_1 j_1' j_2'; kJ) \langle j_1 j_2 kq | v_{12} | j_1 j_2' kq \rangle \end{aligned}$$

Here, the bar indicates the hole state. The method of evaluating the particle-particle matrix element appearing in the above expression has been presented elsewhere.¹

The residual interaction v_{12} is chosen as

$$v_{12} = V^C(\underline{r}_{12}) + V^T(\underline{r}_{12}) S_{12}$$

Here

$$\begin{aligned} V^C(\underline{r}_{12}) &= \left[V_{TE}^C P_{TE} \exp(-\beta_{TE}^C r_{12}^2) + V_{SE}^C P_{SE} \right. \\ & \exp(-\beta_{SE}^C r_{12}^2) + V_{TO}^C P_{TO} \exp(-\beta_{TO}^C r_{12}^2) \\ & \left. + V_{SO}^C P_{SO} \exp(-\beta_{SO}^C r_{12}^2) \right], \end{aligned}$$

and

$$\begin{aligned} V^T(\underline{r}_{12}) &= \left[V_{TE}^T P_{TE} \exp(-\beta_{TE}^T r_{12}^2) \right. \\ & \left. + V_{TO}^T P_{TO} \exp(-\beta_{TO}^T r_{12}^2) \right], \end{aligned}$$

where P_{TE} , P_{SE} , P_{TO} , and P_{SO} are the projection operators for the triplet-even, singlet-even, triplet-odd, and singlet-odd states, respectively, and the V 's are the corresponding strength parameters. The operator S_{12} is the tensor-force operator defined as

$$S_{12} = \frac{3(\boldsymbol{\sigma}_1 \cdot \underline{r}_{12})(\boldsymbol{\sigma}_2 \cdot \underline{r}_{12})}{r_{12}^2} - \boldsymbol{\sigma}_1 \cdot \boldsymbol{\sigma}_2$$

The strength and range parameters V and β , which were used by Kim and Rasmussen as Potential II in the Bi²¹⁰ and Po²¹⁰ calculation,

were used for Tl^{208} and Bi^{208} without any modifications. The experimentally observed levels in Tl^{208} and Bi^{210} are shown in Figs. A.16-1 and A.16-2, respectively. The calculated re-

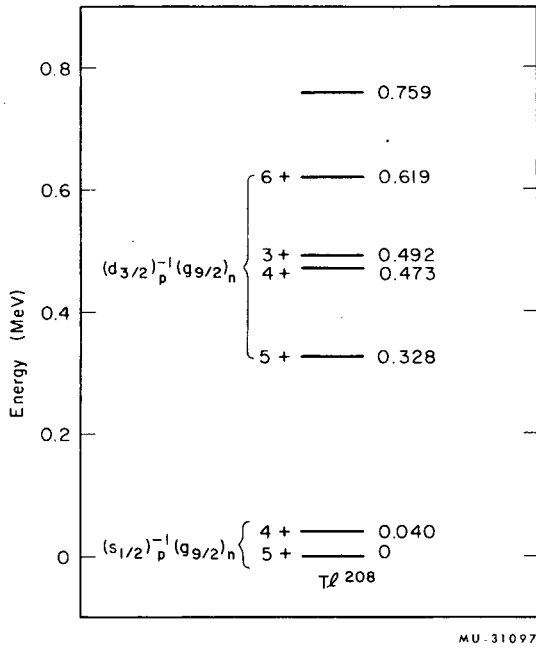


Fig. A.16-1. Experimentally observed low-energy levels in Tl^{208} .

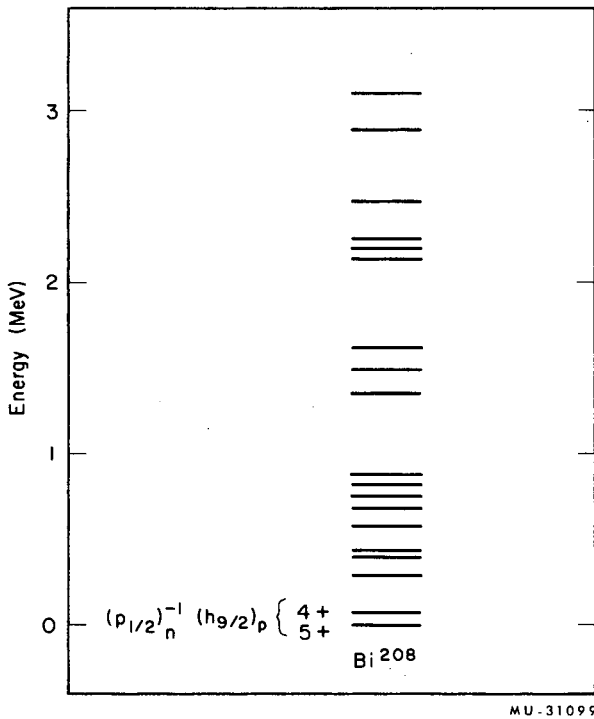


Fig. A.16-2. Experimentally observed low-lying levels in Bi^{208} .

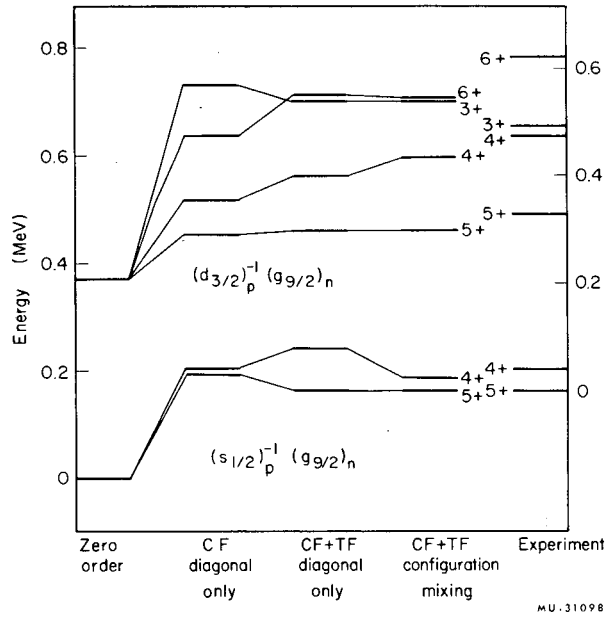


Fig. A.16-3. Comparison of the experimental and calculated spectra of Tl^{208} . The abbreviations CF and TF refer to the central and tensor forces, respectively.

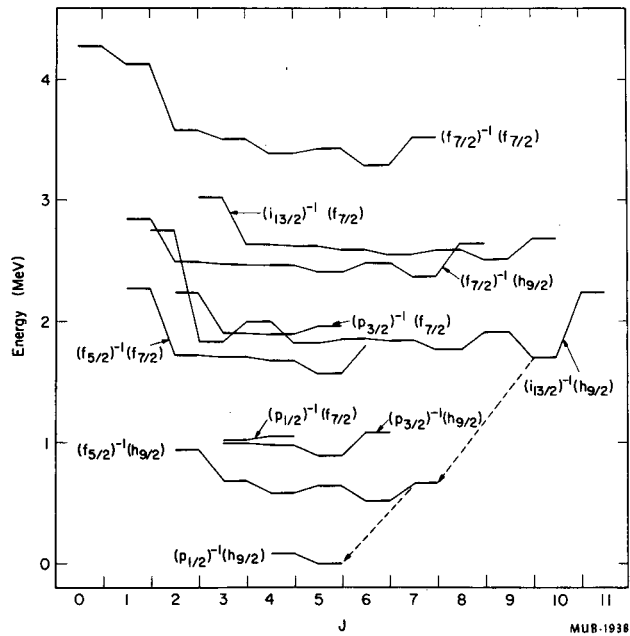


Fig. A.16-4. Calculated energy levels of Bi^{208} . For each spin the left column lists the odd-parity states, and the right column the even-parity states. The various spin-J states arising from the same configuration are connected by lines, and possible E3 and E2 transitions from the isomeric state $[(i_{13/2})^{-1}(h_{9/2})]^{j=10-}$ are shown by arrows and dashed lines.

sults for Tl²⁰⁸ and Bi²⁰⁸ are presented schematically in Figs. A.16-3 and A.16-4, respectively. For Tl²⁰⁸, the agreement of calculated and experimental spectra as seen in Fig. A.16-3 is rather good if one considers that the same potential used in Bi²¹⁰ and Po²¹⁰ was used with-

out any modifications. For Bi²¹⁰, as in Tl²⁰⁸, we obtain rather good agreement on the ground-state doublet. Detailed comparison and discussion of the calculated results for both Tl²⁰⁸ and Bi²⁰⁸ will appear in a forthcoming Physical Review article.

17. A BROAD SURVEY OF TENSOR FORCE EFFECTS ON SPECTRA OF SPHERICAL ODD-ODD NUCLEI

John O. Rasmussen and Yeong E. Kim*

In view of the clear importance of the tensor force components in detailed shell-model calculations of levels of Bi²¹⁰, Y⁹⁰, Bi²⁰⁸, and Tl²⁰⁸,¹ we felt it worthwhile to make a broad survey of the sort of spectra our Bi²¹⁰ force mixture (Bi²¹⁰) would produce in many other nuclei. The main features of a multiplet spectrum of an odd-odd nucleus are determined by the diagonal matrix elements of the n-p residual force, and the effects of taking configuration mixing into account are secondary. For this survey we have, therefore, calculated many diagonal matrix elements with our potential II (given in Table A.17-I) and have plotted them vs the spin of the state. The force components are of Gaussian form, and harmonic oscillator wave functions are used. The oscillator parameter is chosen for a mass region where the con-

figuration could occur, using the formula $\hbar\omega_0 \approx 41 A^{-1/3}$ MeV. The results will be discussed in the following categories:

- I. j_p, j_n , or both equal $1/2$.
- II. $j_p = l_p - 1/2, j_n = l_n - 1/2$ (Nordheim weak rule).
- III. $j_p = l_p \pm 1/2, j_n = l_n \mp 1/2, j_p = j_n$ (Nordheim strong rule).
- IV. Same as III except $j_p \neq j_n$ (strong rule).
- V. $j_p = l_p + 1/2, j_n = l_n + 1/2$ (weak rule).

Figure A.17-1 displays several cases of class I, where at least one $j = 1/2$. The solid lines give the levels for the total force, and the dashed lines for the central force components alone. The difference is due to the tensor com-

Table A.17-I. Values of the force parameters for Potential II used in Bi²¹⁰ and Po²¹⁰ calculations.

Components	Strength (MeV)	Range (F)
Central triplet-even	-355.24	0.706
Central singlet-even	-133.20	1.018
Central triplet-odd	0.0	-----
Central singlet-odd	11.01	1.476
Tensor triplet-even	- 99.28	1.407
Tensor triplet-odd	9.50	1.845

* Present address: Bell Telephone Laboratories, Murray Hill, New Jersey.

1. Y. E. Kim, Phys. Rev. **131**, 1712 (1963); P. A. Mello and J. Flores, Nucl. Phys. **47**, 177 (1963); Y. E. Kim and J. O. Rasmussen, Nucl. Phys. **47**, 184 (1963); Y. E. Kim and J. O. Rasmussen, Energy Levels of Tl²⁰⁸ and Bi²⁰⁸, to be submitted to Phys. Rev; cf. also Y. E. Kim, I. Tensor Force Effects in Nuclear Shell Theory. II. Nuclear Spectroscopic Studies of Isomeric States in Odd-Odd Yttrium Nuclei (Ph.D. Thesis), UCRL-10865, June 1963 (unpublished).

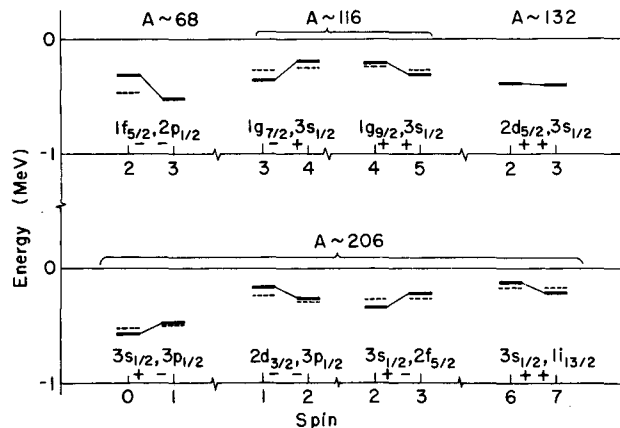


Fig. A.17-1. Energy levels (diagonal matrix elements of n-p force) for several configurations where at least one of the j values is $1/2$. Solid lines are for the complete force including tensor, while dashed lines are for central force components only. The + and - signs denote type of orbital, whether $j = l + 1/2$ or $j = l - 1/2$.

ponents. We see that Nordheim's strong rule² is always obeyed (where $j_p = l_p \pm 1/2$, $j_n = l_n \mp 1/2$, the lower state is the lesser spin) in the three cases given; however, it is the tensor force and not the central force that causes the main splitting in each case. In the other five cases the higher spin lies lower, and again most of the splitting is due to the tensor force. The $2d_{5/2}$, $3s_{1/2}$ configuration is unusual in that the tensor force matrix elements are especially small. For all cases considered in class I, it is seen that the coupling rule of de-Shalit and Walecka³ is always obeyed; the lowest state is the even or odd spin state depending upon whether the parity of the configuration is odd or even, respectively.

Figure A.17-2 displays both "pp" particle-particle (lower half of diagram) and "ph" particle-hole (upper half) spectra for Nordheim weak rule cases with $j_p = l_p - 1/2$ and $j_n = l_n - 1/2$. There is always a close competition for the lowest pp states between the smallest and highest spin states. In the two cases in which $j_p = j_n$ and in the $2f_{7/2}$, $2g_{9/2}$ case, the smallest spin came lowest, and in the other two cases the highest spin came lowest in energy. In the pp

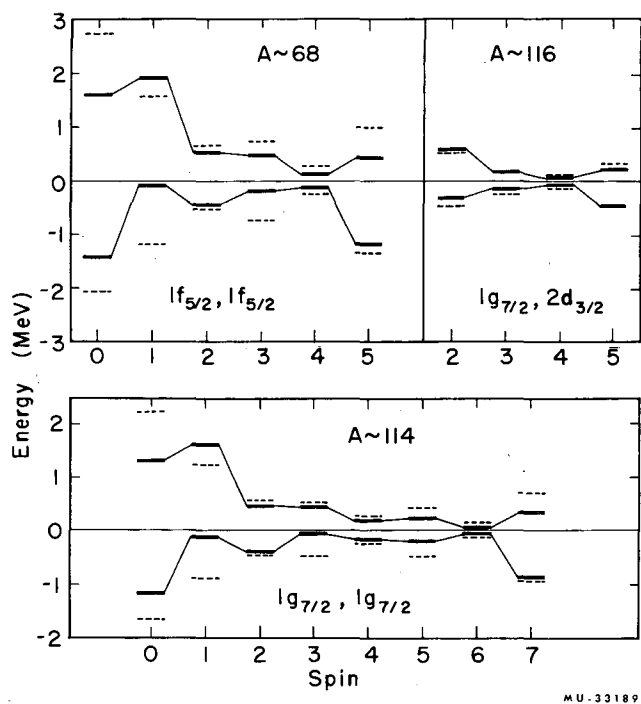


Fig. A.17-2. Theoretical energy levels for $j_p = l_p - 1/2$, $j_n = l_n - 1/2$. The lower half of the diagram applies to the particle-particle (or hole-hole) case, and the upper half to particle-hole.

2. L. W. Nordheim, Phys. Rev. 78, 294 (1950).

3. A. De-Shalit and J. D. Walecka, Nucl. Phys. 22, 184 (1961).

spectra the tensor force is everywhere repulsive except sometimes in the highest spin state. The tensor force has its largest effect on the lower spin states; with central force alone the smallest spin always lies lowest. The overall multiplet splittings where identical orbitals are involved are always larger than in the other cases. For the particle-hole situations, the lowest-lying spin is always $I = j_p + j_n - 1$, and this result is true for the full force or just the central force. This rule was proposed earlier by Brennan and Bernstein⁴ on the basis of data and delta-force calculations of Schwartz.⁵

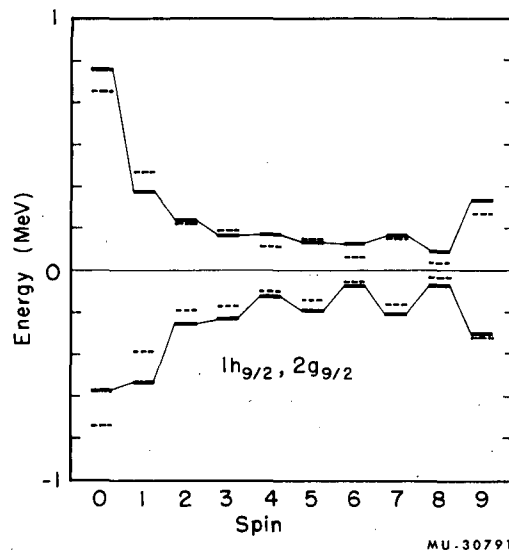


Fig. A.17-3. Energy levels for ground multiplet in Bi^{210} (Nordheim strong rule case with $j_p = j_n$).

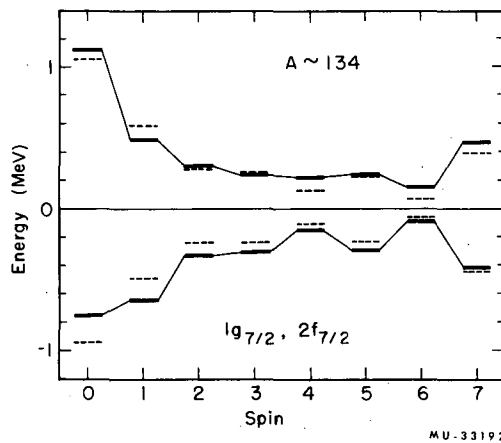


Fig. A.17-4. Energy levels for ground multiplet in Sb^{134} (strong rule with $j_p = j_n$).

4. M. H. Brennan and A. M. Bernstein, Phys. Rev. 120, 927 (1960).

5. C. Schwartz, Phys. Rev. 94, 95 (1954).

Turning now to the Nordheim strong rule cases (classes III and IV), we see in Fig. A.17-3 the diagonal matrix elements from the Bi²¹⁰ study. Here the tensor force is attractive for spins 1 through 8 but small and repulsive for maximum spin 9 and large and repulsive for minimum spin 0. The more detailed study of Bi²¹⁰ showed configuration mixing to lower the 1- more than the 0-, thus making 1- the ground state. Figure A.17-4 shows an entirely analogous behavior for the 1g_{7/2}, 2f_{7/2} configuration, which would be expected lowest in the highly neutron-excess Sb¹³⁴. Figure A.17-5 shows for particle-particle cases a tensor force everywhere attractive [exception: (1f_{5/2}, 2p_{3/2})₄], being largest for the lower spins and enhancing the separation of |j_p-j_n| and j_p+j_n states.

Again all particle-hole cases for classes III and IV have j_p+j_n-1 lowest.

Figures A.17-6, 7 show more weak-rule cases, here with j_p = l_p+1/2 and j_n = l_n+1/2. In contrast to the strong-rule cases we see again as in class II that the tensor force is usually repulsive (exception: (2p_{3/2}, 1f_{7/2})₅).

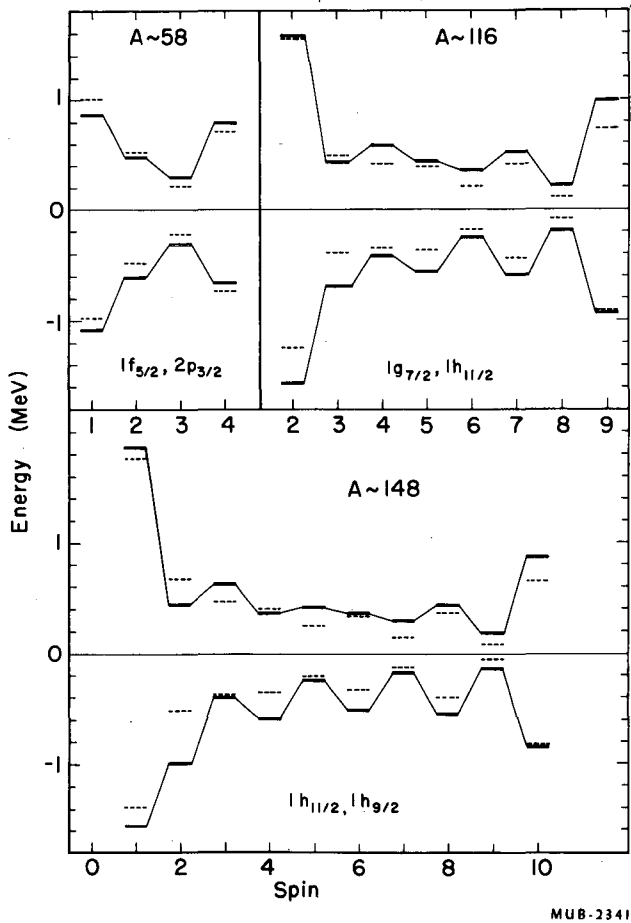


Fig. A.17-5. Energy levels for strong rule cases with j_p ≠ j_n.

Again the overall splittings are largest where identical orbitals are involved, and the smallest spin easily comes lowest in the two cases considered. For the two cases where different orbitals are involved, the competition for ground state between minimum and maximum spins is closer, with the two cases giving different outcomes.

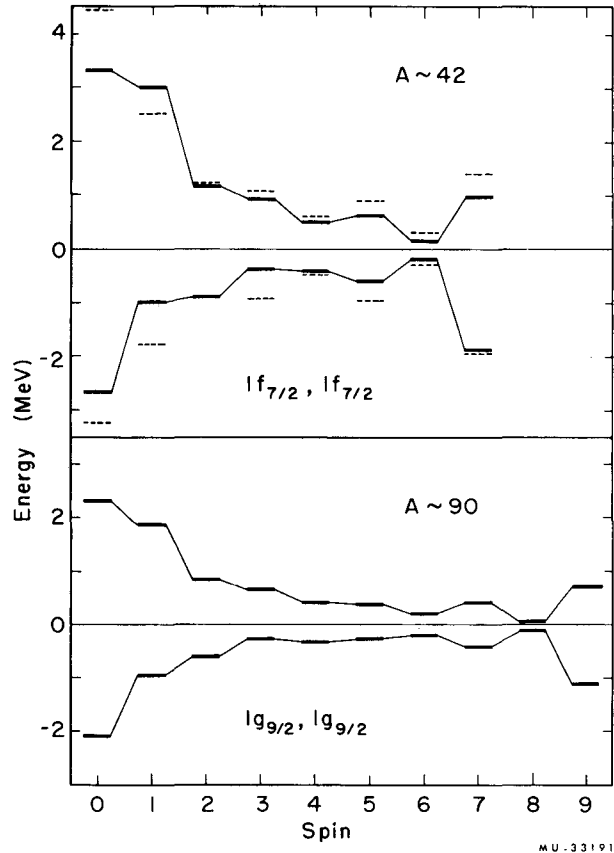


Fig. A.17-6. Energy levels for weak rule cases, where j_p = l_p+1/2, j_n = l_n+1/2.

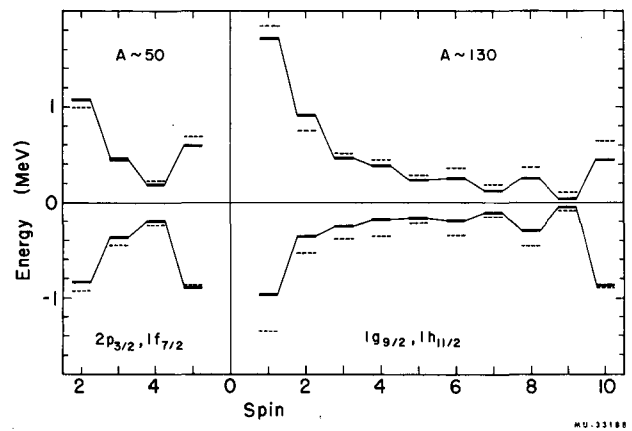


Fig. A.17-7. Energy levels for weak rule cases, where j_p = l_p+1/2, j_n = l_n+1/2.

Again the Brennan-Bernstein rule that $j_p + j_n - 1$ is lowest for p-h cases always holds true.

We see the general tendency for isomerism within multiplets for p-p cases. It would appear unlikely for isomerism to arise in p-h multiplets, since cascade radiation of M1 or E2 transitions would always provide an easy path from any state down to the lowest one.

We would caution against quantitative reliance on these calculations for interpretation of nuclear spectra, for the effects of configura-

tion mixing may not be negligible. Furthermore, the force used was not uniquely determined by the Bi²¹⁰ calculation. In nearby Tl²⁰⁸ it appeared that a stronger tensor force was needed. In using forces without hard cores we are using renormalized effective forces and the renormalization may be different for different nuclei and dependent on how many distant configurations are brought into consideration. Nevertheless we hope that these results can serve as a useful guide to interpretation of experiments, and that further experimental information will be forthcoming to give a deeper insight into shell-model residual forces.

18. QUASI-PARTICLE INTERACTIONS IN EVEN-EVEN SPHERICAL NUCLEI*

Mannque Rho and John O. Rasmussen

The "residual" terms arising from the Bogoliubov-Valatin transformation are studied by perturbation-theory technique in the angular momentum representation. There are three residual interaction terms designated $H_{22}(\eta)$, $H_{40}(\eta)$, and $H_{31}(\eta)$, where η denotes the quasi-particle operator. With these terms as the interaction, one can derive a set of coupled equations that are quite general, and in principle goes beyond the random-phase approximation. It turns out that for excited states in even-even spherical nuclei, $H_{22}(\eta)$ is sufficient,¹ and thus as a first step toward practical calculations, we drop the H_{40} and H_{31} terms. In this approximation, the set of equations reduces to a simple eigenvalue equation. For the case in which ground-state correlation is considered to be important, we introduce the $H_{40}(\eta)$ term to the lowest order into the ground state. Further improvements to the above approximations involve difficult algebra, and we are not sure how significant such treatments could be in view of the fact that the RPA is so far the easiest, and perhaps the best way of approach. However, we aim to investigate the improvements in the future, even though they may be only academic. In this paper, we report the results that were computed to clarify the importance of the quasi-particle behavior through the simplified interactions.

The matrix elements of the residual operators taken between noninteracting quasi-particle states turn out to be a combination of particle-

particle and particle-hole types of interaction (not surprising, since a quasiparticle is a combination of a particle and a hole). For this reason the arguments used for the conventional shell-model calculation are usually inapplicable. Applying the formulas to the single-closed-shell 82-neutron nuclei, we find the following features:

(a) The pairing solutions seem to be satisfactory for force depth $V_0 \approx 33$ MeV, range of interaction $\beta^{-1/2} \approx 1.73$ F, and triplet-to-singlet force ratio $t \approx 0$ (Serber mixture).

(b) For the quasi-particle interactions, the same parameter with $t \approx 1$ seems to fit the experiments satisfactorily. We do not have space to go into details of arguments here, but it can

Table A.18-I. Unperturbed single-particle energies used to solve the Bardeen-Cooper-Schrieffer equation (a) and force constants and ranges used in the "gap" matrix elements (b). We use Set I for most of the calculations.

		Set I	Set II
a	ϵ_a		
	$1g_{7/2}$	0	0
	$2d_{5/2}$	1.00	0.75
	$2d_{3/2}$	2.88	2.90
	$3s_{1/2}$	3.20	3.40
	$1h_{11/2}$	2.18	2.60
	$1h_{9/2}$	∞	5.40
b	v_0	-32.9x MeV	-32.44y MeV
	$\beta^{-1/2}$	1.732 F	1.755 F
		x = 1.0, 1.15, 1.20	
		y = 1.0, 1.05, 1.1	

* Short version of paper to be submitted to Nucl. Phys. (UCRL-11225, Jan. 1964).

1. Robert Arvieu, Description des noyaux sphériques dans un modèle de quasi-particules en interaction. Application aux isotopes de l'étain (Thesis), University of Paris, 1962.

be shown that indeed we need a large attractive triplet force component. The difference in t between (a) and (b) may be accounted for in terms of tensor force effect.

(c) The four-quasi-particle effect on the electric quadrupole transition from first excited $2+$ to $0+$ ground state is coherent with the H_{22} interaction in quadrupole-quadrupole interaction approximation, but may not be so in general finite-range force. In general, the H_{40} interaction is quite small compared with H_{22} interaction.

The results of numerical calculations are given in Tables A.18-I and A.18-II and Figs. A.18-1 through A.18-8. The detailed discussions are presented elsewhere; and hence without justification, we take $t \approx 1$ for the quasi-particle excitations. Let us just mention, however, that many experimental data seem to indicate that our choice of t is a reasonable one, and also that such value may vary significantly depending

upon what values we choose for other parameters.

Finally, we point out that the main results worth attention are (a) energy spectra for $2+$ and $4+$ states, (b) large enhancement of $2+ \rightarrow 0+$ transition probability $[B(E2)]$ for first $2+$, and smaller $B(E2)$ for crossover transition, and (c) considerably large retardation of $B(E2; 4+ \rightarrow 2+)$, both states being first excited J states.

Even though the results given are for $t = 0$ for the BCS solutions and $t \approx 1$ for the pairing interactions, we have also examined the variation of t where the same t is used for both interactions. It turns out that it is difficult to fit experiments [energy level, $B(E2)$, etc.] consistently in this manner.

For formal discussions, and the detail of arguments used in choosing parameters, one should refer to our original paper.

Table A.18-II. $B(E2)$ values for $2+ \rightarrow 0+$ and $4+ \rightarrow 2+$ transitions in units of $10^{-48} \text{ cm}^4 e^2$. Wave functions used in the calculation correspond to those obtained with $V_0 = -32.9x \text{ MeV}$ for $x = 1.15$ and 1.20 , $\beta^{-1/2} = 1.732 F$, $V_{TO}/V_{SE} = 1.0$, and Set I ($e_{\text{eff}} = 2e$).^a

	2+ → 0+ transitions					4+ → first 2+ transitions				
	x	First 2+ → 0+		Second 2+ → 0+		4+ → first 2+			Second	
		B(E2)		B(E2)		B(E2)	B(E2) _{sp}		2+ → 4+	
	H ₂₂ ^b	H ₂₂ +H ₄₀ ^c	B(E2) _{cal} ^c B(E2) _{sp}	B(E2) _{exp} B(E2) _{sp}	H ₂₂	B(E2) _{cal} B(E2) _{sp}	B(E2)	B(E2) _{sp} B(E2) _{cal}	B(E2) _{sp} B(E2) _{cal}	
52Te ¹³⁴	1.15	0.101	0.101	4.9			0.993	2.0		56
	1.20	0.103	0.103	5.0			1.05	1.8		
54Xe ¹³⁶	1.15	0.178	0.169	8.1	0.0122	0.58	0.203	10.0		415
	1.20	0.180	0.174	8.3			0.233	9.0		
56Ba ¹³⁸	1.15	0.228	0.231	10.8	0.0103	0.48	0.29×10 ⁻⁴	7.2×10 ⁴		49
	1.20	0.237	0.240	11.2	14		0.29×10 ⁻²	7.2×10 ²		
58Ce ¹⁴⁰	1.15	0.271	0.284	13.1	0.0038	0.18	0.079	28		14
	1.20	0.283	0.300	13.9	17		0.052	42	17	
60Nd ¹⁴²	1.15	0.331	0.358	16.1	3.02×10 ⁻⁴	0.014	0.084	26		20
	1.20	0.353	0.385	17.3	15		0.077	29		
62Sm ¹⁴⁴	1.15	0.417	0.458	20.2	0.0007	0.025	0.16×10 ⁻³	1.5×10 ⁴		17
	1.20	0.436	0.481	21.1			0.026	86		
64Gd ¹⁴⁶	1.15	0.431	0.469	20.3	0.0365	1.58	1.003	2.3		6.6
	1.20	0.453	0.495	21.5			0.879	2.6		

a. Although it is not shown here, if one uses smaller t (say, $t \approx 0.5$), the matrix elements of the transition operator (for $2+ \rightarrow 0+$) become incoherent, and hence $B(E2)$ for the first $2+ \rightarrow 0+$ transition is reduced. This strongly favors $t \approx 1$ independently of t values used for gap matrix elements.

b. The effect of the H_{22} term on the $B(E2; 2+ \rightarrow 0+)$.

c. The effect of the $H_{22} + H_{40}$ on the $B(E2; 2+ \rightarrow 0+)$.

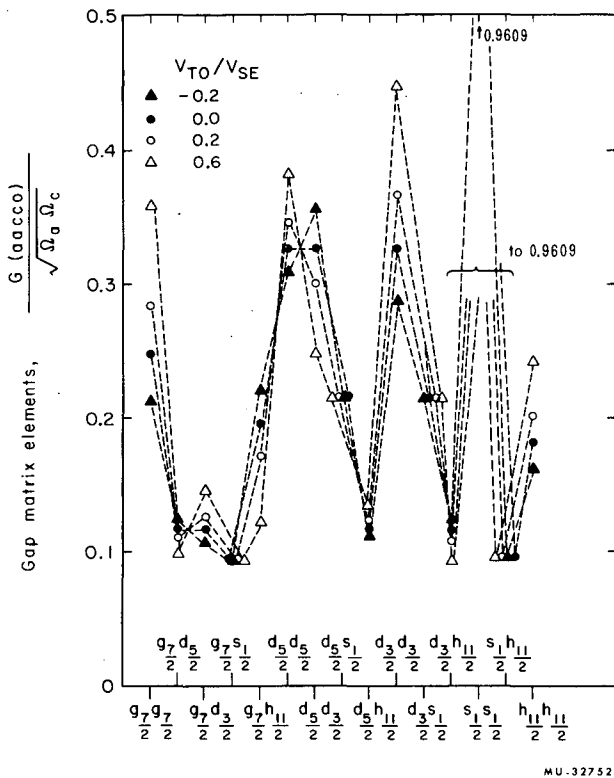


Fig. A.18-1. Gap matrix elements given by $\langle j_a j_a 0 | V | j_b j_b 0 \rangle / [(j_a + 1/2)(j_b + 1/2)]^{1/2}$ (which replace the constant matrix element in the BCS equations) computed with the following parameters: $V_{SE} = -32.4$ MeV, $\beta^{-1/2} = 1.76$ F, oscillator parameter $(\nu^{-1/2}) = 2.29$ F, and $t \equiv V_{TO}/V_{SE} = -0.2, 0.0, 0.2, 0.6$. It is simple to deduce gap matrix elements for other values of t , if two different t values are given, since the matrix element is linear in t .

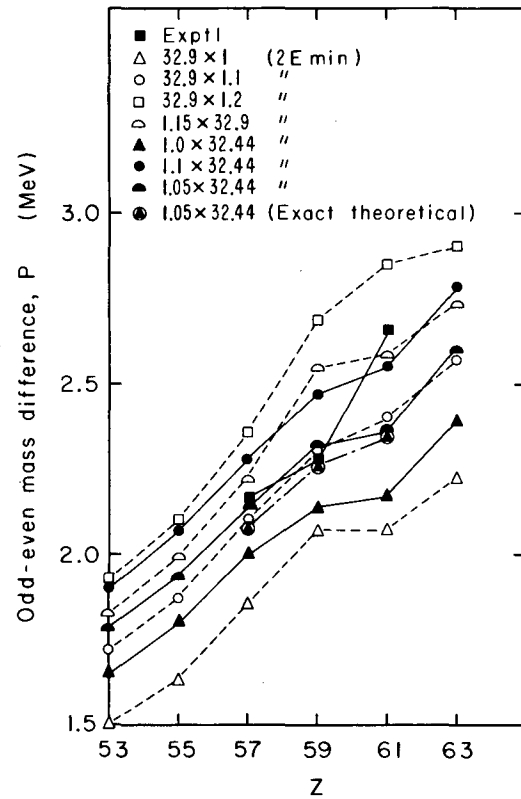


Fig. A.18-2. Theoretical and experimental odd-even mass differences. The experimental points are obtained by the four-point formula $P = 1/2 [-E(Z+1, N) + 3E(Z, N) - 3E(Z-1, N) + E(Z-2, N)]$, and theoretical points are approximated by $2E_{min}$. Various numbers with the symbols correspond to force constants. We have taken $V_{TO}/V_{SE} = 0$. The solid points correspond to Set II and the dashed lines to Set I (Table A.18-I), and the experimental points are given by solid squares connected by a solid line.

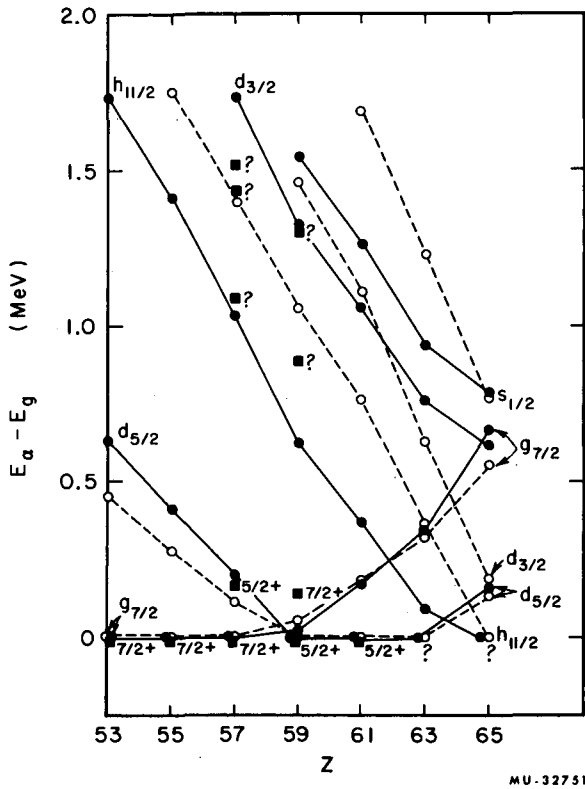
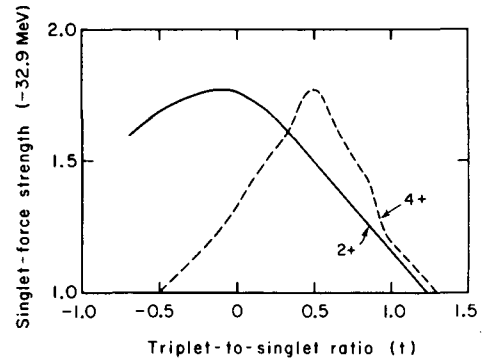


Fig. A.18-3. Single quasi-particle energy (E_i) of 82-neutron odd-A nuclei computed with Sets I and II. The plot corresponds to $E_i - E_g = \sqrt{(\epsilon_i - \lambda)^2 + \Delta_i^2} - \sqrt{(\epsilon_g - \lambda)^2 + \Delta_g^2}$, where subscript g corresponds to the lowest quasi-particle state, $\lambda =$ chemical potential, $\epsilon_i =$ the single-particle energy of i state (as given in Table A.18-I), $\Delta_i =$ half the energy gap of i state. Notice that we have neglected quasi-particle interactions in this computation.

- --- $V_0 = -34.1$ MeV (Set II) with self-energy term
 - — $V_0 = -37.8$ MeV (Set I) without self-energy term
- experiment



MU-33048

Fig. A.18-4. Equi-energy diagram of 2+ and 4+ state for Ce^{140} . This diagram corresponds to $f_J(x, t) =$ constant, where f_J is an eigenvalue (for J state) of our simplified Hamiltonian as a function of x and t [x is the multiplicative factor of $V_{SE} (= -32.9$ MeV), i. e., $xV_{SE} = V_{SE}$, thus corresponding to an effective singlet force; t is the ratio of force mixtures as given by V_{TO}/V_{SE}]. We have set $f_{J=2}(x, t) =$ experimental (lowest) 2+ excitation energy (1.60 MeV), and $f_{J=4}(x, t) =$ experimental (lowest) 4+ excitation energy (2.08 MeV). Other parameters are as given in Set I (Table A.18-I), t for the BCS gap matrix elements is held fixed at $t = 0$, and we have used the following two-quasi-particle configurations: $(d_{5/2}^2)$, $(d_{5/2}g_{7/2})$, $(g_{7/2}^2)$, $(d_{3/2}^2)$, $(h_{11/2}^2)$, $(d_{5/2}d_{3/2})$, $(g_{7/2}d_{3/2})$. The point is to find the values of x and t at which two curves (for 4+ and 2+) come closest. Notice the closest position is at $t \approx 0.3$, $x \approx 1.6$, and then the range $0.9 \lesssim t \lesssim 1.3$, $1 \lesssim x \lesssim 1.2$. It turns out that the $B(E2; 2+ \rightarrow 0+)$, magnetic g factor and odd-even mass difference eliminates the first possibility. Therefore, we choose the latter, which seems to be consistent with other experimental data.

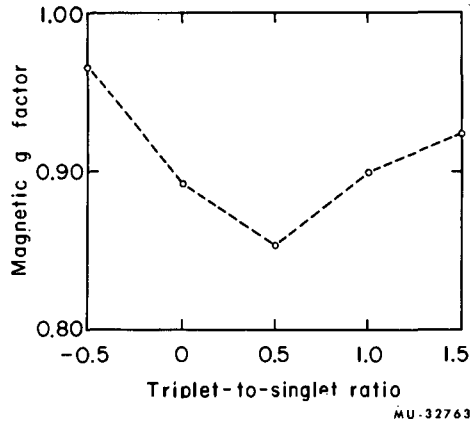


Fig.A.18-8. Magnetic g factor of first excited state of Ce^{140} as a function of t . Only $(d_{5/2}^2)$, $(d_{5/2}g_{7/2})$, and $(g_{7/2}^2)$ are taken into account, with Set I, $x=1.15$. Though the result indicates that $t < 0$ is favored, we have seen that the $B(E2)$ value and relative motion of $2+$ and $4+$ states rule out this possibility. For a given x , the g factor is minimum at $t \approx 0.5$; this and $B(E2)$ results seem to rule out $t \approx 0.3$.

19. COMPARISON OF EXACT AND BCS SOLUTIONS IN PAIRING-FORCE PROBLEMS*

John O. Rasmussen and Mannque Rho

In recent times, many nuclear structure calculations have been made based on the variational method of Bardeen, Cooper, and Schrieffer¹ or, equivalently, the transformation method of Bogoliubov.² The qualitative concepts of the energy gap and the superfluid properties of nuclei have been much used. By comparison with exact solutions, we have sought to examine the validity of the variational methods in finite nuclei, especially for pairing-force strength near the critical strength to produce an energy gap. The properties of a system with complete orbital degeneracy under the influence of a pairing force have been much studied.³

First, we compare exact and BCS solutions in a system such as is encountered in spherical nuclei, where there is some (but incomplete) magnetic degeneracy within orbitals. We shall look at the occupation probability of an upper orbital as a function of pairing-force strength. A convenient measure is the half of the expectation value of the number operator for a certain level η , denoted by $\langle N_{\eta}/2 \rangle$. The relevant e-

quations in the BCS method are given by Belyaev.⁴

In the BCS method, we have

$$\left\langle \frac{N_{\eta}}{2} \right\rangle = \Omega_{\eta} v_{\eta}^2,$$

where Ω_{η} is the pair degeneracy $\Omega_{\eta} = j_{\eta} + 1/2$.

To compare the BCS approximation with an exact treatment, we need to compute the wave function exactly by directly diagonalizing the Hamiltonian matrix. This can be done by employing the "quasi-spin" method introduced originally by Anderson,⁵ and later applied to nuclei by Kerman et al.⁶ This method turns out to be particularly convenient for systems with magnetic degeneracies. To be specific, let us take an example of two orbitals denoted by ξ and η with $\Omega_{\xi} = 4$ and $\Omega_{\eta} = 3$, corresponding to angular momenta of $j_{\xi} = 7/2$ and $j_{\eta} = 5/2$. We take the separation between these two levels to be E , with ξ lying lower, and examine the system of eight particles. In this case, there are four nondegenerate total angular momentum zero states, namely $(7/2)^8(5/2)^0$, $(7/2)^6(5/2)^2$, $(7/2)^4(5/2)^4$, and $(7/2)^2(5/2)^6$. The Hamiltonian matrix ob-

* Condensed version of paper to be published in Phys. Rev. (UCRL-11224, Jan. 1964).

1. J. Bardeen, L. N. Cooper, and J. R. Schrieffer, Phys. Rev. **108**, 1175 (1957).

2. N. N. Bogoliubov, *Nuovo Cimento* **I**, 794 (1958); J. G. Valatin, *Nuovo Cimento* **7**, 843 (1958).

3. B. Mottelson, in *The Many Body Problem* (Dunod, Paris, 1959).

4. S. T. Belyaev, Kgl. Danske Videnskab. Selskab, Mat.-Fys. Medd. **31**, No. 11 (1959).

5. P. W. Anderson, Phys. Rev. **112**, 1900 (1958).

6. A. K. Kerman, R. D. Lawson, and M. H. Macfarlane, Phys. Rev. **124**, 162 (1961).

tained from the reduced Hamiltonian (which assumes only the scattering of a pair of particles with zero total projection of J) can be computed to yield

$$H_{\text{red}} = \begin{bmatrix} -4G & -2\sqrt{3}G & 0 & 0 \\ -2\sqrt{3}G & 2E-9G & -2\sqrt{6}G & 0 \\ 0 & -2\sqrt{6}G & 4E-10G & -3\sqrt{2}G \\ 0 & 0 & -3\sqrt{2}G & 6E-7G \end{bmatrix} \quad (1)$$

where we have taken a constant pairing-force matrix element $G > 0$. This Hamiltonian can be easily diagonalized, and from the eigenvector for the lowest eigenvalue we calculate the value of $\langle N_{\eta}/2 \rangle$ to compare to the BCS result. The results for both the BCS method and the exact solution are plotted in Fig. A.19-1, where we have taken the orbital energy difference E to be 1 MeV. The two solutions approach each other for sufficiently large coupling constant, exhibiting that the BCS method is exact in the strong-coupling limit. In our case, as $G \rightarrow \infty$, it is clear the BCS solution yields

$$v_{\xi}^2 = v_{\eta}^2 = \frac{4}{7}, \text{ and } \frac{N_{\xi}}{2} = \frac{16}{7}.$$

The reduced Hamiltonian can be shown in the strong coupling limit (dropping the unperturbed energy terms) to be diagonal if we choose a slightly different representation from that which led to the above Hamiltonian. [The Hamiltonian given by (1) is obtained through "m-representation," while the one diagonal in strong-coupling limit can be derived through "j-representation."]

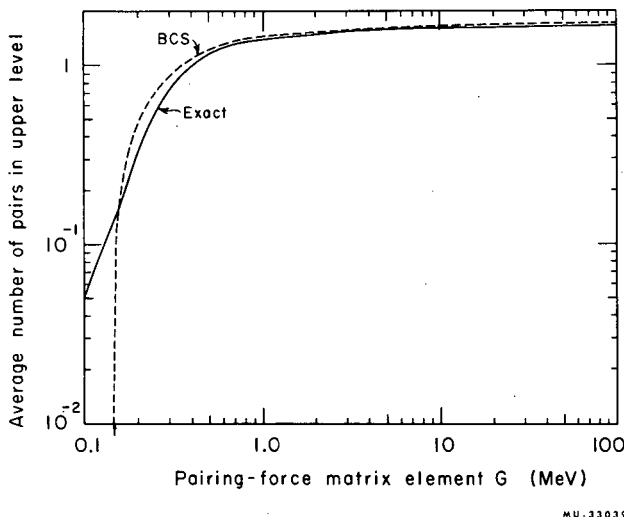
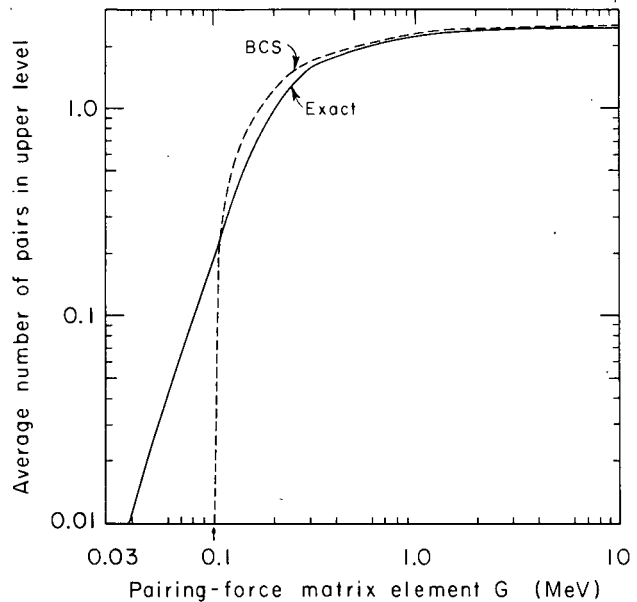


Fig. A.19-1. Average number of pairs in the upper level $\langle N_{\eta}/2 \rangle$, where $j_{\xi} = 7/2$, $j_{\eta} = 5/2$, $N = 8$, $E = 1$ MeV. The arrow indicates the critical force strength.



MU-33040

Fig. A.19-2. Average number of pairs in the upper level $\langle N_{\eta}/2 \rangle$, where $j_{\xi} = j_{\eta} = 9/2$, $N = 10$, $E = 1$ MeV. The arrow indicates the critical force strength.

It can be shown exactly that this method yields $\langle N_{\xi}/2 \rangle = 16/7$. The two methods seem to agree exactly at $G \approx 0.16$ MeV, and then deviate in the opposite direction. It is interesting to notice that the agreement comes just above the "threshold," below which the BCS method yields only the trivial solution with no configuration mixing.

The nuclear system closest to our example is Ce^{140} , which Kisslinger and Sorensen⁷ studied with $G = 0.174$ MeV, but with inclusion of three higher orbitals. The equivalent G for Fig. A.19-1 would thus be a renormalized value somewhat greater than 0.17, but probably well within the region where the BCS method considerably overestimates configuration mixing.

In Fig. A.19-2 we plot the analogous results for a somewhat larger system, ten particles in two orbitals with $\Omega_{\xi} = \Omega_{\eta} = 5$. Behavior similar to the previous example is evident.

Next we consider an example more appropriate to the deformed nuclei. We take six particles in six equally spaced nondegenerate levels, assumed to be 100 keV apart. The exact eigenfunctions in the presence of a constant- G pairing force have $\binom{6}{2} = 20$ components. The amplitudes of the lowest solution will be designated C_{ijk} , where i, j, k run from 1 to 6 and label the orbit-

7. L. S. Kisslinger and R. A. Sorensen, Kgl. Danske Videnskab. Selskab, Mat.-Fys. Medd. 32, No. 9 (1960).

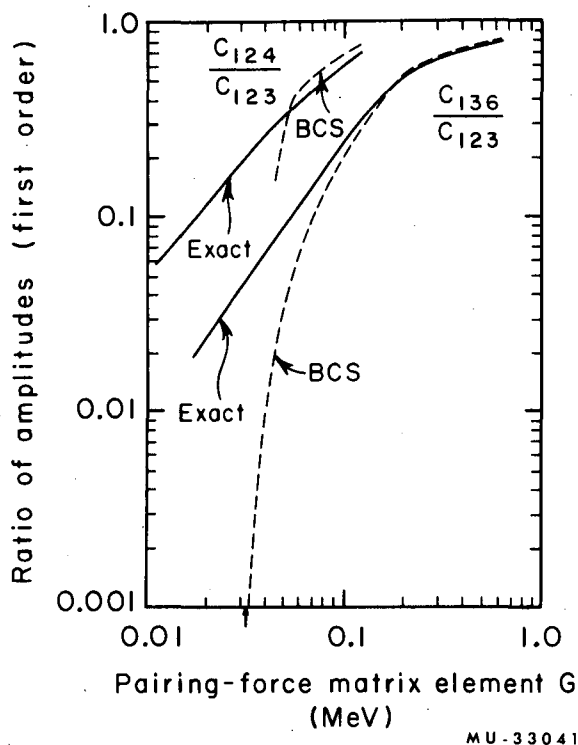


Fig. A.19-3. The ratios of amplitudes, C_{124}/C_{123} and C_{136}/C_{123} in the six-level three-pair nondegenerate model with $E = 100$ keV. The arrow indicates the critical force strength.

als occupied by a pair. We have evaluated exact solutions with the usual pairing force Hamiltonian [see Kisslinger and Sorensen's⁷ Eq. (2) with $Q-Q$ force set to zero] by diagonalizing a 20 by 20 secular determinant on the IBM 7090 computer. The comparison with BCS solutions is most conveniently made by means of the ratio of amplitude C_{ijk} to C_{123} . We actually compare with the parts of the BCS solution containing the proper number of particles (i. e., six particles). Corresponding to C_{ijk}/C_{123} would be

$$\frac{v_i v_j v_k u_l u_m u_n}{v_1 v_2 v_3 u_4 u_5 u_6}$$

where l , m , and n are the three unoccupied orbitals in question.

Figure A.19-3 shows the comparison for two of the nine amplitudes that involve a single-pair promotion from the lowest levels 1, 2, 3 across the Fermi level to 4, 5, or 6. The limiting slope in the weak-force limit is unity, corresponding to the first power dependence on G from first-order perturbation theory. For the ratio C_{124}/C_{123} the BCS value crosses the exact value for a force strength just above critical value. The behavior resembles that in the pre-

ceding examples. For the other ratio plotted, the BCS ratio only very slightly ever exceeds the exact. The second-order amplitudes plotted in Fig. A.19-4 do not cross until about three times critical force strength, while for the third-order amplitude of Fig. A.19-5 the BCS always lies below the exact.

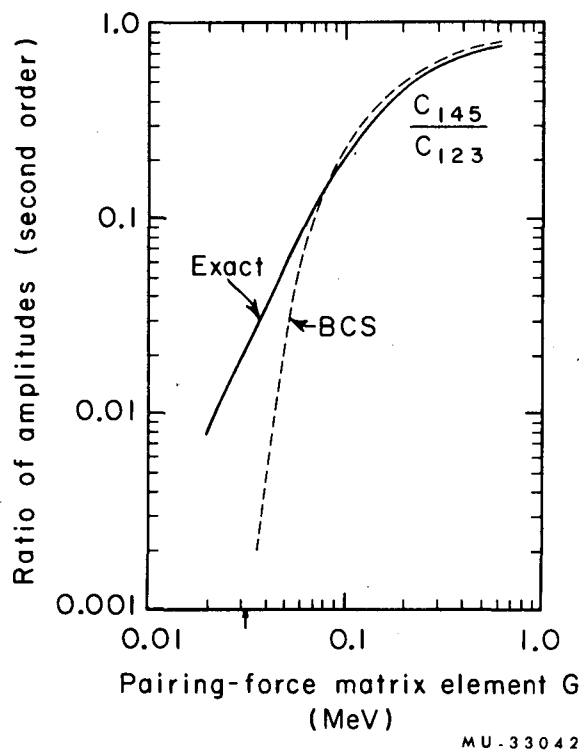


Fig. A.19-4. The ratio of amplitude (second order) C_{145}/C_{123} in the six-level three-pair nondegenerate model with $W = 100$ keV. The arrow indicates the critical force strength.

An important point to be drawn from these examples is that the BCS solutions, even after projection of fixed particle number, are untrustworthy where the ratio of pairing-force strength to level density approaches the critical value. Furthermore, it would appear that in deformed nuclei the pairing force is usually only slightly stronger than needed to produce a gap in the BCS method. In the work of Soloviev⁸ it frequently happened that when two levels were blocked in the deformed rare earths, only the trivial solution ($\Delta=0$) resulted. Thus, it is a matter of real practical importance to consider the errors of the BCS variational methods for force strengths near the critical value. One source of error that has received attention is the fluctuation in particle number. When we project out just the terms of the BCS wave function that contain the

8. V. G. Soloviev, Kgl. Danske Videnskab. Selskab, Mat-Fys. Medd. 33, No. 11 (1961).

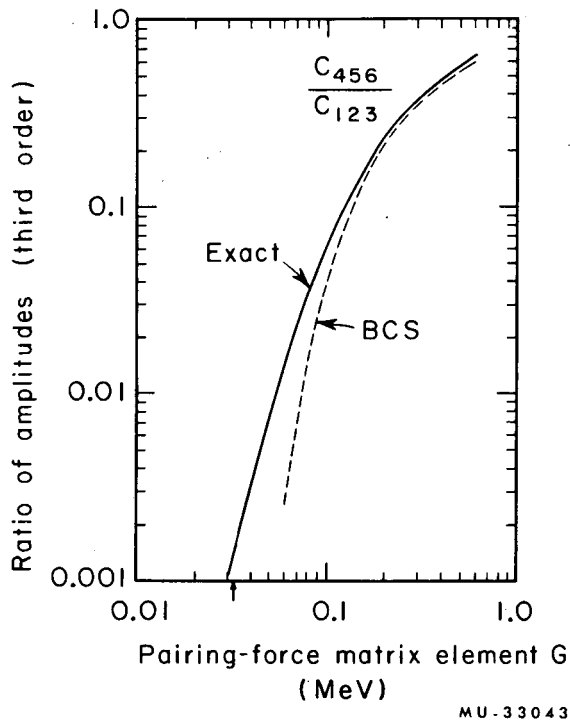


Fig. A.19-5. The ratio of amplitude (third order) C_{456}/C_{123} in the six-level three-pair nondegenerate model with $E = 100$ keV. The arrow indicates the critical force strength.

proper particle number, we have always found the eigenvalue to be lowered. For force strength below critical the trivial BCS solution is obtained. It already conserves particle number, and the projection procedure gives no change. In Fig. A.19-6 is plotted the error in eigenvalues of ordinary and projected BCS solution of the six-level three-pair problem, as deduced by comparison with exact solutions of the 20-by-20 matrix. The curves are superimposed up to the critical force strength and thereafter the projected solution shows much less error. The maximum error for the projected solution comes at a force less than twice critical strength, and this error is about 17 keV, or one sixth the single-particle level spacing of 100 keV. The ordinary BCS eigenvalue may show an error of as much as half the single-particle level spacing.

One other source of error which is inherent in the conventional BCS method is the neglect of higher-order terms in the pairing matrix element. It can be shown qualitatively in a simple

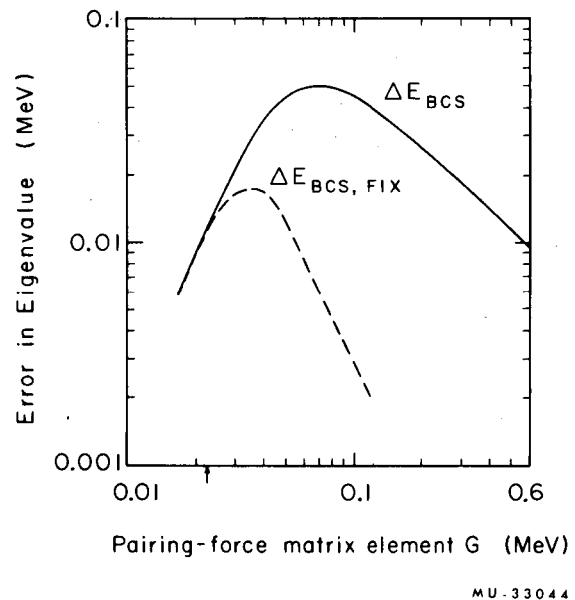


Fig. A.19-6. Error in eigenvalues for ordinary and projected BCS solutions of the six-level three-pair model as deduced by comparison with exact solutions of the 20-by-20 matrix.

model that the second-order correction tends to reduce the gap Δ in an attractive potential, and for the force strength around the critical point, the change in the wave function may turn out to be rather significant.⁹ Thus as a whole, the two effects (number fluctuation and the higher-order effect) tend to go in the same direction.

The main point we would make is that for nuclear systems with their relatively small number of particles outside closed shells, the transition between superfluid and nonsuperfluid states is never sharp nor clearly defined. The trivial ($\Delta=0$) solution that is obtained upon blocking sufficient states by nucleon excitation or going sufficiently high in a rotational band is an artificial feature of the BCS approximation; there always remains configuration mixing of the pair-promotion type. There is need for improved variational methods for handling the pairing-force problem in nuclei.

9. J. O. Rasmussen and M. Rho (to be published); similar discussion on the effect of higher-order terms in superconductivity is given by E. M. Henley and L. Willets, Phys. Letters 11, 326 (1963).

20. THEORETICAL α -DECAY RATE CALCULATIONS FOR SPHERICAL NUCLEI

John O. Rasmussen, R. Macfarlane,* and Mannque Rho

The shell-model microscopic theory of α -decay rates was first formulated and applied to the polonium isotopes by Mang, assuming pure shell-model configurations. Zeh has repeated the calculations for the even-even poloniums, using the superfluid-BCS wave functions of Kisslinger and Sorensen (KS). The configuration mixing of the BCS wave function greatly enhances and smooths the decay-rate trends for the series of isotopes.

We present here the results of a similar set of calculations for the 84-neutron even-even isotones which exhibit α decay. Our BCS wave functions are of a more general type than those of KS, for we take pairing-matrix elements of a finite-range Gaussian singlet force. Thus, instead of a single gap parameter Δ , we derive characteristic Δ_j values for each proton orbital, here taking the set $1g_{7/2}$, $2d_{5/2}$, $1h_{11/2}$, $2d_{3/2}$, $3s_{1/2}$, $1h_{9/2}$. Parallel calculations were carried out for three different pairing-force strengths; those with strength about 10% greater than the free-space p-p force ($V_0 = -32.44$ MeV, range = 1.755 F) gave best agreement with the odd-even mass difference, as is seen in Fig. A. 20-1. The assumption of a 2.44-MeV spacing between the $d_{5/2}$ and $h_{11/2}$ orbital at the proton subshell of 64 together with the above pairing-force strength also brought about essential agreement with the discontinuous drop in two-proton binding energy just beyond 64. (This discontinuity has long been noted in the abnormally large increase in α -decay energy between $^{64}\text{Gd}^{148}$ and $^{66}\text{Dy}^{150}$.) Figure A. 20-2 illustrates that our intermediate-force strength about matches the size of the experimental discontinuity.

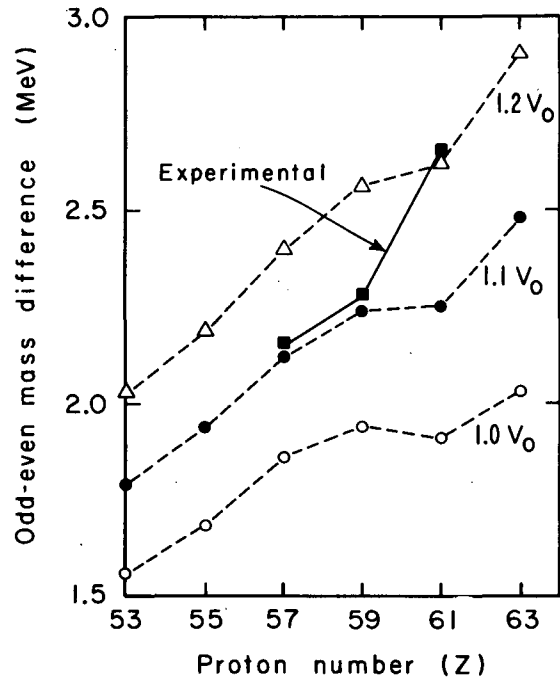
The large orbital spacing at $Z = 64$ leads to a significant decrease in Δ_j values, i. e., decreased configuration mixing, in the BCS solutions at $Z = 64$.

Our theoretical α rate calculations are based on the approximate expression of Rasmussen for even-even nuclei with factorable neutron and proton wave functions (i. e., no n-p residual force mixing) decaying to a closed shell,

$$\gamma_\alpha^2 = C^2 \left| \left(\sum_{j_p} (-)^{l_p} P_c(j_p) (2j_p + 1)^{1/2} B_p(l_p) Y_{j_p}(R_0) \right)^2 \right. \\ \left. \times (\text{similar factor for neutrons}) \right|^2,$$

where γ_α^2 is the reduced width, C^2 is a constant dependent on a size among other things, j_p and l_p are total angular momentum and orbital angular momentum for proton orbitals, $c(j_p)$ is the amplitude of the $(j_p)_{j_p}^2$ admixture in the parent wave function, $Y_{j_p}(R_0)$ is the value of the proton radial wave function at the nuclear surface R_0 , and $B_p(l_p)$ is a correction factor for finite α size taken as $B_p \approx \exp[-0.013 l_p(l_p + 1)]$. For the BCS wave functions the shell-model wave amplitude $c(j_p)$ is to be replaced by a weighting factor involving the quantities v_j and u_j . The ordinary BCS wave functions would give us the equivalent factor (we drop the subscript p)

$$c(j) = \left(j + \frac{1}{2}\right)^{1/2} \frac{u_j^l v_j}{(u_j^l u_j + v_j^l v_j)} \prod_{j_i} (u_{j_i}^l u_{j_i} + v_{j_i}^l v_{j_i})^{j_i + 1/2}$$



MU-32912

Fig. A. 20-1. Comparison of experimental odd-even mass differences (■) for 82-neutron nuclei with three BCS calculations (●, ○, △). The lowest theoretical curve is with free-space residual force strength, the middle for force increased by a factor 1.1, and the uppermost with the force increased by a factor 1.2.

*Present address: McMaster University, Hamilton, Ontario.

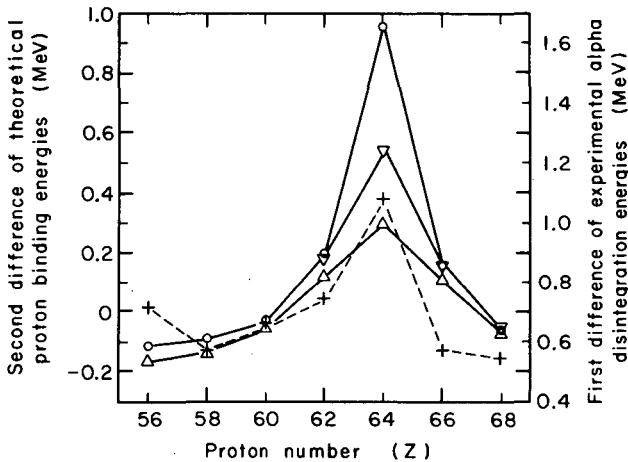


Fig. A.20-2. Comparison of first differences of α -decay energy of even-mass, 84-neutron nuclides and second differences of theoretical BCS binding energies. The experimental points (crosses, dashed line) have their ordinate (MeV) on the right-hand side, and the three theoretical curves have their ordinate scale on the left. The relative vertical position of the experimental curve has been arbitrarily adjusted to facilitate easiest visual comparison of the magnitude of the $Z = 64$ discontinuities between experiment and theory. The uppermost theoretical curve (o) is for free-space residual force strength V_0 , the middle curve (∇) refers to the force strengthened to $1.1 V_0$, the lowest (Δ) for the force of $1.2 V_0$.

MU-32913

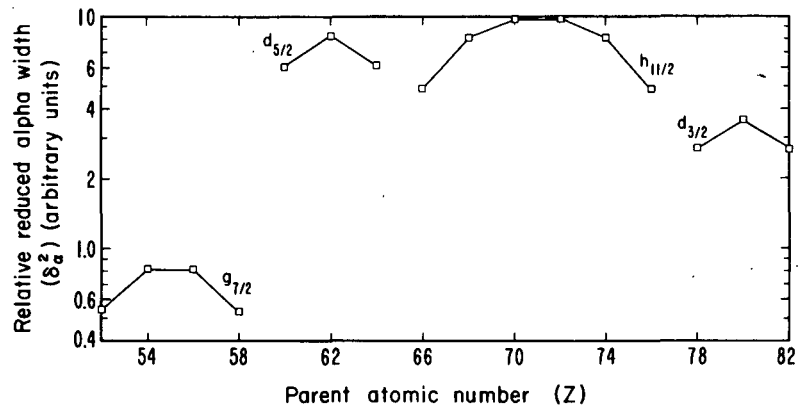
Z_{eh} has dropped the factor in the denominator in order to achieve exact correspondence with the pairing-force zero results, and we have done likewise in the calculations shown by solid dots in Fig. A.20-3. These calculations use the weakest-force BCS wave functions.

er particle number. Using a method and computer subroutine due to Mang we have also performed the reduced-width calculations with only the proper particle-number terms of the BCS wave functions. The results are shown by the open circles of Fig. A.20-3.

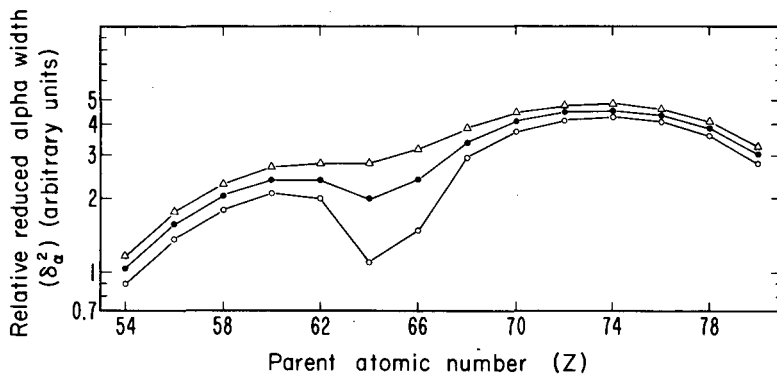
It is well known that the BCS wave functions do not conserve particle number and that improved eigenvalues can be obtained by projecting out just the terms in the eigenfunction with prop-

One sees a dip in a reduced widths for $Z = 64$ and 66 , arising from a "mismatch" of wave functions when either the parent or the daughter is at the subshell $Z = 64$, where there is serious

Fig. A.20-3. Comparison of the theoretical reduced widths for the same set of BCS wave functions (V_0); ●, using the full BCS wave functions; ○, using only the parts of the BCS wave function with correct proton number.



MUB-2291



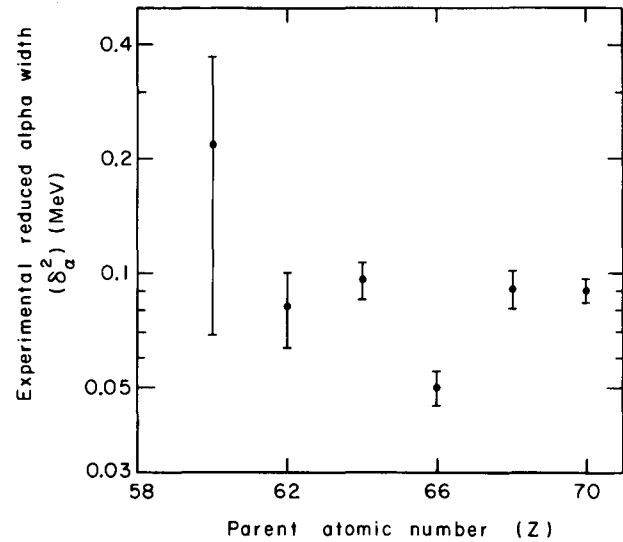
MU-32913

Fig. A.20-4. Theoretical relative reduced alpha widths obtained by using the fixed-proton-number parts of the BCS wave functions for the three different residual force strengths -- V_0 (lowest), $1.1 V_0$ (middle), $1.2 V_0$ (uppermost).

loss of configuration mixing. Except at the subshell the fixed-particle projection method shows that Zeh's formula with the full BCS wave functions does not introduce any appreciable error from fluctuations in particle number.

Figure A.20-4 shows the fixed-particle calculations for the three pairing-force strengths. The magnitude of the dip at the subshell is quite sensitive to pairing-force strength.

Finally, in Fig. A.20-5 we show the experimental reduced widths for 84-neutron α emitters. There is a dip at $Z = 66$, but at $Z = 64$ one sees no dip in reduced width, in marked contrast to theoretical predictions. We believe that this disagreement indicates that the proton structure is not independent of neutron number, and that ${}_{82}^{64}\text{Gd}^{146}$ has lost pairing correlation, while ${}_{84}^{64}\text{Gd}^{148}$ has not.



MU.32914

Fig. A.20-5. Plot of experimental reduced alpha decay widths vs Z for even 84-neutron α emitters.

21. EFFECT OF QUASI-PARTICLE INTERACTIONS ON THE QUADRUPOLE MOMENT OF ODD-A SPHERICAL NUCLEI*

Mannque Rho

In the usual treatment of odd- A nuclei in the superfluid model (BCS treatment) the low-lying states are considered to be pure one-quasi-particle states. Among the neglected interaction terms, the term H_{31} which mixes in three-quasi-particle character is expected to play an important role in odd- A nuclei. The interaction term H_{31} describes coupling of the one-quasi-particle state to the three-quasi-particle state, and inclusion of such terms may be fairly important for the matrix element of single-particle operators. We write an eigenfunction of $H(\eta) = H_0(\eta) + H_{22}(\eta) + H_{31}(\eta)$ by $\Phi_{\lambda J} = \sum_{\nu} |\phi_{\nu J}\rangle \langle \phi_{\nu J} | \Phi_{\lambda J} \rangle$; more explicitly,

$$\Phi_{\lambda J} = \phi_J + \sum_{\mu} |\psi_{\mu J}\rangle \langle \psi_{\mu J} | \Phi_{\lambda J} \rangle, \quad |\psi_{\mu J}\rangle \equiv \text{three-quasi-particle state,} \quad (1)$$

where μ now runs over all higher quasi-particle states (i.e., three-, five-, etc. q-p states). We approximate (1) by dropping terms with quasi-particle number > 3 , and then μ is to include all the possible three-quasi-particle configurations. Here ϕ_J is a single quasi-particle

state with J , where J is the angular momentum or set of all quantum numbers associated with the state we are considering.

With a suitable arrangement of terms, we can obtain Wigner-Brillouin perturbation series for energy as well as wave-function expressions. Kisslinger and Sorensen¹ (KS) studied the effect of quasi-particle interactions on the quadrupole moment (Q) of single-closed-shell odd- A nuclei by phenomenologically introducing a quadrupole field (Q field) and by means of a Langrangian multiplier. Let us see what one obtains if one starts with a completely general interaction term, and then approximates it by the Q - Q force. We obtain it in the following way:

- Use the Wigner-Brillouin perturbation series.
- Include the interactions among three quasi-particles through the term H_{22} , but neglect the antisymmetrization of one quasi-particle with the rest. This treatment is equivalent to a description of one quasi-particle state with the in-

* Short version of a paper to be submitted to Nuclear Physics.

1. L. S. Kisslinger and R. A. Sorensen, Kgl. Danske Videnskab. Selskab, Mat-Fys. Medd. 32, No. 9 (1960).

clusion of self-energy effect, or, in more familiar words, to coupling of one quasi-particle state to a 2+ phonon state. The phonon state is obtained by summing the infinite series of terms arising from successive interactions between two quasi particles.

c. Compute the quadrupole moment in the lowest order in H_{31} , or in other words neglect the effect of higher quasi-particle states (> 3). Using (a), (b), and (c), and some algebra, one gets the total quadrupole moment

$$\bar{Q} = Q^{(0)} \left(1 + \frac{2\xi}{1-\xi} \right), \text{ provided } \xi < 1, \quad (2)$$

where the term $Q^{(0)}$ is the single-quasi-particle quadrupole moment, and

$$\xi = \frac{\chi}{20\pi} \sum_{(il)} \frac{(U_i V_1 + V_i U_1)^2}{E_i + E_1 - \Delta E} N^2 (2j_i + 1) (2j_1 + 1) \times C(j_i j_1 2; \frac{1}{2} - \frac{1}{2} 0)^2 |i | r^2 | l \rangle^2. \quad (3)$$

Here N is a normalization constant of a non-interacting three-quasi-particle state, ΔE is the energy shift from the one-quasi-particle value (E_J) of the state J due to the perturbations, and χ is the coupling constant. Let ξ denote ξ with $N^2 = 1$, $\Delta E = 0$; then the KS result is given by

$$\bar{Q}_{KS} = Q^{(0)} \left(1 + \frac{\xi}{1-\xi} \right). \quad (4)$$

Now compare Eqs. (3) and (4). In Eq. (3), we have the following possibilities (dropping ΔE):

(d) $N = N(il; J) = \text{three quasi-particle normalization factor} \geq 1/\sqrt{2}$.

(e) $N = N(il; 2) = \text{normalization of the two-quasi-particle state} \geq 1/\sqrt{2}$, which is taken into account. (5)

(f) $N = 1$.

One can show that (d) and (e) imply

$$\xi \geq \zeta. \quad (6)$$

If we take $N = 1$ (as KS do in their work),

$$\frac{2\xi}{1-\xi} = 2 \frac{\zeta}{1-\zeta}. \quad (7)$$

Thus we get twice the phonon contribution of KS.

For the cases of (d) and (e), the numerical results show

$$\frac{2\xi}{1-\xi} \approx \frac{\zeta}{1-\zeta}.$$

If we include the term ΔE in Eq. (3), then we see that Eq. (7) is an upper limit, since the conditions a, b, and c lead (calculating from the perturbation in the linear approximation in ΔE) to an equation for ΔE which may be large (in magnitude) in certain cases and satisfies the inequality

$$\Delta E \leq 0.$$

Thus we conclude that neglect of antisymmetrization of one quasiparticle with the rest and taking complete account of two-quasi-particle scattering lead to a result similar to KS's Q-field method. Our method is more convenient for treatment with a more realistic force, and for further improvements.

22. SELF-CONSISTENT CALCULATIONS OF NUCLEAR DEFORMATIONS

Klaus Dietrich, Hans Joerg Mang, and Jean Pradal

We have combined the pairing and the Hartree-Fock method in a calculation of nuclear deformations. A trial wave function of the BCS type is defined as

$$\Psi = \prod_{k, m > 0} (u_{km} + v_{km} b_{km}^+ b_{k-m}^+) \phi_0. \quad (1)$$

In (1), the creation operators b_{km}^+ are obtained by a linear unitary transformation of the creation operator a_{jm}^+ of the original representation,

$$b_{km}^+ = \sum_j D_k^{j(m)} a_{jm}^+, \quad (2)$$

where j and k stand for all quantum numbers,

besides the magnetic quantum number m , that are necessary to define a single-particle state in the original and the transformed representation, respectively; ϕ_0 is the vacuum state; v_{km} , u_{km} are the probability amplitudes for a pair of states (km , $k-m$) being occupied or unoccupied.

The transformation coefficients $D_k^{j(m)}$ have to satisfy the orthogonality conditions

$$\sum_j D_{k_1}^{j_1^*}(m) D_{k_2}^j(m) = \delta_{k_1 k_2}, \quad (3)$$

$$\sum_k D_k^{j_1^*}(m) D_k^{j_2}(m) = \delta_{j_1 j_2}. \quad (3')$$

The expectation value of the number operator must be kept fixed. By not summing over m in Eq. (2), we have made the assumption that the nucleus is axially symmetric. In addition to that, we have to restrict the summations to a suitably chosen subspace of configurations in all practical calculations.

As original representation we use the eigenstates of a harmonic oscillator. We consider the variational principle

$$\delta \left\langle \left\langle \Psi \left| H - E \right| \Psi \right\rangle \right\rangle = 0, \quad (4)$$

where H is the Hamiltonian written in the original representation, and E is the total energy. We derive the Eulex-Lagrange equations corresponding to (4) by variation with respect to u_{km} , v_{km} , and $D_k^j(m)$. These equations are closely related to those derived by Bogoliubov¹ and Baranger.² A computer program has been developed to solve these equations by a rather rapidly converging iteration procedure. It provides a useful basis for studying many interesting problems in nuclear physics.

We have, so far, performed preliminary calculations for rare earth nuclei and for the nucleus Mg^{24} .

Rare Earth Nuclei

So far, we have worked in the following subspace of configurations: the single-particle states of the $N = 4$ shell and the low-lying $h\ 11/2$ state for protons, the single-particle states of the $N = 5$ shell and the low-lying $i\ 13/2$ state for neutrons. One could take into account the polarization of the core and the scattering into higher orbitals by some sort of perturbation treatment. These two effects are certainly of quantitative importance. We should therefore attach only a qualitative meaning to the present results. The parameters that enter the theory are the nuclear radius, the force parameters, and the single-particle energies that describe the interaction of a single nucleon with the nuclear core. They are adjusted so that the odd-even mass differences in the rare earth region and the level spectrum of the Pb^{207} nucleus are correctly reproduced. Furthermore, there is some experimental information about the single-particle energies referred to.

We get an insight into the solutions by choosing the coefficients $D_k^j(m)$ as eigenfunctions of a Nilsson potential of given deformation parameter η and solving the variational equations for each given set of $D_k^j(m)$.

1. N. N. Bogoliubov, Soviet Phys. — Usp. (English Transl.) 67 (2), 236 (1959).

2. M. Baranger, Phys. Rev. 122, 992 (1961).

In Fig. A. 22-1 the difference in energy of the spherical and the deformed configurations is plotted against the deformation parameter η for different rare earth nuclei. A δ^+ quadrupole-quadrupole interaction was used for this calculation. The strength of the quadrupole-quadrupole interaction is very near to the value chosen by Kisslinger and Sorensen.³

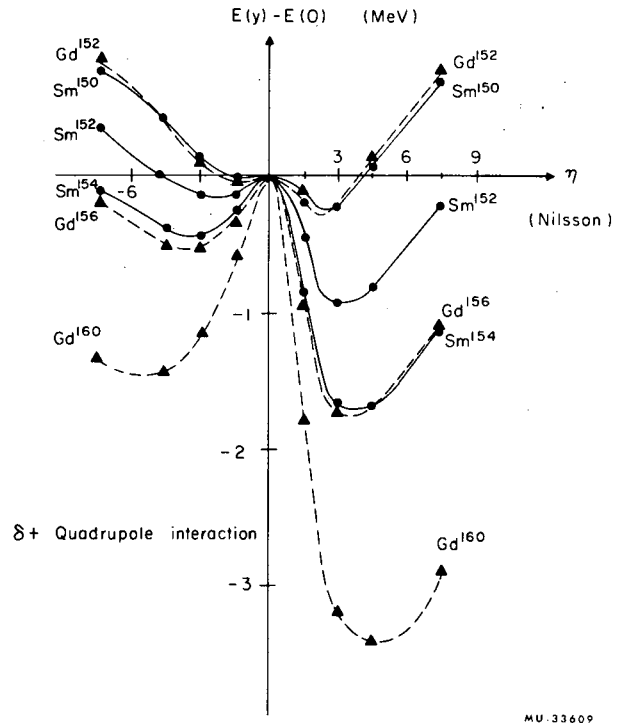


Fig. A. 22-1. Energy difference between deformed and round configuration as a function of the deformation parameter η of Nilsson.

The plot shows how the deformations increase with increasing number of particles outside the core. The sudden increase of deformation in the region of Sm and the preponderance of prolate over oblate shapes is correctly reproduced. The latter effect is largely due to the single-particle energies. The chosen level scheme resembles more that of a square well potential than that of a simple oscillator potential (see also reference 4).

Calculations with finite-range forces of different exchange character were also performed (Serber, Rosenfeld, Ferrell-Visscher type of force). The picture of Fig. A. 22-1 is not dras-

3. L. S. Kisslinger and R. A. Sorensen, Kgl. Danske Videnskab. Selskab Mat.-Fys. Medd. 32, No. 9 (1960).

4. R. H. Lemmer and V. F. Weisskopf, Nucl. Phys. 25, 624 (1961).

tically altered in these cases. The differences between the minimum energies of prolate and oblate shapes are generally smaller, above all in the Sm region. Extreme short-range forces like a δ force above do not lead to any deformation.

Figure A. 22-2 shows the quadrupole moment of the proton and neutron distribution as a function of the deformation parameter η for Sm¹⁵⁴. The quadrupole moment tends to a "saturation" value for increasing deformation η , which is smaller by about a factor of 2 than the experimental value. This shows clearly that the contribution of the core to the total quadrupole moment is essential.

Furthermore, the coefficients $D_k^j(m)$ corresponding to a solution of the full set of variational equations have been compared with the approximate set of $D_k^j(m)$ that corresponds to the Nilsson deformation at a minimum of the energy plot in Fig. A. 22-1. In the case of a

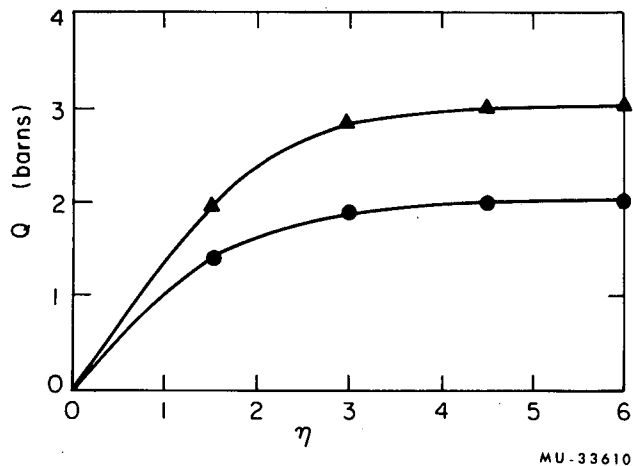


Fig. A. 22-2. Quadrupole moment of the neutron (●) and proton (▲) configurations as a function of the deformation parameter η .

$\delta+$ quadrupole interaction, the Nilsson potential turned out to be a rather good approximation of the self-consistent field.

For finite-range forces the agreement was not as good as one would expect. For the Nilsson potential to be a good approximation of the self-consistent field it turned out to be essential that the spherical part of the Nilsson potential be chosen equal to the "self-energies" h_{jm} in the spherical representation defined by

$$h_{jm} = \epsilon_{jm} + \sum_{k', m' > 0} \left[\langle jmj' m' | v | jmj' m' \rangle + \langle jmj' -m | v | jmj' -m \rangle \right] \times V_{j' m'}^2 \quad (5)$$

On the right-hand side of (5), ϵ_{jm} are the single-particle energies in a nucleus with one extra-core nucleon, and $\langle jmj' m' | v | jmj' m' \rangle$ are the matrix elements of the nucleon-nucleon interaction. This spherical part of the potential differs from nucleus to nucleus.

The Nucleus Mg²⁴

We have performed a preliminary calculation on Mg²⁴ that takes into account all the single-particle states of the N = 0, 1, 2, and 3 shells. So far, only a Serber force has been used. Spin-orbit coupling terms corresponding to 5-MeV spin-orbit splitting in O¹⁷ have been added to the single-particle energies which, in light nuclei, are only kinetic energies. Of course, the nuclear radius has to be kept fixed, since we do not use saturating forces. As one would expect, the pairing effect plays a smaller role than in heavy nuclei. For the negative parity states the Fermi surface is practically sharp, for the positive parity states there is a small smearing out.

23. CONSERVED PARTICLE NUMBER IN THE NUCLEAR PAIRING MODEL

Klaus Dietrich, Hans Joerg Mang, and Jean Pradal

A fixed particle number is projected out of the Bardeen-Cooper-Schrieffer trial state ("BCS" state):

$$\Psi = C \oint \frac{dz}{Z^{n_0+1}} \prod_{\nu} (u_{\nu} + Z v_{\nu} a_{\nu}^{+} a_{-\nu}^{+}) \phi_0, \quad (1)$$

where

ϕ_0 = vacuum state,

ν = quantum numbers of a single particle state with positive magnetic quantum number,

$-\nu$ = quantum numbers of the single-particle state that is time-reversed to ν ,

$a_{\nu}^{+}, a_{-\nu}^{+}$ = creation operators for particles in states $\nu, -\nu$ respectively,

v_{ν}, u_{ν} = probability amplitudes for occupation and nonoccupation of the pair of states $(\nu, -\nu)$,

C = normalization constant,

n_0 = number of pairs.

The Euler-Lagrange equations that correspond to the trial state (1) are derived. They look very similar to the corresponding equations of the BCS theory, but involve contour integrals in the complex plane of the type

$$R_n^N(\nu_1 \cdots \nu_N) = \frac{1}{2\pi i} \oint \frac{dz}{Z^{n_0-n+1}} \prod_{\nu \neq \nu_1 \cdots \nu_N} (u_{\nu}^2 + v_{\nu}^2 \cdot Z), \quad (2)$$

where N is the number of states that are to be excluded from the product on the right-hand side of Eq. (2), and $\nu_1 \cdots \nu_N$ are the specific quantum states that are to be omitted.

Using this notation, we can write the variational equations in the form

$$(\hat{\epsilon}_{\nu} + \Gamma_{\nu} + \Lambda_{\nu}) u_{\nu} v_{\nu} + \Delta_{\nu} \cdot (u_{\nu}^2 - v_{\nu}^2) = 0. \quad (3)$$

The quantities $\hat{\epsilon}_{\nu}, \Gamma_{\nu}, \Lambda_{\nu}, \Delta_{\nu}$ are defined as follows:

$$\hat{\epsilon}_{\nu} = (\epsilon_{\nu} + 2V_{\nu-\nu\nu-\nu}) \cdot \frac{R_1^1(\nu)}{R_0^0}, \quad (4)$$

$$\Gamma_{\nu} = 4 \sum_{\nu_1} (V_{\nu\nu_1\nu\nu_1} + V_{\nu-\nu_1\nu-\nu_1}) \times v_{\nu_1}^2 \frac{R_2^2(\nu_1\nu)}{R_0^0}, \quad (5)$$

$$\Delta_{\nu} = 2 \sum_{\nu_1} V_{\nu-\nu\nu_1-\nu_1} u_{\nu_1} v_{\nu_1} \frac{R_1^2(\nu_1\nu)}{R_0^0}, \quad (6)$$

$$\Lambda_{\nu} = \sum_{\nu_1} (\epsilon_{\nu_1} - 2V_{\nu_1-\nu_1\nu_1-\nu_1}) v_{\nu_1}^2$$

$$\times \frac{R_0^1(\nu)R_2^2(\nu_1\nu) - R_1^1(\nu)R_1^2(\nu_1\nu)}{(R_0^0)^2}$$

$$+ 2 \sum_{\nu_1\nu_2} (V_{\nu_1\nu_2\nu_1\nu_2} + V_{\nu_1-\nu_2\nu_1-\nu_2}) v_{\nu_1}^2 v_{\nu_2}^2$$

$$\times \frac{R_0^1(\nu)R_3^3(\nu_1\nu_2\nu) - R_1^1(\nu)F_2^3(\nu_1\nu_2\nu)}{(R_0^0)^2}$$

$$+ 2 \sum_{\nu_1\nu_2} V_{\nu_1-\nu_1\nu_2-\nu_2} u_{\nu_1} v_{\nu_1} u_{\nu_2} v_{\nu_2}$$

$$\times \frac{R_0^1(\nu)R_2^3(\nu_1\nu_2\nu) - R_1^1(\nu)R_1^3(\nu_1\nu_2\nu)}{(R_0^0)^2}$$

$$+ (\hat{\epsilon}_{\nu} v_{\nu}^2 + \Lambda_{\nu} v_{\nu}^2 + 2\Delta_{\nu} u_{\nu} v_{\nu}) \frac{R_0^1(\nu) - R_1^1(\nu)}{R_0^0}, \quad (7)$$

where ϵ_{ν} are single-particle energies; $V_{\nu_1\nu_2\nu_3\nu_4}$ are matrix elements of the nucleon-nucleon interaction V ,

$$V_{\nu_1\nu_2\nu_3\nu_4} = \frac{1}{4} \langle \nu_1\nu_2 | V | \nu_3\nu_4 \rangle. \quad (8)$$

The "bras" and "kets" on the right-hand side of Eq. (8) are antisymmetrical and normalized products of single-particle wave functions.

The Eqs. (3) have been solved numerically for different strength of the pairing interaction, different level spectra ϵ_{ν} and different pair numbers n_0 , and the results have been compared with the corresponding results of the BCS theory. A δ force and a configuration of 15 pair states were used for these investigations.

Furthermore, comparisons have been made with the results one obtains by solving first the

BCS equations and then projecting from the BCS wave functions an eigenstate of the number operator, according to Eq. (1). In order to measure the accuracy of the BCS solution and of the solution obtained from it by projection, we define the quantities

$$A_v^{BCS} = \frac{e_v^2 - (v_v^{BCS})^2}{e_v^2} \cdot 100 \quad (9)$$

and

$$A_v^P = \frac{e_v^2 - (e_v^P)^2}{e_v^2} \cdot 100, \quad (10)$$

where e_v^2 is the probability for the pair of states $(v_1 - v)$ being occupied in the theory with conserved particle number

$$e_v^2 = v_v^2 \cdot \frac{R_1^1(v)}{R_0^0}, \quad (11)$$

$(v_v^{BCS})^2$ is the probability for occupation in the BCS theory, and $(e_v^P)^2$ is the probability for occupation as obtained from the solution of the BCS equation by subsequent projection.

Figures A. 23-1, A. 23-2, and A. 23-3 show

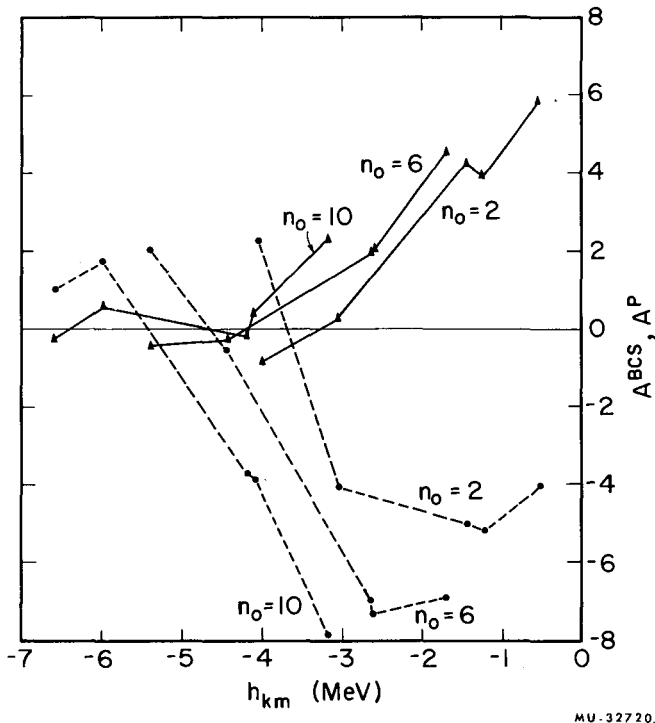


Fig. A. 23-1. Accuracy of occupation probabilities in methods without conservation of particle number for different pair numbers and strength constant $W = -0.9$.
 — BCS method with subsequent projection
 --- BCS method

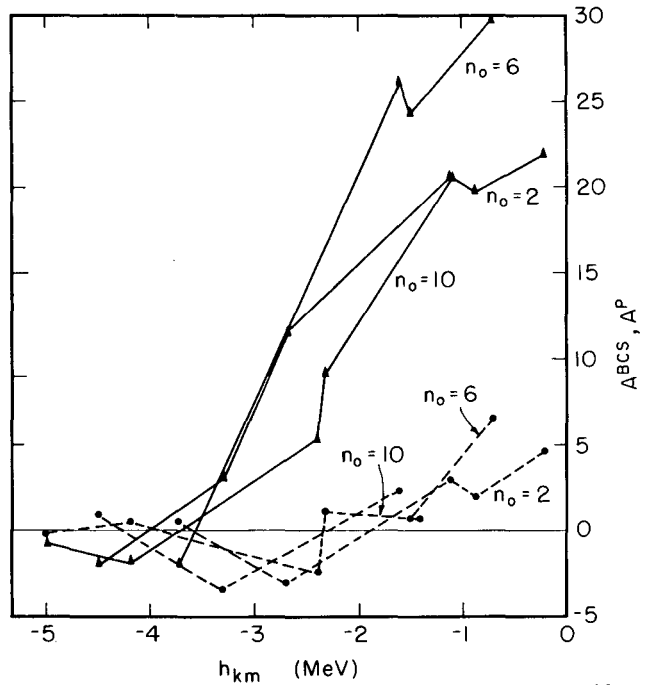


Fig. A. 23-2. As in Fig. A. 23-1 for strength constant $W = -0.45$.

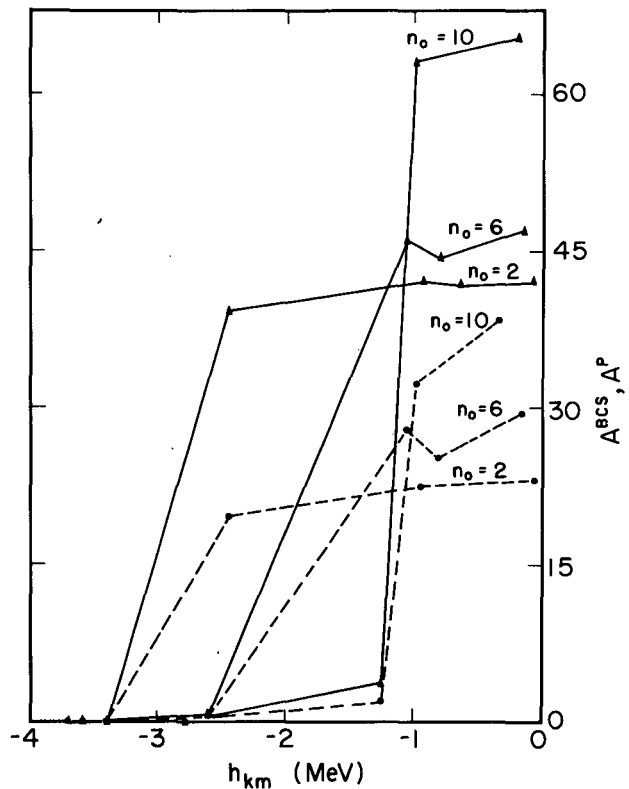


Fig. A. 23-3. As in Fig. A. 23-1 for strength constant $W = -0.2$.

the quantities A_{ν}^{BCS} , A_{ν}^P for the case of a spherical nucleus as a function of the "self-energies" h_{ν} :

$$h_{\nu} = \epsilon_{\nu} + 4 \sum_{\nu_1} (V_{\nu\nu_1\nu\nu_1} + V_{\nu-\nu_1\nu-\nu_1}) (v_{\nu_1}^{BCS})^2. \tag{12}$$

Figures A. 23-4 and A. 23-5 show the same quantities plotted in the case of a deformed nucleus (deformation parameter η of Nilsson ≈ 4.2). The factor W measures the strength of the pairing interaction: $W = 0.9$ is a strong pairing interaction, $W = -0.45$ is slightly weaker than realistic, and $W = -0.2$ is extremely weak.

The results are: (a) The smaller the occupation probabilities of the states in question, the larger the fractional errors both of the BCS occupation probabilities and the ones obtained

by subsequent projection; (b) the weaker the pairing-type interaction the larger the errors of both methods; and (c) in all the cases considered the solution obtained by projection gave too small occupation probabilities for the weakly occupied levels. In other words, the solution obtained by subsequent projection generally underestimates the smearing-out of the Fermi surface.

In the case of odd-even nuclei the excitation spectra can be obtained as additional information. Here, the errors due to nonconservation of the particle number are usually larger than for the occupation probabilities.

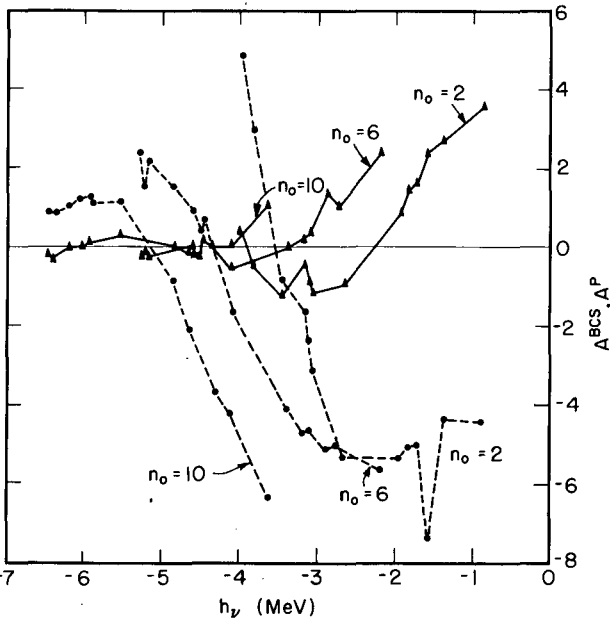


Fig. A. 23-4. As in Fig. A. 23-1 for strength constant $W = -0.9$ and deformed nucleus $\eta_{Nilsson} \approx 4.2$.

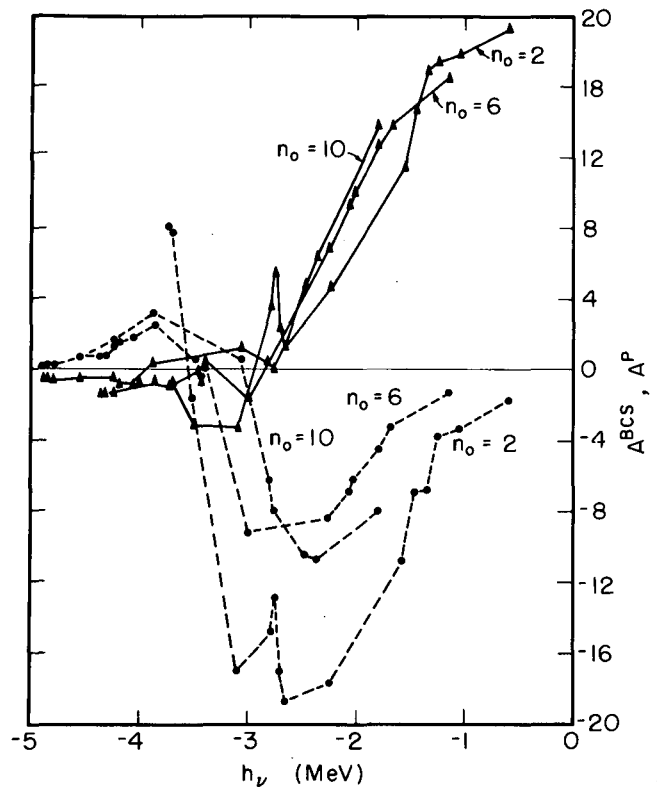


Fig. A. 23-5. As in Fig. A. 23-4 for strength constant $W = -0.45$.

24. DIGITAL COMPUTER CALCULATION OF 3-j, 6-j, and 9-j SYMBOLS WITH MULTIPLE-PRECISION ARITHMETIC

Robert M. Baer* and Martin G. Redlich

In angular-momentum algebra, all quantities can be expressed exactly, in terms of three numbers:

$$\frac{\text{Square root (in numerator), Numerator,}}{\text{Denominator.}} \quad (1)$$

A multiple-precision (multi-word) computer arithmetic has been developed to make possible long calculations in this field without the inaccuracies inherent in decimal-approximation methods.

* Computer Center, Campbell Hall, University of California, Berkeley.

The 3-j, 6-j, and 9-j symbols are widely used in this field and in its applications, especially in nuclear structure and nuclear reactions. Computer subroutines for these symbols with output of form (1) have been written and tested. They can be used for very high angular momenta, including the highest ones observed in reactions between heavy ions and nuclei.

The execution times are small. For example, the average time per 3-j symbol in a run including symbols with large as well as small angular momenta was 63 milliseconds.

25. NOTE ON THE Y_{40} DEFORMATION IN HEAVY NUCLEI

Kichinosuke Harada

Many theoretical analyses on the α -decay rates of deformed nuclei have shown that heavy nuclei should have Y_{40} deformations, though they are small, in addition to the well established Y_{20} deformations. The deformation of the nuclear surface is assumed to be represented by

$$R = R_0(1 + \beta_2 Y_{20} + \beta_4 Y_{40} + \dots). \quad (1)$$

Fröman¹ and Gold'in et al.² have deduced the effective β_4 values from the experimental α decay rates based on the assumption that the α amplitude over the nuclear surface is constant, and they found that the β_4 values near Cm are negative. A theoretical calculation for the equilibrium Y_{40} deformation has been done by Kjällquist.³ Treating the Y_{40} term as a small perturbation of Nilsson potential,⁴ she obtained a result in which the β_4 values of nuclei in the actinide region are all positive.

Recently, Mang and Rasmussen⁵ have developed a fundamental approach for the analysis of a decay. They have calculated the α amplitudes on the nuclear surface by making use of the nucleon configurations in the deformed potential, and obtained a fairly successful result. However, their result shows that when they do not take into account the Y_{40} deformation the calculated α intensities decaying to 4+ states of daughter nuclei are weaker than the experiment, and when they adopt Kjällquist's values as β_4 the intensities decaying to 2+ states become stronger than the experiment. If we could take the negative β_4 values suitably, we might be able to get a better agreement between the theory and the experiment.

It seems to us that there are two points to be re-examined in Kjällquist's calculation. The first is the single particle level order. She used an old Nilsson level order,⁴ which was corrected later by Mottelson and Nilsson.⁶ The second is the use of the asymptotic wave functions in the limit of very strong deformation. Since the Y_{40} deformation is expected to be very small, it is not obvious whether the omission of

1. P. O. Fröman, Kgl. Danske Videnskab. Selskab Mat.-Fys. Medd. 1, No. 3 (1957).

2. Gold'in, Novikova, and Ter-Martirosyan, Soviet Physics JETP (English Transl.) 9, 356 (1959); Gold'in, Adel'son-Velskii, Birggal, Piliia, and Ter-Martirosyan, Soviet Physics JETP (English Transl.) 8, 127 (1959).

3. K. Kjällquist, Nucl. Phys. 9, 163 (1958/59).

4. S. G. Nilsson, Kgl. Danske Videnskab. Selskab. Mat.-Fys. Medd. 29, No. 16 (1957).

5. H. J. Mang and J. O. Rasmussen, Kgl. Danske Videnskab Selskab Mat.-Fys. Skrifter 2, No. 3 (1962).

6. B. R. Mottelson and S. G. Nilsson, Kgl. Danske Videnskab. Selskab Mat.-Fys. Skrifter 1, No. 8 (1959).

$\bar{l} \cdot s$ and l^2 terms is allowable or not. In this note we try to check their effects on the equilibrium β_4 values by the simplest perturbation method.

We now start from the potential

$$V = \frac{1}{2} m \dot{\omega}_0^2 a^2 \left[\left(1 - \frac{4}{3} \delta^2 - \frac{16}{27} \delta^3 \right)^{-1/3} \right. \\ \left. \times \left(1 - \frac{4}{3} \delta \sqrt{\frac{4\pi}{5}} Y_{20} \right) r^2 + \delta_4 \frac{r^4}{R_0^2} Y_{40} \right]. \quad (2)$$

If we put $\delta_4 = 0$ and $a^2 = 1$, the above potential is identical with Nilsson's. From Eq. (2) the equipotential surface becomes

$$R(\theta) = \frac{R_0}{a} \left[1 - \frac{4}{45} \delta^2 + \left(\frac{2}{3} \delta + \frac{4}{21} \delta^2 \right) \sqrt{\frac{4\pi}{5}} Y_{20} \right. \\ \left. + \left(\frac{12}{35} \delta^2 \sqrt{\frac{4\pi}{9}} - \frac{1}{2} \delta_4 \right) Y_{40} \right], \quad (3)$$

neglecting higher order terms in δ and δ_4 . Therefore β_4 is given by

$$\beta_4 = \frac{12}{35} \delta^2 \sqrt{\frac{4\pi}{9}} - \frac{1}{2} \delta_4. \quad (4)$$

The a^2 is determined by the volume conservation condition,

$$\int R^3(\theta) d\Omega = \int R_0^3 d\Omega,$$

and it becomes

$$a^2 = 1 - \frac{16}{105} \frac{1}{\sqrt{\pi}} \delta^2 \delta_4 + \frac{1}{8\pi} \delta_4^2. \quad (5)$$

It is to be noticed that a^2 has a negative linear term in δ_4 . Then the perturbation caused by δ_4 deformation becomes

$$V - V(\delta_4 = 0) = \frac{1}{2} m \dot{\omega}_0^2 \delta_4 \frac{r^4}{R_0^2} Y_{40} \\ + \left(\frac{1}{8\pi} \delta_4^2 - \frac{16}{105} \frac{1}{\sqrt{\pi}} \delta^2 \delta_4 \right) V(\delta_4 = 0). \quad (6)$$

In the first-order perturbation theory the total energy of the nucleus is given by

$$E = \sum_i \epsilon_i + \sum_i \left\langle i \left| \frac{1}{2} m \dot{\omega}_0^2 \delta_4 \frac{r^4}{R_0^2} Y_{40} \right| i \right\rangle \\ + \left(\frac{1}{8\pi} \delta_4^2 - \frac{16}{105} \frac{1}{\sqrt{\pi}} \delta^2 \delta_4 \right) \sum_i \left\langle i \left| V(\delta_4 = 0) \right| i \right\rangle, \quad (7)$$

where ϵ_i and $|i\rangle$ are the single-particle eigenenergy and eigenfunction in Nilsson potential, respectively. The second sum is reduced effectively to the summation over the outer nucleons only, but the last one must be summed up over all nucleons.

To simplify the numerical calculations, we assume the uniform density distribution for nucleus. Then the last sum becomes

$$\frac{1}{2} C \equiv \sum_i \left\langle i \left| V(\delta_4 = 0) \right| i \right\rangle \\ \approx \sum_i \left\langle i \left| \frac{1}{2} m \dot{\omega}_0^2 \left(1 - \frac{4}{3} \delta \sqrt{\frac{4\pi}{5}} Y_{20} \right) r^2 \right| i \right\rangle \quad (8) \\ = \frac{1}{2} m \dot{\omega}_0^2 \left(\frac{3}{5} - \frac{8}{15} \delta^2 \right) A R_0^2 > 0.$$

The equilibrium δ_4 value is determined by the condition

$$\frac{\partial E}{\partial \delta_4} = 0, \quad (9)$$

and the result is

$$\delta_4 = \frac{64}{105} \sqrt{\pi} \delta^2 - \frac{8\pi}{C} \sum_i \left\langle i \left| \frac{1}{2} m \dot{\omega}_0^2 \frac{r^4}{R_0^2} Y_{40} \right| i \right\rangle. \quad (10)$$

The final expression for β_4 thus becomes

$$\beta_4 = -\frac{8}{105} \sqrt{\pi} \delta^2 + \frac{4\pi}{C} \sum_i \left\langle i \left| \frac{1}{2} m \dot{\omega}_0^2 \frac{r^4}{R_0^2} Y_{40} \right| i \right\rangle. \quad (11)$$

Since the first term is very small (≈ -0.007), the sign of β_4 is determined by the sign of $\sum_i \langle i | r^4 Y_{40} | i \rangle$.

For the purpose of illustration, we give two kinds of $\langle i | r^4 Y_{40} | i \rangle$ values calculated by the exact and the asymptotic wave functions in Table A. 25-I. Differences in the cases of $\frac{1}{2}+[660]$, $\frac{3}{2}+[651]$, $\frac{1}{2}-[770]$, and $\frac{3}{2}-[761]$ are remarkable. Nevertheless, we can see $\sum_i \langle i | r^4 Y_{40} | i \rangle$ is positive even for the most heavy nucleus. Then we may conclude the signs of β_4 are still all positive in the actinide region, although we cannot call into question their true magnitude from this simple calculation.

If we neglect the δ dependence of $\sum_i \langle i | r^4 Y_{40} | i \rangle$, we can estimate β_4 values simply from Eq. (11). The result is shown in Fig. A. 25-1. In the course of the calculations we used the relations

$$\hbar \omega_0 = 41A^{-1/3} \text{ MeV}, \quad R_0 = 1.2A^{1/3} \text{ fermi},$$

and δ values in ref. 7. The dotted curves are Kjällquist's. We should find satisfaction in that almost the same results were obtained from the two different methods.

7. S. G. Nilsson and O. Prior, Kgl. Danske Videnskab. Selskab Mat. -Fys. Medd. 32, No. 16 (1961).

Table A. 25-I. The expectation values of $r^4 Y_{40}$ calculated by exact and asymptotic wave functions, given in units of $(\frac{\hbar}{m\omega_0(\delta)})^2$.

configuration	Proton		configuration	Neutron	
	exact ($\eta=4$)	asymptotic ($\epsilon=0.207$)		exact ($\eta=4$)	asymptotic ($\epsilon=0.207$)
$\frac{1}{2}^-$ - [541]	10.39	11.95	$\frac{1}{2}^+$ [651]	21.69	23.58
$\frac{3}{2}^-$ - [532]	- 1.186	- 4.264	$\frac{1}{2}^-$ - [770]	20.23	76.79
$\frac{11}{2}^-$ - [505]	6.350	4.273	$\frac{1}{2}^+$ [640]	7.842	1.722
$\frac{1}{2}^+$ [660]	14.07	55.53	$\frac{3}{2}^+$ [642]	5.064	1.164
$\frac{3}{2}^+$ [651]	4.862	23.58	$\frac{3}{2}^-$ - [761]	12.25	38.65
$\frac{1}{2}^-$ - [530]	5.423	- 3.706	$\frac{5}{2}^-$ - [752]	2.324	10.03
$\frac{5}{2}^-$ - [523]	-12.40	-10.95	$\frac{3}{2}^+$ [631]	- 8.181	-10.61
$\frac{5}{2}^+$ [642]	- 1.507	1.164	$\frac{13}{2}^+$ [606]	9.521	6.795
$\frac{3}{2}^-$ - [521]	- 6.532	- 9.832	$\frac{5}{2}^+$ [633]	- 7.272	-11.72
			$\frac{7}{2}^-$ - [743]	- 5.660	- 9.063
			$\frac{5}{2}^+$ [622]	-12.31	-13.41
			$\frac{1}{2}^+$ [631]	- 1.461	-10.61
			$\frac{7}{2}^+$ [624]	-11.89	-15.08
Total	19.47	67.75	Total	32.15	88.24

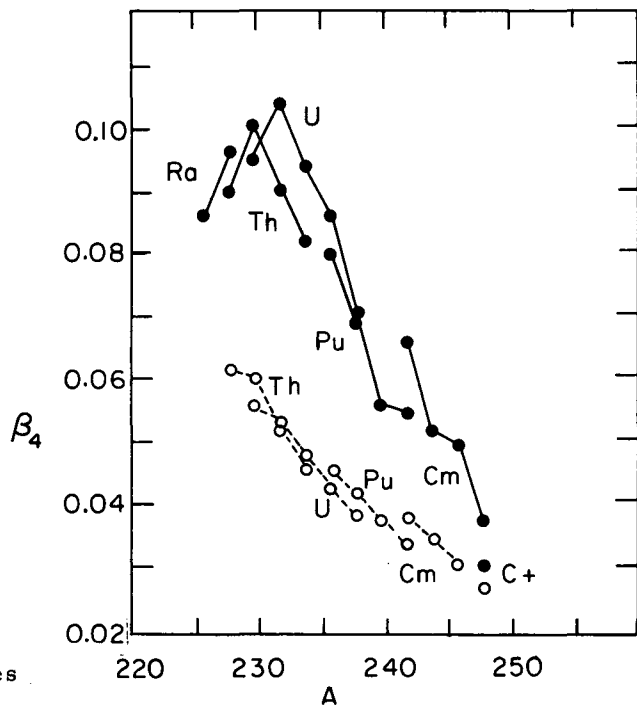


Fig. A. 25-1. Estimated values of β_4 for different isotopes. The dashed curves are the ones calculated by Kjällquist.

B. FISSION

1. GAMMA-RAY SPECTRA FROM SPONTANEOUS FISSION OF Cf^{252} †

Harry R. Bowman, Stanley G. Thompson, and John O. Rasmussen

In this note we report preliminary results of experiments that show well-defined prompt γ -ray peaks ($\tau < 10^{-9}$ sec) associated with fission fragments of selected masses. The dependence of the Doppler shift of the energy of the radiation on fragment direction and mass is found to be a valuable aid in the interpretation of the spectra. These results are of special interest because it has generally been assumed on the basis of early measurements that the γ spectra would be sufficiently complex to preclude observing distinctly resolved spectra.¹ The identification of discrete γ spectra offers the hope of obtaining nuclear energy-level data in a neutron-excess region not accessible by other means, and may also contribute to knowledge concerning the spins and de-excitation processes of the primary fragments.

Our results have come about through measurements of the energies of both members of pairs of fragments and of coincident γ rays from single fission events. A weightless Cf^{252} fission source, prepared by self-transfer onto thin nickel foil, was used in the measurements. The energies of the two fragments were measured and the direction of fission was defined by means of two solid-state counters located about 1 cm from the source. The energies of the γ rays were measured with a 3-by-3-in. NaI(Tl) counter placed at the desired angle with respect to the direction of motion of the coincident fragments. The coincidence resolving times were adjusted to accept γ rays emitted within ± 50 nsec of the time of fission. The data were recorded in three dimensions by using a multidimensional pulse-height analyzer, and were stored event by event in correlated form on magnetic tape. The results were sorted by using an IBM 7094 computer so that the individual γ -ray energy spectra were obtained separately for fragment energy ratios of 1.05 to 1.15, 1.15 to 1.25, 1.25 to 1.35, and 1.35 to 1.45. The fragment energy ratio, R , approximately equals the mass ratio and is referred to hereafter as the mass ratio. The sorting interval above corresponds to about four mass units.

Figure B.1-1a shows the gross γ spectrum in prompt coincidence with fission fragments of all energies (NaI detector at 0 deg with respect to fission). There is some evidence of peaks in this complex spectrum. In order to determine the extent of the contribution of fission neutrons to the observed spectrum (i. e., n, γ reaction in the detector), some experiments were done using lead absorbers. It was found that the n, γ reaction spectrum produced by neutrons was very much smaller in magnitude, and the peaks were of different energy from those discussed here in connection with the prompt γ rays from fission. The absence of effects arising from neutrons can also be shown below in connection with the discussion of the Doppler shift in the energies of certain γ rays that are emitted by moving fragments (i. e., such a shift in the n, γ spectrum would not occur).

When the events were sorted, and the γ -ray spectra associated with a particular fission mass ratio were examined separately, a profusion of definite peaks appeared from 150 to 600 keV, most of which are probably complex. The spectra change markedly for different mass ratios, and we thus find an explanation for the fact that the discrete structure is generally obscured in a total prompt- γ spectrum such as that given in Fig. 1a, where no sorting according to mass ratio is done. Figure 1b shows spectra for several specified mass ratios taken with the NaI detector at 0 deg to the fission direction. In this case, the data are subject to a further restriction in sorting such that the spectra given are associated with the case of heavy fragments moving toward the γ -ray counter and light fragments moving in the opposite direction.

For γ rays emitted during the time of flight to the detectors (about 1 nsec), there should be a detectable Doppler shift in the 0-deg measurements, permitting assignment of γ 's to light or heavy fragments. Those γ rays emitted after 1 nsec but within 50 nsec would be observed, but without Doppler shift, since the fission-fragment detectors are seen by the γ detector in our experimental arrangement. As a result of the Doppler effect, the γ rays emitted by the fragments are changed in energy according to the relation $E_\gamma = E_0(1 \pm v/c)$, where v is the velocity of the fragments and E_0 is the energy of the γ rays emitted by fragments with zero velocity. The sign of v/c is positive when the γ ray is e-

† Paper submitted to Phys. Rev. Letters.

1. H. R. Bowman and S. G. Thompson, in Proceedings of the Second United Nations International Conference on the Peaceful Uses of Atomic Energy, Geneva, 1958, vol. 15, P/652 (United Nations, New York, N. Y., 1958), p. 212

mitted by a fragment moving in the direction of the γ -ray counter and negative when the fragment is moving away from the counter. The maximum difference in energy, ΔE , is $E_0(2v/c)$, which should be about 7% of E_0 for heavy fragments having an average velocity of 1.04×10^9 cm/sec, and 9% for average light fragments having an average velocity of 1.37×10^9 cm/sec.

An example of a fairly well-resolved peak subject to Doppler shifting is provided by the NaI-counter spectra for the mass ratio 1.3. For this mass ratio, the heavy-fragment mass is 140 ± 2 when correction is made for the average emission of four neutrons. Then the masses of the heavy and light fragments total 248; the most

probable charge is calculated as 54.² In Fig. B.1-1c the solid curve represents the spectrum observed when the light fragments travel in the direction of the γ -ray counter. The dashed curve represents heavy fragments traveling toward the γ -ray counter. The peaks of the solid curve at 560, 454, and 361 keV seem to appear at approximately 605, 490, and 390 keV, respectively, in the dashed curve. The general feature of the energy shift observed for all these peaks is that expected for emission from heavy fragments of mass near 140, although changes in the peak shapes occur, suggesting unresolved com-

2. H. R. Bowman, J. C. D. Milton, S. G. Thompson, and W. J. Swiatecki, Phys. Rev. 129, 2140 (1963), Table I.

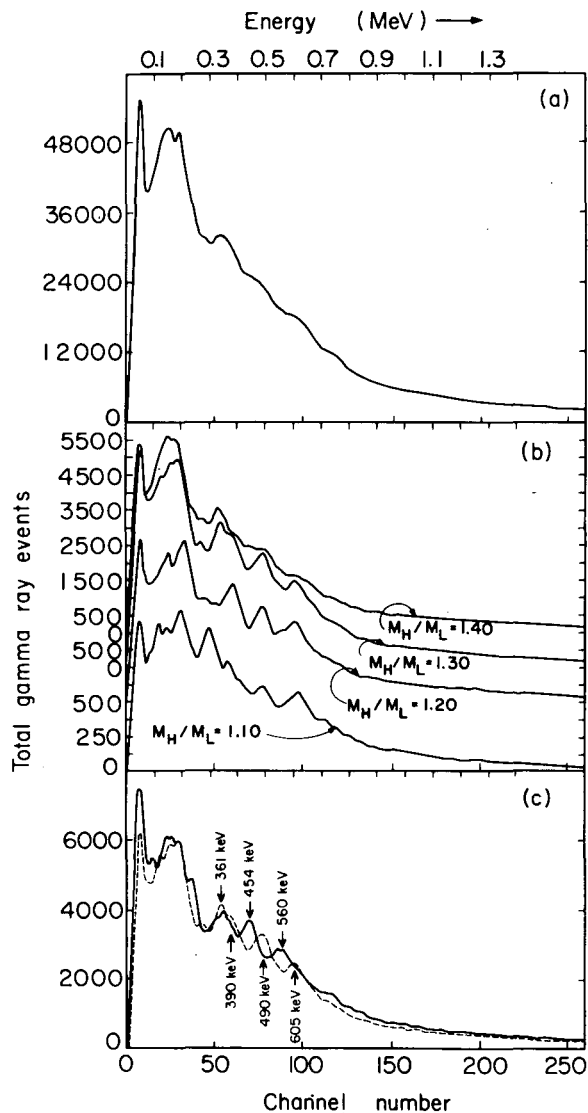


Fig. B.1-1. (a) Total prompt γ -ray energy spectrum from spontaneous fission of Cf^{252} measured with a 3-by-3-in. NaI(Tl) counter in coincidence (50 nsec) with two fission-fragment detectors (NaI counter at 0 deg with respect to fission direction). Events were not selected according to mass or fragment direction. (b) Spectra of prompt γ rays associated with various values of R , the mass ratio. These spectra were then measured with the NaI counter at 0 deg relative to the direction of motion of the fragments. The spectra are also associated only with the events in which the heavy-fragment members of the pairs moved toward the γ -ray counter. (c) Dependence of prompt γ -ray spectra on the direction of motion of the fragments (Doppler shift). The spectra shown were obtained with the NaI counter at 0 deg relative to the direction of motion of the fragments, and are associated only with fragments of mass ratio $R = 1.30 \pm 0.05$ ($M_H = 140 \pm 2$). The solid curve is the spectrum emitted by light fragments moving toward the γ -ray counter, and the dashed curve is for heavy fragments moving in the direction of the γ -ray counter.

ponents not all shifting in the same way. Further evidence for complexity is given by the observed intensity per fission of each of these three peaks summed within mass-ratio limits of 1.15 to 1.35, since each of these intensities is larger than the expected fission yield of any single nuclide in this region. The suspected complexity was confirmed in preliminary experiments using a high-resolution (full width at half maximum = 3 keV) lithium-drifted germanium detector operated at 77° K for the gamma rays.³ Figure B.1-2 shows such γ spectra for mass ratios of 1.2 and 1.3 at an angle of 0 deg (heavy fragment moving toward the γ detector).

In all the γ -ray measurements, a special stabilization system was continuously operated, using the annihilation radiation of Na^{22} as a basis for eliminating drift in the electronic system. As a consequence, the energy measurements are believed to be accurate within 1 to 2 keV in the Ge(Li) measurements and ≈ 5 keV for NaI.

Although a comprehensive interpretation of these complicated results is premature, we have attempted in the following discussion to give one example of an analysis that leads to the tentative assignment of a single line. The peak at ≈ 490 keV in the dashed curve of Fig. B.1-1c lends itself to such a detailed analysis. Under the higher resolution of the germanium counter this line is seen to consist of three principal components -- the most intense at 480 keV (associated with $R = 1.3$, $M_H = 140$), a second about 5% lower in energy, and a third about 1.6% higher in energy. The third is more associated with the $R = 1.2$ spectrum shown in the lower curve of Fig. B.1-2. By further analysis we have found that all three components have the correct Doppler shift ($\approx 7\%$) for emission from the heavy fragment in a time less than 1 nsec. The energy of the principal component at mass 140 ± 2 after subtraction of the Doppler shift is 463 keV, and its intensity per fission is roughly 3%. The lifetime ($< 10^{-9}$ sec) and the sign of the anisotropy of this γ ray (as determined from 90-deg data, not shown here) favor an E2 multipolarity assignment. From these results, it seems reasonable to make a tentative assignment of the 463-keV

3. A. J. Tavendale and G. T. Ewan, A High-Resolution Lithium-Drift Germanium Gamma-Ray Spectrometer, *Bull. Am. Phys. Soc.* **9**, No. 1, 46 (1964) (submitted to *Nucl. Instr. Methods*).

transition to the first 2+ to ground (0+) transition in Xe^{140} .

As regards the significance of the above-mentioned results, one may visualize the possibility of obtaining more data and extending the method to include detailed measurements of angular distributions and γ -ray emission times. In such case one may hope not only to obtain much new information concerning the decay characteristics of nuclides in hitherto inaccessible regions of the periodic table, but also to obtain information on the spins and the de-excitation processes of the primary fission fragments.⁴

It is a pleasure to acknowledge the contribution of Michiyuki Nakamura, Richard La Pierre, John Mendez, and Sam Nolan in connection with the multidimensional analyzer and stabilization systems. We wish to thank Claudette Rugge for help with the computer programs and Joan Phillips for help with this paper.

4. G. Bertram-Hansen, B. Elbek, K. A. Hegemann, and W. F. Hornyak, *Nucl. Phys.* **47**, 529 (1963).

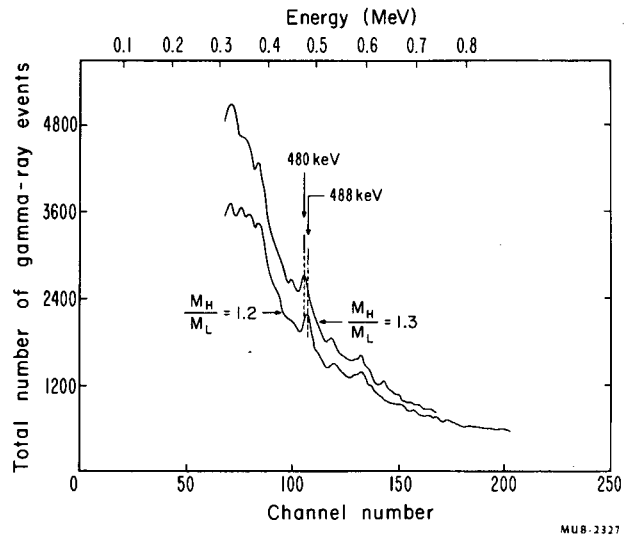


Fig. B.1-2. Prompt γ -ray spectra obtained with a lithium-drifted germanium detector operated at 77° K. The resolution (full width at half maximum) is 8 keV. These spectra are those associated with mass ratios 1.3 and 1.2 and for heavy fragments moving toward the Ge(Li) detector.

2. HILAC OPERATIONS AND IMPROVEMENTS

Albert Ghiorso and Robert M. Main

A major program of improvement, under way at the Hilac during the past year, is designed to increase the duty factor of the accelerator. These improvements, to be carried out over a period of 4 years, provide for incremental increases in the duty factor and will eventually allow for cw (100% duty factor) operation of the accelerator.

The ion source has been improved to produce beam currents of 30 to 40 mA of C^{++} , greater by a factor of 10 than previously possible, and studies are in progress for the redesign of the Cockcroft-Walton accelerator column to make possible the acceptance of this beam. The mercury vapor jet stripper has been replaced by beryllium oxide foils, resulting in an increase in the higher charged states entering the poststripper. A new analyzing magnet has been installed in the cave area.

Increased Duty Factor

The heavy-ion linear accelerator is designed to operate at peak rf gradients which allow for the acceleration of ions with $e/m > 0.3$ in the poststripper. Since both the ion source and the stripper produce a distribution of charged states, the system must be highly versatile, with wide latitude allowable in the mode of operation. The accelerator rf gradients can be decreased to accept higher e/m ratios, and (accepting the attendant decrease in peak beam) for the same average power or x-ray background (whichever is limiting), the pulse rate or width can be increased thus increasing the duty factor.

For the existing system, this versatility is limited: in pulse width by the main amplifier power supplies, which consist of 4-msec pulse lines, and in pulse rate (average power) by the 30-kv Kenotron power supplies that feed the pulse lines and by the ion-source power supplies.

The first increment of improvement (presently planned for completion in mid-1964) consists of the installation of a surplus rectifier from Livermore, the construction of new drivers and modulators for the rf amplifiers, and the addition of increased capability in the ion source arc and extractor power supplies. Although this system will be able to supply approximately 12 times the present rf power, the cooling and x-ray shielding of the cavities will limit its use to a factor of 2 (6% duty factor with $e/m = 0.3$ in the poststripper). With this supply, however, it

will be possible to adjust pulse width and, with maximum e/m ratios, increase the duty factor to about 16% for the lighter elements (carbon, nitrogen, and oxygen).

At present the rectifier building (Building 71A) is nearing completion. The drivers and modulators have been designed and prototypes fabricated and tested. The source supplies are presently being fabricated and will be installed upon completion.

Subsequent improvements will increase the x-ray shielding of the rf cavities and provide additional cooling for the cavities, drift tubes, and stems. In addition, the power delivered to the Cockcroft-Walton terminal will be increased to allow for the continuous operation of the ion source. It is expected that the power will be increased to allow for 18% duty factor ($e/m = 0.3$ in poststripper) in 1965, and 27% in 1966.

Work in Denmark has shown that the average charge distribution of fission fragments is higher when solid foils are used than when gases are used as a stripping medium. Accordingly it was decided to try to supplant the mercury vapor jet stripper which has been used since the earliest operation of the Hilac. An investigation was undertaken by Frank Grobelch to develop the techniques necessary to produce thin foils capable of withstanding the thermal stresses produced by the heavy-ion beam, up to 200 μA peak. These techniques were perfected in early 1963, and it is now possible to produce, essentially on a routine basis, 1-in. -diameter unsupported beryllium foils of approximately 5 to 20 $\mu g/cm^2$.

The foils are produced by vacuum evaporation of beryllium onto a glass substrate. The foil is stripped from the glass by flotation in water and then floated from the surface of the water onto a foil holder. The mounted foils are oxidized in air by heating with a focused infrared heat source. The resulting beryllium oxide foil is transparent and of unusually high strength. Individual foils have been used in the accelerator for periods exceeding 1000 hours, and damage has been attributed primarily to mechanical shock rather than radiation. A small amount of radiant heating of the foil is used to provide a continuous annealing of the foil to overcome radiation damage.

The stripping by the foils has been analyzed and indicates, in general, that the predominant

state of the light ions (lithium, carbon, nitrogen, and oxygen) is essentially one charge greater than that produced by the vapor jet stripper, and that a significant fraction is fully stripped.

The use of the foils has made possible the elimination of the cooled-vapor jet baffles, which consumed approximately \$7500 worth of liquid nitrogen per year. The advantages to be obtained by the increased efficiency of stripping will not be realized fully until the new rf power supply is available for use in mid-1964. By raising the e/m ratio of the various ions entering the poststripper, it will be possible to reduce the rf gradients, thus substantially reducing the x-ray shielding and tank cooling required. The average beam level can thus be increased by lengthening the pulse.

Investigation of the stripping by the foils is continuing not only at the designed stripping velocity ($\beta = 4.6 \times 10^{-2}$) but also at the prestripper entrance velocity ($\beta = 1.2 \times 10^{-2}$), with the hope of decreasing the required prestripper gradient.

Cave System

A new beam-analyzing magnet, Brutus, has been installed in the front cave area. This magnet, powered by a 100-kW solid-state supply which is regulated to 1 part in 50 000, is capable of deflecting a full-energy beam, of $e/m = 0.30$, 60 deg from the accelerator axis. Seven exit ports have been provided: one for the heavy-element cave, one for the Coulomb excitation cave, three for chemistry bombardment in the front cave, one for the 180° 26-in. high-resolution spectrometer (which will be set up shortly in the middle cave), and one axial port to carry the beam to the Jupiter analyzing magnet in the middle cave. Jupiter has five exit ports, three of which carry the beam to the rear cave. The highly stable magnetic deflecting and lens systems allow for the focusing of the beam on 0.040-in. targets at distances up to 45 feet from the exit of the accelerator. The cave system thus provides positions for eight transient set-ups, in addition to the three permanent experimental stations.

3. RATIO OF Cd^{115} ISOMERS PRODUCED IN HEAVY-ION-INDUCED FISSION*

Torbjørn Sikkeland and Gregory R. Choppin†

It has been reported¹ that the ratio of the yield of $\text{Cd}^{115m}(I=11/2)$ to that of $\text{Cd}^{115g}(I=1/2)$ is 20 times as great in the fission of gold by carbon ions as in the fission of U^{235} by thermal neutrons. No correction was made in this work for the growing in of Cd^{115} via Ag^{115} , although the authors state that they estimate that approximately 30% of the Cd^{115} comes by this path rather than by direct production. Consequently, the reported ratios reflect variations in the charge distribution in the fission as well as in any angular momentum in heavy-ion-induced fission,² and it seemed worth while to study more carefully the Cd^{115} isomer ratio in these reactions. The mode of chemical separation allowed correction of the ratio for production of Cd^{115} isomers via Ag^{115} . Thus, the corrected ratios reflect rather accurately the values for direct production in fission.

* Condensation of paper submitted to J. Inorg. Nuclear Chem.

† Florida State University, Tallahassee, Florida.

1. S. M. Polikanov and Yu. T. Chubarkow, Zh. Eksperim. i Teor. Fiz. (USSR) **38**, 295 (1960).

2. John Gilmore, The Effect of Angular Momentum on Fission Probability (Ph. D. Thesis), UCRL-9304, July 1960 (unpublished).

Experimental Procedure

The target foil stacks were bombarded in the Berkeley heavy-ion linear accelerator (Hilac) with C^{12} and O^{16} ions accelerated to 10.4 ± 0.2 MeV per nucleon. A 0.25-mil Al foil preceded the target stack to ensure that the ions were fully stripped. In a typical gold target stack, four accurately weighed gold foils (approximately 1.18 mg/cm^2 thick) were sandwiched between two 0.7-mil aluminum foils. The sandwich arrangement was necessary to catch the recoiling fission fragments through a 4π solid angle. Thus, there were four gold foils and eight aluminum foils in each stack. For the uranium targets, uranium tetrafluoride was evaporated to a thickness of 0.3 to 1.5 mg/cm^2 onto an aluminum foil backing 0.2 mil thick. The stack arrangement was as described for the gold targets. The integrated beams varied between 1 and $2 \mu\text{A-h}$ (about 3 h of irradiation time). A water-cooled copper block target holder was used which also served as the Faraday cup. The range-energy curves compiled by Hubbard for heavy ions in metals³ were used to calculate the

3. Edward L. Hubbard, Range-Energy Relation for Heavy Ions in Metals, UCRL-9053, Jan. 1960.

median energy of the beam as it passed through each target foil. Cd was chemically separated from other fission products and the ratio between the isomers was obtained by resolving the β decay curves.

Results

The values for the σ_m/σ_g ratio for the different systems studied are given in Table B.3-I. A number of other runs on these systems gave similar results.

In addition, several bombardments were performed in which a gold target foil was placed between several layers of 0.25-mil Al foil. Within experimental error there was no variation in the σ_m/σ_g ratio with thickness in aluminum. This means that, within the limitations of these experiments, no difference in angular distribution was observed between isomers.

Discussion

Among the important factors that determine the isomeric ratio are⁴ (a) the distribution in angular momenta J_f of the primary fragment,

4. J. R. Huizenga and R. Vandenbosch, Phys. Rev. 120, 1305 (1960).

(b) the number and types of steps in the de-excitation of the primary fragment to the Cd¹¹⁵ isomer pair, (c) the angular momentum carried away at each step, (d) the probability of forming states of different spins during each step of the cascade, and (e) the spins of the isomeric states.

A variety of primary fragments, of widely distributed masses and excitation energies, can decay to Cd¹¹⁵. This makes a quantitative treatment of the problem almost impossible. We will instead attempt to discuss the isomer ratio in a qualitative way.

Huizenga and Vandenbosch^{4, 5} in their quantitative analysis have shown that the neutron and especially γ emission do not change the average spin of the nuclei appreciably. The cascade, however, spreads out the distribution of the spin states. We limit ourselves to estimation of the average value $\langle l_f \rangle$ of the primary fragment and compare this with the spins of the Cd¹¹⁵ isomer pair, which are 1/2 and 11/2. It is assumed that the excited nucleus just prior to the γ de-excitation chooses to feed the metastable or ground state depending on which transition has the smaller spin change.⁴

5. R. Vandenbosch and J. R. Huizenga, Phys. Rev. 120, 1313 (1960).

Table B.3 I. Experimental ratios σ_m/σ_g and estimated values $\langle l_n \rangle$ and $\langle l_f \rangle$ for various systems

Bombard- mant No.	Ion	Target	Ion energy (lab) (MeV)	σ_m/σ_g	$\langle l_n \rangle$	$\langle l_f \rangle$
1	O ¹⁶	Au ¹⁹⁷	72	1.75	9.1	0.9
			97	2.80	26	2.4
			128	3.72	40.0	3.7
			154	4.23	49.4	4.6
2	O ¹⁶	Au ¹⁹⁷	97	3.14	26	2.4
			128	4.00	40.0	3.7
			154	4.25	49.4	4.6
			73	1.60	20.7	2.0
3	C ¹²	Au ¹⁹⁷	90	2.64	29.4	2.8
			103	3.18	35	3.2
			120	3.43	40.5	3.7
			90	2.80	29.4	2.8
4	C ¹²	Au ¹⁹⁷	103	3.08	35	3.2
			120	3.44	40.5	3.7
			74	0.55	18.4	1.4
			95	0.77	30.4	2.3
5	C ¹²	U ²³⁸	123	0.82	39.6	3.0
			120	0.73	39.6	3.0
			85	2.0 ^a		
			102	2.3 ^a		
Ref. 1	O ¹⁶	Au ¹⁹⁷	89	2.1 ^a		
			64	1.6 ^a		
Ref. 1	C ¹²	Au ¹⁹⁷	78	1.8 ^a		

^aUncorrected for Ag¹¹⁵ decay

Some of the factors determining $\langle l_f \rangle$ are the spin, l_n , of the fissioning nucleus and the fraction of l_n carried off as angular momentum by the primary fragment.

This fraction is a function of the scission shape of the nucleus. Recently Cohen and Swiatecki have, as an approximation to the exact liquid-drop calculations, developed formulae for calculating the total energy of two uniformly charged collinear spheroids.⁶ This energy for varying ratios C/A of the major to minor axis is characterized by a specific minimum for a given value of the fissionability parameter X [where $X = (Z^2/A)/50.13$]. It has been experimentally demonstrated⁷ that this ratio predicts fairly well the fragment kinetic energy release and thus the scission shape. The fragments are emitted along the symmetry axis, which in our case is the C axis.⁸ At high angular momentum the spin axis is along the principal axis, perpendicular to the C axis.⁸ If the moment of inertia is assumed to be that of a rigid body, the intrinsic spin, $\langle l_f \rangle$, of the spheroid with mass m is given by

$$\langle l_f \rangle = l_n (1 + K^2) R^{5/3} / (1 + K^2) (R^{5/3} + 1) + \frac{5K^2}{A_n} R (R^{1/3} + 1)^2. \quad (1)$$

Here $C/A = K$, $m_1/m_2 = R$, and $A_n = m_1 + m_2$ is the mass of the fissioning nucleus. We have assumed C/A to be the same for both fragments. Values for C/A were taken from Cohen and Swiatecki.⁶ Further, we assumed first-chance fission to be the most probable at the excitation energies we are dealing with; thus $A_n = A_{cn}$, the mass of the compound nucleus. The choice of A_{cn} was straightforward when Au was used as a target. In this case the fission occurs only after complete fusion (CF) of the target nucleus and the projectile.⁹ However, when U^{238} is the target, only a part of the fission (75% with C^{12} and 70% with O^{16}) occurs from a CF reaction.¹⁰ The remaining fraction (i. e., 25% with C^{12} , 30% with O^{16}) comes from an incomplete fusion (ICF) reaction, in which approximately four nucleons

are transferred to the target nucleus before fission.¹⁰ We have assumed this ratio to be the same over the entire range of the bombarding energy.

The ratio R represents the primary ratio between the fragment masses before neutron evaporation. Average values for R were obtained from the average number of neutrons emitted, as estimated according to excitation energies and neutron binding energies involved; 4 MeV was chosen as the average kinetic energy of the neutrons.¹⁰

A most difficult problem was connected with the choice of l_n . For a first-chance fission, $l_n = l_{cn}$, the spin of the compound nucleus. Average values, $\langle l_{cn} \rangle$, have been calculated by Thomas for a square potential nuclear well with $r_0 = 1.5 \times 10^{-13}$ cm.¹¹ This model predicts fairly well the total interaction cross section in heavy-ion-induced reaction of U^{238} .¹² As stated above, the CF reaction contributes between 70 and 75% to this cross section. The ICF reactions occur at the expense of the complete amalgamation which produces states of high angular momentum.¹⁰ Therefore, the $\langle l_{cn} \rangle$ values calculated by Thomas¹¹ are too high. Based on the measured cross sections for complete fission, average values $\langle l_{CF} \rangle$ for this process can be calculated by assuming the same ratio between the CF and ICF reactions over the energy range considered. For the ICF reactions, the average spin of the fissioning nucleus may be of the same order as $\langle l_{CF} \rangle$, since the transferred nucleons have maximum impact parameters. Consequently we assume $\langle l_n \rangle \approx \langle l_{CF} \rangle$.

For Au^{197} we can assume the cross section for the CF reaction to be the same as was found for U^{238} . The transfer of four nucleons to Au^{197} does not deposit enough excitation energy in the nucleus for it to undergo fission. Values for $\langle l_n \rangle$, calculated according to a procedure described in Ref. (12), are given in Table B.3-I together with the $\langle l_f \rangle$ values estimated from Eq. (1) for the fragments that decay to Cd^{115} isomers.

We see that $\langle l_f \rangle$ in all cases have values between the spins $11/2$ and $1/2$ of the isomer pair. The ratios observed are therefore, to a first approximation, reasonable. In particular this crude model explains qualitatively the low ratios: the largest fraction of the high spin of the fissioning nucleus is carried off as orbital angular momentum of the fragments. We further observe an expected increase in the ratio with increasing $\langle l_f \rangle$. The calculations also give a higher value for $\langle l_f \rangle$ with Au as target than for

6. S. Cohen and W. J. Swiatecki, The Deformation Energy of a Charged Drop. IV. Evidence for a Discontinuity in the Conventional Family of Saddle-Point Shapes, Aarhus University Report, 1961 (unpublished).

7. V. E. Viola, Jr., and T. Sikkeland, Phys. Rev. 130, 2044 (1963).

8. A. Bohr, in Proceedings of an International Conference on Peaceful Uses of Atomic Energy, Geneva (United Nations, New York, 1956), Vol. 2, p. 151.

9. T. Sikkeland, E. L. Haines, and V. E. Viola, Jr., Phys. Rev. 120, 1350 (1962).

10. T. Sikkeland and V. E. Viola, Jr., in Proceedings of the 2nd Conference on Reactions Between Complex Nuclei, May 1963.

11. T. D. Thomas, Phys. Rev. 116, 703 (1959).

12. V. E. Viola, Jr., and T. Sikkeland, Phys. Rev. 128, 767 (1962).

U at the same bombarding energy; this partly explains the higher isomer ratio for this system. There are, however, large differences between the ratios for the different targets at the same value for $\langle l_f \rangle$. A possible explanation for this discrepancy is that the $\langle l_n \rangle$ values are incorrect. The level width for fission is expected to increase with spin. This might have the effect with Au as target (where the fission threshold is fairly high) of increasing the average value of the spin of the fissioning nuclei compared with the $\langle l_{CF} \rangle$ values. There must, however, be large changes in order to change $\langle l_f \rangle$ appreciably.

Other factors, therefore, are contributing. Because of the spheroidal shape of the fragments at scission, the repulsive Coulomb forces may introduce angular momenta. This would alter the $\langle l_f \rangle$ values estimated above. The fission mode producing Cd^{115} therefore can have a strong influence on the isomer ratio.

For the U + C system, the Cd^{115} is formed by symmetric fission, since $A = 118$ is approximately the center of the mass-yield curve. However, for Au + C and Au + O, Cd^{115} is formed by more asymmetric fission, as $A = 98$ is the center of the mass-yield curve.¹³

In the system U + 100-MeV protons, the Cd^{115} is produced via symmetric fission and the ratio is 0.3,¹⁴ similar to that for U + C. In the fission of Bi by 450-MeV protons, the Cd^{115} ratio was found to have a value of 3.5. $A = 115$ lies on the heavy side of the bismuth mass-yield curve, similar to the systems Au + heavy ion. Consequently, there seems to be evidence that the asymmetry of the fission fragments strongly

13. H. M. Blann, Phys. Rev. 123, 1356 (1961).
14. H. G. Hicks and R. S. Gilbert, Phys. Rev. 100, 1286 (1955).

influences the relative yields of the isomeric states. Porile has suggested that an increase in the fission asymmetry, resulting in an increase in the deformation energy, might result in higher angular momentum for the fission fragments.¹⁵

A few other isomer ratios have been determined for independent fission yields. Talat-Erben et al. found that for Te^{131} formed in the thermal-neutron fission of U^{235} the ratio of high-spin to low-spin isomer was 4.8.¹⁶ Haller and Anderson measured the isomer ratio for Br^{80} in the 70- to 160-MeV proton fission of uranium, and again the high-spin isomer was favored.¹⁷ Croal and Glendenin report that, in the thermal-neutron fission of Pu^{239} , the low-spin isomers of Pd^{111} and Rh^{106} are favored.¹⁸ In all but the Rh^{106} case, these ratios are in agreement with the suggestion that asymmetric fission imparts more angular momentum to the fragments, resulting in increased yield of the high-spin isomer, whereas symmetric fission, having lower angular momentum, favors the low-spin state.

Acknowledgments

We wish to thank Albert Ghiorso for his interest in and encouragement of this work. Mrs. Roberta B. Garrett and Jack E. Clarkson were most helpful in the experimental part. We gratefully acknowledge the cooperation of the operating crew of the Hilac.

15. N. T. Porile, Phys. Rev. 108, 1956 (1957).

16. M. Talat-Erben, L. E. Glendenin, and E. P. Steinberg (Argonne National Laboratory), private communication, 1958.

17. I. B. Haller and G. Anderson, J. Inorg. Nucl. Chem. 20, 12 (1961).

18. I. F. Croal and L. E. Glendenin (Argonne National Laboratory), private communication, 1960.

4. KINETIC ENERGY AND MASS DISTRIBUTIONS FOR NUCLEAR FISSION AT MODERATE EXCITATION ENERGY

Donald S. Burnett and Stanley G. Thompson

Fission fragment kinetic energy measurements using semiconductor detectors have been made for the alpha-induced fission of (a) $Au^{197} + 65.0$ -MeV α , (b) $Bi^{209} + 65.0$ -MeV α , (c) $Th^{232} + 21.4$ -, 25.7 -, 33.0 -, and 65.0 -MeV α , and (d) $U^{238} + 25.7$ -, 33.0 -, and 65.0 -MeV α . The data were obtained in the form of a two-di-

mensional distribution function $N(E_1, E_2)$, i. e., the number of events for a given E_1 and E_2 . The $N(E_1, E_2)$ distribution was then transformed into a two-dimensional mass and total kinetic energy distribution, $N(A_1, E_T)$, by the equations $E_T = E_1 + E_2$ and $A_1 = E_2/E_T(A)$, where A is the mass of the compound nucleus.

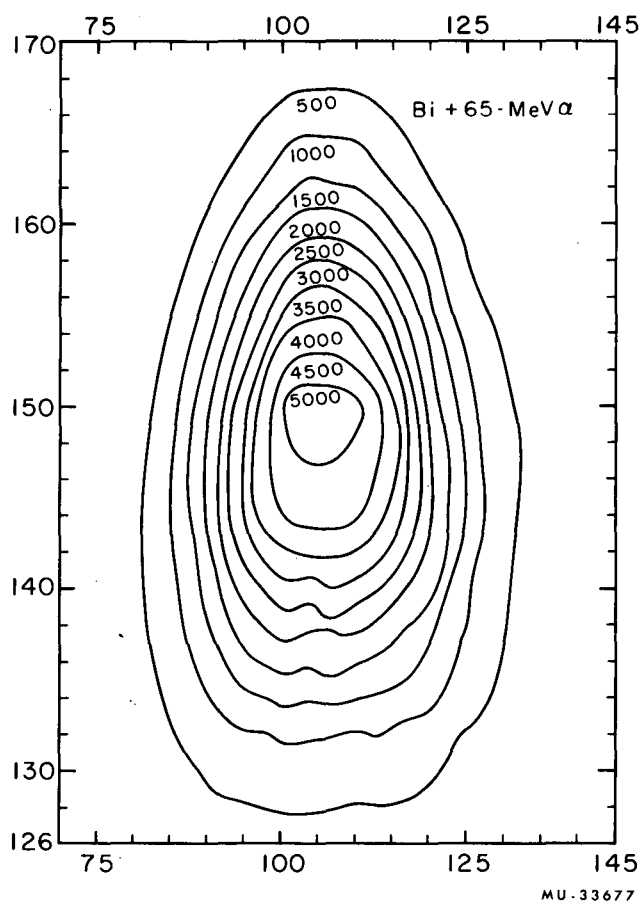


Fig. B.4-1. Experimental contour map for Bi + 65-MeV α 's.

The Bi and Au data may be compared with recent quantitative liquid-drop calculations made by Nix and Swiatecki.¹ An overall qualitative comparison of the experimental data and the theoretical predictions is provided in Fig. B.4-1, which shows the experimental and theoretical contour maps for Bi²⁰⁹ + 65.0-MeV α . Inspection of Fig. B.4-2 will reveal the following features of both maps:

- (a) The average total kinetic energy, taken as a function of mass, decreases slowly from a maximum at symmetric fission ($A_1 = 106.5$).
- (b) The width of the total kinetic energy distributions is approximately constant for masses near symmetric fission (to about $A_1 = 120$).
- (c) The width of the mass distribution, taken as a function of total kinetic energy, increases sharply with decreasing total kinetic energy. Quantitative comparison of the experimental and theoretical distributions were made, using the first and second moments, and good agreement

1. J. R. Nix and W. J. Swiatecki (Lawrence Radiation Laboratory), private communication.

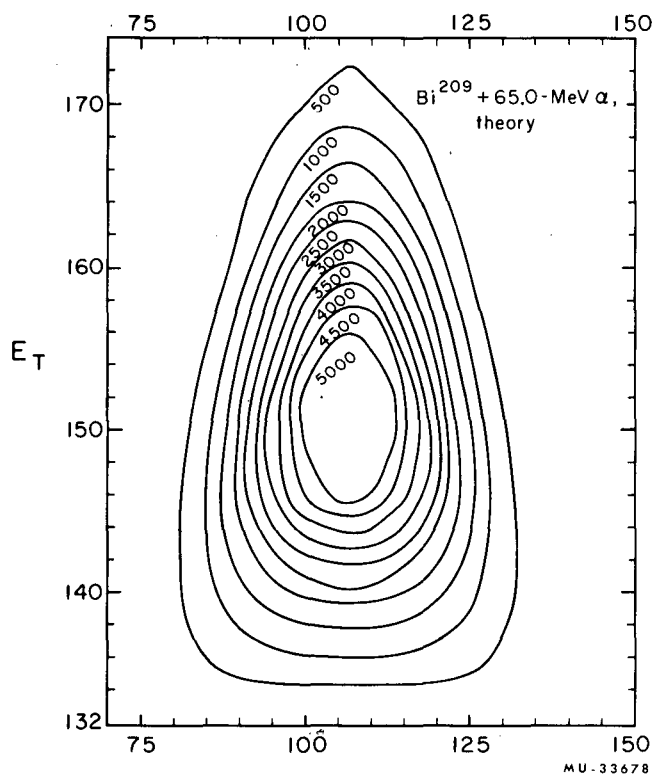


Fig. B.4-2. Theoretical contour map for Bi + 65-MeV α 's.

was obtained.² This indicates that the liquid-drop model of fission may be capable of accounting for the main features of the fission of the lighter elements.

Unfortunately, the above theoretical calculations do not apply to the U and Th data. However, these results are interesting for their own sake. The significant features of fission in this region of Z^2/A are nicely illustrated by mass profiles for a given range of total kinetic energy. These are shown in Fig. B.4-3 for Th²³² for three different total kinetic energies and bombardment energies. The mass-yield curves tend to be triple-peaked at low total kinetic energies and low bombardment energies. These transform with increasing total kinetic energies into asymmetric distributions and with increasing bombardment energy into symmetric distributions. The increasing yield of the symmetric fission relative to the asymmetric is clearly shown. Detailed quantitative analysis of these and the U²³⁸ data is given in reference 2.

2. Donald S. Burnett, Kinetic Energy and Mass Distributions for Nuclear Fission at Moderate Excitation Energy (Ph. D. Thesis), UCRL-11006, Oct. 1963 (unpublished).

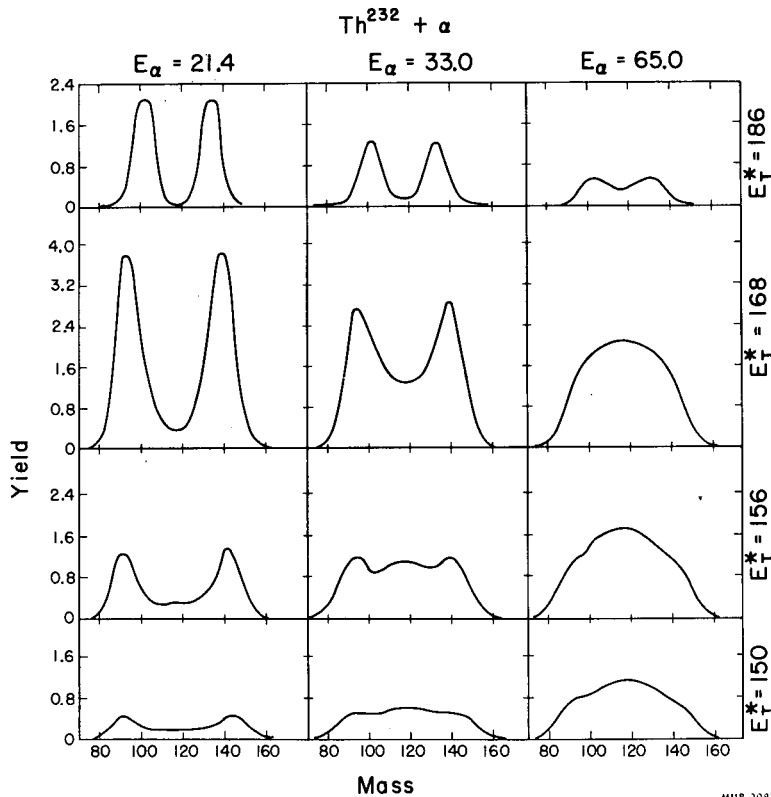


Fig. B.4-3. Mass profiles for various total kinetic energies E_T^* and bombardment energies E_α for $\text{Th}^{232} + \alpha$. Total kinetic energies are not corrected for neutrons. Mass distributions are for range of ± 3 MeV from quoted E_T^* values. Yields are in % per AMV, where the total yield is normalized to 200%.

5. ENERGY-MASS DISTRIBUTIONS AND ANGULAR MOMENTUM EFFECTS IN HEAVY-ION-INDUCED FISSION

Franz Plasil and Stanley G. Thompson

Measurements have been made of the energy and mass distributions of fission fragments produced by the bombardment of a number of relatively light elements with heavy ions. The results have been interpreted in terms of an approximate version of the liquid drop model that applies to this region of elements.

The energies of both fission fragments from every event considered have been measured with solid state detectors and recorded in a correlated manner. The energy data have been transformed, with a random-number technique, to give mass-total kinetic energy density-of-events distributions. The reactions studied were (a) $\text{Er}^{170} + \text{O}^{16} = \text{Os}^{186}$, (b) $\text{Yb}^{174} + \text{C}^{12} = \text{Os}^{186}$, and (c) $\text{W}^{182} + \text{O}^{16} = \text{Pb}^{198}$. Data have been obtained at several bombarding energies in each case. These energies ranged from 102 to 165 MeV. Spontaneous fission of Cf^{252} has been used to calibrate the detectors and the electronic system. Details of experimental procedures and

of data processing are given in reference 1.

The resulting distributions were compared with theoretical distributions, calculated from a modified version of the liquid-drop model in which the deformed nucleus is represented by two tangent or overlapping spheroids.² Such a model is thought to apply to the fission of elements lighter than radium. The statics as well as the dynamics have been worked out by Nix for this model,² and the results, combined with the assumption of statistical equilibrium at the saddle, enabled him to calculate the probability of obtaining a fission event with a given total kinetic energy and a given mass split. Probability distributions obtained in this manner are directly comparable to density-of-events distributions measured here, after the experimental distributions had been corrected for effects of neutrons evaporating from the excited fragments.

The work of Burnett shows that comparisons between experiment and theory of the type

1. F. Plasil, Energy-Mass Distributions and Angular Momentum Effects in Heavy-Ion-Induced Fission (Ph. D. Thesis), in preparation.

2. J. R. Nix and W. J. Swiatecki (Lawrence Radiation Laboratory), private communication.

described above gives good agreement for the magnitudes of the average total kinetic energy released and of the widths of the overall mass and total kinetic energy distributions.³ The work described here has been carried out over a range of excitation energies. It extends the agreement between experiment and theory to the dependence on temperature of the widths of the overall mass-yield and total kinetic energy-yield distributions. Figure B. 5-1 shows the variances (a measure of the square of the width) of the total kinetic energy-yield distributions as a function of the nuclear temperature of the fissioning nucleus for the fission of the Pb^{198} compound nucleus. Figure B.5-2 shows the variances of the mass-yield curves as a function of the temperature for the same cases as Fig. B. 5-1. Theoretical calculations in both cases are given by the solid line. Considering that the theory involves no adjustable parameters and that no normalization of experimental results has been made, the agreement is remarkably good. In general the conclusion drawn from this work is that the liquid-drop model, in this region of relatively light elements, seems to be able to account for the gross features of the fission distributions. To establish this result more

3. D. S. Burnett, Kinetic Energy and Mass Distributions for Nuclear Fission at Moderate Excitation Energy (Ph.D. Thesis), UCRL-11006, Oct. 1963.

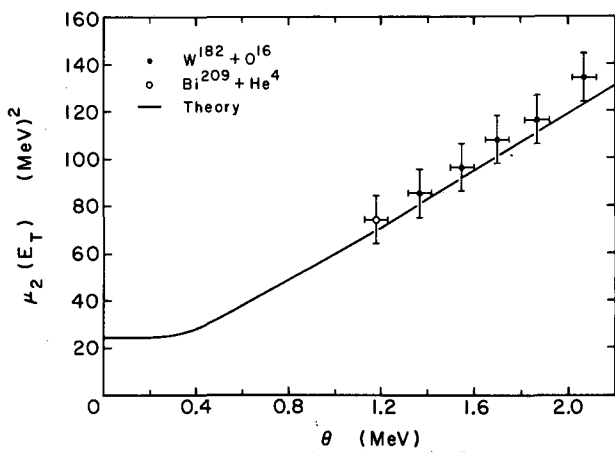


Fig. B. 5-1. Variances of the overall total kinetic energy distributions for the Pb^{198} compound nucleus. The solid line gives the theoretical result.

conclusively, more data of this type for a number of different targets are needed.

Certain disagreements between experiment and theory exist in the fine features of the distributions. They are described more fully in reference 1. The disagreements are believed to be in part due to the high angular momenta encountered in this work.

Angular momentum effects also had to be considered when the nuclear temperatures of Figs. B. 5-1 and B. 5-2 were evaluated. A large amount of rotational energy in the fissioning system lowers the fission barriers.⁴ This effect, along with the possibility of fission occurring after the emission of several neutrons, has been taken into account in calculating fission cross sections from fission widths. These calculated cross sections have been fitted to the experimental results of Sikkeland and Viola,⁵ and from the parameters used in these fits average values of the nuclear temperature at fission have been obtained.

4. S. Cohen, F. Plasil, and W. J. Swiatecki, Equilibrium Shapes of a Rotating Charged Drop and Consequences for Heavy-Ion-Induced Nuclear Reactions, UCRL-10775, April 1963. This reference also gives earlier references on the effect discussed in the above text.

5. T. Sikkeland and V. E. Viola (Lawrence Radiation Laboratory), private communication.

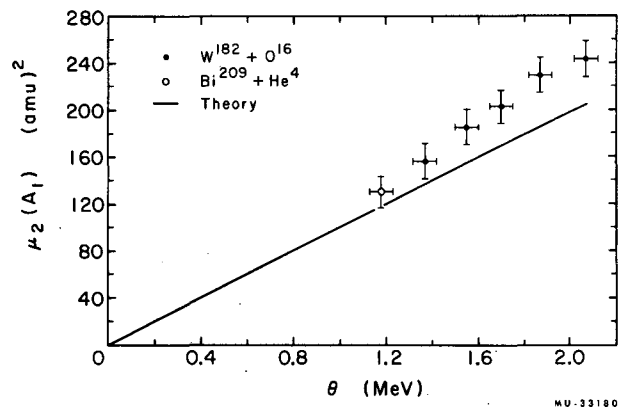


Fig. B. 5-2. Variances of the overall mass-yield curves for the Pb^{198} case. Theoretical results are given by the solid line.

6. FISSION BARRIER OF THALLIUM-201(*)

Donald S. Burnett, Raymond C. Gatti, Franz Plasil, P. Buford Price,
Wladyslaw J. Swiatecki, and Stanley G. Thompson

The primary purpose of this work was the determination of the fission barrier of the compound nucleus Tl^{201} produced by the bombardment of Au^{197} with helium ions.

A new method, developed by Price and Walker, was used for detection of the fission fragments and measurement of the fission cross sections. In this method strips of mica were used to detect the fragments. Tracks produced in the mica by fragments become easily visible under an ordinary microscope when the mica is treated with hydrofluoric acid. Background tracks from particles lighter than about mass 30 are not visible.

The helium ion beams were produced by acceleration in the Berkeley 88-inch variable-energy cyclotron.

The gold targets were prepared by standard volatilization methods, using gold of the highest available purity. Self-supporting foils of thickness $\approx 3 \text{ mg/cm}^2$ were obtained; the thickness of the foils was measured by weighing a piece with known area. The target was mounted at the standard angle of 45 deg relative to the beam direction. The beam passed through the target and entered a Faraday cup that was connected to an integrator which measured the integrated beam current. The energies of the helium ions were measured by the usual absorber methods before the bombardments were started.

The fission fragment detectors were rectangular strips of mica of 1 cm wide, 1.25 cm long, and of a convenient thickness ($\approx 10^{-2} \text{ cm}$). The strips were cleaved along planes in order to obtain fresh surfaces. The strips were pre-etched by placing them in contact with 27 M hydrofluoric acid for 2 hours at room temperature. The mica strips were then removed, washed with water and alcohol, and dried. A customary inspection of the strips under a microscope shows occasional very large fission tracks (from impurities), but the large size of these tracks makes them easily distinguishable from the smaller ones produced during the bombardments because the subsequent "developing" time with hydrofluoric acid is much shorter.

In final preparation for their use in each of the experiments, two mica strips were glued

into a position in the aluminum V block as illustrated in Fig. B. 6-1, and were mounted in the target assembly as indicated. In all experiments the target was mounted at the standard angle relative to the beam direction and the distance between the end of the block (edges of mica strips) and the target was held constant at $\approx 1 \text{ cm}$. Under these conditions, the geometry was such that roughly 7% of the total fission events produced in the target were detected.

Upon completion of the bombardments the mica detectors were soaked in 27 M hydrofluoric acid for thirty minutes and were washed and dried as described above. Finally the strips were mounted between two microscope cover-glass plates. The density of fission tracks in a "standard area" was determined by scanning under a microscope with a suitable magnification such as 500 to 1000. The standard area refers to a strip 1.195 cm long and 0.0170 cm wide (see Fig. B. 6-1).

The measured fission cross sections as a function of excitation energy are shown in Fig. B. 6-2. These results are shown in the form of the ratio of decay probabilities Γ_f/Γ_n in Fig. B. 6-3. In the latter case, the data obtained at helium ion energies above 40 MeV were not used, in order that complications due to second-chance fission would not be introduced. The curve drawn through the points in Fig. B. 6-3 is the result of making least-squares fits of a newly derived theoretical expression having four parameters. The formula for Γ_f/Γ_n used in interpreting the experimental data is similar to that used

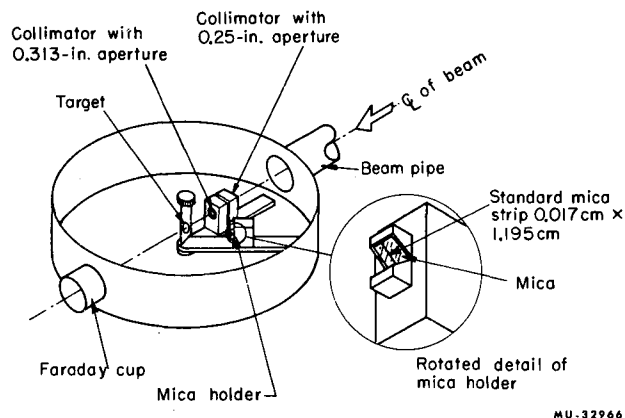


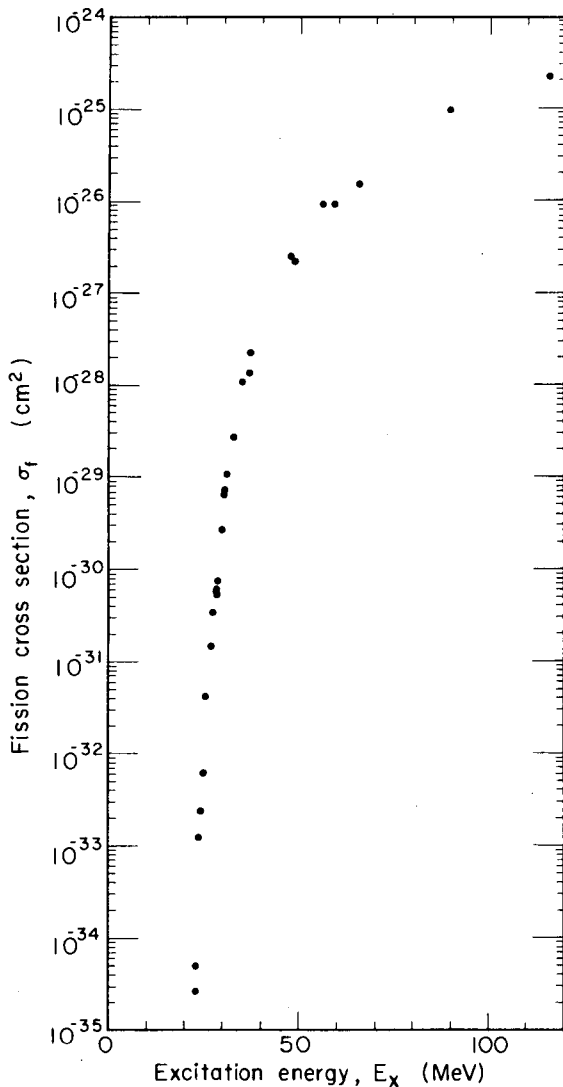
Fig. B. 6-1. Schematic drawing of the target and detector assembly.

* Condensation of paper submitted to Phys. Rev. (UCRL-11079, Nov. 1963).

by Huizenga et al. ¹ with one important difference, namely that an attempt was made to allow for the quantum-mechanical penetrability of the barrier. The resulting expression may then be used for excitation energy above and below the barrier, and--with some reservations-- in the region of the barrier. Further details concerning the expression used and its derivation may be found in reference 2.

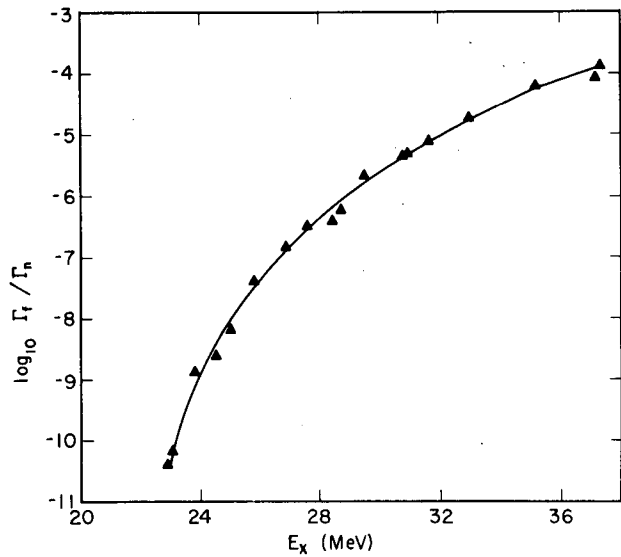
1. J. R. Huizenga, R. Chaudhry, and R. Vandenbosch, Phys. Rev. 126, 210-219 (1962).

2. Donald S. Burnett, Raymond C. Gatti, Franz Plasil, P. Buford Price, Wladyslaw J. Swiatecki, and Stanley G. Thompson, Fission Barrier of Thallium-201, Phys. Rev. (to be published).



MUB-2301

Fig. B. 6-2. Measured fission cross section versus excitation energy for the reaction $^{79}\text{Au}^{197} + ^2\text{He}^4 \rightarrow ^{81}\text{Tl}^{201}$.



MU-32967

Fig. B. 6-3. $\text{Log}_{10} \Gamma_f/\Gamma_n$ versus excitation energy.

The comparison of the experimental measurements with the theoretical expression proceeded in several stages, which showed that the experimental points cover a sufficient range in energy and cross section and provide a curve with sufficient structure to determine four parameters. The absolute magnitude, slope, and curvature of the experimental curve determine the values of the fission barrier, B_f , and the level density parameters a_f and a_n . A further shape characteristic, related to the third derivative (an increase of curvature at low energies), serves to place limits on the barrier penetrability factor $\hbar\omega$.

The best fits as judged by the sum of the squares of the deviations are found in the neighborhood of $B_f = 22$ or 23 MeV, with $\hbar\omega$ between 0 and 1.4 MeV, and the pair a_f between 18.9 and 14.0 and a_n between 14.3 and 10.6. The value of B_f adopted is 22.5 ± 1.5 MeV.

Accepting the value $B_f = 22.5 \pm 1.5$ MeV for the fission barrier of Tl^{201} , we shall deduce the ratio of the electrostatic energy to the surface energy for this nucleus--or, equivalently, the value of the fissionability parameter, x , defined as

$$\begin{aligned} x &= \frac{(\text{charge})^2}{10 (\text{volume}) (\text{surface tension})} \\ &= \frac{(\text{electrostatic energy of sphere})}{2 (\text{surface energy of sphere})} \\ &= (Z^2/A)/(Z^2/A) \text{ critical,} \end{aligned}$$

for a nucleus idealized as a charged drop. We estimate that of the 22.5 ± 1.5 MeV, 4.3 MeV is due to the extra stability of the ground state

of Tl^{201} ,³ leaving 18.2 ± 1.5 MeV to be accounted for by the increase in the sum of surface and electrostatic energies in the saddle-point configuration of the nucleus. According to the liquid-drop model, this energy increase may be written in units of the surface energy, $a_2 A^{2/3}$, as

$$B_f = a_2 A^{2/3} \xi(x), \quad (1a)$$

or, in units of the electrostatic energy, $a_3(Z^2/A^{1/3})$, as

$$B_f = a_3 \frac{Z^2}{A^{1/3}} \frac{\xi(x)}{2x}. \quad (1b)$$

Here $\xi(x)$ is a known dimensionless function of x (see Cohen and Swiatecki⁴).

Taking Green's value, 17.80 MeV, for the surface energy coefficient a_2 , we find the ratio $B_f/a_2 A^{2/3} = (18.2 \pm 1.5)/17.80 A^{2/3} = 0.0298 \pm 0.0025$. From Eq. (1a) and reference 4, we then obtain

$$x(Tl^{201}) = 0.675 \pm 0.013$$

and, consequently,

$$(Z^2/A)_{crit} = 48.4 \pm 0.5.$$

Had we used Green's value of the electrostatic energy coefficient $a_3 = 0.710$ MeV and Eq. (1b), we would have found instead $x(Tl^{201}) = 0.672$ and $(Z^2/A)_{crit} = 48.6$. The values of $x(Tl^{201})$ and $(Z^2/A)_{crit}$ required to reproduce the experi-

mental barrier for Tl^{201} are quite insensitive to the absolute values of a_2 or a_3 . Thus, increasing a_3 by 5% (to 0.746 MeV) leads to $x(Tl^{201}) = 0.676$, $(Z^2/A)_{crit} = 48.3$, a change of about half a percent. This is a consequence of the sensitivity of the barrier, B_f , to the value of the fissionability parameter, x . One may thus determine the ratio of the electrostatic to the surface energy rather precisely even in the absence of an accurate absolute determination of either quantity. As a result, we may adopt with some confidence the equation for calculating the fissionability parameter for a nucleus idealized as a charged drop,

$$x = (Z^2/A)/(48.4 \pm 0.5).$$

This relation may be regarded as a consequence of interpreting our barrier measurement, $B_f = 22.5 \pm 1.5$ MeV, in terms of the liquid-drop model. Another way of stating our result, which is independent of the assumption of this model, is that we have determined the mass of the Tl^{201} nucleus in that (saddle-point) configuration in which the cohesive and disruptive forces are just balanced in unstable equilibrium. This mass is equal to the ground-state mass of Tl^{201} (reference 5) plus 22.5 MeV, or

$$M_{\text{saddle-point}}(Tl^{201}) = 200.9949 \pm 0.0015$$

mass units on the carbon scale.

An adequate semi-empirical mass formula ought to reproduce this saddle-point mass as well as the ground-state masses of nuclei.

3. W. J. Swiatecki, Semi-Empirical Interpretation of Nuclear Masses and Deformation (Talk presented at the Vienna Conference on Nuclear Masses, Aug. 1963).

4. S. Cohen and W. J. Swiatecki, Ann. Phys. N. Y. 22, 406 (1963).

5. L. A. König and J. H. E. Mattauch, Nucl. Phys. 31, 18-42 (1962).

7. FISSION BARRIER OF MERCURY-198

Raymond C. Gatti, Arastoo Khodai-Joopary, and Stanley G. Thompson

The primary purpose of this work was to determine the fission barrier of the compound nucleus mercury-198 produced by the bombardment of gold-197 with protons from the Berkeley 88-inch variable-energy cyclotron. The same experimental equipment, techniques, and theoretical approach were used as described in the previous paper, on the Fission Barrier of Thallium-201, by Burnett et al.

The measured fission cross sections as a function of excitation energy are shown in Fig. B.7-1. The corresponding results, in the form of a plot of $\log_{10} \Gamma_f / \Gamma_n$, are given in Fig. B.7-2.

From the liquid-drop theory, using

Fission cross section vs excitation energy

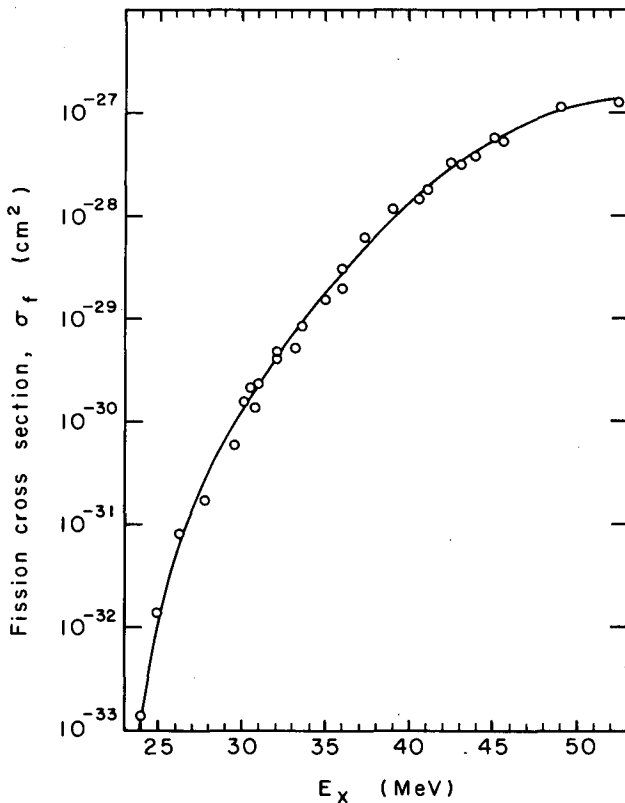
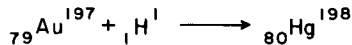


Fig. B.7-1. Fission cross section as a function of excitation energy for ${}_{79}\text{Au}^{197} + {}_1\text{H}^1 \rightarrow {}_{80}\text{Hg}^{198}$.

$(Z^2/A)_{\text{crit}} = 48.4 \pm 0.5$, we calculate the fission barrier of mercury-198 as 22.1 MeV. We find at this stage of the work that the lower limit on the fission barrier is $\approx 21.3 \pm 1.0$ MeV. The best fit to the measured data was with values of the penetrability factor, $\hbar\omega$, in the range 0 to 1 MeV and with the level density parameters $a_n \approx 15$ MeV⁻¹ and $a_f \approx 18$ MeV⁻¹. We are still in the process of measuring lower fission cross sections, so that more precise limits on the values of the fission barrier and the parameters $\hbar\omega$, a_n , and a_f can be established.

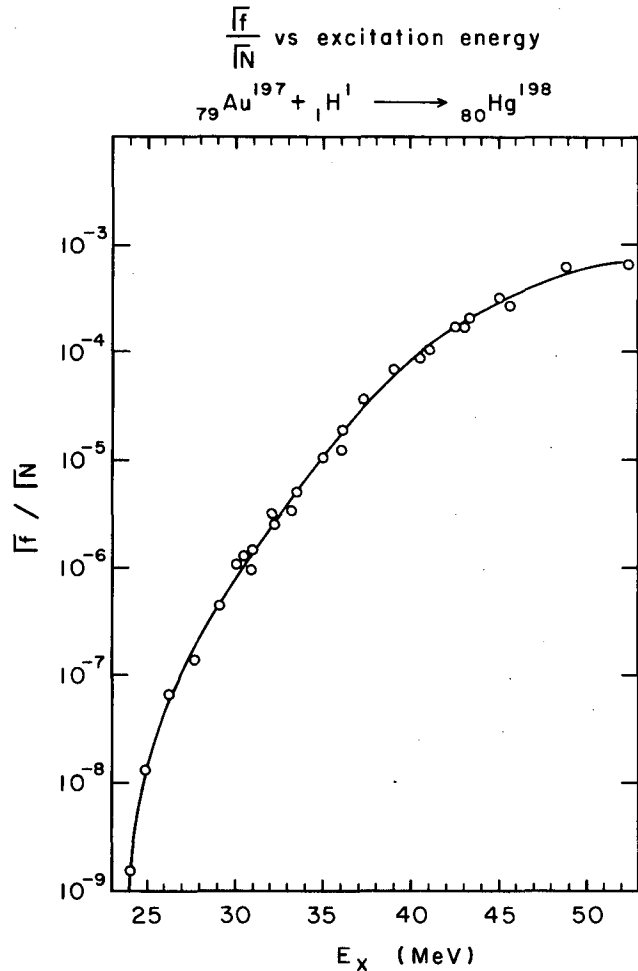


Fig. B.7-2. Γ_f / Γ_n as a function of excitation energy for ${}_{79}\text{Au}^{197} + {}_1\text{H}^1 \rightarrow {}_{80}\text{Hg}^{198}$.

C. NUCLEAR REACTIONS

1. POLARIZATION IN ELASTIC SCATTERING OF 22-MeV PROTONS FROM DEUTERONS*

Homer E. Conzett, G. Igo, and William J. Knox†

The measurement and interpretation of the polarization in the scattering of low-energy nucleons by deuterons should have an important bearing on the understanding of nucleon-nucleon interactions in nuclear matter. Even though the two-body interaction may not be completely known, one would hope to predict the results of nucleon-deuteron scattering in terms of measured nucleon-nucleon scattering parameters, and to determine whether or not any specifically three-body interaction would be required to explain the results. Unfortunately, at low energies, at which the results are of greatest interest with respect to their bearing on nuclear structure, the interactions among the three particles during the scattering are roughly equally strong and thus the three-body analytic solution of the problem becomes difficult. The maximum polarization is known to be small in p-p scattering ($\lesssim 1\%$)^{1, 2} and in n-p scattering ($\lesssim 5\%$)^{3, 4} near 20 MeV bombarding energy. On the other hand, the polarization in the scattering of protons from complex nuclei reaches values of up to 100% at energies as low as 6 MeV. In scattering from the lightest nuclei, in particular, the maximum polarization is approximately 100% in p-He⁴ scattering at 6 to 14.5 MeV^{5, 6} and 55% in p-H³ and p-He³ scattering at 14.5 MeV.⁶ The former is understandable in terms of the splitting of the $j = 1 + 1/2$ and $j = 1 - 1/2$ phase shifts due to the strong spin-orbit forces acting in the p-He⁴ (Li⁵) system. Such an explanation might be considered for the p-H³ and p-He³ results, treating the target as a spin-zero nucleus and thereby ignoring any tensor interaction. How-

ever, an extension of this argument to the p-d system does not seem warranted, since measurements of the polarization in p-d scattering have been consistent with zero or very small polarization at energies below 17 MeV.⁷ Thus, determinations of polarization in p-d or n-d scattering at energies below 50 MeV could provide information useful to the understanding of this remarkable difference between the polarization induced in nucleon-nucleon scattering and that resulting from the scattering of the nucleon from a few-nucleon system.

A general theory of nucleon-deuteron scattering, including tensor forces but neglecting the distortion of the deuteron, has been developed,⁸ but calculations based on this formalism are not presently available. An approximate calculation has been made which includes, also, the effect of deuteron distortion in n-d scattering below 3.5 MeV,⁹ and this calculation predicted a rapid variation with energy of the neutron polarization at 90° c. m., reaching a maximum of 12% near 1 MeV. Experimental results to date are not in agreement with respect to confirmation of this prediction.¹⁰ Previous calculations¹¹ carried out for central forces alone had compared well with differential cross section data up

*Short version of a paper published in Phys. Rev. Letters 12 (March 1964).

†Department of Physics, University of California, Davis, California.

1. W. A. Blanpied, Phys. Rev. 116, 738 (1959).

2. H. E. Conzett, G. Igo, and A. Nir, International Symposium on Polarization, Helv. Phys. Acta, Suppl. VI, 253 (1960).

3. W. Benenson, R. L. Walter, and T. H. May, Phys. Rev. Letters 8, 66 (1962).

4. R. B. Perkins and J. E. Simmons, Phys. Rev. 130, 272 (1963).

5. L. Rosen and J. E. Brolley, Jr., Phys. Rev. 107, 1454 (1957); L. Rosen, J. E. Brolley, Jr., M. L. Gursley, and L. Stewart, Phys. Rev. 124, 199 (1961).

6. L. Rosen and W. T. Leland, Phys. Rev. Letters 8, 379 (1962).

7. At 17 MeV, K. W. Brockman, Jr., Phys. Rev. 110, 163 (1958); at 14.5 MeV, ref. 5; at 10 MeV, L. Rosen, J. E. Brolley, Jr., and L. Stewart, Phys. Rev. 121, 1423 (1961); near 3.5 MeV, M. R. Shafroth, R. A. Chalmers, E. N. Strait, and R. E. Segal, Phys. Rev. 118, 1054 (1960); at 1 to 2.5 MeV, R. Chalmers, R. S. Cox, K. K. Seth, and E. N. Strait, Bull. Am. Phys. Soc. II, 8, 38 (1963).

8. B. H. Bransden, K. Smith, and C. Tate, Proc. Roy. Soc. (London) A 247, 73 (1958).

9. L. M. Delves and D. Brown, Nuclear Phys. 11, 432 (1959); L. M. Delves, Nuclear Phys. 33, 482 (1962).

10. Data of A. T. G. Ferguson and R. E. White, Nuclear Phys. 33, 477 (1962), and of S. E. Darden, C. A. Kelsey, and T. R. Donoghue, Nuclear Phys. 16, 351 (1960) agree with the prediction of reference 8. Data of A. J. Elwyn, R. O. Lane, and A. Langsdorf, Jr., Phys. Rev. 128, 779 (1962) do not agree.

11. R. A. Buckingham and H. S. W. Massey, Proc. Roy. Soc. (London) A 179, 123 (1941); R. A. Buckingham, S. J. Hubbard, and H. S. W. Massey, Proc. Roy. Soc. (London) A 211, 183 (1952); R. A. Christian and J. L. Gammel, Phys. Rev. 91, 100 (1953).

to 10 MeV but could not result in any nucleon polarization. At higher energies, calculations employing the impulse approximation have had some success in fitting p-d polarization results at 150 MeV, and these calculations have been extended to energies as low as 40 MeV.¹²

We have measured in a double scattering experiment the proton polarization produced in the elastic scattering of 22-MeV protons by deuterons. The results are presented in Fig. C.1-1. The error associated with each point is only the statistical error. Most systematic errors would merely shift the zero of the polarization scale, and it is believed that the effect of all systematic errors is less than $\pm 2\%$. The results show a substantial polarization in p-d scattering at 22 MeV. The large values reached by the polarization suggest that it may be difficult to explain the results in terms of nucleon-nucleon scattering parameters even with maximum constructive interference in the scattering of the incident proton from the two particles of the deuteron.

Also shown in Fig. C.1-1 are the somewhat smaller back-angle values of $P(\theta)$ in n-d scattering, determined recently at 23.7 MeV.¹³ That experiment utilized, from the $T(d,n)He^4$ reaction, a beam of neutrons whose polarization was taken to be $P_1 = 0.60$, the value of the proton polarization from the mirror reaction $He^3(d,p)He^4$.¹⁴ Values for the neutron polarization, which range from 0.46³ to 0.64,¹⁵ are less precise because of uncertainties in the analyzing power of the helium analyzer used. Thus, if a smaller value of P_1 had been taken, larger values of $P(\theta)$ in n-d scattering would have resulted. More precise data on both systems will be required before any significant back-angle difference between the p-d and n-d results can be claimed.

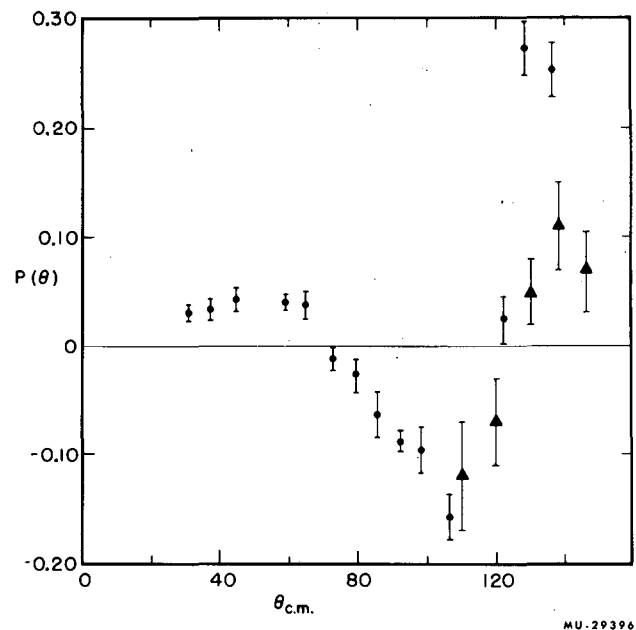


Fig. C.1-1. Polarization, $P(\theta)$, as a function of center-of-mass angle, $\theta_{c.m.}$, in the elastic scattering of 22-MeV protons by deuterons. The triangular points are data from reference 13.

12. L. Castillejo and L. S. Singh, *Nuovo Cimento* **11**, 131 (1959); K. L. Kowalski and D. Feldman, *Phys. Rev.* **130**, 276 (1963).

13. R. L. Walter and C. A. Kelsey, *Nuclear Phys.* **46**, 66 (1963).

14. R. I. Brown and W. Haeberli, *Phys. Rev.* **130**, 1163 (1963).

15. R. B. Perkins and J. E. Simmons, *Phys. Rev.* **124**, 1153 (1961).

2. OPTICAL-MODEL ANALYSIS FOR 48-MeV ALPHA PARTICLES ON CARBON

Richard H. Pehl and Bruce D. Wilkins

An optical-model analysis of 48-MeV alpha particles scattered by C^{12} , making use of the parameter search routine GULLEY,^{1,2} has been

1. Bruce D. Wilkins, *Total-Reaction Cross-Section Measurements for Charged Particles* (Ph.D. Thesis), UCRL-10783, May 1963 (unpublished).

2. Richard H. Pehl, *Studies in Nuclear Spectroscopy by Two-Nucleon Transfer Reactions* (Ph.D. Thesis), UCRL-10993, Aug. 1963 (unpublished).

carried out. The analysis was fitted to the experimental elastic scattering data of Vaughn.³ This analysis demonstrated that elastic scattering and reaction cross-section data enable one to determine very accurately the extreme outer surface of both real and imaginary parts of the nuclear potential. This is a consequence of the

3. Franklin J. Vaughn, *Elastic and Inelastic Scattering of 48-MeV Alpha Particles by Carbon and Magnesium* (Ph.D. Thesis), UCRL-3174, Oct. 1955 (unpublished).

α particle's having a very short mean free path for absorption in nuclear matter. Thus α -particle scattering and σ_R data can give no information on the nuclear potential lying inside the extreme outer surface of the nucleus, since the α particle as such does not exist inside this extreme outer surface. Igo, from an analysis of elastic-scattering data for α 's on several heavier nuclei, came to a similar conclusion concerning the shape of the real part of the optical-model potential at the surface of the nucleus.⁴

Figures C.2-1 and C.2-2 show plots of the real and imaginary potential for several sets of

4. G. Igo, Phys. Rev. 115, 1665 (1959).

parameters that gave good fits to the elastic scattering data. These parameters are listed in Table C.2-I. A comparison of the experimental and predicted values of σ/σ_{Ruth} , using parameter set B, appears in Fig. C.2-3. An experimental value of 901 ± 16 mb obtained¹ for 40-MeV alphas on C^{12} compares favorably with the predicted value of σ_R for set B.

As seen in Fig. C.2-1, it is meaningless to speak of the α -particle interaction in terms of a Gaussian shape or Woods-Saxon shape for the imaginary potential. It is necessary only to adjust the parameters of the potential until it matches a certain shape at the very edge of the nucleus. Figure C.2-4 shows the imaginary po-

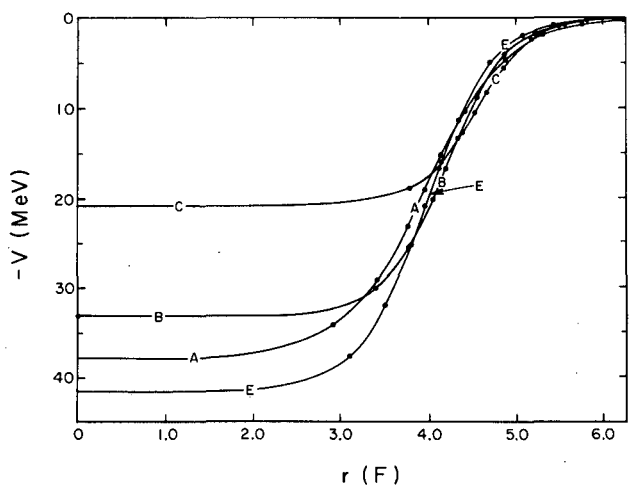


Fig. C.2-1. Comparison of several real potentials that give good fits to the elastic scattering data for 48-MeV α particles on C^{12} . The letters refer to parameter sets listed in Table C.2-I.

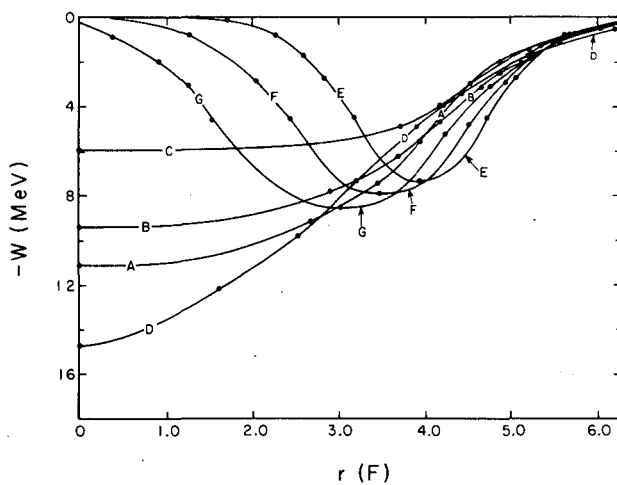


Fig. C.2-2. Comparison of several imaginary potentials that give good fits to the elastic scattering data for 48-MeV α particles on C^{12} . The letters refer to parameter sets listed in Table C.2-I.

Table C.2-I. Sets of parameters that give good fits to $\sigma_{SE}(\theta)$ for 48-MeV alpha particles on C^{12} ; $r_1 = 1.20$ F.

Curve	Form factor	r_0 (F)	r_w (F)	b (F)	a (F)	-V (MeV)	-W (MeV)	χ^2	σ_R (mb)
A	Volume	1.20	1.20	0.70	0.45	37.9	11.1	200	887
B	Volume	1.30	1.30	0.70	0.34	33.0	9.4	177	899
C	Volume	1.45	1.45	0.50	0.32	20.7	5.9	470	764
D	Volume	1.30	0.88	1.00	0.36	32.2	14.7	166	1001
E	Surface	1.20	1.20	0.80	0.37	41.5	7.3	274	770
F	Surface	1.20	1.00	1.00	0.385	40.8	7.9	220	795
G	Surface	1.20	0.80	1.20	0.40	40.1	8.5	180	822

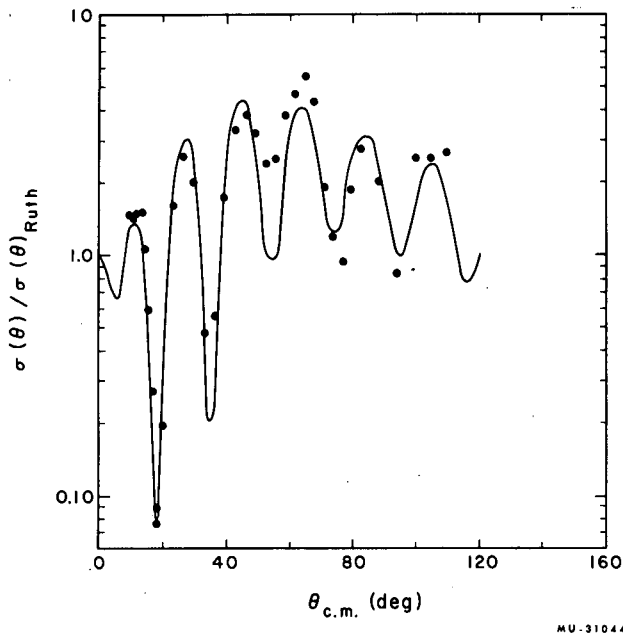


Fig. C.2-3. A plot of σ/σ_{Ruth} for 48-MeV α particles scattered from C^{12} . The solid line is the predicted value of σ/σ_{Ruth} obtained by using parameter set B listed in Table C.2-I.

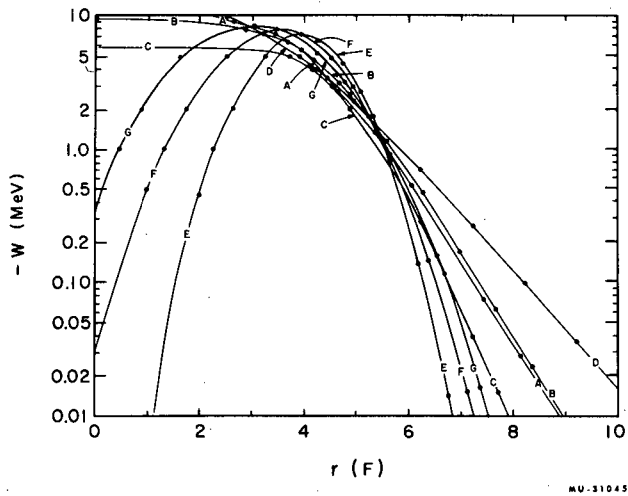


Fig. C.2-4. Comparison of the imaginary potentials listed in Table C.2-I at large values of r .

tential at large values of r , and illustrates that a direct relationship exists between the strength of the imaginary potential and the predicted σ_R in the region of about 5.5 to 7.0 F. From this it can be inferred that the α particle does not penetrate with appreciable probability within about 5.2 F and still have a chance to escape as an elastic event; otherwise, the optical model, using potentials E, F, and G, would be expected to predict a large σ_R .

Figure C.2-5 shows a plot of the various "best fit" real potentials in this surface region. Proper adjustment of the parameters that lead to the same shape potential beyond 5 F gives almost equally good fits. This explains how the nonuniqueness of parameters arises from the use of a nuclear potential form factor by which one attempts to describe the interaction in a region that the α particle does not sample.

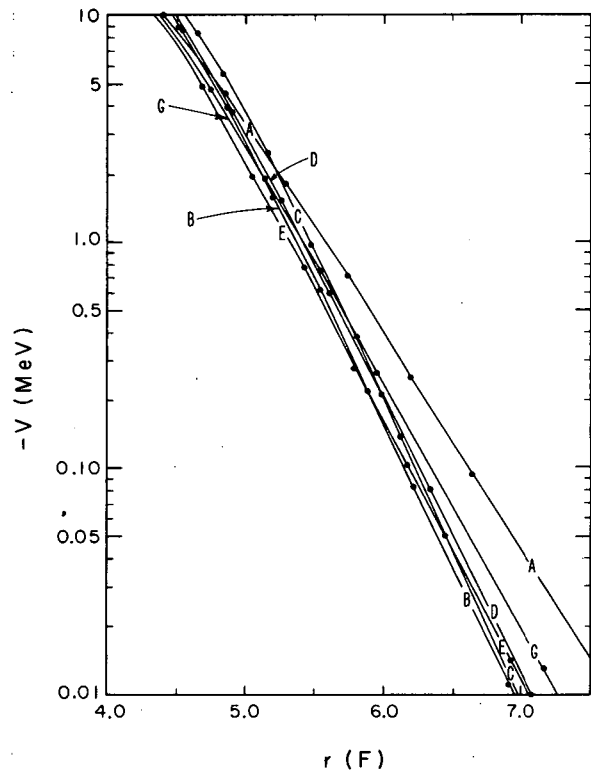


Fig. C.2-5. Comparison of the real potentials listed in Table C.2-I at large values of r .

3. PROTON-INDUCED TWO-NUCLEON PICKUP REACTIONS ON O^{16}

Joseph Cerny and Richard H. Pehl

Although investigation of the various two-nucleon transfer reactions has been increasing in recent years, little experimental work has been done on (p, t) reactions and virtually none on (p, He^3) reactions. Chief interest in (p, t) studies in light elements lies in a potentiality for elucidating the spectroscopy of such poorly known nuclides as Mg^{22} , Ar^{34} , and Ca^{38} . A comparison of the results of (p, He^3) reactions with previous work on direct-interaction (d, a) reactions¹ may provide a means for establishing the mechanism of the latter; this is possible since (p, He^3) reactions are simply visualized as occurring primarily by pickup processes, while (d, a) transitions may occur by pickup or knockout. Lastly, a comparison of the (p, t) and (p, He^3) reactions may provide information on the neutron-proton distribution in the target nucleus.

Oxygen-16 was chosen as the initial target, since the spectroscopy of the product nuclei was well known. The 43.7-MeV proton beam of the 88-inch cyclotron, after energy analysis, was brought into a 36-in. scattering chamber. Reaction products were identified by a dE/dx -E counter telescope whose pulses fed an improved particle identifier.² The dE/dx counter was a 40 mg/cm² phosphorus-diffused silicon detector and the E counter was a 480-mg/cm² lithium-drifted silicon detector; these thicknesses were sufficient to stop all the tritons, He^3 , and He^4 produced. A typical identifier spectrum is shown elsewhere in the report.² Total energy pulses (acquired by adding the dE/dx and E pulses) were fed into a Nuclear Data analyzer which was appropriately gated so that the (p, t), (p, He^3), and (p, a) spectra were recorded simultaneously, each spectrum in a separate 1024-channel group. A RIDL 400-channel analyzer continuously monitored the identifier spectrum.

Figures C.3-1 and C.3-2 present representative $O^{16}(p, t)O^{14}$ and $O^{16}(p, He^3)N^{14}$ spectra, respectively; the average energy resolution (FWHM) was 190 keV for the tritons and 240 keV for the He^3 . The most striking feature of these spectra is the dominance of the ground-state

1. Richard H. Pehl, Studies in Nuclear Spectroscopy by Two-Nucleon Transfer Reactions (Ph. D. Thesis), UCRL-10993, Aug. 1963 (unpublished).

2. F. S. Goulding and J. Cerny, "An Improved Particle Identifier", Paper E. 8 of this report.

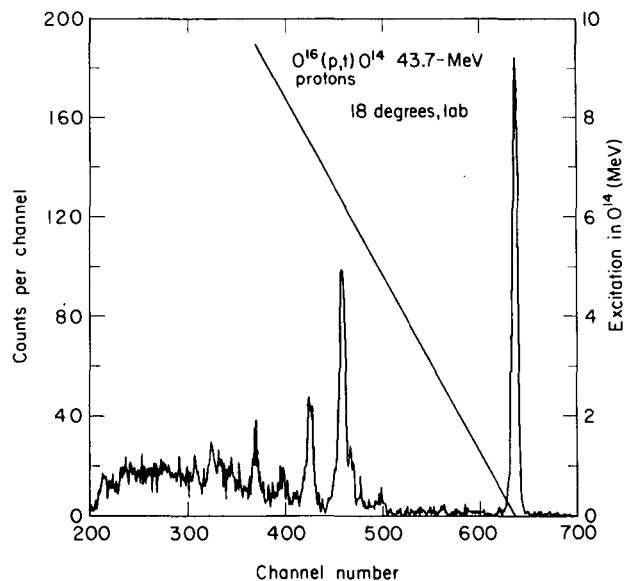


Fig. C.3-1. Triton energy spectrum from the reaction $O^{16}(p, t)O^{14}$. Excitation values for the various peaks are shown.

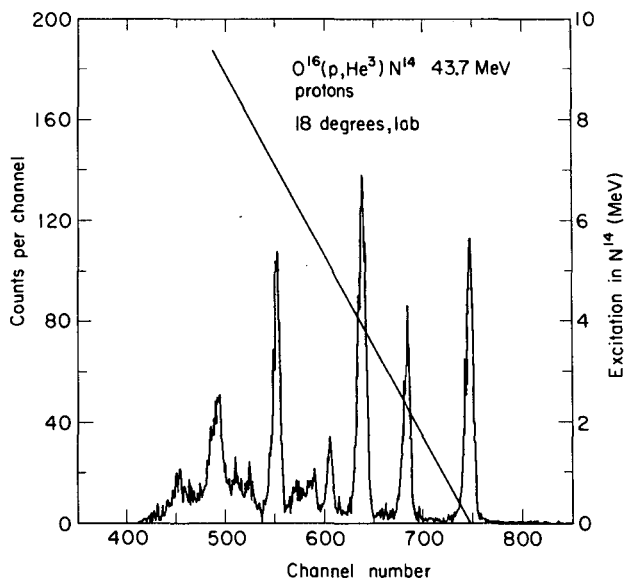


Fig. C.3-2. He^3 energy spectrum from the reaction $O^{16}(p, He^3)N^{14}$. Excitation values for the various peaks are shown.

transition in the (p, t) data--an effect not observed in the (p, He³) transitions.

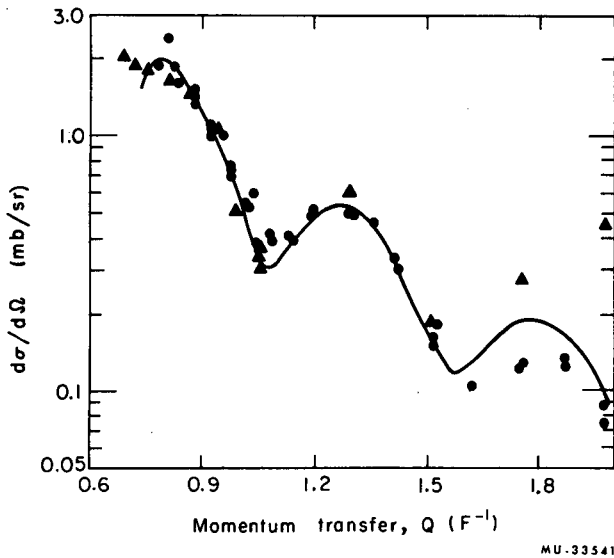


Fig. C.3-3. Angular distributions of the $O^{16}(p, He^3)N^{14}_{gs}$ reaction (shown as \blacktriangle), the $O^{16}(d, \alpha)N^{14}_{gs}$ reaction (shown as \bullet), and a two-nucleon DWBA fit to the (d, α) data for a pure $L=2$ transition.

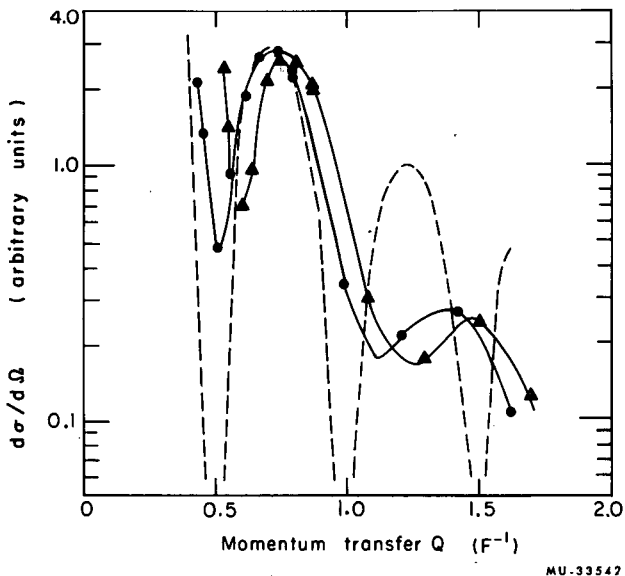


Fig. C.3-4. Angular distributions of, \bullet , the $O^{16}(p, t)O^{14}_{gs}$ and, \blacktriangle , the $O^{16}(p, He^3)N^{14*}$ (2.31-MeV) transition. Also shown is a plane-wave fit to the (p, t) data for $L=0$, $R=6.3$ fermi.

Using the Visscher and Ferrell³ wave functions for the N^{14}_{gs} of $\psi = 0.920 \ ^3D_1 + 0.173 \ ^3S_1 + 0.355 \ ^1P_1$, we would expect the (p, He³) transition to this state [and the equivalent (d, α) transition] to be dominated by a total orbital angular momentum transfer, L , of 2. Figure C.3-3 presents (a) the $O^{16}(p, He^3)N^{14}_{gs}$ angular distribution, (b) the $O^{16}(d, \alpha)N^{14}_{gs}$ angular distribution,¹ and (c) a two-nucleon DWBA fit to the (d, α) data for a pure $L=2$ transition.¹ The (p, He³) and (d, α) data have been compared, since the two incident particles have nearly equal momenta. [The (p, He³) differential cross sections were normalized to the (d, α) data, and in addition the (p, He³) momentum transfer, Q , was increased by 13%--the latter is equivalent to increasing the interaction radius for the (p, He³) reaction over that of the (d, α) reaction.] The similarity between these angular distributions, and the excellence of the SWBA fit, is remarkable, though an independent analysis of the (p, He³) data must be completed before detailed comparison of these and other resolved transitions is possible.

There are several pairs of transitions in which, in an isobaric spin formalism, a (p, t) and a (p, He³) reaction proceed on the same nucleus to the same final state. An instance of this is the pair of transitions $O^{16}(p, t)O^{14}_{gs}$ [0^+ , $T=1$] and $O^{16}(p, He^3)N^{14*}$ [2.31 MeV, 0^+ , $T=1$], which might be expected to possess identical differential and total cross sections, except for Coulomb energy differences in the final states. These angular distributions are shown in Fig. C.3-4. Both these reactions should occur by $L=0$ transfer, and a simple plane-wave fit to the (p, t) data for this L value is also given in Fig. C.3-4 ($d\sigma/d\Omega \approx |J_L(QR)|^2$).

Once the (p, He³) data have been multiplied by a factor of two, it can be seen that the two angular distributions are virtually identical, except that the (p, He³) points are displaced to slightly larger values of momentum transfer. A factor-of-2 difference in cross section was also obtained in comparing the $C^{12}(He^3, n)O^{14}_{gs}$ and $C^{12}(He^3, p)N^{14*}$ (2.31-MeV) transitions;⁴ this factor is predicted by the isobaric spin coupling in those reactions. Though no DWBA two-nucleon transfer calculations have yet been performed, it is unlikely that the greater part of this displacement can be accounted for by Coulomb interactions.

3. W. M. Visscher and R. A. Ferrell, Phys. Rev. 107, 781 (1957).

4. H. W. Fulbright et al., Nucl. Sci. Abstr. 17, 38087 (1963).

4. SCATTERING OF 65-MeV HELIUM IONS BY O^{16}

Bernard G. Harvey, Ernest J-M Rivet, Arthur Springer, John R. Meriwether,
W. Barclay Jones, Jack H. Elliott, and Pierre Darriulat

The elastic and inelastic scattering of 65-MeV helium ions by O^{16} was studied with better energy resolution than has previously been possible. The energy spectra of scattered particles were measured with a resolution of 250 keV with a lithium-drifted silicon counter. The main contribution to the peak widths came from the angular resolution of the counter collimator system (0.8°). The target was either O_2 or CO_2 gas at a pressure of 10 cm Hg, contained in a cell with 0.0001-in. -thick nickel windows. Table C. 4-I shows the energy levels of O^{16} that were observed to be excited. Figure C. 4-1 shows an energy spectrum at 31° (laboratory system). The negative parity levels listed in Table C. 4-I are believed to belong to the configuration $p^{-1}(s, d)$. Thus they are all formed by promotion of a p-shell nucleon to the (s, d) shell. All the levels of this configuration that would be observable were actually observed. The 0-level at 10.95 MeV was not visibly excited, as expected. (The $0+ \rightarrow 0-$ transition with $0+$ particles is unable to conserve parity.) Excitation of the 3- level of the $p^{-1}(s, d)$ configuration at 11.63 MeV should not be forbidden by any selection rules, but the level is too broad to be seen in the present experiment. The negative parity 9.59 MeV level is believed to be of more complex excitation than $p^{-1}(s, d)$. It was not observably excited.

The 2- level at 8.876 MeV was quite strongly excited even though it is of unnatural parity

*Short form of paper published in Nucl. Phys.

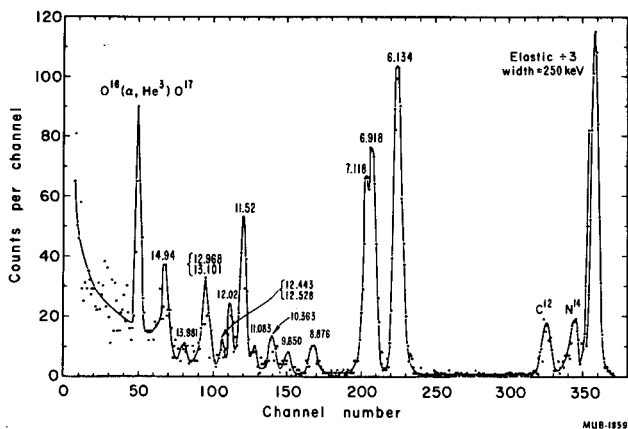


Fig. C. 4-1. Energy spectrum of elastic and inelastic groups from the scattering of 65-MeV helium ions by O^{16} at 31° (lab).

[i. e., parity $(-1)^{J+1}$]. The angular distribution of particles scattered from this level is in phase with the elastic group at small angles, suggesting excitation of the level through an odd angular momentum transfer.

The $T = 1$ levels at 12.968 and 13.101 MeV were both excited, presumably through the presence of a $T = 0$ component. Such strong mixing is presumably due to the presence of a pair of $T = 0$ levels of the same spins as the $T = 1$ pair, and very close in energy. The $T = 1$ pair was actually excited about as strongly as the $T = 0$ pair.

The 6.134-MeV 3-, 6.918-MeV 2+, and 7.118-MeV 1- levels were strongly enough excited to suggest that they are collective.

Table C. 4-I. Levels of O^{16} excited by $O^{16}(\alpha, \alpha')O^{16}$

Level energy (MeV)		
This work	Previous work	J II, T
6.137 ^a	6.134	3-, 0
6.903	6.918	2+, 0
6.973	7.118	1-, 0
8.876 ^a	8.876	2-, 0
9.797	9.850	2+, 0
10.308	10.363	4+, 0
11.069	11.083	3+, 0
11.480	11.520	2+, 0
11.997	12.02	?
12.492	12.443	1-, 0
	12.528	2-, 0
12.989	12.968	2-, 1
	13.101	1-, 1
13.966	13.981	2-, ?
14.975	14.94	4+, ?

a. Used to establish energy scale

5. THE FORMATION OF STRONGLY POPULATED HIGH SPIN LEVELS IN (α, d) REACTIONS

Ernest J-M Rivet, Joseph Cerny, Bernard G. Harvey,
Richard H. Pehl, and James Haag

The strong formation of certain levels in (α, d) reactions was first observed by using the 48-MeV helium ion beam of the 60-inch cyclotron. The spectra from the product nuclei N^{14} , O^{16} , O^{17} , and F^{18} showed one or more very large peaks.

These strongly excited levels were reported¹ as being of $(d_{5/2})^2$ character. The target core is unchanged during the reaction, while the captured proton and neutron each enter the $d_{5/2}$ shell. In such cases previous analysis has shown that the state of highest allowable total angular momentum (i. e., $J = 5$) will be preferentially populated.¹

The investigation of these highly populated levels has been continued with the 45-MeV and 50-MeV helium ion beam of the 88-inch cyclotron.

The $(d_{5/2})^2$ states have been observed in the $Mg^{24}(\alpha, d)Al^{26}$ and $Ne^{20}(\alpha, d)Na^{22}$ reactions. The Q values of these high spin states follow the trend established by the initial investigation. (See Fig. C. 5-1.)

The formation of the corresponding higher spin states in the $f_{7/2}$ region was also observed. Strongly populated peaks of $(f_{7/2})^2$ character

1. B. G. Harvey, J. Cerny, R. H. Pehl, and E. Rivet, Nucl. Phys. 39, 160 (1962).

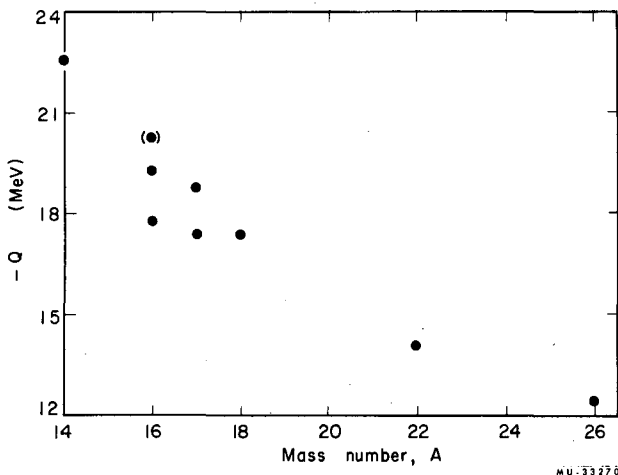


Fig. C. 5-1. Dependence of Q on Mass Number A , for (α, d) reaction to $(d_{5/2})^2$ levels.

were found in the $Ca^{40}(\alpha, d)Sc^{42}$ reaction at 0.61 MeV excitation and in the $A^{40}(\alpha, d)K^{42}$ reaction at 1.87 MeV excitation. The presence of presumably $(f_{7/2})^2$ levels was also observed in the $Mg^{24}(\alpha, d)Al^{26}$ and the $Ne^{20}(\alpha, d)Na^{22}$ reaction at 6.91 MeV and 7.6 MeV respectively. The angular distributions of most of these states were obtained. Figure C. 5-2 shows the angular distribution of the $A^{40}(\alpha, d)K^{42}$ reaction. This forward peaking is typical for the angular distributions of the $(d_{5/2})^2$ and the $(f_{7/2})^2$ levels.

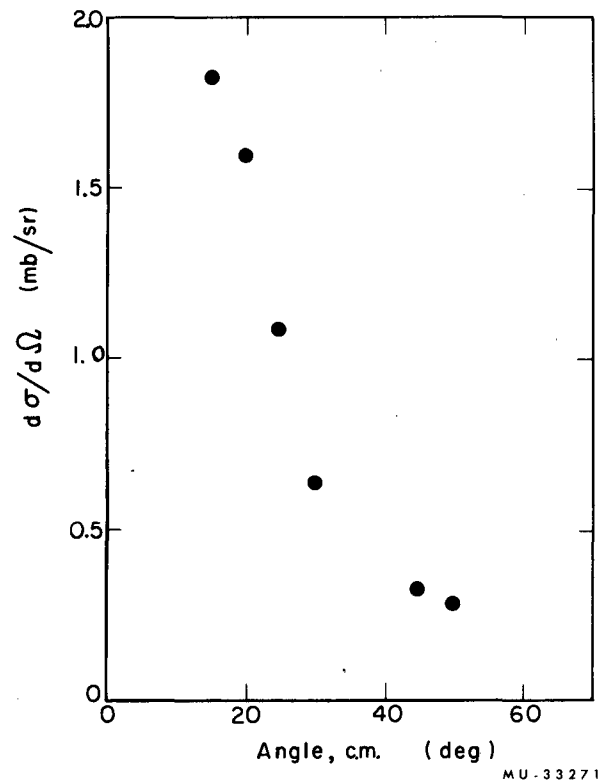


Fig. C. 5-2. Angular distribution of deuterons from $A^{40}(\alpha, d)K^{42}$ 1.87 MeV level.

Figure C. 5-3 presents the energy spectrum of the $Ca^{40}(\alpha, d)Sc^{42}$ reaction at 40 deg. The energy resolution of this spectrum was 270 keV, thus making possible the identification of levels other than the highly populated ones. The energy analysis of this reaction was particularly interesting, since the Sc^{42} nucleus has been stud-

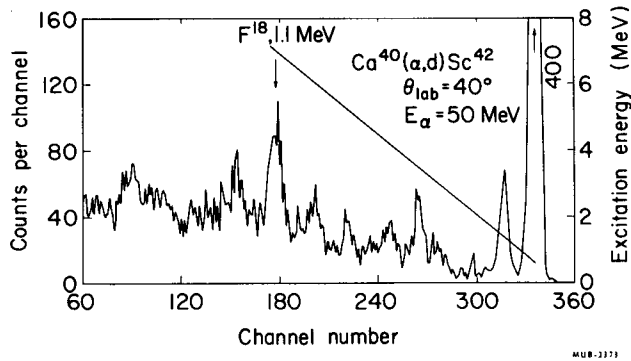


Fig. C. 5-3. Deuteron energy spectrum at 40 deg (lab) for the reaction $\text{Ca}^{40}(\alpha, d)\text{Sc}^{42}$.

ied by the (He^3, p) reaction² and because a high spin isomer was known³ to exist at 0.61 MeV above the ground state. For two particles captured in the $f_{7/2}$ shell on a spin zero target, population of only the odd spin levels of this configuration is allowed in the (α, d) reaction, while transitions to both the odd and the even spin states are permitted in the (He^3, p) investigation. Levels at 0, 0.617, 1.035, 1.509, 2.248, and 2.998 MeV were seen by the (He^3, p) reaction. The (α, d) work formed levels at 0.60, 1.43, 2.25, 3.0, and 3.55 MeV. No definite spin assignments have been made except for the $J=7$ level at 0.61 MeV, and the present investigation will be helpful in that respect,

2. B. F. Bayman (Palmer Physical Laboratory), private communication.

3. P. C. Rogers and G. E. Gordon, Phys. Rev. 129, 2653 (1963).

6. MUON CAPTURE IN O^{16} AND C^{12}

Vincent Gillet* and David Jenkins†

Mu-meson capture on complex nuclei is a sensitive tool for the measurement of the induced pseudoscalar coupling constant (C_D) appearing in the universal Fermi interaction Hamiltonian, provided one has a good knowledge of the nuclear wave functions. The purpose of the present work is to compute μ capture transition rates, $\text{C}^{12} \rightarrow \text{B}^{12}(1+)$; $\text{O}^{16} \rightarrow \text{N}^{16}(0^-, 1^-, 2^-, 3^-)$, using the following three particle-hole models of nuclear excitations for closed shell nuclei: (a) the independent-particle model (IP), (b) the diagonalization of the residual interaction in the subspace of one-particle-hole pair configurations (I), (c) the random-phase approximation (II).¹ We also intend to determine the uncertainties on C_D arising from the approximate nature of nuclear models, from the scant information one has of the nuclear parameters (effective shell-model two-body force, well parameters, etc.). We use the Morita and Fuji formalism for the reduction of the μ meson-neutrino part of the Fermi interaction Hamiltonian,²

assuming conserved vector current theory.

The calculations are done with and without the small relativistic component of the bound μ -meson wave function.

Results show that

(a) The transition rates are little affected by the neglect of the small relativistic components of the μ wave function, the effect being of 5 to 10%. This is negligible compared with the other uncertainties of the problem, and justify earlier works^{3,4} which neglect the small components.

(b) All three models IP, I, and II give similar results, within 10%. This was to be expected, since the levels considered here are almost pure states in j - j coupling. However, the results are very sensitive to arbitrary variations of the amplitudes and phase of the small nuclear admixtures, since these are generally multiplied by large one-body matrix elements, and cross terms occur between the 16 matrix elements entering in the theoretical expressions for transition rates. The variation of the results is also small when the oscillator length parameter is varied by 10% around the values given by the analysis of elastic electron-scattering data.

(c) The C^{12} calculation reproduces the results

* On leave of absence from Centre d'Etudes Nucléaires, BP2, Gif-sur-Yvette (S. & O.), France.

† Member of Segrè Physics Group.

1. Vincent Gillet, *Théorie des Spectres des Noyaux à Couches Complètes* (Thèse), Paris, 1962, Report CEA No. 2177.

2. Masato Morita and Akihiko Fuji, Phys. Rev. 118, 606 (1960).

3. Ian Duck, Nucl. Phys. 35, 27 (1962).

4. T. Ericson and J. Sens (CERN), private communication.

already obtained by Morita.² We obtain the experimental value⁵ of the transition rate for a ratio $C_p/C_A \approx 8$.

(d) The theoretical capture rate in O^{16} into the 0^- state of N^{16} agrees with the Berkeley

5. G. T. Reynolds, D. B. Scarl, R. A. Swanson, T. R. Waters, and R. A. Zdanis, Phys. Rev. 129, 1790 (1963).

measurement⁶ for $C_p/C_A \approx 12$, and with the Columbia measurement⁷ for $C_p/C_A \approx 20$. Only a preliminary analysis has been done for the theoretical results for capture into the 1^- , 2^- , and 3^- states of N^{16} .

6. David Jenkins and Alan Astbury (Lawrence Radiation Laboratory), private communication.

7. R. Cohen, S. Devons, and A. Kanaris, Phys. Rev. Letters 11, 134 (1963).

7. THE SCATTERING OF 64.3-MeV ALPHA PARTICLES FROM NICKEL-58 AND IRON-58*

Pierre Darriulat, G. Igo, Howel G. Pugh, John R. Meriwether, and Shotaro Yamabe

We have studied, using a high-precision scattering chamber and solid-state detectors, the scattering of 64.3-MeV α particles from Ni^{58} and Fe^{58} isobars. We have tried to obtain as accurately as possible the differential cross section for elastic scattering and for inelastic excitation of the first 2^+ state over an angular range between 10° and 80° . The layout of the 88-inch cyclotron and experimental area is shown in Fig. C.7-1. A beam of α particles is

extracted by means of an electrostatic deflector. An image of the virtual source was produced 20 ft downstream from the first quadrupole doublet. At this focus a 0.1-in. wide slit permitted a momentum analysis (100 keV) of the beam. A second quadrupole doublet produced an image of the analyzing slit in the center of the scattering chamber. This image was about 0.06 in. wide and 0.06 in. high, and the beam at this point had a vertical angular divergence of ± 0.0007 radian.

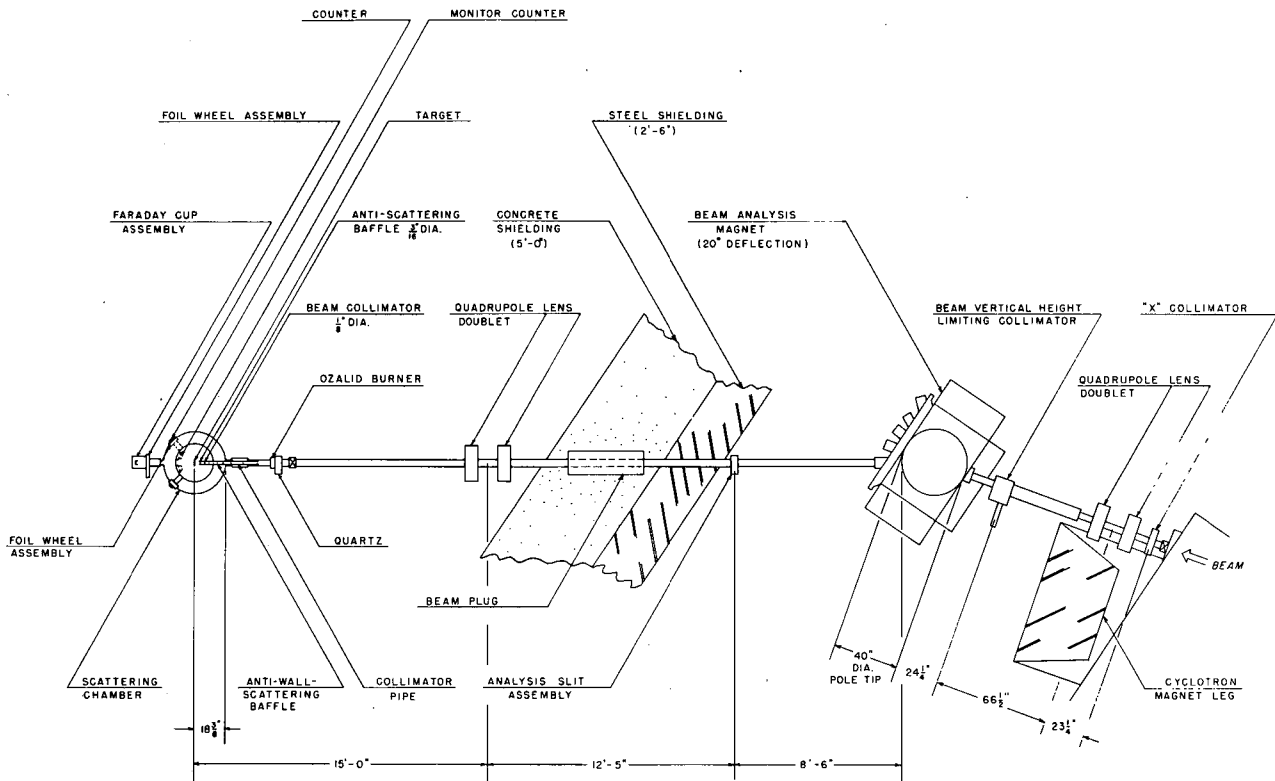
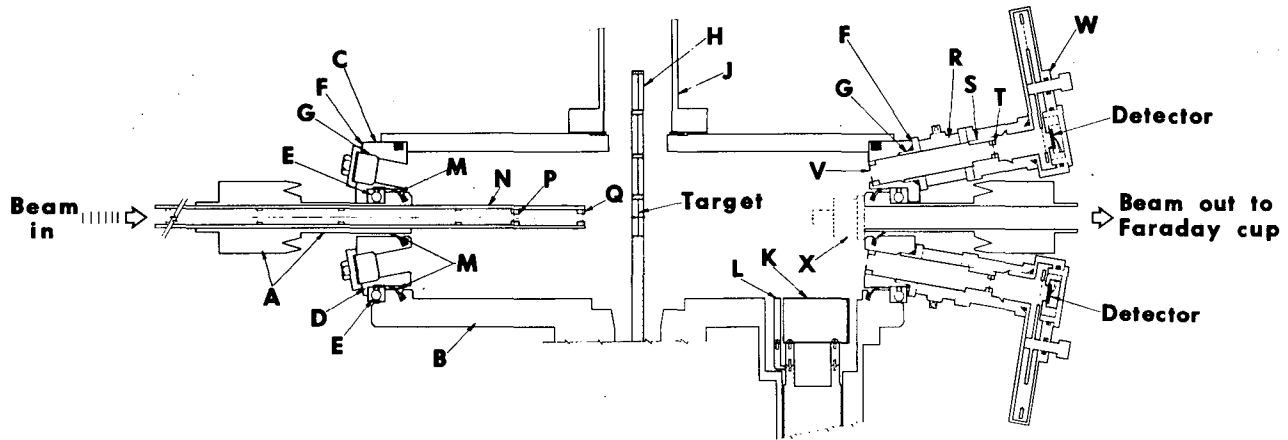


Fig. C.7-1. The experimental layout.



MUB-2153

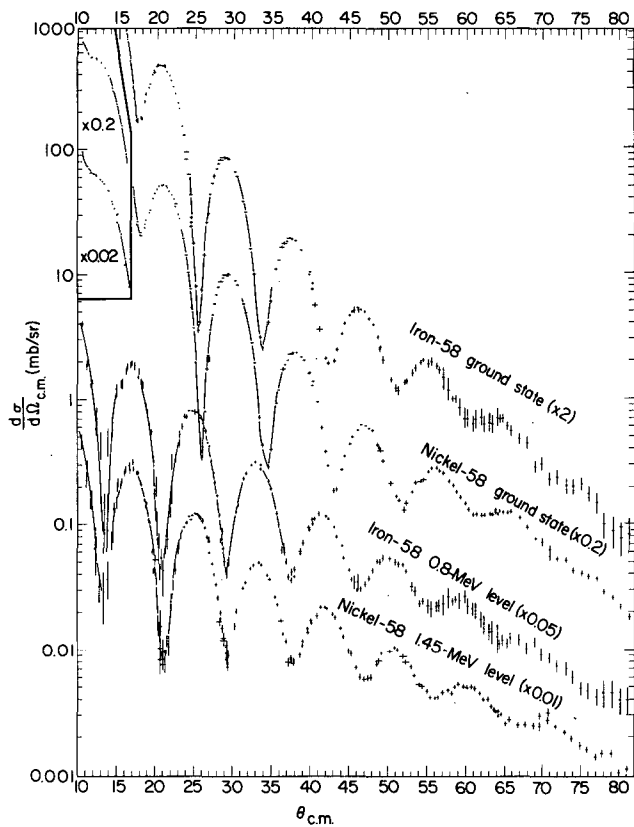
Fig. C. 7-2. Schematic diagram of the scattering chamber and associated equipment.

while its horizontal angular divergence, determined by the X-collimator setting, was ± 0.0014 radian or ± 0.0029 radian in different parts of the experiment. The beam intensity was varied

between 2 m μ A and 500 m μ A by adjustments of the X-collimator, analyzing slit, and the circulating beam intensity.

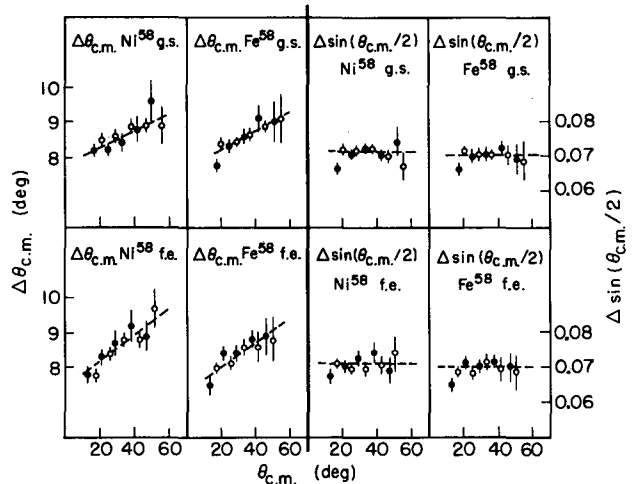
A vertical section of the scattering chamber and associated equipment is shown in Fig. C. 7-2. The angles are read directly on vernier scales which permit them to be set at 0.1° intervals with an accuracy of $\pm 0.005^\circ$. The two monitor counters X were supported on the inside of the center plate by permanent magnets.

The differential cross sections for elastic scattering and excitation for the first 2+ state for Ni⁵⁸ and Fe⁵⁸ are shown in Fig. C. 7-3. The mean energy of the beam in the targets was



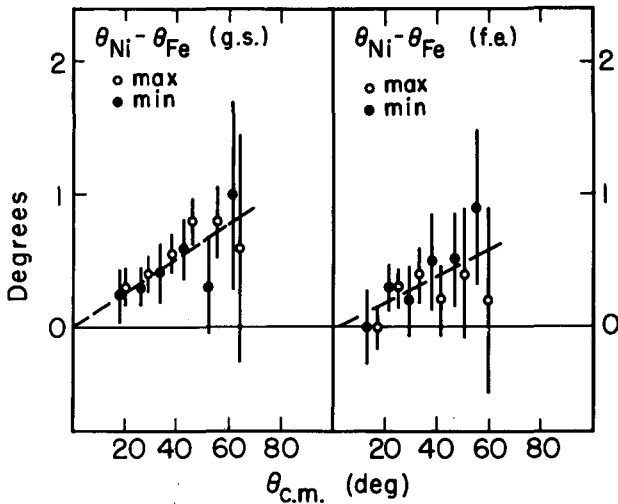
MUB-2154

Fig. C. 7-3. The differential cross sections (c. m.) for elastic scattering and excitation of the first-excited (2+) states in Ni⁵⁸ and Fe⁵⁸.



MU-32079

Fig. C. 7-4. The angular spacings $\Delta\theta_{c.m.}$ and spacings in $\sin\theta_{c.m.}/2$ between consecutive maxima (ϕ) and consecutive minima (\clubsuit) in the angular distributions, plotted against the angle of the maximum or minimum nearer 0 deg.

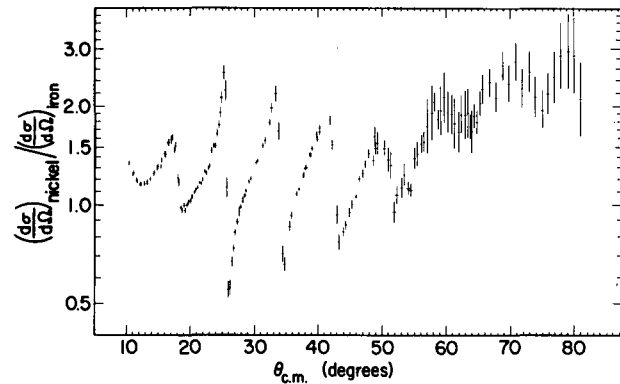


MU-32096

Fig. C. 7-5. The differences $\theta_{\max}(\text{Ni}^{58}) - \theta_{\max}(\text{Fe}^{58})$ (\circ) and $\theta_{\min}(\text{Ni}^{58}) - \theta_{\min}(\text{Fe}^{58})$ (\bullet) between corresponding maxima and minima in the differential cross sections, plotted against the angle of the maximum or minimum.

64.3 ± 0.5 MeV and the energy spread due to the target thickness was 0.5 MeV. The cross sections have not been corrected for the presence of other isotopes. The Ni^{58} target was 99.25% Ni^{58} and 0.75% Ni^{60} ; the Fe^{58} target was 82.04% Fe^{58} , 15.62% Fe^{56} , 1.89% Fe^{57} , and 0.45% Fe^{54} . For comparison with theory, corrections were made to the calculated cross sections for the presence of Fe^{56} . The angular distributions all show marked diffractive behavior, the inelastic cross sections being "out of phase" with the elastic scattering as predicted by Blair for a one-phonon excitation process. The angular spacing between maxima and between minima (see Fig. C. 7-4) increases from about 8° at small angles to about 9° at large angles; the spacing in terms of $\sin \theta_{c.m.}/2$ (proportional to the momentum transfer) is much more constant. The positions of the maxima and minima for Ni^{58} occur at slightly larger angles than for Fe^{58} . The differences are displayed in Fig. C. 7-5. The differences between the two isobars are sensitively displayed in the ratio of the elastic scattering cross section. This ratio is shown in Fig. C. 7-6.

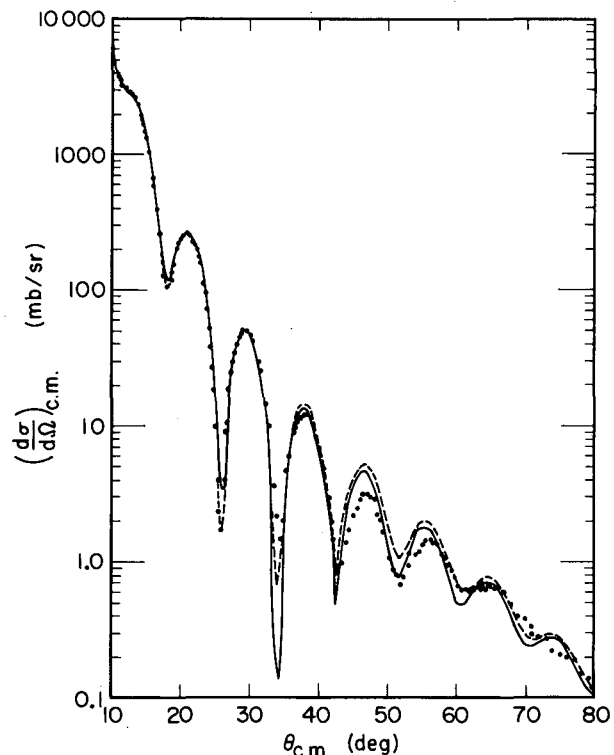
We use a spherical optical potential to obtain fits to the elastic-scattering cross sections for Ni^{58} and Fe^{58} independently. Then, using an average set of nuclear parameters, we attempt to fit the ratio of the Ni^{58} and Fe^{58} angular distributions, first allowing only the charge to be different for the two isobars and then allowing differences in the nuclear parameters one by one. It should be stressed that the anal-



MU-3154

Fig. C. 7-6. The ratio $(d\sigma/d\Omega)_{\text{Ni}^{58}} / (d\sigma/d\Omega)_{\text{Fe}^{58}}$ for the elastic scattering, plotted against the c.m. scattering angle.

ysis is intended to illustrate only the gross features of the results; we would expect to have to use a considerably more refined model to describe the angular distributions in detail. The



MU-32082

Fig. C. 7-7. The "best fit" (—) obtained to the Ni^{58} elastic scattering cross sections (\bullet) with the optical potential parameters, and the fit (--) obtained with $V = -43$ MeV, $a = b = 0.58$ F, $R = 6.1$ F and $W = -19.5$ MeV. The uncertainty in the data is apart from a few instances covered by size of spot.

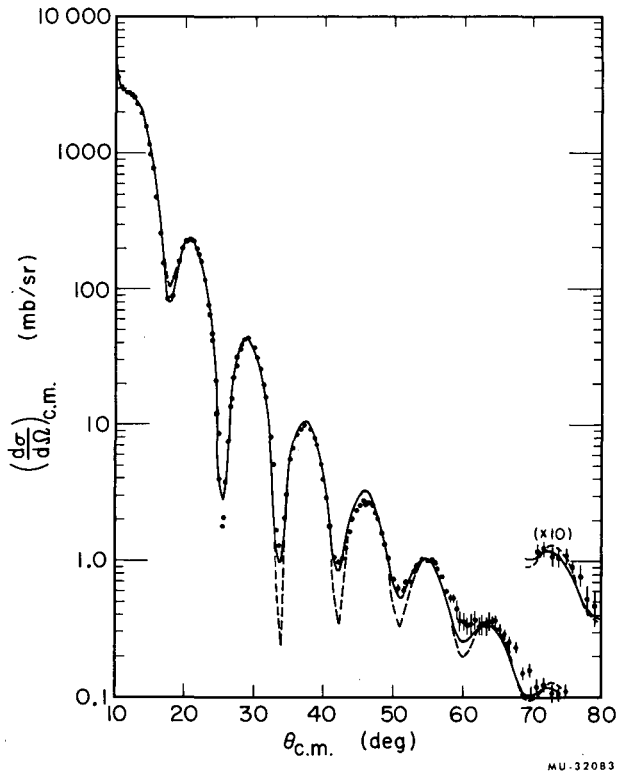


Fig. C.7-8. The "best fit" (—) obtained to the Fe^{58} elastic scattering cross sections (●) with the optical potential parameters, and the fit (---) obtained with $V = -43$ MeV, $a = b = 0.58$ F, $R = 6.1$ F, and $W = -26$ MeV. The uncertainty in the data is apart from a few instances covered by the size of the spot, except at large angles where the uncertainty is shown.

calculated cross sections are compared with experiment in Figs. C.7-7 and C.7-8. It will be noted that the fits are quite good at small angles but become poor at large angles. To study the effect of the different charges of the two isobars, we took various sets of nuclear parameters the same for both nuclei and studied the effect on the ratio of the cross sections of the change in charge. The calculated ratio was almost independent of the nuclear parameters used provided they were the same for both and all within the range between the "best fits" for Ni^{58} and Fe^{58} . In Fig. C.7-9 the solid line shows the ratio calculated with the Ni^{58} "best fit" parameters. It is extremely poor at large angles.

It was found that W , the imaginary potential's depth, was the most sensitive parameter. Therefore, we tried to explain the ratio by varying only W . By using $W = -19.5$ MeV (Ni^{58}) and

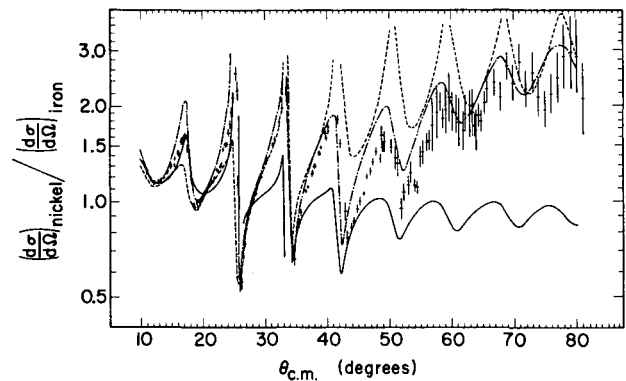


Fig. C.7-9. Optical-model fits to the ratio $(d\sigma/d\Omega)_{\text{Ni}^{58}} / (d\sigma/d\Omega)_{\text{Fe}^{58}}$. (—) $V = 44.99$ MeV; $W = -20.91$ MeV; $a = 0.565$ F; $b = 0.580$ F; and $R = 6.1$ F, for both nuclei. This curve is essentially unchanged for any set of parameters within the limits of the "best fits." (---) $V = -43$ MeV; $a = b = 0.58$ F; $R = 6.1$ F; and $W = -19.5$ MeV (Ni^{58}) and -26 MeV (Fe^{58}). (— · —) The curve given by the "best fits."

$W = -26$ MeV (Fe^{58}) the fit to the ratio was much improved at large angles (dashed lines in Fig. C.7-9). The fits to the individual cross sections were not so good with these sets of parameters as for the "best fits"; they are given by the dashed lines in Figs. C.7-7 and C.7-8. Since the fits to the individual cross sections are not good, no attempt was made to obtain a "best fit" to the ratio by this procedure. In Fig. C.7-9 the ratio given by our "best fits" to the individual cross sections is given for comparison. We may, however, conclude that the differences between the elastic scattering for Ni^{58} and Fe^{58} can be qualitatively explained by (a) a difference in Coulomb scattering and (b) a difference in the absorptive part of the potential.

The smooth-cutoff model of Blair, Sharp, and Willets¹ gives a fair account of the positions and intensities of the first four maxima of the cross sections (See Figs. C.7-10 and C.7-11). The values of the deformation parameter β found with this model are lower than previously reported. Although it is difficult to estimate the reliability of these values because the theory is only approximate, the relationship between the values for Ni^{58} and Fe^{58} may be more trustworthy. The deformation parameter β is smaller for Ni^{58} , which also has a closed shell of protons.

1. J. S. Blair, D. Sharp, and L. Willets, Phys. Rev. 125, 1625 (1962).

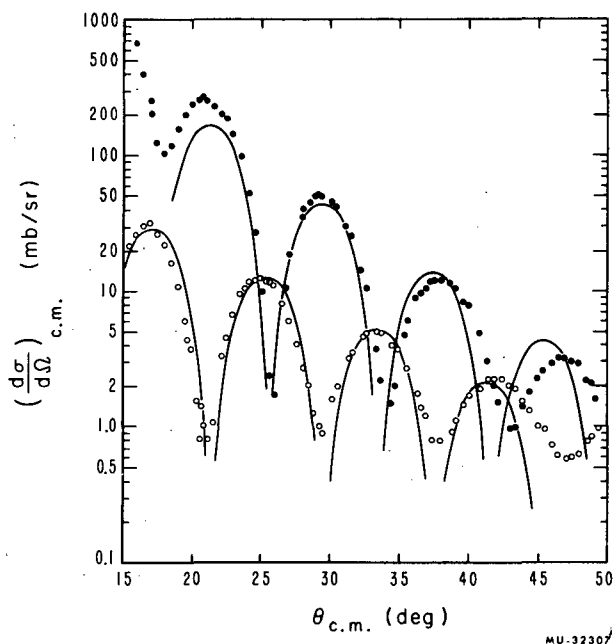


Fig. C.7-10. Fits to the differential cross sections for Ni^{58} obtained by using the smooth-cutoff model of Blair, Sharp, and Wilets. The parameters used are $L = 22.2$, $\Delta/L = 0.054$, and $\beta = 0.15$. The experimental uncertainties are omitted for clarity; in the region of the maxima they are smaller than the points: (●) elastic scattering; (○) inelastic scattering to the $2+$ first-excited state.

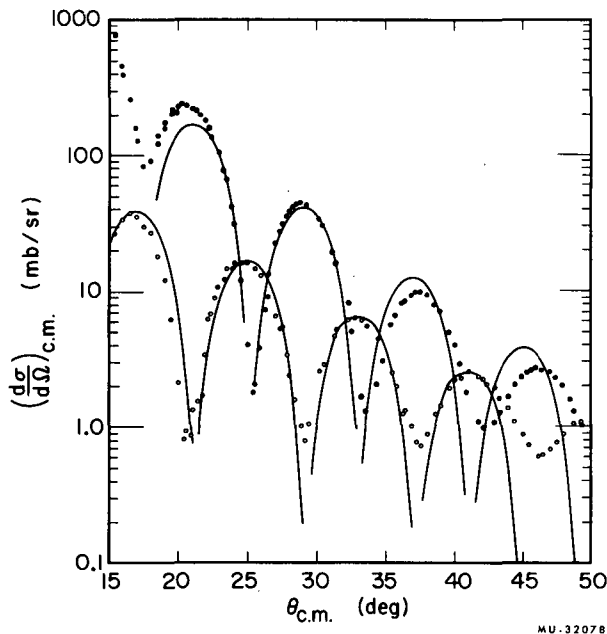


Fig. C.7-11. Fits to the differential cross sections for Fe^{58} obtained by using the smooth cutoff model of Blair, Sharp, and Wilets. The parameters used are $L = 22.4$, $\Delta/L = 0.056$, and $\beta = 0.17$. The experimental uncertainties are omitted for clarity; in the region of the maxima they are smaller than the points: (●) elastic scattering; (○) inelastic scattering to the $2+$ first-excited state.

8. THE SCATTERING OF ALPHA PARTICLES FROM Cu^{63} AND Ni^{62}

Bernard G. Harvey, Daniel J. Horen, and John R. Meriwether

The current study of the elastic and inelastic α -particle groups scattered from Cu^{63} and Ni^{62} is divided into two parts. The first is an investigation into the nature of the Cu^{63} levels. The second deals with the variation of the scattering cross sections and the angular distributions of the Ni^{62} levels as a function of incident α energy. The inelastic α scattering from Cu^{63} has been studied previously,¹ but is being restudied because of the desirability of utilizing the high energy resolution which is available at the 88-inch cyclotron.

The enriched (99.7%) Cu^{63} target was pre-

pared by rolling to a thickness of 1.5 mg/cm^2 . The Ni^{62} target (97.8%) was prepared in a similar manner and was 2.4 mg/cm^2 thick. The cyclotron beam was magnetically analyzed and transported to the target, which was placed in the center of a 36-in. scattering chamber. The energy spectra of the scattered particles were measured with a resolution of 90 to 120 keV with a lithium-drifted silicon counter.

The energy-level diagram for Cu^{63} and Ni^{62} are shown in Fig. C.8-1. The relative intensities are designated by the widths of the lines depicting the levels. The levels of Cu^{63} have been described in terms of a weak coupling between the odd $p_{3/2}$ proton and a Ni^{62} core. Thus one would predict four levels associated

1. Saudinos et al., *Compt. Rend.* **252**, 96 (1961).

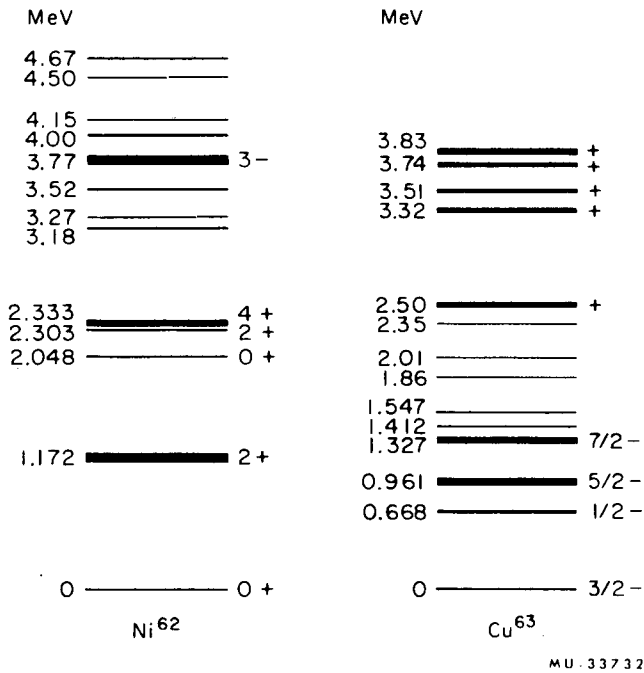


Fig. C. 8-1. Levels of Ni⁶² and Cu⁶³ excited by (α, α').

with the quadrupole vibration in Ni⁶² and four additional levels associated with the octupole vibration.

All these levels should have a rather strong collective nature and thus should exhibit relatively large inelastic scattering cross sections. In addition the relative phase of the angular distribution and the reduced-transition probabilities of these levels should be the same as the parent state in Ni⁶².

The first three levels of Cu⁶³ do in fact behave as though they were a multiplet based on the 1.17-MeV 2+ level of Ni⁶². The angular distribution for the principal Cu⁶³ levels along with that for the elastic group are shown in Fig. C. 8-2. There is, however, no level that has sufficient strength to be considered the 3/2-member of the multiplet.² Other levels in this region (at 1.412 and 1.547 MeV) are weak and could be considered to be the missing level only if a sufficiently large admixture of the 3/2-ground-state wave function were included in the description of the level. This, however, would predict cross sections for the other members of the multiplet 35% larger than are seen.

The simple model for Cu⁶³ again breaks down when the higher-energy group of strongly

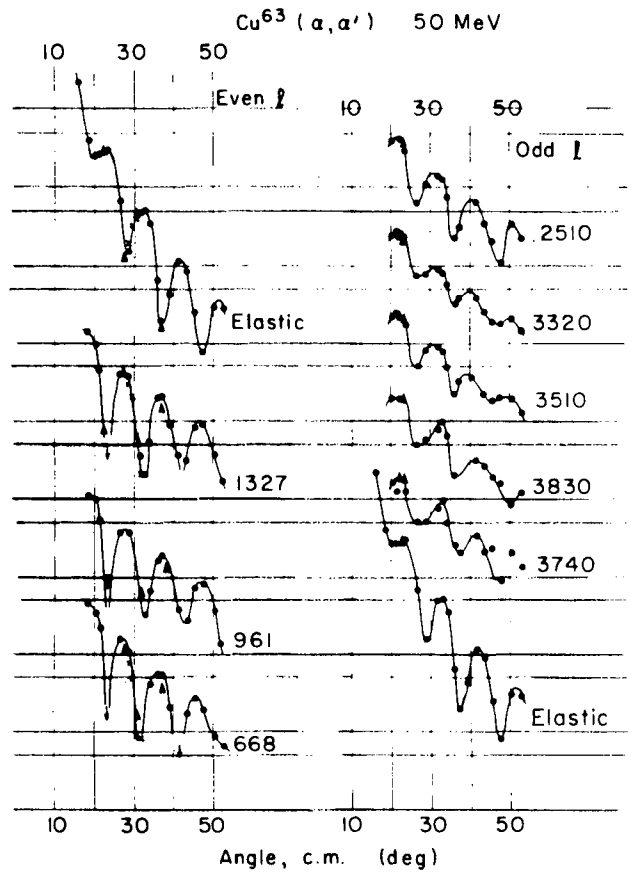


Fig. C. 8-2. Angular distribution for principal Cu⁶³ levels and of elastic group.

excited levels is studied. These levels are in phase with the elastic angular distribution and would be considered to be a multiplet based on the 3.77-MeV 3- level of Ni⁶². One finds, however, five, and possibly six, levels which are similar. There are at present no conclusive arguments to explain the observed data for Cu⁶³.

The second part of the study was the scattering from Ni⁶² at various energies. No "surprises" have been found thus far, and the variations in cross section and angular position of the maxima in the angular distributions follow the predictions of the Blair model. At this time two energies have been used, 50 and 85 MeV. Additional studies are planned, particularly at lower energies, to determine the applicability of the Blair adiabatic approximation.

2. This same result was obtained by H. E. Gove (Chalk River Project), private communication, 1963.

9. NEUTRON AND PHOTON EMISSION FROM Dy AND Tb COMPOUND NUCLEI: RANGE DISTRIBUTIONS

John M. Alexander,^{*} Jacob Gilat,[†] and David H. Sisson

Previous studies of recoil properties of Tb and Dy nuclides produced in heavy-ion-induced reactions^{1, 2, 3} gave strong evidence for the applicability of the compound nucleus and statistical models to these reactions. The average total energies of the emitted neutrons and photons were obtained from an analysis of the angular distributions of these reaction products, by assuming isotropic neutron emission in the center-of-mass system.

In the present study we have attempted to test the assumption of isotropy by measurement of the range straggling of the products due to their distribution of velocities. The recoiling products were stopped in hydrogen gas and electrostatically collected on two parallel plates covered with Al foil and maintained at a potential difference of 500 to 2000 volts. The distribution of radioactive products on the plates was determined by cutting the collector foil into strips which were assayed as previously described. A schematic diagram of the apparatus is shown in Fig. C. 9-1. A similar technique has been used previously by several other workers. The range distributions thus obtained could be well approximated by a Gaussian function, and probability plots were used to obtain the median range R_0 and standard deviation σ of the distributions.

Various tests of the collection method indicate that the distribution of radioactivity on the collecting foil is essentially a projection of the range distribution of the recoiling products in the gas. Theoretical considerations show that in hydrogen this distribution is primarily due to the velocity distribution of the reaction products, and only a small correction for stopping effects has to be applied.

If the angular distribution of the emitted neutrons in the center-of-mass system is represented as

$$W(\theta) = a + b \cos^2 \theta, \quad (1)$$

^{*}Present address: State University of New York, Stony Brook, Long Island, New York.

[†]IAEA fellow from Israel AEC Soreq Research Establishment, Yavneh, Israel.

1. J. M. Alexander and D. H. Sisson, Phys. Rev. 128, 2288 (1962).

2. Gabriel N. Simonoff and John M. Alexander, Phys. Rev. 133, B104 (1964).

3. John M. Alexander and G. N. Simonoff, Phys. Rev. 133, B93 (1964).

then the average total neutron energy T_n is approximately related to the relative variance ($\rho_n^2 = \sigma^2/R_0^2$) of the range distribution and to the mean square recoil angle in laboratory-system coordinates $\langle \theta_L^2 \rangle$ by²

$$\begin{aligned} T_n &= \frac{3E_b A_b (A_b + A_T + A_R)^2}{8(A_b + A_T)^2} \left[\frac{(1+b/3a)}{(1+b/5a)} \right] \langle \theta_L^2 \rangle \\ &= \frac{3E_b A_b (A_b + A_T + A_R)^2}{4N^2 (A_b + A_T)^2} \left[\frac{(1+b/3a)}{(1+3b/5a)} \right] \rho_n^2, \end{aligned} \quad (2)$$

where E_b is the bombarding energy A_b , A_T , and A_R are, respectively, the mass numbers of the bombarding, target, and recoil nuclides, and N is an energy-dependent empirical parameter denoting the dependence of range R on particle velocity V_L , approximated as $R \propto V_L^N$, and the anisotropy is

$$\begin{aligned} \frac{d\sigma(0^\circ) - d\sigma(90^\circ)}{d\sigma(90^\circ)} &= \frac{b}{a} = \frac{5(a-1)}{3-a}; \\ a &= \frac{2\rho_n^2}{N^2 \langle \theta_L^2 \rangle}. \end{aligned} \quad (3)$$

The anisotropies deduced from Eq. (3) are very sensitive to errors in the experimental values of a , which are $\approx 15\%$. Therefore, only qualitative estimates of the magnitude of the anisotropy can be obtained by this method. This, however, introduces only a small uncertainty in the values of the average total neutron energy T_n , which are determined by this procedure with a precision of $< \pm 15\%$.

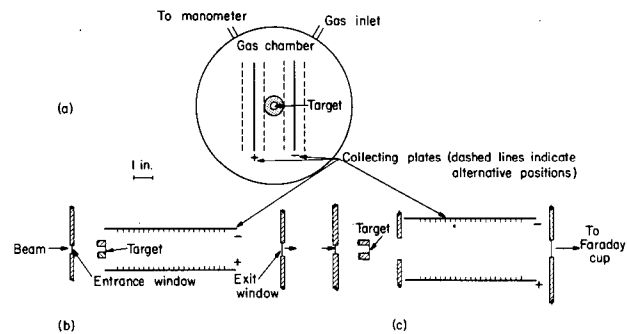


Fig. C. 9-1. Schematic diagram of apparatus. (a) Front view, (b) Top view, normal collector position. (c) Top view, recessed collector position.

Table C. 9-I. Anisotropy and total average neutron and photon energies for reactions leading to Tb^{149g}.

E_b (MeV)	ρ_n^2	a	b/a	$E_{c.m.} + Q$ (MeV)	T_n (MeV)	T_γ (MeV)
<u>Pr¹⁴¹(C¹², 4n)Tb^{149g}</u>						
57.1	0.0188	> 1.8	> 3.5	5.6	7.8	-2.2
64.1	0.0225	2.0	4.8	12.1	10.0	2.1
69.1	0.0214	1.7	2.7	16.7	11.3	5.4
<u>Nd¹⁴⁶(B¹¹, 8n)Tb^{149g}</u>						
89.9	0.0323	1.9	4.4	17.5	19.0	-1.5
97.5	0.0350	1.7	2.6	24.6	24.4	0.4
106.5	0.0431	1.7	2.6	32.9	36.2	-1.3

For the reactions Nd¹⁴⁴(C¹², 5n)Dy¹⁵¹, Nd¹⁴⁴(C¹², 6n)Dy¹⁵⁰, Nd¹⁴⁴(C¹², 7n)Dy¹⁴⁹, Ce¹⁴⁰(O¹⁶, 5n)Dy¹⁵¹, Ce¹⁴⁰(O¹⁶, 6n)Dy¹⁵⁰, and Ce¹⁴⁰(O¹⁶, 7n)Dy¹⁴⁹ only very slight anisotropy bordering on experimental errors is indicated. The values of a range from 0.90 to 1.35, corresponding to anisotropy parameters b/a of -0.24 to 1.0; previously reported values of average total neutron and photon energies are confirmed.

The surprising result of this study is the large anisotropy observed for reactions leading to the low-spin isomer Tb^{149g}, as shown in Table C. 9-I. Reactions leading to the low-spin state of an isomeric pair are usually assumed to proceed mainly from low-spin compound states ($I < 10 \hbar$ for Tb^{149g}).⁴ For such states weak coupling is expected between the angular mo-

mentum of the compound nucleus and the outgoing neutrons, and this should result in an almost isotropic neutron distribution,⁵ in sharp contrast with the experimental data. In the nearly isotropic reactions leading to Dy¹⁴⁹,¹⁵⁰,¹⁵¹ it has been shown that a large fraction of the excitation energy is removed by photons.² In the Tb^{149g} reactions, on the contrary, the total photon energy is very small, particularly in the Nd¹⁴⁴(B¹¹, 8n) case. Apparently the low spin isomer of Tb¹⁴⁹ is produced selectively by those rare evaporation chains in which most of the neutrons are emitted with their angular momenta essentially antiparallel to the compound nucleus spin, and in which the evaporation of the last neutron leads to very low residual excitation energy.

4. J. M. Alexander and G. N. Simonoff, Phys. Rev. 130, 2385 (1963).

5. T. Ericson, in *Advances in Physics*, edited by N. F. Mott (Taylor and Francis, Ltd. London, 1960), Vol. 9, p. 425.

10. STOPPING OF Dy AND Tb IONS IN GASES AND ALUMINUM

Jacob Gilat* and John M. Alexander†

The electrostatic collection method described in Paper C. 9 of this report was used to study the range and range straggling of Dy and Tb ions of 4 to 21 MeV (≈ 25 to 140 keV/amu) in H₂, D₂, He, N₂, Ne, Ar, Kr, and Xe. Recoils from heavy-ion-induced reactions of the T(HI, xn)Dy¹⁴⁹,¹⁵⁰,¹⁵¹ (or Tb^{149g}) were used

for the investigation, and their energies were calculated with the formula

$$E_R = E_b A_b A_R / (A_b + A_T)^2, \quad (1)$$

i. e., assuming total momentum transfer in the nuclear reaction.¹ (E is energy and A mass number, with the subscripts b , T , and R denoting the bombarding heavy ion, target nucleus, and recoiling reaction product, respectively.)

*IAEA fellow from Israel AEC Soreq Research Establishment, Yavneh, Israel.

†Present address: State University of New York, Stony Brook, Long Island, New York.

1. J. M. Alexander and D. H. Sisson, Phys. Rev. 128, 2288 (1962).

The measurements provide a rather wide region for comparison with the comprehensive theory recently published by Lindhard et al.² This theory is based on a statistical (Thomas-Fermi) approach to the interacting atoms. The energy E_R and the range R of a particle of mass M_R and nuclear charge Z_R stopped in a medium of atomic mass M_S and atomic number Z_S are represented respectively by the dimensionless variables

$$\epsilon = aM_S E_R / Z_R Z_S e^2 (M_R + M_S) \quad (2)$$

and

$$\rho_L = RN M_S 4\pi a^2 M_R (M_R + M_S)^{-2}, \quad (3)$$

where

$$a = 0.8853 a_0 (Z_R^{2/3} + Z_S^{2/3})^{-1/2} \quad (4)$$

is a Thomas-Fermi screening length, a_0 is the Bohr radius of the hydrogen atom, e is the charge of the electron, and N is the atomic density of the medium.

In these coordinates the range-energy relationship for any combination of projectile and stopping materials is given by a set of curves characterized by a single parameter k , related to the energy loss by ionization or electronic stopping. The theory assumes that this process can be approximated as

$$\left(\frac{d\epsilon}{d\rho_L} \right)_{elec} = k\epsilon^{1/2}, \quad (5)$$

i. e., energy loss to electrons is proportional to the velocity of the particle. The proportionality constant k depends, in a complex manner, on the atomic masses and numbers of the two interacting species and is usually between 0.1 and 0.2. The theory is expected to be valid for ion velocities $V \leq V_0 Z_R^{2/3}$, where $V_0 (=2.2 \times 10^8 \text{ cm/sec})$ is the Bohr velocity of the electron in hydrogen.

Figure C. 10-1 shows the range-energy data obtained for hydrogen, along with similar data for Al.¹ The agreement is quite good, but the rate of increase of experimental ranges with energy is somewhat less than the theory predicts. A similar trend is observed for other gases, as shown in Fig. C. 10-2. In addition, except for the case of deuterium, the absolute magnitude of the parameter k indicated by the experimental results is considerably smaller than the theoretically calculated value.

The measured values of the range straggling

2. J. Lindhard, M. Scharff, and H. E. Schiott, Kgl. Danske Videnskab. Selskab Mat.-Fys. Medd. 33, No. 14 (1963).

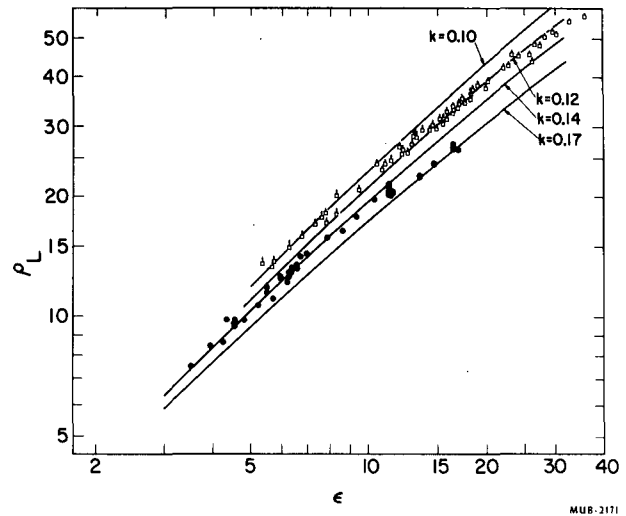


Fig. C. 10-1. Range-energy curves for Tb and Dy in H_2 and Al, using the dimensionless variables ρ_L and ϵ . The tops of the arrows indicate the result of correction of projective range to "true range." Solid lines are theoretical, with the indicated values of the parameter k .

- Tb149, Dy149, 150, 151 stopped in hydrogen, $k_{th} = 0.15$;
- Tb149, Dy149 stopped in Al, $k_{th} = 0.11$.

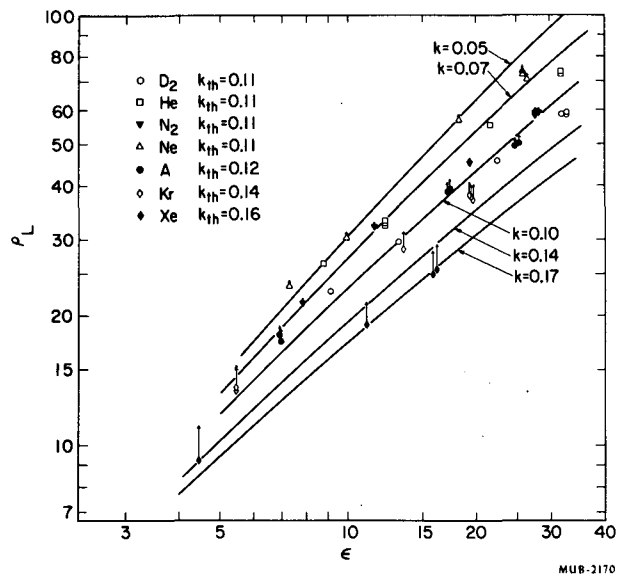


Fig. C. 10-2. Range-energy curves for Dy in various gases, using the dimensionless variables ρ_L and ϵ .

(expressed as the variance of the range distribution) corrected for the initial velocity

distribution of the recoils (see paper C. 9 of this report) are compared in Fig. C. 10-3 with the Lindhard theory. Since in H_2 and D_2 the straggling is dominated by the initial velocity distribution, only values for He and heavier materials are given. The deviations of the experimental results from theory are very similar to those noted above for the average ranges.

It appears that the approximation $(d\epsilon/d\rho_L)_{elec} = k\epsilon^{1/2}$ is not quite adequate, and

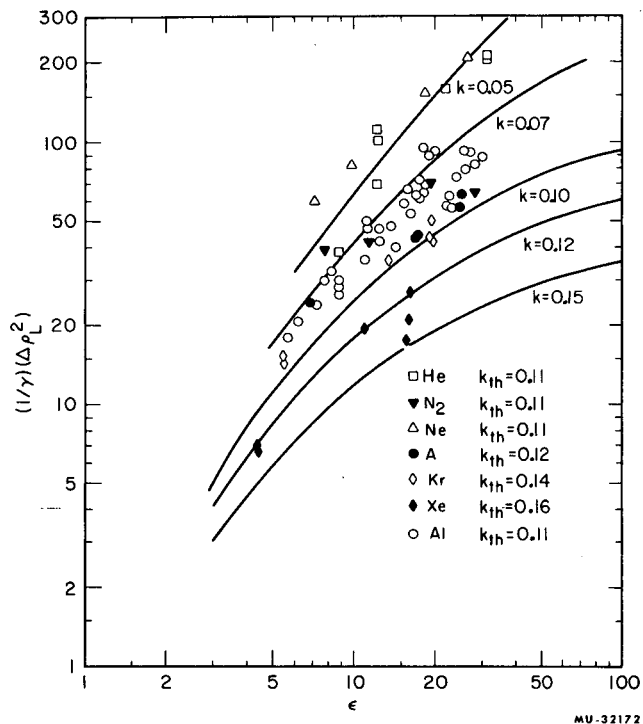


Fig. C. 10-3. Range straggling $\langle \Delta \rho_L^2 \rangle / \gamma$ (where $\gamma = 4A_S A_R (A_S + A_R)^{-2}$; $\langle \Delta \rho_L^2 \rangle = \rho^2 \langle \rho_L^2 \rangle$) as a function of reduced energy ϵ .

a more detailed theoretical treatment of the electronic stopping process is desirable. In our energy region, the Lindhard theory can predict ranges to within $\approx 30\%$, and range straggling parameters (relative standard deviations) to within $\approx 60\%$. If we no longer regard k as a theoretical constant, but rather as an empirical parameter, slightly dependent on energy much better agreements can be obtained. Table C. 10-I lists the empirical values of k derived from the two independent sets of data along with theoretical values (in the empirical results the two values quoted are for ≈ 6 MeV and ≈ 21 MeV, respectively). The agreement between the two empirical sets for gases is gratifying, except for the heaviest gases Kr and Xe at ≈ 6 MeV. In this case, uncertainties due to the difference between the projected and true range could give rise to the discrepancy. In Al, the empirical k values are not in agreement. This discrepancy may be due to foil inhomogeneities, or to a genuine difference between the stopping processes in gases and solids.

Table C. 10-I. Values of the parameter k .

Stopping medium	Theoretical	Empirical	
		From ranges ^a	From straggling
H_2	0.15	0.14 - 0.17	
D_2	0.11	0.09 - 0.12	
He	0.11	0.05 - 0.09	0.055
N_2	0.11	0.07 - 0.09	0.065 - 0.085
Ne	0.11	0.04 - 0.06	0.04 - 0.05
Al	0.11	0.08 - 0.12	0.07 - 0.08
A	0.12	0.07 - 0.10	0.075 - 0.95
Kr	0.14	0.06 - 0.11	0.09 - 0.10
Xe	0.16	0.09 - 0.14	0.12 - 0.14

a. Based on range data corrected for the difference between true and projected ranges.

11. INELASTIC SCATTERING OF 166-MeV O^{16} IONS BY Ta^{181} (*)

Akira Isoya, † Homer E. Conzett, Evangelas Hadjimichael,
and Edward Shield

The relative yields of inelastic and elastic scattering of 166-MeV O^{16} ions by Ta^{181} have been measured at several forward scattering angles. The inelastic events were identified by coincidence detection of deexcitation γ rays of known energy (136 and 166 keV). The objects of the experiment were twofold: first, to determine the previously unresolved inelastic contribution to our elastic differential cross-section measurements, and second, to compare this determination with that calculated from

*Abstract of paper published in Proceedings of the Third Conference on Reactions Between Complex Nuclei, Asilomar, California, April 15, 1963.

†Present address: Department of Physics, Kyushu University, Fukuoka, Japan.

Coulomb excitation theory¹ at scattering angles where the latter is applicable; that is, at forward angles where the (classical) trajectory of the O^{16} ion does not pass through the nucleus even though the incident ion energy is well above the Coulomb barrier. Inelastic excitation of the 136-keV and 303-keV levels of Ta^{181} predominated, and the ratio of inelastic to elastic scattering yield agrees with that calculated within an experimental uncertainty of \pm (< 20%). The observed ratio begins to fall below the calculated value at the (larger) angles, where the corresponding incident ion trajectory begins to pass through the target nucleus.

1. K. Alder, A. Bohr, T. Huus, B. Mottelson, and A. Winter, *Rev. Mod. Phys.* **28**, 432 (1956).

12. PHASE-SHIFT ANALYSIS OF HEAVY-ION SCATTERING*

Homer E. Conzett, Akira Isoya, † and Evangelos Hadjimichael

A comparison is made between (complex) phase-shift analysis and optical-model analysis of elastic scattering data. In the former treatment,¹⁻³ one works directly with the scattering amplitude by parameterizing the partial-wave phase shifts. The optical model achieves the same result by working through the intermediary of a parameterized complex potential. The equivalence of the two procedures is shown. The heretofore somewhat arbitrary^{2, 3} phase-

*Abstract of paper published in Proceedings of the Third Conference on Reactions Between Complex Nuclei, Asilomar, California, April 15, 1963.

†Present address: Department of Physics, Kyushu University, Fukuoka, Japan.

shift parameterization is altered to a form based on theoretical considerations. Several advantages of phase-shift analyses of heavy-ion scattering data are pointed out. The apparent "discrepancy" between "interaction radii" as measured by heavy-ion scattering and those determined by optical-model analyses is explained.

1. J. S. Blair, *Phys. Rev.* **95**, 1218 (1954); *Phys. Rev.* **108**, 827 (1957).

2. J. A. McIntyre, K. H. Wang, and L. C. Bechar, *Phys. Rev.* **117**, 1337 (1960).

3. J. Alster and H. E. Conzett, in Proceedings of Second Conference on Reactions Between Complex Nuclei, Gatlinburg, Tennessee (John Wiley and Sons, New York, 1960), p. 175.

13. PRODUCTION OF Be^7 IN He^3 - AND He^4 -INDUCED NUCLEAR REACTIONS

Arthur J. Pape and Samuel S. Markowitz

Excitation functions for (He^3, Be^7) and (He^4, Be^7) reactions on carbon and aluminum are presented; the goal being to study "a pick-up" and "a clustering" in nuclei.

The He^3 beams were obtained at the Hilac; the He^4 beams were obtained at the 60-inch and 88-inch cyclotrons. The targets used in the excitation-function determinations were stacks of foils mounted on a water-cooled copper holder assembly. Bombardments were often of several hours' duration. The integrator that recorded the total beam current on the target was calibrated with a standard cell immediately following the experiment.

The aluminum target foils used were commercially available, high-purity foils. After several unsuccessful runs with plastic foils used as a carbon target, pure carbon foils made from filter paper were obtained.¹ Discs of filter paper were carbonized between graphite bricks. These discs, each approximately 2.5 mg C per cm^2 , were then heated to 1000°C by electron bombardment and cooled to room temperature while being outgassed. This treatment rendered the carbon foils oxygen-free, a condition they retained even after storage in the atmosphere, as shown by a He^3 activation analysis experiment.² (This heating and outgassing procedure was included because an oxygen impurity in carbon contributes to the Be^7 yield.)

Radiochemical separation of the product Be^7 from aluminum targets was necessary. After addition of holdback carriers and a known amount of Be^{++} (equivalent to approximately 25 mg BeO per sample), each target foil was dissolved. Standard chemical procedures, including use of EDTA, which complexes most elements very strongly and Be very weakly,³ were used to obtain a final product of spectroscopically and radiochemically pure $\text{Be}(\text{OH})_2$. This $\text{Be}(\text{OH})_2$ was ignited for several hours at 1000°C in a platinum crucible to a slightly hygroscopic form of BeO . The BeO was crushed and slurried with ethanol, then layered uniformly on a weighed filter paper disc which had previously been treated with ethanol. After being dried under a heat lamp, the filter disc

plus BeO was weighed and the chemical yield of beryllium was determined. All weighings in the filter disc before and the filter disc plus BeO

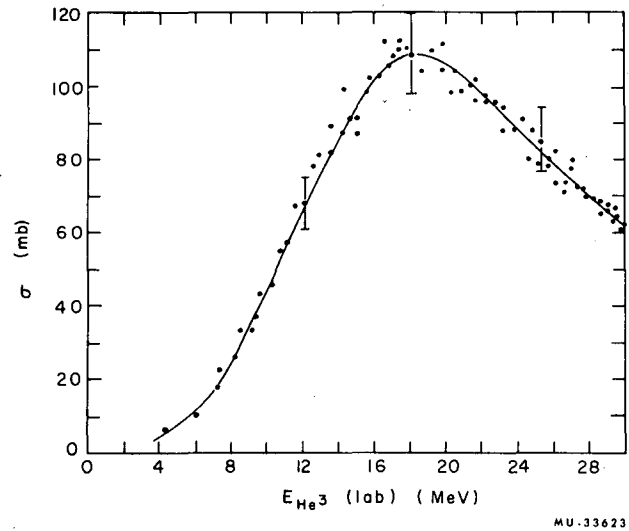


Fig. C.13-1. Excitation function for $\text{He}^3 + \text{C}^{12} \rightarrow \text{Be}^7$ reaction (see reference 8).

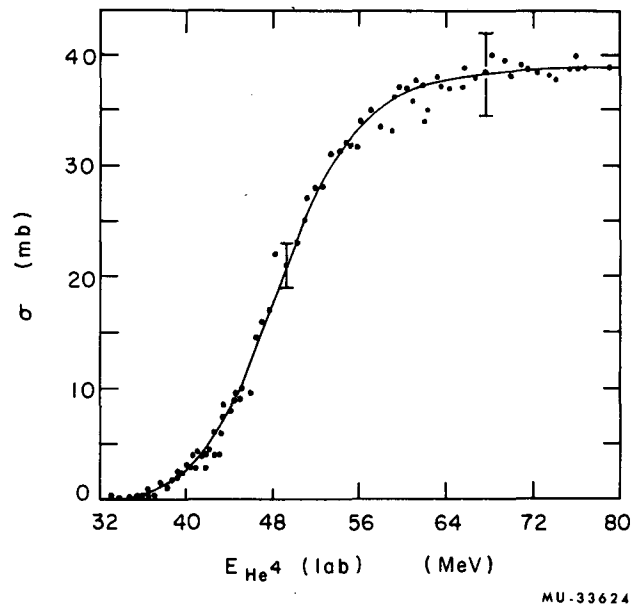


Fig. C.13-2. Excitation function for $\text{He}^4 + \text{C}^{12} \rightarrow \text{Be}^7$ reaction.

1. Carbon foils were fabricated by Mr. Dan O'Connell.

2. S. S. Markowitz and J. D. Mahony, Anal. Chem. 34, 329 (1962).

3. A. Fairhall, The Radiochemistry of Beryllium, NAS-NS-3013, (1960) p. 6.

after were made repeatedly until two successive weighings agreed to 0.1 mg. A typical chemical yield was 80%.

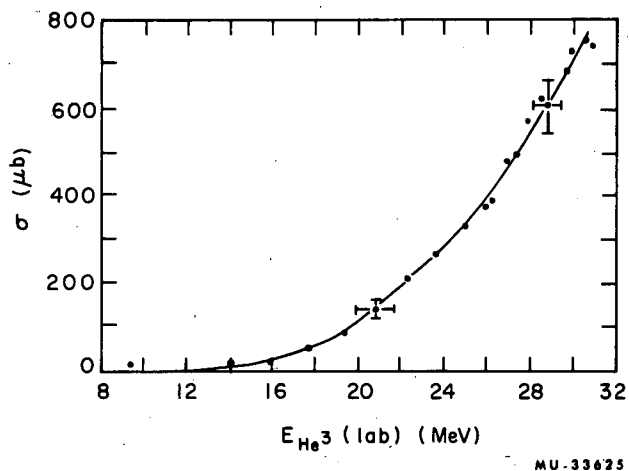


Fig. C. 13-3. Excitation function for $\text{He}^3 + \text{Al}^{27} \rightarrow \text{Be}^7$ reaction (see reference 9).

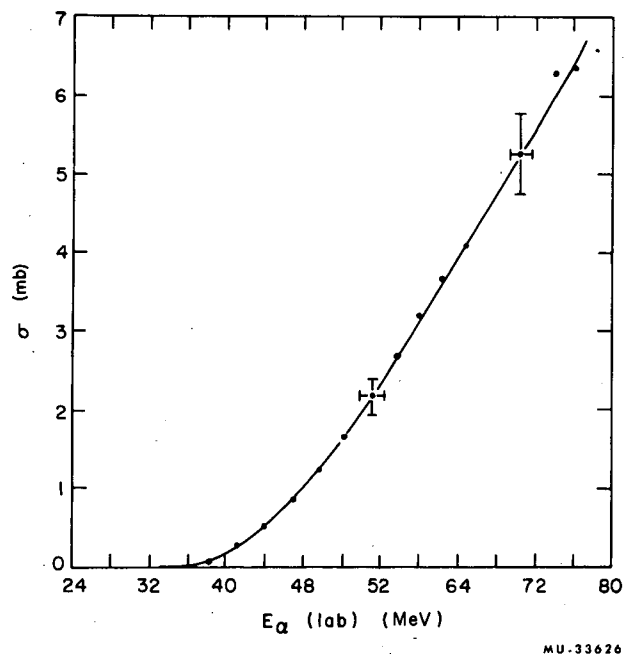


Fig. C. 13-4. Excitation function for $\text{He}^4 + \text{Al}^{27} \rightarrow \text{Be}^7$ reaction (see reference 10).

Radiochemical separation of Be^7 from carbon foils was not necessary because no radio-nuclides produced in the bombardments of carbon interfere with the gamma detection of the Be^7 product.

The Be^7 was counted with a 100-channel NaI scintillation spectrometer calibrated in both energy and efficiency. In all cases, the spectra produced by the samples were identical with background except for the Be^7 events. As a further check that the gamma peak at 0.477 MeV was due to Be^7 , the half-life of the peak was determined to be approximately 54 days, in agreement with the known half-life of Be^7 .

The half-life of Be^7 was taken to be 53.6 days,⁴ and the branching ratio to the 0.477-MeV level of Li^7 was taken to be 0.1032.⁵ Range-energy curves for He^3 in various materials were taken from Bromley and Almqvist⁶ and Rich and Madey.⁷ Range-energy curves for He^4 in various materials were calculated by means of the formula $R_{\text{He}^4} = R_{\text{He}^3}(4/3)$ for He^3 and He^4 ions of the same velocity. The excitation functions are shown in Figs. C. 13-1 through C. 13-4.

Excitation functions have been explored in a preliminary manner for $\text{He}^3 + \text{O}$, Fe, Ni, Cu, Ag, and Au.

Recoil and angular-distribution studies are in progress to elucidate the mechanisms of the (He^3 , Be^7) and (He^4 , Be^7) reactions.

4. Kraushaar, Wilson, and Bainbridge, Phys. Rev. 90, 610 (1953).

5. Taylor and Merritt, Can. J. Phys. 40, 926 (1962).

6. D. A. Bromley and E. Almqvist, He^3 -Induced Reactions, Atomic Energy of Canada, Chalk River Report, CRP-881 (1959) p. 9.

7. Marvin Rich and Richard Madey, Range-Energy Tables, UCRL-2301, March 1954.

8. The same excitation function for He^3 ion energies from 6 to 24 MeV is given in Cochran and Knight, Phys. Rev. 128, 1281 (1962). Our cross sections at the peak are approximately 3% above those given by Cochran and Knight.

9. Four points on this excitation function were determined roughly by Cochran and Knight, Phys. Rev. 128, 1281 (1962).

10. This reaction has been studied at He^4 -ion energies of 34-41 MeV: N. Porile, Phys. Rev. 127, 224 (1962).

14. NUCLEAR REACTIONS INDUCED BY π MESONS.
THE $C^{12}(\pi^-, \pi^-n)C^{11}$ REACTION*

Paul L. Reeder[†] and Samuel S. Markowitz

The excitation function for the reaction $C^{12}(\pi^-, \pi^-n)C^{11}$ was measured from 53 to 1610 MeV by bombarding targets of plastic scintillator with pions. The intensity of the pion beam was monitored with a two-counter telescope and 40-Mc scaling system. The scintillator target was mounted on a phototube and became the detector for the C^{11} positron activity. Corrections were made for muon contamination in the beam, coincidence losses in the monitor system, C^{11} activity produced by stray background at the accelerator, C^{11} activity produced by secondaries in the target, and the efficiency of the C^{11} detection system.

* Full paper in Phys. Rev. 133, B639 (1964).

[†] Present address: Department of Chemistry, Brookhaven National Laboratory, Long Island, Upton, New York.

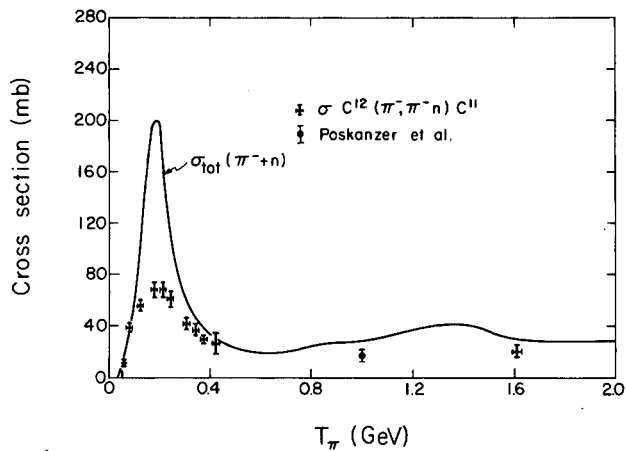
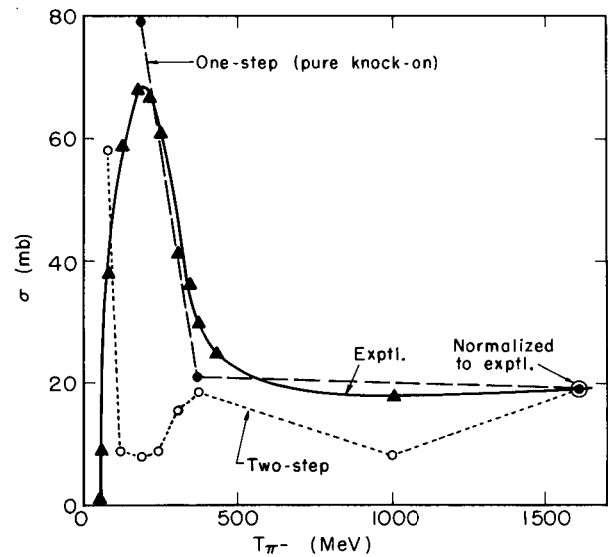


Fig. C. 14-1. Cross section for $C^{12}(\pi^-, \pi^-n)C^{11}$ reaction plotted vs incident-pion energy. The smooth curve is the total cross section for π^-n scattering, which is equal to the total cross section for π^+p scattering by charge symmetry. [Poskanzer et al., Bull. Am. Phys. Soc. 6, 38 (1961)].

The $C^{12}(\pi^-, \pi^-n)C^{11}$ cross sections rise from a threshold at about 50 MeV to a peak of about 70 mb at 190 MeV, after which they decrease to 30 mb at 373 MeV and are relatively constant at higher energies (Fig. C. 14-1). The (π^-, π^-n) peak occurs at the same energy as the resonance in free-particle π^-n scattering at 190 MeV. Calculations based on a one-step "knock-on collision" mechanism and "sharp cutoff" nuclear density reproduce the shape of the experimental excitation function, but the magnitudes of the calculated cross sections are low by a factor of about 5 or 6 (Fig. C. 14-2). This simple model indicates that the $C^{12}(\pi^-, \pi^-n)C^{11}$ reactions occur in the nuclear surface region at all bombarding energies.



MU-31392

Fig. C. 14-2. Comparison of experimental and calculated $C^{12}(\pi^-, \pi^-n)C^{11}$ excitation functions. Solid curve is experimental. Dashed curve connects the cross sections calculated on the one-step model. The dotted curve connects the points calculated on the two-step model. Both calculated curves have been normalized to the experimental curve at 1610 MeV.

D. PHYSICAL CHEMISTRY

1. ACTIVATION ANALYSIS FOR CARBON AND NITROGEN BY He³-INDUCED NUCLEAR REACTIONS*

John D. Mahony, Bahman Parsa,† and Samuel S. Markowitz

Activation analysis using He³ ions has been extended to the determination of carbon. This was accomplished by using He³ ions to induce the reaction C¹²(He³, α)C¹¹. The reactions C¹²(He³, d and np)N¹³ were also studied. The activities of the products, C¹¹ and N¹³, both positron emitters with half-lives of 20.4 min and 10.0 min, respectively, were measured by conventional proportional-counter techniques.

The excitation functions for the production of C¹¹ and N¹³ from C¹² with He³ ions of kinetic energy up to 31 MeV (lab) have been determined.

Introduction

Activation analysis consists of the determination of the amount of a certain element in a sample by bombarding it with a suitable nuclear projectile and measuring the activity of the radionuclide produced. The activity induced is proportional to the amount of element present. This relation is given by the relationship

$$D_0 = nI\sigma \left[1 - e^{-\frac{0.693}{T_{1/2}} t} \right],$$

where D_0 = disintegration rate of the product at end of bombardment, in disintegrations per minute;

n = number of target atoms per cm² of the nuclide being determined;

I = average beam intensity, in incident number of projectiles per minute;

σ = cross section for the reaction, in cm² per atom-incident ion;

t = length of the bombardment, in minutes;

and $T_{1/2}$ = half-life of product, in minutes.

The disintegration rate of the product at the end of bombardment, D_0 , is determined by the relationship

$$D_0 = A_0/ODC,$$

where A_0 is the activity of a source at the end of bombardment, in counts per minute, and ODC is the over-all detection coefficient, which includes

* To be submitted to Anal. Chem.

† Undergraduate Honors Research Student, Department of Chemistry, University of California, Berkeley. Present address: Massachusetts Institute of Technology, Cambridge, Mass.

counter efficiency, geometry, decay scheme, absorption, scattering, and any other counter factors.

In the relative method of analysis, an unknown and a standard sample are bombarded simultaneously in the same beam. The activities of the products are measured under identical conditions. By this method it is not necessary to determine the absolute cross section for the reaction, the beam intensity, or the over-all detection coefficient; the number of target atoms per cm² of unknown, n , can be calculated by

$$n(\text{unknown}) = n(\text{standard}) \times \frac{A_0(\text{unknown})}{A_0(\text{standard})}.$$

Activation analysis using He³ ions is a new method for the determination of oxygen and other elements.¹ This method has considerable advantage over the use of other projectiles. The method is nondestructive and requires only milligrams of sample. Because of the low binding energy of He³, relatively low-kinetic-energy beams are sufficient to induce simple reactions in many elements. An 8-MeV-He³ small cyclotron with a radius of 9 inches would permit analysis of nearly all the elements up to calcium. The ultimate sensitivity for this method can reach fractions of a part per billion; the estimated precision and accuracy are about 5%.

Experimental Procedure

The production of C¹¹ and N¹³ from C¹² was induced by the bombardment of 3/4-mil stacked polystyrene foils (Dow Chemical Trycote) of 13/16-in. diameter (average superficial density was 2 mg per cm²), with 0- to 31-MeV He³ ions at the heavy-ion linear accelerator (Hilac). (Polystyrene contains 92.3% carbon and 7.7% hydrogen.) The length of bombardment varied from 10 to 20 minutes; the average beam current was about 0.010 μA.

After bombardment the irradiated foils were mounted on aluminum cards and covered with 0.9 mg/cm² of "Videne," a clear plastic foil. Their position-emission rate was measured with proportional counters. The activity at the end of the bombardment, A_0 , and its

1. S. S. Markowitz and J. D. Mahony, Anal. Chem. 34, 329 (1962).

standard deviation were calculated with the aid of an IBM-7090 computer program (Lenic).

The excitation functions for production of C^{11} and N^{13} from C^{12} are shown in Fig. D. 1-1. The $C^{12}(He^3, \alpha)C^{11}$ reaction peaks at about 300 mb at 10 MeV and has considerable cross section (≈ 100 mb) down to 4 MeV He^3 energy. The N^{13} production decreases sharply below 7 MeV.

In Fig. D. 1-2 the excitation function for F^{18} production from $O^{16} + He^3$ is shown. ¹ This peaks at 400 mb at 8 MeV.

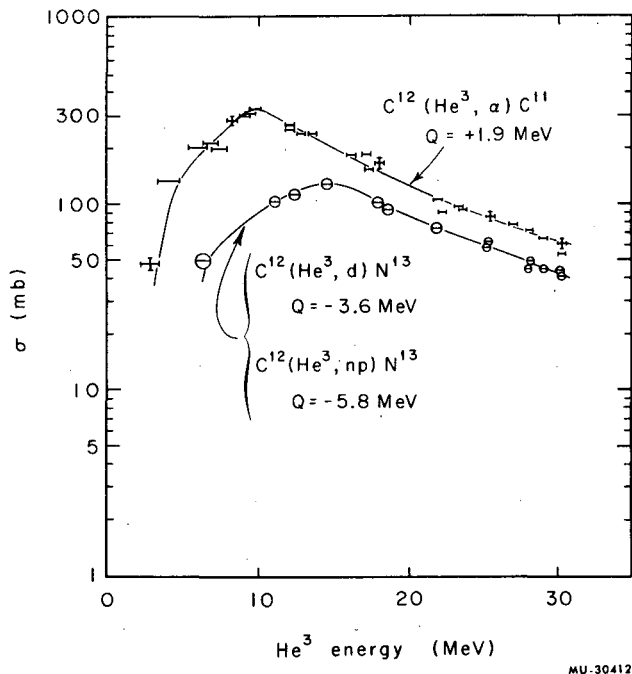
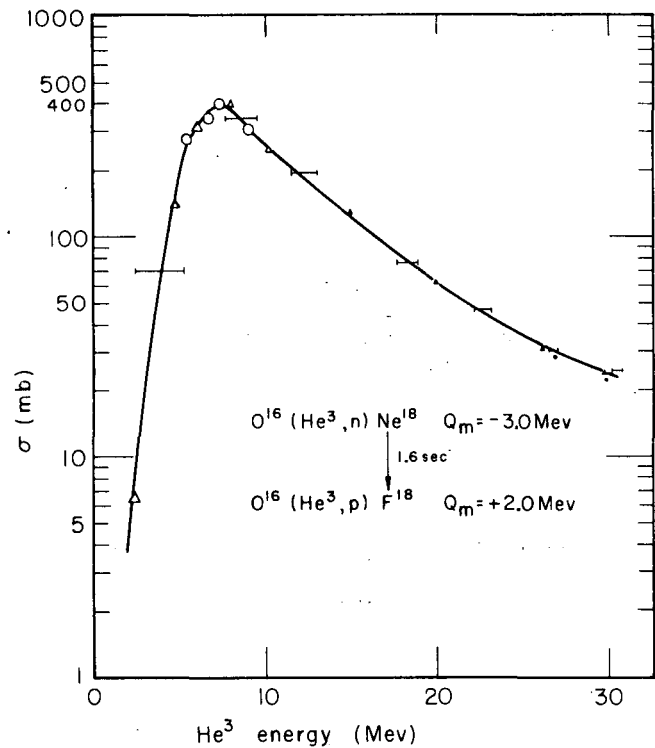


Fig. D.1-1 Excitation functions for production of C^{11} and N^{13} from C^{12} .

An attempt was made to determine the excitation function for the production of N^{13} from N^{14} according to the reaction $N^{14}(He^3, \alpha)N^{13}$. The nitrogen source chosen was melamine-formaldehyde resin, which contains 60.8% nitrogen, 34.8% carbon, and 4.4% hydrogen. Because the resin is not available in thin foils it was coated on 1/4-mil gold foils. Counting techniques similar to those described above were employed. Unfortunately, owing to the presence of oxygen impurities from unwashed formaldehyde and the large amount of carbon, too many interfering reactions were involved and inconsistent results were obtained. This reaction is being measured, however, with other nitrogen-containing target materials.

The excitation functions obtained are in general agreement with those of Cochran and



MU-24829

Fig. D.1-2. Excitation function for production of F^{18} from O^{16} .

Knight.² The "resonances" observed in their C^{12} excitation functions may be due to the fine beam-energy homogeneity produced by their variable-energy cyclotron; this contrasts with our use of the "stacked-foil" technique with resultant loss of energy homogeneity.

Interferences

1. Interfering radioactivities from the "host" material may, in many cases, be eliminated by bombardment with He^3 at an energy below the Coulomb barrier between He^3 and the host material. In Fig. D. 1-3, the Coulomb barrier for He^3 is plotted vs target atomic number up to element 100.

2. By taking advantage of favorable "Q value" for the desired reaction vs unfavored Q value for an interfering reaction, a proper choice of He^3 -beam energy serves to eliminate or minimize interferences. For example, C^{11} is produced from C^{12} by (He^3, α) reaction in good yield at 4 MeV, but it is thermodynamically impossible to produce C^{11} from O^{16} below 5.3 MeV (c.m.)

3. When He^3 -energy selection does not eliminate interferences a change of radioactive detec-

2. D. R. F. Cochran and J. D. Knight, Phys. Rev. 128, 1281 (1962).

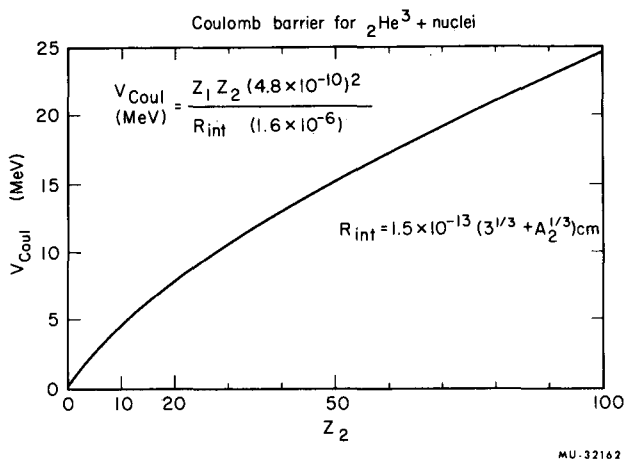


Fig. D.1-3. Coulomb barrier between ${}^3\text{He}$ and the elements up to atomic number 100.

Some Reactions of Low-Energy ${}^3\text{He}$

$\text{C}^{12}(\text{He}^3, \text{He}^4) \text{C}^{11}$	20.4m	+ 1.9 MeV "q"
$\text{N}^{14}(\text{He}^3, \text{He}^4) \text{N}^{13}$	10.0m	+10.0
$\text{O}^{16}(\text{He}^3, \text{p}) \text{F}^{18}$	110.0m	+ 2.0

Elimination of Interfering Reactions by ${}^3\text{He}$ Energy

$\text{O}^{16}(\text{He}^3, 2\text{He}^4) \text{C}^{11}$ (good)	-5.3
$\text{C}^{12}(\text{He}^3, \text{d}) \text{N}^{13}$ (better)	-5.8

Elimination of Interfering Reactions by Change of Product

$\text{F}^{19}(\text{He}^3, \text{He}^4) \text{F}^{18}$ (bad for O^{16})	+10.1
$\text{F}^{19}(\text{He}^3, \text{n}) \text{Na}^{21}$ 23 sec	+ 7.6
$\text{O}^{16}(\text{He}^3, \text{He}^4) \text{O}^{15}$ 2.1m	+ 4.9

MU-32163

Fig. D.1-4. Some reactions of low-energy ${}^3\text{He}$. (See text for discussion.)

ting product may be accomplished. For example, if oxygen is the element to be determined by $\text{O}^{16}(\text{He}^3, \text{p})\text{F}^{18}$ reaction, any F^{19} present will also produce F^{18} by the favorable $\text{F}^{19}(\text{He}^3, \text{a})\text{F}^{18}$ reaction. Then, instead of using the $\text{O}^{16}(\text{He}^3, \text{p})\text{F}^{18}$ reaction for oxygen, the 2.1-min O^{15} could be measured because the F^{19} cannot produce this nuclide at low ${}^3\text{He}$ energies.

In Fig. D. 1-4 some reactions of low-energy ${}^3\text{He}$, the half-lives of the products, and Q values are shown to illustrate the flexibility in elimin-

ating interferences that the use of ${}^3\text{He}$ as the projectile affords, in contrast with neutrons and other charged particles.

Figure D.1-5 shows a "synthetic" decay curve that would be produced by a 1-min bombardment of an organic compound, diamino benzoic acid, $\text{C}_7\text{H}_8\text{O}_2\text{N}_2$, with only 0.010 μA of 3.5-MeV ${}^3\text{He}$. The curve can be analyzed to give 110-min F^{18} , 20.4-min C^{11} , and 10.0-min N^{13} , which are unambiguous products for O^{16} , C^{12} , and N^{14} , respectively, at 3.5-MeV ${}^3\text{He}$ energy. If hydrogen is determined by difference, the ${}^3\text{He}$ method, if done accurately, would enable the simultaneous determination of the empirical formula of an organic compound with only milligram amounts of sample.

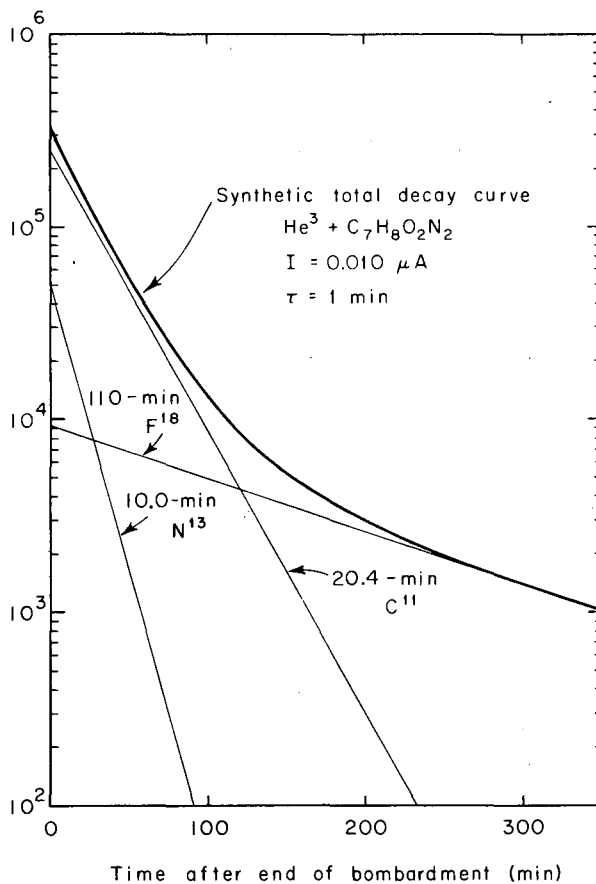


Fig. D.1-5. "Synthetic" decay curve produced by bombardment of diamino benzoic acid with 3.5-MeV ${}^3\text{He}$ ions. The ordinate is disintegrations per minute.

Summary

Several gold foils were analyzed for carbon and oxygen simultaneously and found to contain 0.006% O^{16} and 0.01% C^{12} .

Activation analysis using He^3 ions as the projectile is a feasible method for the determination of carbon and other elements in various materials. It may ultimately be used to analyze simultaneously for nitrogen, carbon, and oxygen in the same sample.

Microactivation analyses for oxygen in the actinide metals using the He^3 method have been carried out by DeMildt³ and Cunningham, in their studies of the chemical and physical prop-

erties of the actinides. DeMildt analyzed thick-target powder samples and found the method "ideal",³ estimating that oxygen could be determined "at a concentration as low as 0.001% (10 ppm) in a few hundred μg of matrix material."

3. Andre C. DeMildt, Microactivation Analysis for Oxygen in the Actinide Metals (UCRL-10324-Rev., Jan. 1963) submitted to Anal. Chem.

2. CRYSTAL STRUCTURE AND MELTING POINT OF CURIUM METAL

B. B. Cunningham and J. C. Wallmann

Abstract

Curium metal has been found to crystallize in a double hexagonal close-packed structure, similar to that of alpha lanthanum. The lattice parameters are:

$$\begin{aligned} a &= 3.496 \pm 0.003 \text{ \AA} \\ c &= 11.331 \pm 0.005 \text{ \AA} \end{aligned}$$

The melting point of the metal was observed to be $1340 \pm 40^\circ \text{C}$.

Crystal structures of the actinide metals have been reported only through americium.¹ The present paper extends the data on the metals to curium, the midpoint of the actinide series. The structure and lattice parameters of curium are of interest in connection with proposals made regarding the metallic bonding in the lighter transuranium metals.²

Experimental Procedure

Materials

Approximately 10 mg of curium, as Cm^{3+} , was separated from other actinide and rare earth elements by ion exchange.³

Curium trifluoride was precipitated from the effluent hydrochloric acid solution by the addition

of excess aqueous hydrofluoric acid to make the final solution approximately 2 M in HF. The precipitation was carried out in a polystyrene centrifuge cone. After centrifuging, the precipitate was washed twice with about 40 times its volume of redistilled water and twice with similar amounts of absolute ethyl alcohol. It was then allowed to air-dry by leaving the cone open to the atmosphere. Upon drying, the trifluoride compacted into a few small pieces of hard translucent material of porcelain-like appearance. This material presumably is hydrated, since air-dried aqueous precipitates of PuF_3 have been shown to contain chemically bound water.⁴

This material was transferred to a platinum container and placed in a desiccator over phosphorus pentoxide. Consecutive reductions of this material were made after periods of storage ranging from 3 days to several months.

Metal preparation

Pieces of curium trifluoride, 200 to 500 μg , were reduced to metal by reaction with barium metal vapor in a microscale reduction apparatus, consisting essentially of a small double crucible of tantalum, fitted with a plug pierced by a 1/3- to 1/2-mm effusion hole. This general technique for preparing the actinide metals has been described in detail in an earlier publication.¹

Curium metal of good appearance was obtained in high yield by maintaining a reduction temperature of from 1315 to 1375°C for 2 min. Additional heating for 3 min at 1235°C served to remove excess barium as well as the barium fluoride slag.

No detectable loss of curium from the crucible system was observed under these condi-

1. D. B. McWhan, B. B. Cunningham, and J. C. Wallmann, *J. Inorg. Nucl. Chem.* **24**, 1025 (1962).

2. W. H. Zachariasen, *The Metal Plutonium*, Ed. by A. S. Coffinberry and W. N. Miner, Chicago University Press, Chicago, 1961, Chap. 10, p. 99.

3. S. G. Thompson and M. L. Muga, in *Proceedings of Second International Conference on the Peaceful Uses of Atomic Energy, Geneva, 1958* (United Nations, Geneva, 1959), P/825.

4. J. K. Dawson and R. M. Elliot, AERE Report C/R-1207, Aug. 1953.

tions; hence the vapor pressure of curium must be much lower than that of americium, since at these temperatures samples of americium metal of similar size would have vaporized completely.

Elemental curium prepared as described exhibited a bright silvery surface that did not tarnish readily when exposed to the air.

In attempts to determine the melting point (described below), it was found that molten curium dissolves appreciable amounts of tantalum. Thereafter, the reduction technique was altered, by inserting the piece of trifluoride between two parallel tungsten wires held in a tantalum frame, which was then inserted into the crucible.

Melting point determination

A technique for determining the melting points of small samples of the lanthanide and actinide metals has been described by McWhan et al.¹ The only modification required in the case of curium was the substitution of tungsten for tantalum wires. When melting point determinations were attempted using tantalum wire, the melting point of the curium rose gradually with increasing time of contact of the metals at temperatures near the melting point. A similar phenomenon has been reported by Spedding and Daane for the rare earth metals.⁵

On substitution of tungsten for tantalum the observed melting point appeared to be independent of heating rate, and was found to be $1340 \pm 40^\circ \text{C}$.

No tungsten was detected by spectrographic emission analysis of a sample of curium used for melting point determinations. (See "Analyses and Purity of Materials" below.)

Analyses and purity of materials

Samples of curium weighing 58, 125, and 136 μg were analyzed separately by spectrographic emission analysis using copper spark excitation. Limits of detection by this method of analysis for various cationic impurities are given in reference 1. Barium was not detected ($< 1 \mu\text{g}$) in Sample 1, nor by special analysis (limit 0.01 μg of Ba) in Sample 2. Barium was found to be present at a level of 0.01 atom % in sample three, which was not analyzed for other cationic impurities. The only cationic impurities detected in the first two samples were 0.1 and 0.2 atom % of calcium and magnesium respectively in Sample 1.

Analysis of one sample of metal for oxygen,

5. F. H. Spedding and A. H. Daane, in *Progress in Nuclear Energy* (Pergamon Press, New York, 1956) Vol. 1, Series V, Chap. 5.

using ^3He activation,⁶ showed the presence of ≈ 4000 ppm.

Mass analysis showed the isotopic composition of the curium used in this work to be: ^{244}Cm , 96.59%; ^{245}Cm , 1.59%; ^{246}Cm , 1.82%.

x-Ray diffraction

A few micrograms of metal were loaded into thin-walled quartz capillaries and the diffraction pattern was obtained with a Jarrell-Ash Model 80-010 microfocus x-ray unit, using the vertical tube, Y27, and a horizontal line filament cathode, Y37, in conjunction with a Norelco 57-mm-diameter camera. Similar patterns were obtained from samples taken from three reductions, and from two separately purified batches of curium.

With few exceptions (see "Results and Conclusions" below) all lines could be indexed on the basis of a double hexagonal close-packed cell, isostructural with the α forms of La, Pr, and Nd, and with the double hexagonal form of americium. Reflections from the 10.1, 10.3, and 10.5 planes of the double hexagonal cell distinguished this structure from a simple hexagonal system.

Observed intensities were compared with calculated values obtained from the 7090 computer, using the intensity program of Smith.⁷

The diffraction data from one of our samples (297-15A) are given in Table D.2-I.

Results and Conclusions

All lines on film 1675A could be indexed on the basis of a double hexagonal unit cell with $a = 3.496 \pm 0.003$, $c = 11.331 \pm 0.005 \text{ \AA}$. Satisfactory agreement was obtained between observed and calculated line intensities, as shown in the table.

The double hexagonal structure was identified in two additional samples of metal prepared by separate reductions of portions of the trifluoride used to make sample 297-15A, and in a third sample prepared from a new batch of CmF_3 resulting from repurification of the curium. The lattice parameters for all samples were found to be the same as those quoted for sample 297-15A, within the stated error limits.

One sample of metal showed the presence of three extra lines which could be indexed as fcc

6. Andre C. DeMildt, *Microactivation Analysis for Oxygen in the Actinide Metals*, UCRL-10324-Rev., Jan. 1963.

7. Deane K. Smith, *A FORTRAN Program for Calculating x-Ray Powder Diffraction Patterns*, UCRL-7196, April 1963.

with $a = 5.09 \text{ \AA}$, and which may be due to CmO. Two additional lines on this film could not be identified with certainty. Metal prepared from repurified curium showed one extra line which was not identified. All lines from the other sample indexed as dhcp.

Thus, a crystallographic form of metallic curium has been identified and shown to be isostructural with a La and the dhcp form of amer-

icium. There are four atoms per unit cell, with curium's at 2(a) 000, 001/2, and 2(c) at 1/3, 2/3, 1/4; 2/3, 1/3, 3/4. The space group is $P6_3/mmc (D_{6h}^4)$. The calculated density (for ^{244}Cm) is 13.51 g cm^{-3} .

Each curium atom is surrounded by twelve near neighbors— six in the same plane at a distance of 3.496 \AA and three above and three below at 3.478 \AA to give an average radius of 1.74 \AA .

Table D.2-I. Curium metal-dhcp (20° C) Sample No. 297-15A; Film No. 1675A; $a = 3.496 \pm 0.003 \text{ \AA}$; $c = 11.331 \pm 0.005 \text{ \AA}$

hk·l	\sin^2 (obs)	\sin^2 (calc)	$I_{(obs)}$	$I_{(calc)}$
10.0	0.0652	0.0648	t	22
10.1	0.0691	0.0695	m	122
00.4	0.0738	0.0741	s	100
10.2	0.0828	0.0833	s	288
10.3	0.1056	0.1065	w	69
11.0	0.1940	0.1945	m+	75
10.6	0.2309	0.2315	m+	64
11.4	0.2677	0.2685	m	90
20.2	0.2763	0.2778	w+	48
00.8	0.2963	0.2962	w	13
20.6	0.4261	0.4260	w-	25
10.9	0.4386	0.4397	w-	8
21.2	0.4717	0.4723	m-	44
11.8	0.4918	0.4907	m-	37
10.10	0.5260	0.5277	m-	20
30.0	0.5836	0.5835	m-	16
21.6	0.6218	0.6204	m-	36
30.4	0.6573	0.6775	m	32
20.10	0.7214	0.7222	t	19
22.4a ₁	0.8490	0.8506	m+	30
11.12a ₁	0.8589	0.8596	s	30
31.2a ₁		0.8599		
30.8a ₁	0.8792	0.8783	m	33
21.10a ₁	0.9146	0.9152	m-	44
10.14a ₁	0.9708	0.9704	w	40

3. THE CRYSTAL STRUCTURE OF THORIUM TETRAIODIDE*

Allan Zalkin, J. D. Forrester, and David H. Templeton

In 1950 we made and analyzed crystals of thorium tetraiodide, but because of the complexity of the problem we suspended work on it. With the advent of high-speed computers and improved techniques for intensity measurement we reactivated this problem and successfully deter-

mined the crystal structure.

In 1954 Jantsch et al. reported on the basis of a powder diffraction pattern that ThI_4 might be tetragonal.¹ D'Eye et al. concluded that the crystal is orthorhombic and reported cell dimen-

* Brief version of paper to be published in *Inorganic Chemistry*.

1. G. Jantsch, J. Homayr, and F. Zemek, *Monatsh. Chem.* **85**, 526 (1954).

Table D.3-I. Final positional parameters and standard deviations for ThI₄.

Atom	\bar{x}	\bar{y}	\bar{z}	$\sigma(\bar{x})$	$\sigma(\bar{y})$	$\sigma(\bar{z})$
Th	0.1835	0.0149	0.1769	0.0001	0.0002	0.0002
I(1)	0.0587	0.9098	0.8094	0.0002	0.0003	0.0003
I(2)	0.1801	0.2535	0.4984	0.0002	0.0003	0.0003
I(3)	0.0972	0.6917	0.3251	0.0002	0.0003	0.0003
I(4)	0.1517	0.3638	0.0014	0.0002	0.0003	0.0003

sions.² In this work we show conclusively that ThI₄ is monoclinic in space group P2₁/n.

ThI₄ was prepared by heating thorium metal foil at about 500° in an iodine atmosphere in an evacuated Pyrex T-shaped tube for a week. After reaction was completed the material was distilled to the other side arm and sealed off. As the ThI₄ is very reactive to the atmosphere it was necessary to handle the material in a dry box; our dry box is charged with dry nitrogen.

The ampule of ThI₄ was broken open, and small fragments of the yellow material were loaded into 0.3-mm-diameter vitreous silica capillaries. The capillaries were sealed and baked in a furnace at about 550°. There was enough thermal gradient to allow crystals to grow on the cooler walls of the capillary.

A suitable small crystal plate of dimensions approximately 0.15×0.10×0.03 mm was attached to the wall of the capillary with its b axis in the plate and along the axis of the tube. It was mounted in a goniostat on a General Electric XRD-5 apparatus equipped with a molybdenum x-ray tube, a scintillation counter, and a pulse-height discriminator. Intensities were measured for the 1454 independent reflections permitted by the space group out to a limit of $\sin \theta/\lambda = 0.596$ ($2\theta = 50^\circ$). Of these intensities 106 were recorded as zero.

2. R. W. M. D'Eye, I. F. Ferguson, and E. J. McIver, in *Congres international de chimie pure et applique 16^e Paris, 1957*, Mem. section de chimie minerale, 341 (Pub. 1958).

The crystals are monoclinic with unit cell dimensions

$$\begin{aligned} \underline{a} &= 13.216 \pm 0.007, \quad \underline{b} = 8.068 \pm 0.006 \text{ \AA}, \\ \underline{c} &= 7.766 \pm 0.006 \text{ \AA}, \quad \beta = 98.68 \pm 0.05^\circ, \\ \underline{V} &= 819 \text{ \AA}^3. \end{aligned}$$

With four formula units (ThI₄) per unit cell, the density calculated from the x-ray data is 6.00 g/cc.

The systematic absence of hOl reflections if h + l is odd and of OkO reflections if k is odd is characteristic of space group P2₁/n (C_{2h}⁵). This space group is confirmed by the structure determination.

Determination of the Structure

In order to obtain a trial structure we calculated a three-dimensional Patterson function. By inspection of this function with due regard to packing and interatomic distances we found a complete trial structure that accounted satisfactorily for the largest peaks. The positional parameters obtained from the Patterson function were all within 0.03 of the corresponding final values given in Table D.3-I.

After least-squares refinement with anisotropic thermal factors R was 0.09. The final positional parameters and their standard deviations are listed in Table D.3-I. The anisotropic thermal parameters and the average root mean square displacements of the atoms are reported in Table D.3-II.

Table D.3-II. Anisotropic thermal parameters ($\times 10^4$) and average root-mean-square displacements.

Atom	β_{11}	β_{22}	β_{33}	B_{12}	β_{13}	β_{23}	$\bar{\mu}$ (\AA)
Th	22	42	31	-1	13	0	0.12
I(1)	25	80	45	2	15	-16	0.14
I(2)	30	67	37	-6	26	-3	0.14
I(3)	25	68	82	3	25	15	0.15
I(4)	34	59	51	-2	2	7	0.15

Description of the Structure

The ThI_4 consists of layers with the iodine atoms arranged in sheets parallel to (101) and the thorium atoms located in alternate spaces between iodine sheets (Fig. D.3-1). Each thorium atom has eight iodine neighbors arranged at the corners of an irregular polyhedron which is approximately a square antiprism (Fig. D.3-2). The Th-I distances (Table D.3-III) range from 3.128 to 3.291 Å with a mean value of 3.202 Å.

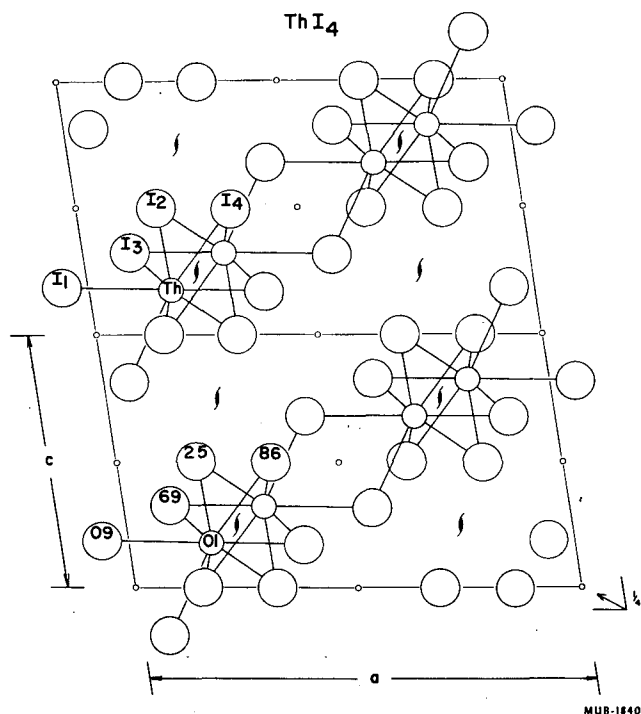


Fig. D.3-1. Projection of the ThI_4 structure into the ac plane. The numbers on atoms in the lower part of the figure are y -coordinates ($\times 100$).

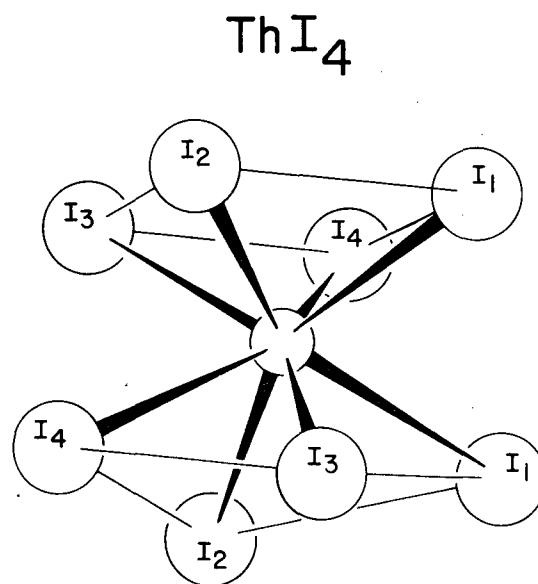


Fig. D.3-2. The approximately square antiprism arrangement of iodine about thorium in ThI_4 .

Table D.3-III. Distances to nearest neighbors of thorium

Atom	Distances ^a (Å)
I(1)	3.188, 3.276
I(2)	3.159, 3.208
I(3)	3.134, 3.232
I(4)	3.128, 3.291

^a Each standard deviation is 0.004 Å.

4. CRYSTAL STRUCTURE OF TERBIUM TRICHLORIDE*

J. D. Forrester, Allan Zalkin, David H. Templeton, and J. C. Wallmann

Bommer and Hohmann observed from x-ray powder photographs that the trichlorides of the rare-earth elements have three different crystal structures.¹ The trichlorides of the elements

lighter than terbium, as well as many bromides and hydroxides, have the UCl_3 -type structure.² The trichlorides of the elements heavier than terbium have the YCl_3 -type structure.³ Terbium

* Brief version of paper to be published in Inorganic Chemistry.

1. H. Bommer and E. Hohmann, *Z. anorg. allgem. Chem.* **248**, 373 (1941).

2. W. H. Zachariasen, *Acta Cryst.* **1**, 265 (1948).

3. D. H. Templeton and G. F. Carter, *J. Phys. Chem.* **58**, 940 (1954).

trichloride and a second form of DyCl_3 have a third structure which was determined in this investigation. After the structure was known it became obvious that it was the same as the structure determined by Zachariasen for PuBr_3 .⁴ Many other bromides and iodides have this structure also:^{2, 5} NdBr_3 , SmBr_3 , EuBr_3 , $\beta\text{-NpBr}_3$, AmBr_3 , LaI_3 , CeI_3 , PrI_3 , NdI_3 , UI_3 , NpI_3 , PuI_3 , and AmI_3 .

It is much more difficult to prepare single crystals of TbCl_3 than of the other lanthanide chlorides, but after some failures we prepared the samples by the following method. Terbium oxide (Tb_4O_7) was dissolved in hydrochloric acid and evaporated to dryness. The oxychloride formed was broken up and treated with HCl at 400° for two hours to produce the trichloride. This trichloride was dumped in vacuum into a sidearm tube, sublimed into the sidearm (of vitreous silica), and sealed off. The trichloride in the silica tube was passed through a crystal-growing furnace at a temperature slightly above the melting point,⁶ $588 \pm 15^\circ$.

To prevent formation of the oxychloride, the silica tube was broken open in a dry box, and samples of TbCl_3 were loaded into Lindemann glass capillaries. A diffraction pattern of a powder sample was in agreement with the powder diagram reported by Bommer and Hohmann,¹ and confirmed the absence of the oxychloride.

Only poor single crystals were obtained. They were long thin plates of a fibrous nature. The x-ray patterns showed the best specimens to have various domains rotated by up to 15 or 20° about the fiber axis (a axis) with respect to each other. This rotation resulted in a corresponding elongation of the diffraction spots, which diminished our sensitivity for observation of weak reflections and made difficult the estimation of intensities. With one specimen we obtained Weissenberg photographs (layers 0 and 1) with rotation about a and with Cu radiation ($\lambda = 1.5418 \text{ \AA}$). This crystal then suffered a mishap. Further photography of a poorer crystal with Mo radiation ($\lambda = 0.7107 \text{ \AA}$) and the same setting gave Weissenberg diagrams (layers 0 through 2) and precession photographs ($h0l$ and $h1l$ reflections).

Intensities were estimated for 69 independent reflections on the zero-layer Weissenberg

4. W. H. Zachariasen, *Natl. Nuclear Energy Ser. Div. IV*, **14B**, 1473 (1949).

5. EuBr_3 , NdI_3 , PrI_3 , and CeI_3 are said to have this structure by F. H. Spedding and A. H. Daane, Ames Laboratory Report IS-350, Sept. 1961 (unpublished).

6. D. M. Yost, H. Russell, and C. S. Garner, *The Rare Earth Elements and their Compounds* (John Wiley & Sons, Inc., New York, 1947).

pattern (Cu radiation). Of these, 13 were recorded as zero. The crystals are orthorhombic. The cell dimensions are $a = 3.86 \pm 0.02$, $b = 11.71 \pm 0.03$, $c = 8.48 \pm 0.03 \text{ \AA}$.

The systematic absences (hkl absent if $h+k$ is odd, $h0l$ absent if l is odd) are characteristic of space groups $\text{Cmc}2_1$, $\text{C}2\text{cm}$, and Cmcm . We find a satisfactory structure in the centric group Cmcm (D_{2h}^{17}).

With $Z = 4$, the calculated density is 4.60 g/cc . Atoms are located in special positions, Tb and $\text{Cl}(1)$ in $4(c)$ and $\text{Cl}(2)$ in $8(f)$,
 $4(c): \pm(0, y, 1/4) + (0, 0, 0; 1/2, 1/2, 0)$,
 $8(f): \pm(0, y, z; 0, y, 1/2 - z) + (0, 0, 0; 1/2, 1/2, 0)$.
 Atomic parameters were refined by least squares with the $0kl$ data. With isotropic temperature factors of the form $\exp(-B \sin^2 \theta / \lambda^2)$ and a scale factor there were eight independent parameters. R was reduced to 0.18 for the 69 observations. The final parameters are listed in Table D.4-I.

Table D.4-I. Atomic parameters and standard deviations.^a

Atom	x	y	z	B (\AA^2)
Tb	0	0.244 ± 0.001	1/4	0.4 ± 0.2
Cl(1)	0	0.583 ± 0.003	1/4	0.4 ± 0.6
Cl(2)	0	0.145 ± 0.002	0.56 ± 0.002	0.0 ± 0.4

^a Standard deviations are estimated by least squares and include no allowance for the systematic errors.

Interatomic distances are listed in Tables D.4-II and D.4-III. Each Tb has eight nearest Cl neighbors at an average distance of 2.81 \AA . Each Cl has either 11 or 12 Cl neighbors closer than 4 \AA . The only unreasonable distance is $\text{Cl}(2) - \text{Cl}(2) = 3.07 \text{ \AA}$, which is a function only of z for $\text{Cl}(2)$. We can make this distance 3.22 \AA with $z = 0.560$ without much effect on other distances or on the agreement with the data, but 3.31 \AA ($z = 0.555$) seems to be in significant conflict with the data. Distances as short as 3.2 \AA are not uncommon for chlorine atoms shared by two cations.

Table D.4-II. Neighbors of Tb atom.

Neighbor	Number	Distance (\AA)
Cl(1)	2	$2.70 \pm .02^a$
Cl(2)	4	$2.79 \pm .02$
Cl(2)	2	$2.95 \pm .02$
Cl(1)	1	$3.97 \pm .03$

^a Standard deviations include no allowance for systematic errors.

Table D.4-III. Cl-Cl Distances.

Atom	Neighbor	Number	Distance (Å)
Cl(1)	Cl(2)	4	3.40 ± 0.02^a
	Cl(2)	2	3.53 ± 0.04
	Cl(2)	4	3.63 ± 0.03
	Cl(1)	2	3.86 ± 0.02
Cl(2)	Cl(2)	1	3.07 ± 0.04
	Cl(2)	2	3.35 ± 0.03
	Cl(1)	2	3.40 ± 0.02
	Cl(1)	1	3.53 ± 0.04
	Cl(2)	1	3.58 ± 0.04
	Cl(1)	2	3.63 ± 0.03
	Cl(2)	2	3.86 ± 0.02

^a Standard deviations include no allowance for systematic errors.

The structure is closely similar to that determined for PuBr_3 by Zachariasen.⁴ The atomic coordinates, after interchange of \underline{a} and \underline{b} and a shift of origin, are compared with the PuBr_3 coordinates in Table D.4-IV. In this setting, the space group symbol is $C_{2/m}$. The agreement of these independent determinations is gratifying.

Table D.4-IV. Atomic coordinates of TbCl_3 and PuBr_3 .^a

Parameter	TbCl_3	PuBr_3^b
\bar{x} (Tb or Pu)	0.256	0.25
\bar{x} (Cl(1) or Br(1))	-0.083	-0.07
\bar{x} (Cl(2) or Br(2))	0.355	0.36
\bar{z} (Cl(2) or Br(2))	-0.069	-0.05

^a Alternative setting, space group $C_{2/m}$.

^b Zachariasen, reference 4.

The structure can be described as consisting of triangular prisms with Tb at the centers and Cl at the corners. These prisms share triangular faces to form columns parallel with \underline{a} . The UCl_3 -type structure can be described in terms of similar triangular columns, but the two structures differ in the way the columns are packed together (Fig. D.4-1). In the UCl_3 -type structure there are three neighboring columns arranged so that each U atom has three Cl neighbors adjacent to the lateral faces of the prism. In TbCl_3 there are four neighboring columns, but only two of them provide a close Cl neighbor to the Tb atom. A ninth neighbor is in the direction of the third lateral face, but it is more than 1 Å further away than the others.

This arrangement of eight nearest neighbors is similar to the environment of Y in YF_3 , though in YF_3 the ninth neighbor is relatively much closer.⁷

The direction of the triangular columns corresponds with the direction of the fibers into which the crystal breaks. From the structure one would predict cleavage on 010, since no strong bonds cross that plane. Apparently the forces holding one column to another in the \underline{c} direction are also weaker than the forces within the column.

From the numerous bromides and iodides which have this structure, it is surprising that its occurrence in the rare-earth chloride series is limited to two examples. If it were stable over as wide a range of radius ratio as it is for the bromides and iodides, two or three other rare-earth chlorides would have this structure. Obviously some more delicate factor than radius ratio is involved in determining the structures of these substances.

7. A. Zalkin and D. H. Templeton, J. Am. Chem. Soc. 75, 2453 (1953).

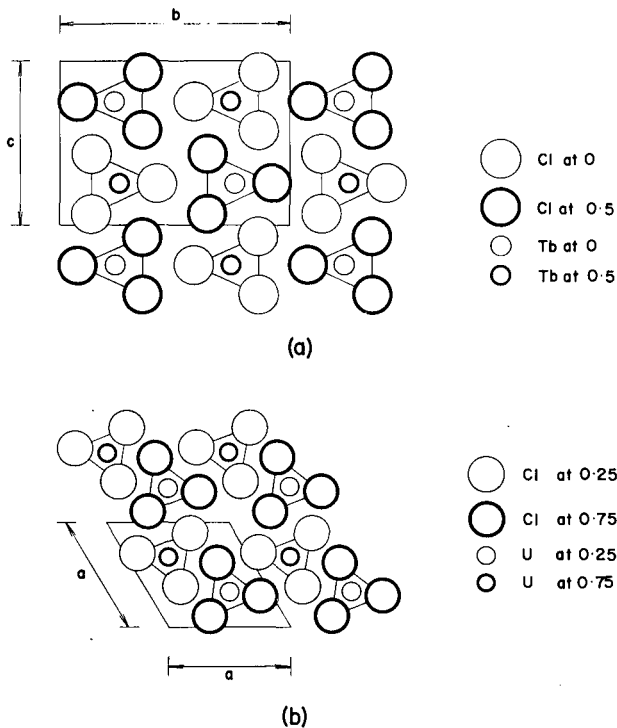


Fig. D.4-1. Comparison of orthorhombic TbCl_3 structure and hexagonal UCl_3 structure.

(a) Projection of TbCl_3 down \underline{a} axis.

(b) Projection of UCl_3 down \underline{c} axis.

5. REFINEMENT OF THE CRYSTAL STRUCTURE OF MERCURIC SULFATE MONOHYDRATE

Lieselotte K. Templeton, David H. Templeton, and Allan Zalkin

In making a survey of hydrogen bonding in hydrated sulfate crystals we became interested in the structure of mercuric sulfate monohydrate. This crystal structure was determined by Bonefačić by analysis of x-ray data for two projections,¹ but the accuracy of this determination is not sufficient to permit the hydrogen bonding to be established with confidence. We have refined this structure on the basis of three-dimensional data obtained by direct counting of diffracted x-ray intensities. We confirm the general features of the atomic arrangement. The atomic positions imply that each water molecule is involved in one hydrogen bond.

Well-formed crystals of $\text{HgSO}_4 \cdot \text{H}_2\text{O}$ are readily obtained by dissolving anhydrous HgSO_4 in 2.5 M H_2SO_4 and allowing the solution to stand at room temperature. We obtained colorless thin plates of HgSO_4 if the concentration of acid were too high, and colorless elongated plates like those described by Hoitsema² as $2\text{HgSO}_4 \cdot \text{HgO} \cdot 2\text{H}_2\text{O}$ if the acidity were slightly lower. At lower acidity a yellow precipitate appeared.

Intensities were measured with a crystal which could be circumscribed by a nearly square prism with dimensions $0.06 \times 0.06 \times 0.03$ mm. The main faces were [100] and [011], with the short dimension in the a direction. x-Ray measurements were made with a scintillation counter with $\text{MoK}\alpha$ radiation; 618 independent reflections permitted by the space group were recorded.

The structure was refined by least squares.

1. A. Bonefačić, *Acta Cryst.* **14**, 116 (1961).
2. C. Hoitsema, *Z. Phys. Chem.* **17**, 657 (1895).

For the orthorhombic unit cell we find dimensions

$$a = 5.416 \pm 0.003 \text{ \AA} (5.42 \pm 0.01 \text{ \AA}),$$

$$b = 8.964 \pm 0.003 \text{ \AA} (8.94 \pm 0.02 \text{ \AA}),$$

$$c = 7.874 \pm 0.003 \text{ \AA} (7.82 \pm 0.02 \text{ \AA}),$$

which are in reasonable agreement with the values (in parentheses) which were reported by Bonefačić.¹ The space group is $\text{Pm}\bar{c}n$ (D_{2h}^{16}).

The refinement by least squares was started with the published coordinates¹ as trial structure. The resulting parameters are listed in Tables D.5-I and D.5-II. We have retained the setting and choice of origin as given by Bonefačić,¹ which corresponds to the general position 8(d):

$$\pm(x, y, z; 1/2 - x, 1/2 - y, 1/2 + z; 1/2 + x, \bar{y}, \bar{z}; x, 1/2 + y, 1/2 - z).$$

Some interatomic distances and angles are listed in Tables D.5-III and D.5-IV.

Some circumstantial evidence for the correctness of the structure comes from the dimensions we find for the sulfate ion, which deviates from regular tetrahedral by less than a standard deviation. The average S-O bond length is 1.48

Table D.5-I. Atomic coordinates in $\text{HgSO}_4 \cdot \text{H}_2\text{O}$.

Atom	x	y	z	$\sigma(y)$	$\sigma(z)$
Hg	1/4	0.2086	0.1329	0.0001	0.0001
S	3/4	0.1421	-0.0955	0.0005	0.0006
O(1)	3/4	0.078	0.075	0.002	0.002
O(2)	-0.026 ^a	0.234	-0.120	0.001	0.001
O(3)	3/4	0.020	-0.224	0.002	0.002
O(H ₂ O)	1/4	0.456	0.094	0.002	0.002

^a $\sigma(x) = 0.002$.

Table D.5-II. Anisotropic thermal parameters and standard deviations.

Atom	β_{11}	β_{22}	β_{33}	β_{23}	$\sigma(\beta_{11})$	$\sigma(\beta_{22})$	$\sigma(\beta_{33})$	$\sigma(\beta_{23})$
Hg	115	38	53	1	3	1	1	1
S	68	32	46	6	12	4	6	4
O(1)	191	64	59	10	54	19	22	16
O(2) ^a	70	49	100	-1	25	11	16	12
O(3)	143	28	77	-2	48	15	22	15
O(H ₂ O)	278	28	86	-10	63	15	25	16

^a For O(2), $10^4\beta_{12} = -25 \pm 15$; $10^4\beta_{13} = 4 \pm 20$.

Table D.5-III. Interatomic distances in $\text{HgSO}_4 \cdot \text{H}_2\text{O}$.

Atom	Neighbor	Number	Distance (Å)
Hg	O(2)	2	2.50 ± 0.01
	O(2)	2	2.51 ± 0.01
	O(3)	1	2.17 ± 0.01
	O(H ₂ O)	1	2.24 ± 0.01
S	O(1)	1	1.46 ± 0.02
	O(2)	2	1.48 ± 0.01
	O(3)	1	1.49 ± 0.02
O(H ₂ O)	Hg	1	2.24 ± 0.01
	O(1) ^a	1	2.83 ± 0.02
	O(3)	1	2.96 ± 0.02
	O(2) ^b	2	3.00 ± 0.02
	O(2)	2	3.04 ± 0.02
	O(3)	2	3.07 ± 0.02
	O(H ₂ O)	2	3.18 ± 0.02
	O(2) ^b	2	3.20 ± 0.02

^a Neighbor connected by hydrogen bond.

^b Neighbor in same octahedron.

Å. We estimate that thermal motion, if oxygen rides on sulfur, requires a correction of 0.01 Å. The corrected average, 1.488 Å, is to be compared with the corrected average value 1.486 Å found in $\text{Mg}(\text{NH}_4)_2(\text{SO}_4)_2 \cdot 6\text{H}_2\text{O}$ (Margulis and Templeton³) and in $\text{MgSO}_4 \cdot 6\text{H}_2\text{O}$ (Zalkin, Ruben, and Templeton⁴).

Each mercury atom has two close ligands, O(3) at 2.17 Å and O(H₂O) at 2.24 Å, which are approximately collinear with a bond angle 169°. The other four neighbors, O(2) at 2.50 or 2.51 Å, are at the corners of a rectangle whose shorter sides are perpendicular to the mirror plane containing Hg, O(3), and O(H₂O). The Hg atom is 0.37 Å from the plane of this rectangle, on the side toward O(3). The six neighbors thus are the corners of an octahedron which is considerably distorted. The octahedra share edges (Fig. D.5-1).

The tendency toward twofold coordination is prevalent among mercuric compounds (Wells,⁵) but frequently is more extreme. For example, in the two forms of HgO, (Aurivillius,⁶ Aurivillius and Carlsson,⁷) each Hg has two oxygen

3. T. N. Margulis and D. H. Templeton, *Z. Krist.* **117**, 344 (1962).

4. A. Zalkin, H. Ruben, and D. H. Templeton, *Acta Cryst.* (1964) (in press).

5. A. F. Wells, *Structural Inorganic Chemistry* (Clarendon Press, Oxford, 1962), 891.

6. K. Aurivillius, *Acta Chem. Scand.* **10**, 852 (1956).

7. K. Aurivillius and I. -B Carlsson, *Acta Chem. Scand.* **12**, 1297 (1958).

Table D.5-IV. Angles in $\text{HgSO}_4 \cdot \text{H}_2\text{O}$.^a

O(H ₂ O)-Hg-O(3)	169°
O(H ₂ O)-Hg-O(2)	78°, 85°
O(3)-Hg-O(2)	86°, 111°
O(2)-Hg-O(2)	73°, 73°, 104°, 163°
O(1)-S-O(2)	110°
O(1)-S-O(3)	109°
O(2)-S-O(2)	110°
O(2)-S-O(3)	109°
Hg-O(H ₂ O)-O(1)	105°
O(1)-O(H ₂ O)-O(3) ^b	146°
O(1)-O(H ₂ O)-O(3) ^c	63°
O(1)-O(H ₂ O)-O(2) ^d	65°

^a Standard deviations are 1° or less.

^b O(3) at 2.96 Å.

^c O(3) at 3.07 Å.

^d O(2) at 3.04 Å.

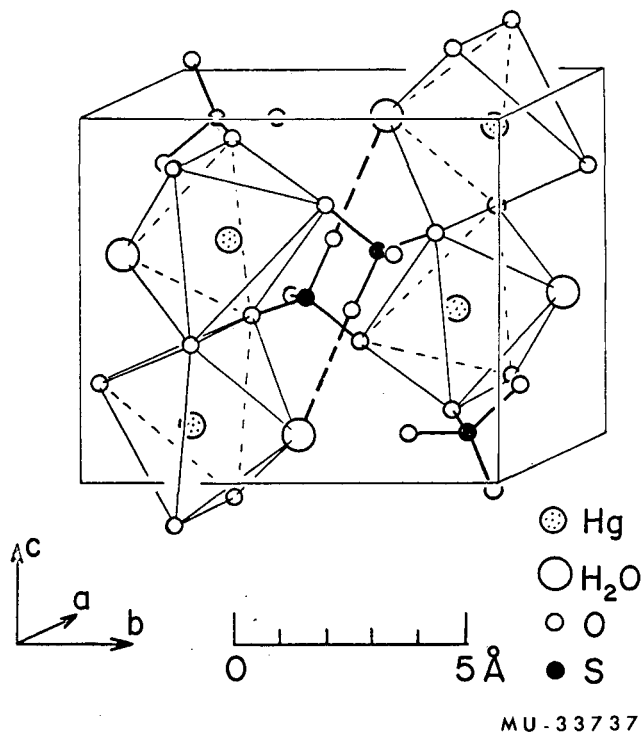


Fig. D.5-1. Crystal structure of $\text{HgSO}_4 \cdot \text{H}_2\text{O}$. A heavy broken line indicates the hydrogen bond.

neighbors at 2.03 Å and four others at distances 2.79 Å or more. In these cases, of course, the oxygen atoms are unhampered by other bonds.

Each water molecule has one neighbor, O(1) at 2.83 Å, at a suitable distance for a hydrogen bond. The angle that this bond makes with the

O(H₂O)-Hg vector (105°) is in the range in which such angles commonly fall in other hydrated salts. The fact that O(1) is the only oxygen atom not adjacent to a mercury atom makes it the most appropriate one to accept a hydrogen bond.

The next nearest oxygen neighbor of water is O(3) at 2.96 Å. Such a distance is near the upper limit for a hydrogen bond. The angle with respect to the O(H₂O)-Hg vector (109°) is acceptable, but the angle O(3)-O(H₂O)-O(1) = 146° is incompatible with a normal H-O-H angle. From the present evidence we conclude that there is only one hydrogen bond.

We calculated an electron density difference

function in the section at $x = 0.25$ as an attempt to locate the hydrogen atoms. The result showed spurious peaks as high as 1.2 electron/Å³ in locations distant from the water molecule and therefore cannot be considered to be reliable for the hydrogen atoms. However, a peak of height 0.8 electron/Å³ appeared at 0.25, 0.51, 0.20, which is very close to the expected position for a hydrogen atom in the bond to O(1). No peak appeared at a reasonable position for the second hydrogen atom. We expect a nonbonded hydrogen atom to have large thermal motion and therefore to be difficult to see.

We thank Dr. J. D. Forrester for assistance in this research.

6. THE CRYSTAL STRUCTURE OF MANGANESE DICHLORIDE TETRAHYDRATE*

Allan Zalkin, J. D. Forrester, and David H. Templeton

Groth¹ reports two monoclinic crystal modifications of MnCl₂·4H₂O. One form is metastable at room temperature (Dawson and Williams²), and is isomorphous with FeCl₂·4H₂O, the structure of which has been described by Penfold and Grigor³ with comments on the proton sites by Saffar and Murtz.⁴ Our paper deals with the form that is stable at room temperatures, and in keeping with the nomenclature of Dawson and Williams² we refer to this modification as the α form, and to the metastable modification as the β form. It should be noted here that Groth¹ in his publication has reversed the naming of these two forms from the above convention.

Delain has reported the cell dimensions and space group of the α form,⁵ and Gardner has reported some preliminary results on the proton sites.⁶ We became interested in the structure of this crystal after learning of its use as a sample for low-temperature magnetic measurements by Professor W. F. Giaque.

* Brief version of paper to be published in *Inorganic Chem.*

1. P. Groth, *Chemische Kristallographie* (Wilhelm Engelmann, Leipzig, 1908), Vol. I.
2. H. M. Dawson and P. Williams, *Z. Physik. Chem.* 31, 59 (1899).
3. B. R. Penfold and J. A. Grigor, *Acta Cryst.* 12, 850 (1959).
4. Z. M. El Saffar and C. R. K. Murtz, *Acta Cryst.* 15, 285 (1962).
5. C. Delain, *Compt. Rend. Acad. Sci. Paris* 238, 1245 (1954).
6. W. E. Gardner, *Bull. Am. Phys. Soc.* 5, 458 (1960).

An aqueous solution of manganous chloride was allowed to evaporate at room temperature, and the tetrahydrate crystals grew readily in the form of approximately hexagonal plates. A suitable crystal with maximum dimension of 0.1 mm was mounted and used for collecting the intensity data with a scintillation counter.

All told, 848 independent reflections were measured, and of these, 49 were assigned zero intensity.

The primitive cell is monoclinic, contains four formula units (MnCl₂·4H₂O) per unit cell, and has the dimensions

$$a = 11.186 \pm 0.006 \text{ \AA}, \quad b = 9.513 \pm 0.005 \text{ \AA}, \\ c = 6.186 \pm 0.002 \text{ \AA}, \quad \beta = 99.74 \pm 0.04^\circ, \\ V = 648.8 \text{ \AA}^3, \quad a : b : c = 1.1759 : 1 : 0.6503.$$

From the x-ray data the calculated density is 2.03 g/cm³, which compares with the value of 2.01 g/cm³ reported in the *Handbook of Chemistry and Physics*.⁷

Reflections h0l are absent unless $h + l = 2n$, and Ok0 reflections are absent unless $k = 2n$. This is characteristic of the space group $P2_1/n(C_{2h}^2)$, and the success of our structure determination confirms this symmetry. All atoms are in fourfold general positions: $4(e) \pm (x, y, z; 1/2 + x, 1/2 - y, 1/2 + z)$.

The parameters of the seven sets of atoms were refined by least squares using all the data.

7. *Handbook of Chemistry and Physics*, 39th Edition (Chemical Rubber Publishing Co., Ohio, 1957), p. 554.

each with an assignment of unit weight.

An electron density difference function with all atoms except hydrogen subtracted out was calculated with the terms for which $\sin \theta/\lambda$ is less than 0.48. Eight out of the ten highest peaks in this function corresponded to reasonable positions for the eight independent hydrogen atoms in general positions. Four of these hydrogen atoms form hydrogen bonds.

Four cycles of least-squares refinement, with all eight hydrogen atoms each having isotropic temperature factors and the remaining seven heavier atoms having anisotropic temperature factors, resulted in an R factor of 0.041.

The final positional parameters and thermal parameters are listed in Tables D.6-I and D.6-II respectively.

The structure consists of discrete octahedral groups with each manganese atom coordinated to two chlorine atoms at an average distance of 2.488 Å and to four oxygen atoms at an average distance of 2.206 Å. Of the eight hydrogen atoms only four are involved in hydrogen bonding, which is discussed below. The overall packing is illustrated in Fig. D.6-1 and the dimensions of the octahedron are shown in Table D.6-III. A complete list of distances less than 4.0 Å is shown in Table D.6-IV; the hydrogen atom distances are excluded.

Table D.6-I. Final positional parameters and standard deviations for $\text{MnCl}_2 \cdot 4\text{H}_2\text{O}$.

Atom	x	y	z	$\sigma(x)$	y	$\sigma(z)$
Mn	0.2329	0.1714	0.9865	0.0001	0.0001	0.0001
Cl(1)	0.0610	0.3076	0.0938	0.0001	0.0001	0.0002
Cl(2)	0.3817	0.3662	0.0355	0.0001	0.0001	0.0002
O(1)	0.3010	0.1127	0.3334	0.0004	0.0005	0.0006
O(2)	0.1568	0.2280	0.6446	0.0004	0.0005	0.0007
O(3)	0.1323	0.9736	0.9590	0.0005	0.0006	0.0011
O(4)	0.3695	0.0381	0.8764	0.0004	0.0005	0.0007
H(1)1 ^a	0.39	0.15	0.37	0.01	0.01	0.01
H(1)2	0.30	0.02	0.35	0.01	0.01	0.01
H(2)1	0.08	0.20	0.62	0.01	0.01	0.01
H(2)2	0.19	0.21	0.56	0.01	0.01	0.02
H(3)1	0.11	0.95	0.87	0.01	0.01	0.02
H(3)2	0.10	0.99	0.01	0.02	0.02	0.03
H(4)1	0.43	0.09	0.81	0.01	0.01	0.02
H(4)2	0.35	0.95	0.86	0.01	0.01	0.01

^a H(i)j means that it is the jth hydrogen of water oxygen O(i).

Table D.6-II. Thermal parameters^a and standard deviations.

Atom	B_{11} ^b	B22	B33	B12	B13	B23
Mn	1.98 ± 0.04	1.81 ± 0.04	1.50 ± 0.04	-0.02 ± 0.03	0.36 ± 0.03	0.01 ± 0.03
Cl(1)	2.16 ± 0.06	2.76 ± 0.07	2.51 ± 0.06	0.43 ± 0.05	0.65 ± 0.05	-0.29 ± 0.05
Cl(2)	2.22 ± 0.06	2.03 ± 0.06	2.38 ± 0.06	-0.29 ± 0.05	0.35 ± 0.05	0.00 ± 0.05
O(1)	3.3 ± 0.2	2.2 ± 0.2	2.0 ± 0.2	-0.1 ± 0.2	0.2 ± 0.1	0.1 ± 0.1
O(2)	2.5 ± 0.2	3.2 ± 0.2	2.2 ± 0.2	-0.2 ± 0.2	0.5 ± 0.2	0.3 ± 0.2
O(3)	4.1 ± 0.2	3.1 ± 0.2	3.4 ± 0.3	-1.2 ± 0.2	1.0 ± 0.2	-0.6 ± 0.2
O(4)	3.5 ± 0.2	2.6 ± 0.2	3.7 ± 0.2	0.1 ± 0.2	1.5 ± 0.2	-0.1 ± 0.2
Atom	\underline{B} ^c	Atom	\underline{B}	Atom	\underline{B}	
H(1)1	2 ± 2	H(2)2	5 ± 3	H(4)1	6 ± 3	
H(1)2	3 ± 2	H(3)1	6 ± 5	H(4)2	5 ± 2	
H(2)1	1 ± 1	H(3)2	21 ± 9			

^a Units are Å².

^b The anisotropic values $B_{ij} = 4\beta_{ij}/a_i^* a_j^*$ where a_i^* is the *i*th reciprocal cell length.

^c Isotropic.

Table D. 6-III. Dimensions of the octahedron around manganese in $\text{MnCl}_2 \cdot 4\text{H}_2\text{O}$.

Atoms		Distance, Å	
Mn - Cl(1)		2.500 ± 0.002	(2.506) ^a
- Cl(2)		2.475 ± 0.002	(2.478)
- O(1)		2.224 ± 0.004	(2.229)
- O(2)		2.209 ± 0.004	(2.215)
- O(3)		2.185 ± 0.006	(2.198)
- O(4)		2.206 ± 0.005	(2.216)

Atoms	Angles	Atoms	Angles
Cl(1) - Mn - Cl(2)	96°	O(1) - Mn - O(2)	177°
- O(1)	92°	- O(3)	87°
- O(2)	87°	- O(4)	92°
- O(3)	93°	O(2) - Mn - O(3)	92°
- O(4)	174°	- O(4)	90°
Cl(2) - Mn - O(1)	88°	O(3) - Mn - O(4)	82°
- O(2)	94°		
- O(3)	169°		
- O(4)	89°		

^a Distances in parentheses are values corrected for thermal motion, assuming that the O and Cl atoms "ride" on the Mn.

Table D. 6-IV. Distances less than 4.0 Å with standard deviations in $\text{MnCl}_2 \cdot 4\text{H}_2\text{O}$.^a

Atom	Distance (Å)	Atom	Distance (Å)
Cl(1) - O(2)	3.233 ± 0.005^b	O(1) - O(3)	3.033 ± 0.008^b
- O(1)	3.391 ± 0.005^b	- O(4)	3.185 ± 0.006^b
- O(3)	3.414 ± 0.006^b	O(2) - O(4)	3.117 ± 0.007^b
- Cl(2)	3.708 ± 0.003^b	- O(3)	3.146 ± 0.008^b
- O(1)	3.169 ± 0.005^c	- Cl(2)	3.166 ± 0.005^c
- O(4)	3.292 ± 0.005^c	- Cl(1)	3.477 ± 0.005
- O(2)	3.477 ± 0.005	O(1) - O(2)	2.926 ± 0.006^c
Cl(2) - O(1)	3.254 ± 0.005^b	- Cl(1)	3.169 ± 0.005^c
- O(4)	3.285 ± 0.005^b	- O(4)	3.339 ± 0.006
- O(2)	3.442 ± 0.005^b	O(3) - O(4)	2.872 ± 0.008^b
- O(2)	3.166 ± 0.005^c		
- O(3)	3.815 ± 0.007		

^a Hydrogen atom distances are not included.

^b Octahedral edge.

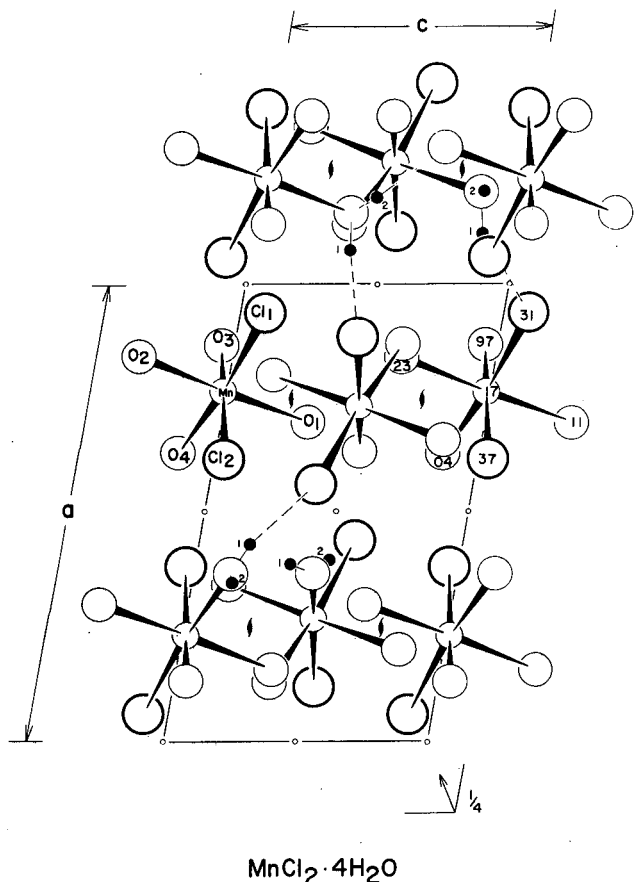
^c Hydrogen bond.

The octahedron is only slightly distorted, with the primary distortion due to the packing of the two larger chlorine atoms with the four somewhat smaller oxygen atoms. The chlorine atoms are adjacent in each octahedron and not opposite as in the $\text{FeCl}_2 \cdot 4\text{H}_2\text{O}$ structure,³ although both structures have discrete octahedra. Also in the $\text{FeCl}_2 \cdot 4\text{H}_2\text{O}$ structure there are two different octahedral Fe-O distances (2.09 Å and 2.59 Å), whereas in the $\text{MnCl}_2 \cdot 4\text{H}_2\text{O}$ all four Mn-O distances are almost equivalent (2.19 Å to 2.22 Å). The densities of the two substances are very similar (2.03 g/cm³ for the Mn compound,

1.98 g/cm³ for the Fe compound), indicating that the efficiency of packing is also comparable. These comparisons suggest a rather interesting phase transformation if the metastable β form of $\text{MnCl}_2 \cdot 4\text{H}_2\text{O}$ is indeed isomorphous with $\text{FeCl}_2 \cdot 4\text{H}_2\text{O}$, as is suggested by Groth.¹

According to Groth,¹ $\text{MnBr}_2 \cdot 4\text{H}_2\text{O}$ has axial cell ratios and β angle very close to $\text{MnCl}_2 \cdot 4\text{H}_2\text{O}$ and is presumably isostructural with the structure described in this paper.

There is a similarity between the



MUR-2101

Fig. D.6-1. Atomic arrangement in $\text{MnCl}_2 \cdot 4\text{H}_2\text{O}$; y coordinates ($\times 100$) are indicated as numbers inside some of the circles. The small solid circles represent hydrogen atoms, and only one of each type is shown.

$\text{MnCl}_2 \cdot 4\text{H}_2\text{O}$ structure and that reported by Culot et al.⁸ for $\text{NaBr} \cdot 2\text{H}_2\text{O}$. Dawson and Williams remark that $\text{MnCl}_2 \cdot 4\text{H}_2\text{O}$ and $\text{NaCl} \cdot 2\text{H}_2\text{O}$ are isomorphous.² If the monoclinic cell for $\text{NaBr} \cdot 2\text{H}_2\text{O}$ is doubled along its a axis and a different setting chosen, the resulting cell has axial ratios and β angle as follows, $a : b : c = 1.71 : 1 : 0.653$ with $\beta = 97.3^\circ$; this is quite similar to the values for $\text{MnCl}_2 \cdot 4\text{H}_2\text{O}$ reported here. The $\text{NaBr} \cdot 2\text{H}_2\text{O}$ structure also consists of octahedra with the halide atoms adjacent. These octahedra, however, each share an edge with each of three adjacent octahedra--consistent with one extra cation in the formula--and form sheets, in contrast with discrete octahedra in $\text{MnCl}_2 \cdot 4\text{H}_2\text{O}$.

All eight independent H atoms were located from the difference function calculated after an anisotropic refinement of the seven heavier atoms. Four of these are in a suitable environment to participate in hydrogen bonding, but the other four have no close neighbors that would indicate such bonding. A representative of each independent H atom is shown in Fig. D.6-1, and appropriate distances for the four bonded hydrogens are indicated in Table D.6-IV. The four hydrogen bonds are as follows:

O(1)	_____	H(1)1	Cl(1)	3.17 Å,
O(2)	_____	H(2)1	Cl(2)	3.17 Å,
O(2)	_____	H(2)2	O(1)	2.93 Å,
O(4)	_____	H(4)1	Cl(1)	3.29 Å.

All the distances above represent hydrogen bonding between atoms in different octahedra.

8. J. P. Culot, P. Piret, and M. Van Meerssche, Bull. Soc. Franc. Miner. Crist. 85, 282 (1962).

7. DETERMINATION OF THE CRYSTAL STRUCTURE OF XENON TRIOXIDE*

David H. Templeton, Allan Zalkin, J. D. Forrester, and Stanley M. Williamson

Xenon trioxide was characterized by determination of its crystal and molecular structure by x-ray diffraction. The material used in this work resulted from the hydrolysis of XeF_4 , after which the solution was evaporated to dryness. A very small amount of the white powder was placed in a glass slide in air and was allowed to pick up water from the atmosphere until

* Brief version of paper in Noble Gas Compounds (University of Chicago Press, Chicago, 1963).

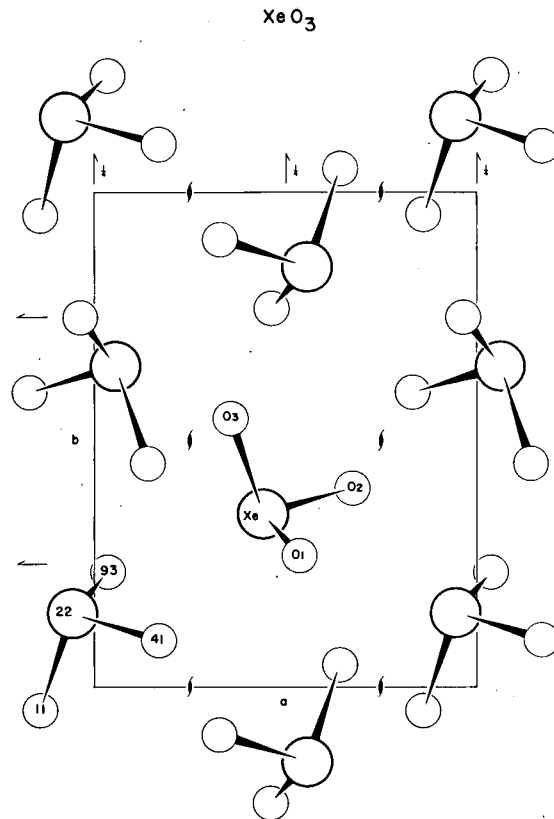
it completely dissolved. Crystals were then grown by focusing a microscope lamp on the saturated drops on the slide to provide gentle heating. With a microscopy of about 40 power, crystals were observed to develop as very fine needles which grew in a few minutes to elongated rods.

Several crystals were required for the work because of decomposition during the irradiation. The first five or six crystals were used in learn-

ing how to handle the substance and to take Weissenberg patterns to establish the crystal symmetry. An additional four or five crystals were required to get accurate cell dimensions and to take intensity data. These measurements were made with a General Electric XRD-5 apparatus equipped with a goniostat and scintillation counter and with Mo K α x rays. Ultimately 482 independent reflections were observed, 16 of which were below the detection limit and recorded as zero. The intensities were measured only for 2θ below 60° .

The crystals contained a film of moisture on their surfaces, probably acquired during their exposure to the room before sealing. During irradiation the crystal would decompose and the resulting gas would form bubbles in this film. Where the crystal contacted the capillary these bubbles caused the crystal to move out of alignment, necessitating frequent realignment of the crystal. The crystal could be observed to break up during the measurements. The decomposition rate decreased markedly when the irradiation was stopped; therefore to diminish this damage a beam stop was used which exposed the crystal to x rays only during the actual 10 seconds of counting. Even with these precautions, a crystal would last for only about 4 to 6 hours of measurements.

The structure was refined by least squares. The unreliability index R was finally reduced to 0.098 with the parameters listed in Table D.7-I. The crystal structure is shown in Fig. D.7-1.



MUR-1594

Fig. D. 7-1. Molecular packing in XeO₃.Table D. 7-I. Crystal structure data for XeO₃.

Cell data				
Orthorhombic				
Space group $P2_12_12_1$ (D_2^4)				
$a = 6.163 \pm 0.008 \text{ \AA}$				
$b = 8.115 \pm 0.010 \text{ \AA}$				
$c = 5.234 \pm 0.008 \text{ \AA}$				
$Z = 4$				
$V = 261.8 \text{ \AA}^3$				
Molecular weight = 179.30				
x-Ray density = 4.55 g/ml				
Atomic parameters - all atoms in the general position				
4a $x, y, z; 1/2-x, \bar{y}, 1/2+z; 1/2+x, 1/2-y, \bar{z}; \bar{x}, 1/2+y, 1/2-z.$				
	x	y	z	$B(\text{\AA}^{-2})$
Xe	0.9438 ± 0.0003	0.1496 ± 0.0003	0.2192 ± 0.0004	1.3 ± 0.04
O1	0.537 ± 0.004	0.267 ± 0.004	0.066 ± 0.006	2.3 ± 0.5
O2	0.171 ± 0.005	0.096 ± 0.004	0.406 ± 0.006	2.2 ± 0.5
O3	0.142 ± 0.004	0.454 ± 0.003	0.142 ± 0.006	1.8 ± 0.4

The molecular shape is triangular pyramidal, with bond distances and angles which are equal within the experimental error. We report the average bond distance as 1.76 Å and the average bond angle as 103°. These dimensions may be compared with 1.82 Å for the average

bond distance and 97° for the average bond angle for the isoelectric iodate ion.

Xenon trioxide is a dangerous explosive which may detonate without warning, and it should be handled with great caution.

8. SODIUM PERXENATE HEXAHYDRATE*

Allan Zalkin, J. D. Forrester, David H. Templeton, Stanley M. Williamson, and Charles W. Koch

Some hydrated sodium salts of xenon in the +8 oxidation state were produced by Malm, Bane, and Holt¹ by hydrolysis of XeF₆ in the presence of sodium hydroxide. Crystal data were reported by Siegel and Gebert² for three phases produced in this way. By determination of the crystal structure Hamilton, Ibers, and Mackenzie³ have shown that one of these phases in Na₄XeO₆·6H₂O, containing perxenate ion (XeO₆⁻⁴) in the shape of a regular octahedron.

We have produced another salt which is characterized as Na₄XeO₆·6H₂O by determination of the crystal structure. We find the same shape for the perxenate ion with dimensions close to those reported in the work on the octahydrate.³ This hexahydrate is not one of the phases reported by Siegel and Gebert.²

The crystals of Na₄XeO₆·6H₂O were obtained from the reaction of pure xenic acid (aqueous XeO₃) and sodium hydroxide. When 0.100 ml of 0.208 M XeO₃ (Aq) and 0.060 ml of 6 M NaOH were mixed the resulting solution was pale yellow. After one day in a refrigerator at 5° crystals grew as very thin fragile sheets. The production of crystals from the reaction is much more rapid at elevated temperatures, about 60°, but at this higher temperature the product is the octahydrate.

The hexahydrate is much less stable than the octahydrate. The x-ray study was made of crystals sealed in thin-walled glass capillaries containing some of the mother liquor. Most crystals survived only a few hours in the capillaries, and several preparations were necessary before adequate data were obtained.

* Brief version of paper published in *Science* **142**, 501 (1963).

1. J. G. Malm, R. W. Bane, and B. D. Holt, in *Noble-Gas Compounds* (University of Chicago Press, Chicago, 1963), p. 167.

2. S. Siegel and E. Gebert, *ibid.* p. 193.

3. W. C. Hamilton, J. A. Ibers, and D. R. Mackenzie, *Science* **141**, 532 (1963).

The crystals are orthorhombic, space group Pbc_a, with $a = 18.44 \pm 0.01$, $b = 10.103 \pm 0.007$, $c = 5.873 \pm 0.005$ Å. The density is calculated as 2.59 g/ml with four molecules per unit cell. The crystals were observed to sink in ethylene bromide (density 2.17 g/ml).

All atoms (except hydrogen, which is not detected with these data) were recognized in the Patterson function. Refinement by least squares eventually reduced R to 0.072 with the atomic parameters listed in Table D. 8-1. Standard deviations of coordinates correspond to 0.01 Å for sodium and 0.02 Å for oxygen. A three-dimensional Fourier synthesis of $F_o - F_c$ showed no peaks as high as 2 electrons/Å³.

The perxenate ion is centric by the space-group symmetry. The three independent Xe-O distances are

Xe-O(1)	1.85 ± 0.02 Å,
Xe-O(2)	1.86 ± 0.02 Å,
Xe-O(3)	1.81 ± 0.02 Å.

The deviations from the average value 1.84 Å are not significant. Our data concerning thermal motion are incomplete, but we estimate that the correction for thermal motion would increase this distance less than 0.01 Å. The bond angles O-Xe-O, which would be 90° for regular octahedral shape, range from 87.1° to 92.9° with standard deviations of about 1°. We do not consider these deviations from 90° to be significant. These results are in accord with those from the octahydrate.³

The overall structure (Fig. D.8-1) is quite different from that of the octahydrate. It consists of layers perpendicular to the a axis. Layers containing the perxenate and half the sodium (Fig. D. 8-2) alternate with layers containing the rest of the sodium and all the water. The six independent hydrogen atoms are assigned to hydrogen bonds which all have reasonable distances and angles. Five of these bonds, between water and oxygen of perxenate, hold the layers to each other.

Table D. 8-1. Atomic coordinates and thermal parameters in $\text{Na}_4\text{XeO}_6 \cdot 6\text{H}_2\text{O}$.

Atom	\underline{x}	\underline{y}	\underline{z}	\underline{B} (\AA^2)
Xe	0	0	0	$(0.85 \pm 0.04)^a$
Na(1)	0.009	0.164	0.492	1.4 ± 0.2
Na(2)	0.252	0.155	0.539	1.7 ± 0.2
O(1)	0.060	0.005	0.252	1.2 ± 0.2
O(2)	0.064	0.115	0.854	1.8 ± 0.4
O(3)	0.951	0.136	0.127	1.0 ± 0.4
O(W1)	0.169	0.200	0.242	1.6 ± 0.3
O(W2)	0.339	0.183	0.836	1.5 ± 0.3
O(W3)	0.192	0.518	0.242	2.2 ± 0.4

^a Isotropic \underline{B} equivalent to average of anisotropic temperature factor.

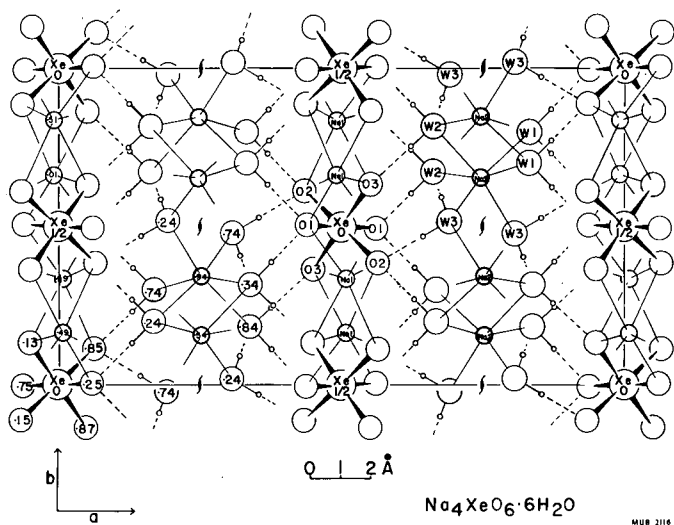


Fig. D. 8-1. Sodium perxenate hexahydrate structure as seen projected down the c direction. Hydrogen bonds are indicated by dotted lines.

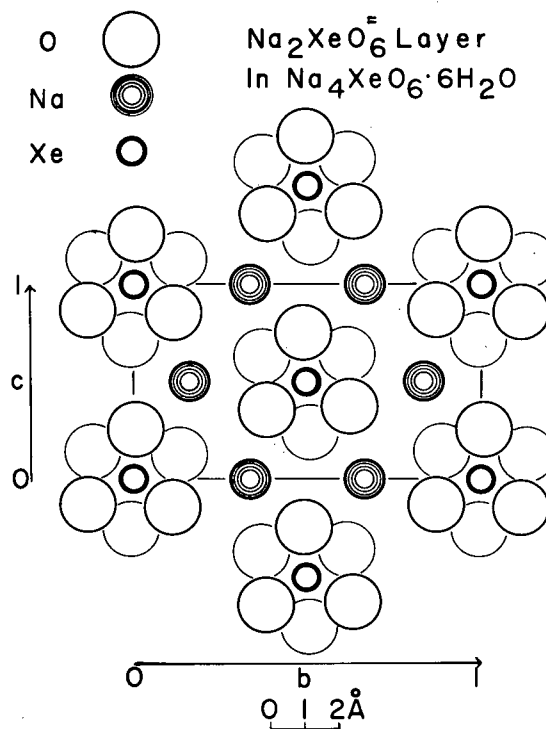


Fig. D. 8-2. Layer containing perxenate ion and sodium ions in the bc plane.

9. CHEMISTRY OF XeO₃ IN AQUEOUS SOLUTION

Stanley M. Williamson and Charles W. Koch

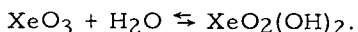
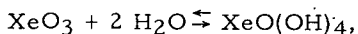
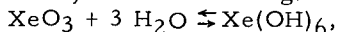
The reaction of XeF₄ with water or aqueous solutions was first mentioned by Claassen, Selig, and Malm,¹ and has been studied in more detail by Williamson and Koch.² The detailed studies showed that, in addition to the direct oxidation of water by XeF₄ to give O₂, Xe, and HF, the reaction gave a very soluble Xe(VI) species. Evaporation of this resulting solution in Teflon-ware at room temperature gave the white crystalline XeO₃.³

Since it was known that nonbasic solutions yield XeO_{3(s)} on evaporation,^{2,3} the nature of the aqueous Xe(VI) species was investigated in four ways. First, the XeO_{3(s)} was dissolved in a large excess of 57.0% O¹⁸ water and allowed to stand in a quartz tube in one experiment for 15 minutes and in another for 1 hour before the excess water was pumped off. The XeO₃ was decomposed and the gases were analyzed. The data for the two experiments are given in Table D. 9-I.

Table D. 9-I. Oxygen exchange by XeO₃ on solution in water.

Time for equilibration (min)	O ¹⁸ (%)	O/Xe
15	51.4	2.76
60	54.0	2.95

It can be seen from the data that one hour may not have been sufficient for complete exchange. This experiment does not give the true nature of the aqueous species because the major equilibrium could be any of the following:



As a second approach, the NMR spectrum was obtained on an acidified aqueous solution. Small-intensity resonances were observed both at lower and higher field strength than the water resonance (presumably due to protons associated with the xenon). The water resonance sharpened and

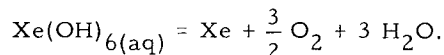
1. H. H. Claassen, H. Selig, and J. C. Malm, *J. Am. Chem. Soc.* **84**, 3593 (1962).

2. S. M. Williamson and C. W. Koch, *Science* **139**, 1046 (1963).

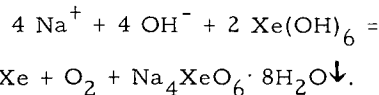
3. D. H. Templeton, A. Zalkin, J. D. Forrester, and S. M. Williamson, *J. Am. Chem. Soc.* **85**, 817 (1963).

became more intense as the acidity of the solution was increased, but the small resonances remained nearly unchanged.

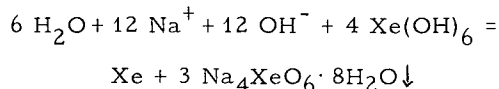
The third approach was a direct titration of the solution with strong base. Titration of a weighed sample of XeO₃ dissolved in H₂O with 1 M NaOH produced a linear increase in pH as a function of the amount of base added until pH 10. Between pH 10 and 11 there was a slight change in slope. If this change in slope is related to an end point the corresponding equivalent weight is 254. The titration of one hydrogen from Xe(OH)₆ would give 233. The stability of the Xe(VI) species in alkaline solution with regard to decomposition (loss of oxidizing power) was determined. It was found that when the initial NaOH concentration was less than 0.10 M the decomposition corresponded to the equation



For the NaOH concentration range, 0.25 to 7.0 M, disproportionation occurs according to



When the concentration of NaOH exceeds 7 M and approaches 20 M our data indicate that the disproportionation reaction



becomes increasingly important.

Additional evidence as to the nature of the aqueous species was sought by investigating its uv spectrum. At pH 1.2 and 1.8 the absorption was beginning at 270 mμ and extending without

Table D. 9-II. Oxidizing action of Xe(VI) in aqueous solution.

Reactant	pH	Product	Comments
NH ₃	6 M NH ₄ OH	N ₂	vigorous
excess I ⁻	7 or less	I ₃ ⁻	fast
3% H ₂ O ₂	7	O ₂	very vigorous
excess Br ⁻	1 or less	Br ₃ ⁻	slow
Fe ⁺⁺	2	Fe ⁺⁺⁺	fast
Hg	1 M H ₂ SO ₄	Hg ₂ SO ₄	fast

peaking to 185 m μ . At pH 5.5 the absorption sharpened (beginning at 250 m μ) and peaked at 198 m μ . The absorption in $5 \cdot 10^{-4}$ M OH $^-$ had its maximum at 202 m μ and in $6 \cdot 10^{-3}$ M OH $^-$ at 210 m μ . The shift appeared to be linear between the two OH $^-$ concentrations. At pH 5.5 the molar extinction coefficient was 3600. It increased approximately 8% in going from $1 \cdot 10^{-3}$ to $6 \cdot 10^{-3}$ M OH $^-$. An exact measurement of the change in the extinction coefficient was not possible owing

to the slow decomposition of the species. The uv absorption, titration, and decomposition data suggest the presence of one or more charged xenon species in basic solution.

Since pure XeO $_3$ (s) can be readily obtained, solutions of known concentration were made. These were used to investigate the behavior of the Xe(VI) species as an oxidizing agent. Table D.9-II lists some qualitative results.

10. THE REACTION OF XeO $_3$ (aq) WITH BROMIDE AND IODIDE ANION: A KINETIC STUDY

Charles W. Koch and Stanley M. Williamson

The reaction of XeO $_3$ (aq) with Br $^-$.

Spectrophotometric analyses for Br $_3^-$ as a function of time were carried out, starting with different initial concentrations of XeO $_3$, H $^+$, and Br $^-$ in order to determine the dependence of the rate on each species. To determine the total bromine concentration it was necessary to prepare standard curves for the absorbance at 265 m μ for each Br $^-$ concentration employed. The results were consistent with the equilibrium constant reported by Latimer,¹

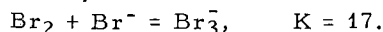


Table D.10-I lists the concentrations and initial slopes and the experimental order of the rate law.

An Arrhenius plot of rate data at 0.2 $^\circ$ C, 24.8 $^\circ$ C, and 39.9 $^\circ$ C gives an activation energy of 15.5 kcal/mole.

The reaction of XeO $_3$ (aq) with I $^-$.

The (I $_3^-$)-versus-time curves were obtained at different concentrations of XeO $_3$, H $_2$ PO $_4^-$, HPO $_4^{2-}$, and I $^-$. The total iodine concentration was determined by measuring the I $_3^-$ band at 287 m μ . Measurements at two different iodide concentrations were in agreement with the equilibrium constant listed by Latimer,¹



The initial slope data show a relatively rapid deviation from a straight-line relationship. This suggests that there is more than one reaction occurring in the pH range investigated. As discussed earlier, the reason may be the alkaline decomposition of XeO $_3$. Initial slope calculations and the experimental order of the rate law are listed in Table D.10-II. An Arrhenius plot of the initial slopes at 24.8 $^\circ$ C and 39.9 $^\circ$ C gives an activation energy equal to 12.2 kcal per mole.

Table D.10-I. Determination of order of the rate law at $\mu = 1.03$.

Temp. $^\circ$ C	XeO $_3$ (M)	H $^+$ (M)	Br $^-$ (M)	Init. slope (moles liter $^{-1}$ min $^{-1}$) $\Delta(\text{Br}_2 + \text{Br}_3^-)/\Delta t$
24.8	$15.08 \cdot 10^{-5}$	0.923	0.1000	$4.86 \cdot 10^{-7}$
24.8	$15.08 \cdot 10^{-5}$	0.462	0.1000	$1.12 \cdot 10^{-7}$
24.8	$15.08 \cdot 10^{-5}$	0.462	0.2000	$4.56 \cdot 10^{-7}$
24.8	$60.32 \cdot 10^{-5}$	0.959	0.1000	$25.0 \cdot 10^{-7}$
0.2	$15.08 \cdot 10^{-5}$	0.923	0.1000	$0.594 \cdot 10^{-7}$
39.9	$15.08 \cdot 10^{-5}$	0.923	0.1000	$19.7 \cdot 10^{-7}$

$$\frac{d(\text{Br}_2 + \text{Br}_3^-)}{dt} = k(\text{XeO}_3)^{1.19}(\text{H}^+)^{2.17}(\text{Br}^-)^{2.04}$$

1. W. M. Latimer, "Oxidation Potentials," 2nd Ed. (Prentice Hall, Inc., New York, 1952).

Table D. 10-II. Determination of order of the rate law:
Ionic strength variable depending upon pH of the phosphate buffer.

Temp. (° C)	XeO ₃ (M)	pH	I ⁻ (M)	Init. slope (moles liter ⁻¹ min ⁻¹) $\Delta(I_2 + I_3^-) / \Delta t$
24.8	$15.08 \cdot 10^{-5}$	7.01	0.0100	$7.15 \cdot 10^{-7}$
24.8	$9.05 \cdot 10^{-5}$	7.01	0.0100	$4.57 \cdot 10^{-7}$
24.8	$15.08 \cdot 10^{-5}$	7.01	0.00500	$3.76 \cdot 10^{-7}$
24.8	$9.05 \cdot 10^{-5}$	6.74	0.00500	$2.15 \cdot 10^{-7}$
24.8	$9.05 \cdot 10^{-5}$	6.43	0.00500	$2.40 \cdot 10^{-7}$
24.8	$9.05 \cdot 10^{-5}$	6.01	0.00500	$3.55 \cdot 10^{-7}$
39.9	$9.05 \cdot 10^{-5}$	6.74	0.00500	$5.81 \cdot 10^{-7}$

$$\frac{d(I_2 + I_3^-)}{dt} = k(\text{XeO}_3)^{0.94}(\text{I}^-)^{0.95}(\text{H}^+)^0$$

11. XENON TETRAFLUORIDE: REACTION WITH AQUEOUS SOLUTIONS

Stanley M. Williamson and Charles W. Koch

In the original report on the preparation of XeF₄¹ it was stated that after the initial hydrolysis of XeF₄ was complete, a substance with oxidizing properties remained in solution. We have observed that XeF₄ oxidizes water directly to O₂, Xe, and HF and that it also reacts to give Xe and a Xe(VI) species by a mechanism not yet understood. Evaporation of the solution that contains the Xe(VI) species yields the white crystalline xenon(VI) oxide.

For the hydrolysis experiments samples of XeF₄ weighing 3 to 20 mg were sublimed into weighed, thin-walled Pyrex bulbs. The bulbs were broken in the reaction vessel, which contained the degassed reaction medium. A Toepler pumping system was used to measure directly the amounts of Xe and O₂. Since the reaction of XeF₄ with an aqueous solution is heterogeneous, reproducible results were not obtained from identical samples. Hydrolysis in 6 M NaOH gave nearly quantitative liberation of O₂ and Xe, assuming the sample to be pure XeF₄. In 3 M H₂SO₄ 52 mole % O₂ and 72 mole % Xe were liberated. The remaining Xe (but no additional O₂) was liberated when solid KI was added to the acidic solution. When XeF₄ was added to distilled water, the O₂ recovered ranged from 40 to 50%. The remainder of the oxidizing power was collected later as I₂. All hydrolyses tended to give a total recovery of Xe a few percent greater than 100, and of O₂ a few percent less than 100. This observation suggests a small

amount of XeF₂ contamination. During hydrolysis at 0° C or lower, the white XeF₄ turns yellow on the surface. At a few degrees below zero the yellow solid in 3 M H₂SO₄ had a lifetime of the order of 20 minutes, whereas the lifetime of the yellow solid in 6 M NaOH at a comparable temperature was approximately 10 seconds. A sample of the yellow solid (the composition of which is unknown to us) did not show an electron-spin resonance spectrum.

The solution that results from the disproportionation of XeF₄ and that contains the new Xe species is the most interesting part of the study. The aqueous species is without doubt the same one that Dudley, Gard, and Cady² have described from the hydrolysis of XeF₆. We can add several observations to the description of its chemistry.

The aqueous Xe(VI) species is very stable in acidic solution. The concentration of a solution that is $3.85 \cdot 10^{-3}$ M in Xe(VI) in 3 M H₂SO₄ has not changed over a period of 40 days. The concentration was not affected by boiling for 5 minutes. The same solution when made basic loses 33 to 50% of its oxidizing power overnight. The HF can be removed by passing the solution through a MgO column. A solution treated in this manner has given an I/Xe ratio for its oxidation number of 6.06. The degree of hydration in solution is not known, but hydrolysis of the XeF₄ in Teflon vessels open to the air has yield-

1. C. L. Chernik et al., *Science* **138**, 136 (1962).

2. F. B. Dudley, G. Gard, and G. H. Cady, *Inorg. Chem.* **2**, 228 (1963).

ed the anhydrous Xe(VI) oxide after evaporation at room temperature in a desiccator over Drierite or BaO. The anhydrous oxide detonates readily.

Because of the extreme hygroscopic nature of the oxide, the sample weights were not useful for obtaining data on percentage composition. Our Toepler pumping system made it possible to measure the O₂-to-Xe ratio on a sample of arbitrary weight, if the evacuated quartz tube could withstand the shock of the thermal decomposition.

After addition of the sample to a quartz bomb tube, the tube was constricted, evacuated under high vacuum conditions for 45 minutes, sealed and heated to 500° C in an iron container for 15 minutes. A trap at -210° C was employed to collect the xenon quantitatively while the O₂ was being pumped into the measuring buret. Another trap at -95° C held back the water. Re-

sults of the determination of the ratio of oxygen to xenon are as follows:

Table D. 11-I. Analysis of xenon(VI) oxide.

O ₂ (μmoles)	Xe (μmoles)	H ₂ ^a (μmoles)	O/Xe	H ₂ O/Xe
11.500	7.692	1.243	2.990	0.16
11.228	7.493	0.544	2.997	0.07

^a The water was measured as H₂ gas after it had been passed over uranium turnings at 750° C.

It can be seen that not all the water was removed even with extensive pumping. To check the recovery of O₂ from the Toepler pumping system, KClO₃ was used as a standard; 2.994 gram atoms of oxygen were recovered per mole of KClO₃.

12. ION-EXCHANGE STUDIES IN CONCENTRATED SOLUTIONS. III. THE ALKALINE EARTH CATIONS WITH A SULFONIC ACID RESIN*

David C. Whitney and Richard M. Diamond

A study of the elution behavior of the alkali metal cations from a sulfonic acid cation-exchange resin (Dowex-50) has been reported previously.¹ Similar studies are reported here for trace concentrations of Be, Ca, and Ba in HClO₄, HCl, and HNO₃ solutions ranging in concentration from 0.1 to 10 M. In dilute acid solutions the normal elution order is found, and the distribution ratios decrease as expected from the mass-action effect. As in the previous paper, the order is explained as resulting from the competition of the water molecules, the resin sulfonate anions, and the macro-anions in the dilute external phase to solvate the cations; that cation most in need of solvation goes to the phase providing the best solvation and forces the remaining cation into the other phase. In the systems discussed here, the driving force for the exchange seems to be the aqueous-phase hydration of the smaller cation, and not any special interactions in the resin phase.

With concentrated solutions an increase in the value of the distribution ratio with increasing

acid concentration occurs in certain cases, leading to an inversion in the elution order of the ions. These results are interpreted in terms of the increase in resin invasion by nonexchange electrolyte, the decrease in water activity and hence the ability of water molecules to compete for solvating the cations, and the increase in the importance of cation-anion interactions. The higher charge, and charge density, of the alkaline earth ions over the alkalis makes the first and last factors more important for the former ions. Thus, the higher charge of the alkaline earths than of the alkalis contributes to much stronger cation-resin anion interactions, and leads to steep increases in the distribution ratios for some of the alkaline earth ions with increasing (high) acid concentrations. But very small cations such as Be hold onto their primary hydration shell as well as the hydronium ion, even in the concentrated acid solutions, and so do not show the large increases in distribution ratios.

The only major anomaly observed was with nitric acid elutions; apparently nitrate ion interacts with the cations, but does so more strongly the larger the cation.

*Brief form of UCRL-10984, Oct. 1963.

1. D. C. Whitney and R. M. Diamond, *Inorg. Chem.* **2**, 1284 (1963).

13. THE EXTRACTION OF ACIDS BY BASIC ORGANIC SOLVENTS. IV.
 TRIBUTYL PHOSPHATE AND TRIOCTYL PHOSPHINE OXIDE-- HAuCl_4 AND HAuBr_4 *

Mab I. Tocher, David C. Whitney, and Richard M. Diamond

Previous studies^{1,2} on the nature of the extracting species from aqueous HClO_4 and HBr solutions into dilute solutions of tributylphosphate (TBP) in CCl_4 have been extended to the extraction of tracer amounts of the strong metalloacids HAuCl_4 and HAuBr_4 from aqueous solutions of the corresponding hydrohalic acids. Dilute solutions of TBP in xylene, CCl_4 , and iso-

* Brief form of a paper (of the same title) accepted for publication in *J. Phys. Chem.* (UCRL-10912, 1963).

1. D. C. Whitney and R. M. Diamond, *J. Phys. Chem.* 67, 209 (1963).

2. D. C. Whitney and R. M. Diamond, *J. Phys. Chem.* 67, 2583 (1963).

octane and of trioctyl phosphine oxide (TOPO) in CCl_4 were used, and the number of organic extractant molecules per extracted species was determined in each case to be three. Such a trisolvated species is almost certainly analogous to the trisolvated hydronium species previously found for HClO_4 , HReO_4 , and HBr extracted into dilute TBP solutions, so that its formula can be written $\text{H}_3\text{O}^+ \cdot 3\text{R}_3\text{PO} \cdot y\text{H}_2\text{O} \cdot \dots \text{AuX}_4^-$, even though the number of water molecules associated with the extracted complex was not determined for any of these gold acid systems. The large size of the AuCl_4^- and particularly of the AuBr_4^- anions is the principal reason for the superior extraction of these strong acids over the HClO_4 , HReO_4 , and HBr previously studied.

14. THE EXTRACTION OF TETRAALKYL AMMONIUM HYDROXIDES
 AND THE SOLVATION OF THE HYDROXIDE ION*

Bharat R. Agarwal and Richard M. Diamond

The nature of the solvation of the hydroxide ion has received relatively little attention compared with the discussions in the literature on the hydration of the hydronium ion, H_3O^+ . For the latter ion, the existence of three sites of partial positive charge (the protons) leads quite naturally to a model in which three water molecules are hydrogen-bonded tightly in the first hydration shell. Various considerations suggest that the hydroxide ion in aqueous solution also might hold a first shell of three water molecules by unusually strong hydrogen bonds and so be trisolvated, too. Ackermann, from a comparison of the specific heats of dilute solutions of strong acids and bases has suggested such a model,¹ and Frank has made a similar proposal on the basis of the similarity of the broad Raman bands of HCl and KOH solutions, the relation to each other of the single-ion partial molal entropies of H^+ and of OH^- , and the rates of proton transfer in acidic and basic solutions.²

* Brief form of a paper (of the same title), *J. Phys. Chem.* 67, 2985 (1963).

1. T. Ackermann, *Disc. Faraday Soc.* 24, 133 (1957).

2. H. S. Franck, Abstracts of Papers, IT, Division of Physical Chemistry, 140th meeting ACS, Chicago, Ill., Sept. 1961.

The present authors hoped that experimental verification of the trisolvation of the OH^- ion could be obtained from solvent extraction studies by a method similar to that used recently to investigate the solvation of the hydronium ion.^{3,4}

The extraction of tetrahexyl and tetrapentyl ammonium hydroxides into dilute solutions of alcohols in benzene and of tetrabutyl and tetrapropyl ammonium hydroxides into dilute solutions of alcohols in nitrobenzene was studied. The variation of the extraction into benzene as a function of the aqueous base concentration at a fixed alcohol concentration indicated that the extracting ions associate as ion pairs. The dependence of the extracting species on alcohol concentration at a fixed aqueous base concentration indicated that three molecules of alcohol are complexed by each extracted ion pair of the base. A similar study with a solution of benzyl alcohol in nitrobenzene of fixed concentration indicated that the extracted species in a solvent of such a high dielectric constant is in the form of two dissociated ions. The extractions of the

3. D. C. Whitney and R. M. Diamond, *J. Phys. Chem.* 67, 207 (1963).

4. D. C. Whitney and R. M. Diamond, *J. Phys. Chem.* 67, 2583 (1963).

smaller substituted ammonium bases into varying concentrations of alcohols in nitrobenzene also showed that three alcohol molecules are bound in the extracted hydroxide, as observed with the associated systems in benzene. It is suggested that the OH^- ion alone provides the three sites for hydrogen bonding to the alcohol molecules, and possible structures for the extracted species are shown in Fig. D. 14-1.

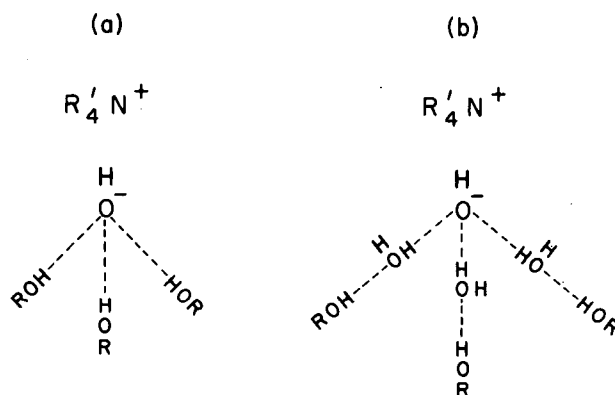


Fig. D. 14-1. Possible structure for the solvated hydroxide ion.

MU-31113

15. THE AQUEOUS SOLUTION BEHAVIOR OF LARGE UNIVALENT IONS: A NEW TYPE OF ION PAIRING*

Richard M. Diamond

For large, relatively unhydrated monovalent ions, a tightening of the surrounding water structure is a dominant feature of their aqueous solution behavior. As represented by their osmotic and activity coefficients, this corresponds to a rise in the coefficients above the Debye-Hückel limiting law, and the increase is larger, the larger the ion. Examples are the sodium salts of the fatty acids and the chloride salts of the tetraalkyl ammonium ions.

But if both the cation and anion of a salt are such large hydrophobic ions, the hydrogen-bonded water structure forces them together in order to maximize the water-water interactions and to minimize the disturbance to itself. This new type of ion pairing, which we shall call water structure-enforced ion pairing, has the opposite dependence on ionic charge and size to that of electrostatic (Bjerrum) ion pairing. The latter is least likely to occur in a solvent with as high a dielectric constant as water, and is greater the smaller and more highly charged the ions, while the former can occur only in water solutions (or other highly structured and hydrogen-bonded solvents), and is greater the larger and more lowly charged the ions. The resultant ion pairing leads to a negative correction to the osmotic and activity coefficients of large-ion salt solutions, and shows up experimentally in the dilute-solution osmotic coefficient sequence $\text{NMe}_4\text{I} > \text{NEt}_4\text{I} > \text{NPr}_4\text{I} > \dots$, all of whose coefficients fall below the values obtained accord-

ing to the Debye-Hückel limiting law.^{1, 2}

Such water structure-enforced ion pairing may also be the explanation, or part of the explanation, for the phenomenon of hydrotropism, the "salting in" of neutral molecules in water that occurs with electrolytes containing large ions, either cations or anions.^{3, 4} This type of ion pairing almost certainly applies to the "salting in" observed in the extraction of strong acids containing large anions, such as FeCl_4^- , AuCl_4^- , InBr_4^- , etc., into low-dielectric-constant basic organic solvents when the hydrohalic acid in the aqueous phase is gradually replaced by the cesium or tetraalkyl ammonium halide.⁵ It may well also be the explanation for the phenomenon that although the selectivity of strong-base anion-exchange resins for halide ions decreases with decreasing cross-linking of the resins, the decrease is far less than would be expected in comparison with the drop to zero selectivity observed with a corresponding series of sulfonic acid cation-exchange resins and the alkali ions.⁶

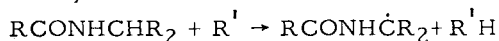
1. J. Lange, Z. Physik. Chem. 168A, 147 (1934).
2. S. Lindenbaum, private communication, Aug. 1963.
3. C. Neuberg, Biochem. Z. 76, 107 (1916).
4. F. A. Long and W. F. McDevit, Chem. Revs. 51, 119 (1952).
5. R. M. Diamond, J. Phys. Chem. 63, 659 (1959).
6. G. E. Boyd, S. Lindenbaum, and G. E. Myers, J. Phys. Chem. 65, 577 (1961).

* Extract from J. Phys. Chem. 67, 2513 (1963).

16. RADIATION CHEMISTRY OF PEPTIDES: γ -RAY-INDUCED OXIDATION OF POLY-L-GLUTAMIC ACID IN AQUEOUS SOLUTION*

Harvey A. Sokol, Winifred Bennett, and Warren M. Garrison

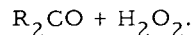
A radiation-chemical property of peptides is susceptibility to radical attack via



[Garrison, Jayko, and Bennett, Radiation Res. 16, 483 (1962)]. In aqueous solutions containing oxygen as a second solute, the yield of $\text{RCONH}\dot{\text{C}}\text{R}_2$ radicals formed by OH attack may be determined through measurement of ammonia and carbonyl function liberated on mild hydrolysis of the irradiated solution. The overall reaction including the hydrolysis step is given by

$$\text{RCONHCHR}_2 + \text{O}_2 + 2\text{H}_2\text{O} \xrightarrow{\gamma} \text{RCOOH} + \text{NH}_3 +$$

* Abstract of paper prepared for the 12th Annual Meeting of the Radiation Research Society, Miami Beach, Florida, May 18-20, 1964.



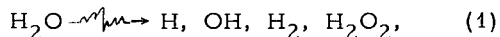
The 100-eV yield of this reaction in the radiolysis of a particular peptide system depends of course on the relative reactivities of other substituent groups and linkages in the molecule.

We have studied the γ -ray-induced oxidation of poly-L-glutamic acid in dilute aqueous solution and find that the C-H bond of the peptide chain represents a major locus of OH attack over the pH range 3 to 9. At pH 6.5 for example, we find $G(\text{NH}_3) \approx G(\text{R}_2\text{CO}) \approx 2.3$. Chromatographic analysis of the carbonyl fraction shows α -keto-glutaric acid to be a major component. Detailed effects of pH on the radiation-induced reactions are described in terms of the degree of ionization and the conformation of the poly-L-glutamic acid.

17. REACTIONS OF ORGANO-NITROGEN COMPOUNDS WITH THE OXIDIZING AND REDUCING SPECIES FORMED IN WATER RADIOLYSIS: REACTIONS OF ALANINE*

Boyd M. Weeks, Sibyl A. Cole, and Warren M. Garrison

The earliest chemically detectable products of water radiolysis have been represented by

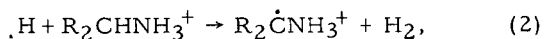


where H and OH correspond to the reactive intermediates available for reaction with solutes in the bulk of the solution and H_2 and H_2O_2 represent the molecular products formed within the spur.¹ For γ rays the 100-eV yields are $G_{\text{H}} = 2.9$, $G_{\text{OH}} = 2.4$, $G_{\text{H}_2} = 0.45$, and $G_{\text{H}_2\text{O}_2} = 0.71$.

Now, one of the characteristic features of the radiolysis of aqueous solutions of the simpler α -amino acids at decimolar concentrations in oxygen-free solutions is that the experimentally observed values of $G(\text{NH}_3)$ under most conditions of pH are considerably greater than the

yield of either the reducing or oxidizing intermediate formed in the primary Reaction (1).²

To explain those observations and to account for the stoichiometry involved in the formation of other products, we proposed several years ago³ that the radiation chemistry of aqueous amino acids and amines generally was consistent with the following mechanism, assuming Reaction (1) to be the primary process,



followed by

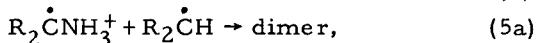
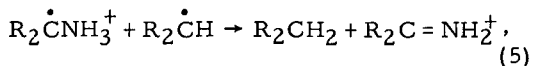
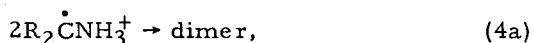


* Condensed version of paper in preparation for J. Phys. Chem.

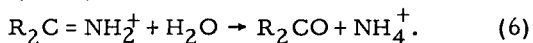
1. A. O. Allen, The Radiation Chemistry of Water and Aqueous Solutions (D. Van Nostrand, Company, Inc., New York, 1964).

2. A. J. Swallow, Radiation Chemistry of Organic Compounds (Pergamon Press, Inc., New York, 1960).

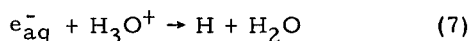
3. B. M. Weeks and W. M. Garrison, Radiation Res. 9, 291 (1958).



and the hydrolysis



Quite recently, however, it has been shown that the H atom which is indicated as a primary product in Eq. (1) is in fact a secondary product derived from the reaction of a proton with a negatively charged precursor.⁴ This precursor has been shown to have the properties of a solvated electron and to react with the proton via⁵

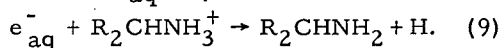


with a rate constant of $\approx 2 \times 10^{10} \text{ M}^{-1} \text{ sec}^{-1}$. Conversion of e_{aq}^- to H is not specific to the H_3O^+ ion. Inorganic acids in general appear to be effective in this regard, and the relative rates of such conversion by a number of inorganic acids have been shown to correlate with the pH values of those acids as implied by the Brønsted acid catalysis law.⁶ The ammonia ion as a very weak acid is relatively inefficient in the conversion⁶



with $k_8 \approx 10^4 \text{ M}^{-1} \text{ sec}^{-1}$.

These developments, of course, immediately raise a question as to the nature of the reactions of e_{aq}^- in neutral solutions of the amino acids that would be stoichiometrically equivalent to Reactions (2) and (2a). One possibility is that the zwitterion form of the amino acid reacts as a proton donor with e_{aq}^- to yield H:



However, in a recent re-interpretation⁷ of the available literature on the radiation chemistry of nitrogen compounds in aqueous solution, it was shown that the data on the radiation-induced reactions of the monosubstitution products of ammonia--both organic and inorganic--are not consistent with the concept that species of the

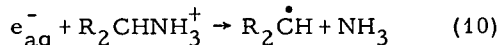
4. G. Czapski and H. A. Schwarz, *J. Phys. Chem.* **66**, 471 (1962).

5. E. S. Hart and J. W. Boag, *J. Am. Chem. Soc.* **84**, 4090 (1962).

6. J. Jortner, M. Ottolenghi, J. Rabani, and G. Stein, *J. Chem. Phys.* **37**, 2488 (1962).

7. W. M. Garrison, *Actions of Ionizing Radiations on Nitrogen Compounds in Aqueous Media*, presented at Conference on Basic Mechanisms in the Radiation Chemistry of Aqueous Media, Gatlinburg, Tenn., May 8-10, 1963, Radiation Research, in Press (UCRL-10827, May 1963).

type RNH_3^+ react with e_{aq}^- simply to produce H via Step (9). Consideration of the published data on the effects of pH on the course of radiolysis in solutions of ammonia derivatives indicated rather that reductive cleavage reactions of the type



are involved and that such reaction may be fast compared with reactions of $R_2CHNH_3^+$ species as proton donors. We report experimental evidence for the occurrence of Reaction (10) as a major process in the γ -ray radiolysis of aqueous solutions of alanine.⁸

Experimental Procedure

Major degradation products formed in the γ -ray irradiation of oxygen-free solutions of alanine include ammonia, pyruvic acid (plus acetaldehyde), propionic acid, and hydrogen. Higher-molecular-weight products are also formed but in low yield.

Solutions were irradiated in evacuated Pyrex ampoules with Co^{60} γ rays at a dose rate of either $\approx 6 \times 10^{16} \text{ eV/ml/min}$ or $1.5 \times 10^{18} \text{ eV/ml/min}$. Radiometric techniques were employed in the detection and quantitative determination of organic products in solutions containing C^{14} -labeled alanine. Carbonyl products were also determined as the 2,4-dinitrophenyl hydrazones.

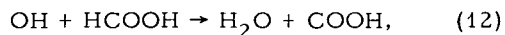
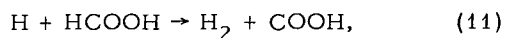
Product compounds containing nitrogen were examined chromatographically on Dowex-50. Organic acids were analyzed by methods of partition chromatography on silicic acid. The Conway diffusion method was used to separate ammonia, which was then assayed by means of the Nessler reaction. Details of the analytical methods and irradiation procedures have been given.³

Results and Discussion

We consider first the nature of the γ -ray-induced reactions in neutral solutions of the alanine zwitterion. Now, if the NH_3^+ group of the zwitterion is reacting with e_{aq}^- simply as a proton donor to yield H, then, addition of a second solute known to be an effective scavenger of H (and OH) radicals might be expected to lead to a pronounced decrease in $G(NH_3)$ with increasing scavenger concentration. We have found the formate ion useful in this regard,⁹ since it reacts rapidly with both H and OH,⁹

8. Some preliminary results of this study are discussed briefly in reference 7.

9. E. J. Hart, *Radiation Yields and Reactions in Dilute Solutions*, presented at Conference on Basic Mechanisms in the Radiation Chemistry of Aqueous Media, Gatlinburg, Tenn., May 8-10, 1963, *Radiation Res.*, in Press.

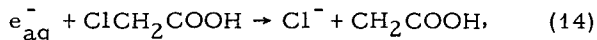


with $k_{11} \approx 2 \times 10^8 \text{ M}^{-1} \text{ sec}^{-1}$, $k_{12} \approx 10^9 \text{ M}^{-1} \text{ sec}^{-1}$, and relatively slowly with e_{aq}^- ,



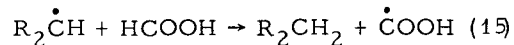
with $k_{13} < 10^5 \text{ M}^{-1} \text{ sec}^{-1}$. Irradiation of neutral 1.0 M alanine solutions containing increasing concentrations of added formate leads to a sharp decrease in the ammonia yield to give $G(\text{NH}_3) \approx 2.8$ at a scavenger concentration of 0.05 M. The yield curve begins to level off above 0.1 M and remains essentially constant at $G(\text{NH}_3) \approx 2.5$ as the formate concentration is increased to values as high as 1.0 M. The pyruvic acid yield also decreases and its formation is completely quenched at a formic acid concentration of 0.25 M. In contrast, the propionic acid yield shows no decrease with increasing formate concentration up to a value of at least 1.0 M.

These results are consistent with the view that the alanine zwitterion reacts with e_{aq}^- directly to give ammonia and the radical of propionic acid, according to Eq. (10). Additional evidence for this conclusion is obtained from studies of the effects of added chloracetate which, unlike formate, is extremely reactive towards

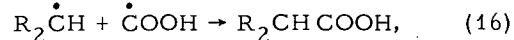


with $k_{14} \approx 10^{10} \text{ M}^{-1} \text{ sec}^{-1}$. Now, in 1 M alanine containing 0.25 M formate the removal of e_{aq}^- via Reaction (10) represents a principal source of both ammonia and propionic acid, and it has been shown that the reaction is not influenced by formate concentrations as high as 1.0 M. However, the presence of 0.1 M chloracetate in the 1.0 M alanine-0.25 M formate system reduces the yield of both ammonia and propionic acid by about 80%. From the initial slope of the concentration-yield plots we estimate that the velocity constant for the reaction of e_{aq}^- with the alanine zwitterion via Step (10) is approximately $k_{10} \approx 10^8 \text{ M}^{-1} \text{ sec}^{-1}$.

Reactions (10) and (3), then, are taken to represent the principal paths for removal of e_{aq}^- and OH respectively in neutral solutions. Subsequent steps leading to formation of propionic acid, pyruvic acid, and additional ammonia correspond to (4) and (5). In the presence of added formate, Reaction (3) is replaced by (12) and Reaction (5) by



or



or both. Examination of the proposed reaction scheme shows that the difference,

$G(\text{NH}_3) - G(\text{R}_2\text{CO})$, provides a direct measure of electron capture by the amino acid.¹⁰ In the neutral pH range there is no competing reaction for removal of e_{aq}^- , so we have

$$G(\text{NH}_3) - G(\text{R}_2\text{CO}) \approx G(e_{\text{aq}}^-).$$

The effect of added formate is to make $G(\text{R}_2\text{CO}) \approx 0$, so under those conditions

$$G(\text{NH}_3) \approx G(e_{\text{aq}}^-). \quad (17)$$

Consider now the effects of increasing acid concentration on the course of the radiolysis.

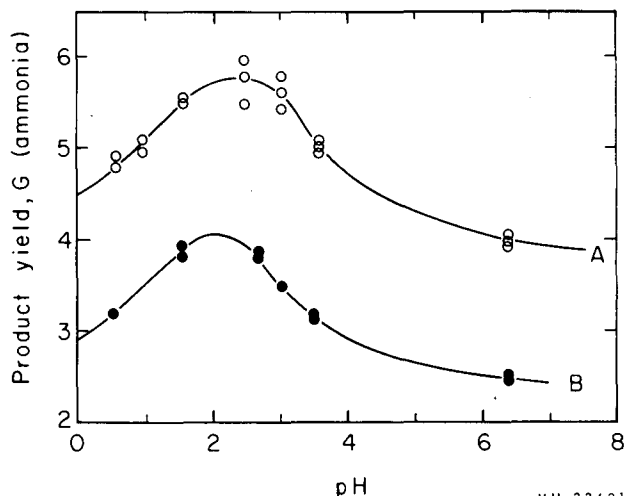


Fig. D.17-1. Yield of ammonia as a function of pH for (A), 1.0 M alanine, (B) 1.0 M alanine-0.25 M formic acid.

Figure D.17-1, curves A and B give ammonia yields as a function of pH for 1.0 M alanine and in 1.0 M alanine-0.25 M formic acid respectively. In both cases, the ammonia yields increase with decreasing pH, reach a maximum with pH range ≈ 2.5 , and then decline as the pH is reduced further to the lowest pH values. The occurrence of this maximum at pH 2.5 for the major degradation products is of particular interest in that a change in acid concentration from pH 7 to lower pH values would be expected to result in an increase in the relative importance of Reaction (7) over (10) with a resultant decrease in $G(\text{NH}_3)$. This follows since reaction of H with the amino acid in the absence of added scavenger ultimately yields 0.5 molecules of

10. We are assuming here that any conversion of e_{aq}^- to H via reaction 9 is in low yield. Hydrogen yields from aqueous alanine indicate that H-atom production via Reaction (9) corresponds to a G value of < 0.5 . Equation (17) does not involve any assumptions regarding H-atom production via (9).

ammonia whereas reaction of e^- yields 1.5. Of course, this conclusion regarding the predicted effect of pH on $G(\text{NH}_3)$ is predicated on the assumption that the velocity constant for reaction of e_{aq}^- with the amino acid is the same for both the cation and anion forms. In this regard, we note (Fig. D. 17-2) that the yield of propionic acid also reaches a maximum in the pH range ≈ 2.5 , and--as has been shown elsewhere--so does the pyruvic acid yield.¹¹ Since, at pH 7, the alanine zwitterion at a concentration of 1 M removes all e_{aq}^- and all species outside the spur column, as evidenced by the concentration-yield curves, we conclude that the increase in product yields that occurs in the pH range 5 to 2.5 results from a more efficient scavenging from within the spur of e_{aq}^- (and OH) by the cation form. The yields then decrease with decreasing pH below 2.5, since it is only in the more acid solutions that H_3O^+ competes effectively with 1.0 M alanine in the cation form for e_{aq}^- . We estimate very roughly from the data of Fig. D. 17-2 that $k_{10}/k_7 \approx 0.3$.

We thank Miss Harriet Leong and Mr. Harvey A. Sokol for assistance in product analysis.

11. N. E. Sharpless, A. E. Blair, and C. R. Maxwell, *Radiation Res.* 3, 417 (1955).

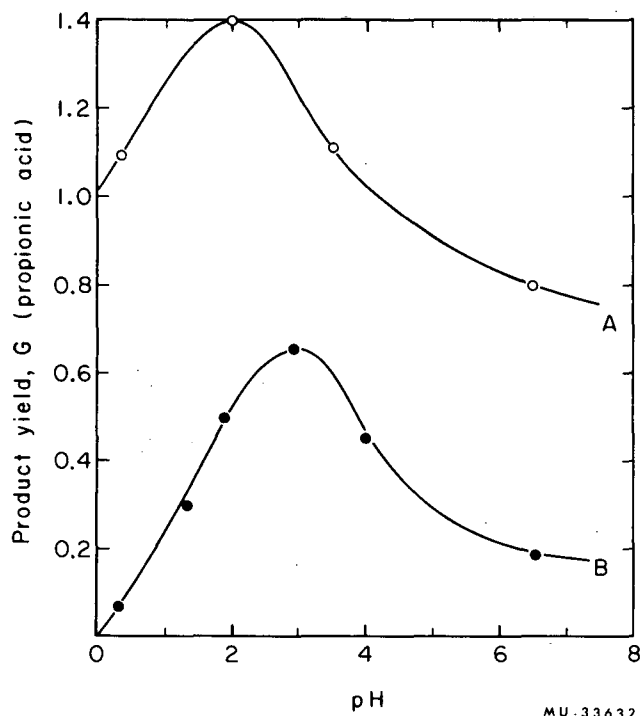


Fig. D.17-2. Yield of propionic acid as a function of pH for (A) 1.0 M alanine, (B) 0.1 M alanine.

18. A METASTABLE STATE OF THE DOUBLY CHARGED CARBON DIOXIDE ION*

Amos S. Newton and A. F. Sciamanna

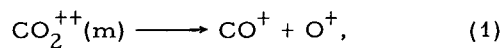
A metastable state of CO_2^{++} dissociating into CO^+ and O^+ has been studied, the half life measured, and the corresponding metastable peaks observed. The appearance potentials and fragmentation of normal and isotopically enriched CO_2^{++} have been studied.

The mass spectrometer used was a Consolidated Electrodynamics Corp. Model 21-103A. Isotopically enriched CO_2 ($\approx 58\% \text{ }^{18}\text{O}$) was prepared by reaction of C_2N_2 and O_2 and purified.

The voltage discrimination curves of CO_2^{++} and Ar^{++} show that while that of Ar^{++} was almost flat, that of CO_2^{++} increased by almost 20% when the accelerating voltage (V_a) was changed from 300 to 3800 volts. Subtraction of the curves after normalization of the Ar^{++} ion currents yields a straight-line semilog plot. Conversion of the abscissa from a voltage scale to

a time scale (time of formation to collection) gives a half life of $2.3 \pm 0.2 \mu\text{sec}$ for the metastable ion of CO_2^{++} , as shown in Fig. D. 18-1.

The decay scheme of the metastable state of CO_2^{++} is shown to be



and according to the generalized metastable transition equation the apparent mass $(M/q)^*$ of the product ions is given by

$$(M/q)^* = (M_f/q_f)^2 / (M_i/q_i). \quad (2)$$

Calculations using Eq. (2) show that in Reaction (1) the metastable ions should appear at apparent masses of 35.6 for CO^+ and 11.6 for O^+ . Figures D. 18-2 and D. 18-3 respectively show broad peaks at about masses 11.6 and 35.6. No other metastable peaks were seen.

* Brief version of paper in *J. Chem. Phys.* 40, 718 (1964).

The metastable suppressor voltage (V_{mss})

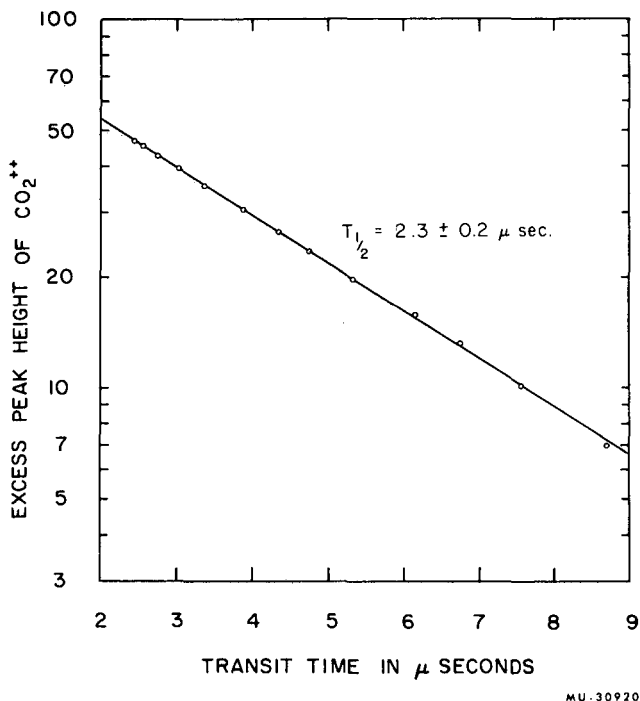


Fig. D. 18-1. Decay of $\text{CO}_2^{++}(\text{m})$ in transit from formation in ion source to collector.

required for cutoff of metastable peaks is a measure of the kinetic energy of these ions, and is given by

$$V_{\text{mss}} = \frac{V_a (M/q)^*}{(M_f/q_f)} = \frac{V_a (M_f/q_f)}{(M_i/q_i)} \quad (3)$$

Calculations with Eq. (3) show that the mass 11.6 peak should be cut off at 72% of V_a , while the mass 35.6 peak requires 127% V_a for cutoff. In Fig. D. 18-2, run B, at a normal V_{mss} setting of 1.6% above V_a , the mass 11.6 peak is eliminated. In Fig. D. 18-3 examples B and C show that even at the maximum setting of the metastable suppressor (4.8% above the V_a), there is no effect on the mass 35.6 peak. A metastable peak can have a higher kinetic energy than its parent ion only when the fragment ion is of higher M/q than the parent ion.

Studies on the effect of pressure on the metastable peaks at masses 11.6 and 35.6 show their respective peak heights to be linear with pressure, hence both arise from a unimolecular process. The width of the metastable peak is caused by charge repulsion of the fragments on separation. From the change in peak width with change in accelerating voltage--i. e., transit time--the kinetic energy of these ions has been calculated and is shown in Table D. 18-I. The calculated energy for each ion results in good

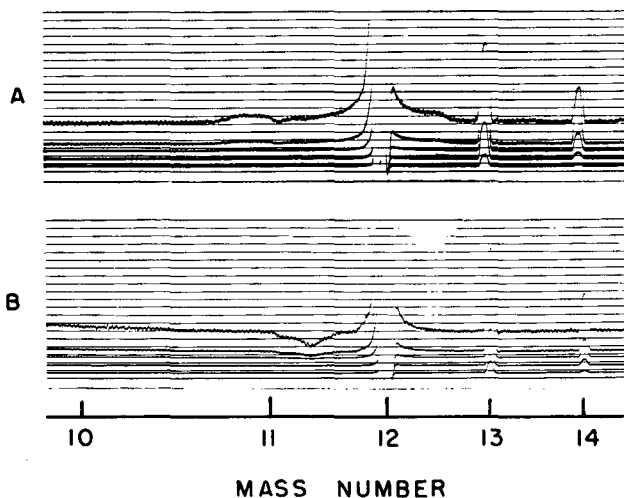


Fig. D. 18-2. Metastable peak from $\text{CO}_2^{++}(\text{m})$ at $(M/q)^* = 11.6$, scanned at $MV_a = 38\,000$, $400\ \mu$ pressure CO_2 , nominal $V_i = 70\ \text{V}$: A, Metastable suppressor grounded, B, Metastable suppressor at $1.016\ V_a$.

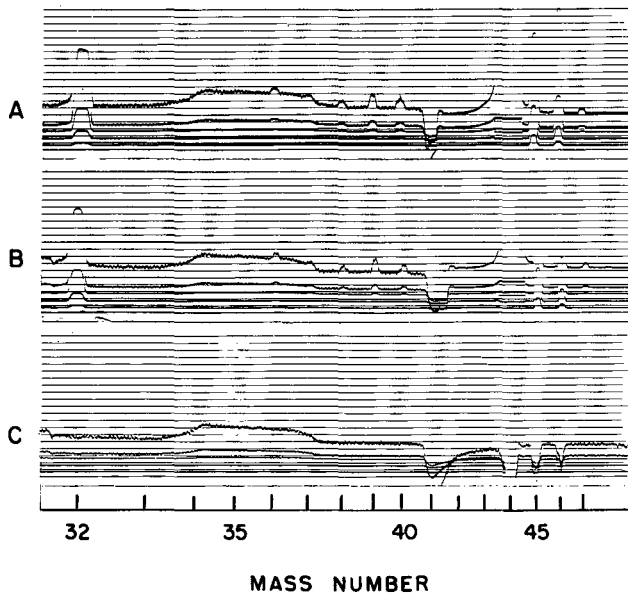


Fig. D. 18-3. Metastable peak from $\text{CO}_2^{++}(\text{m})$ at $(M/q)^* = 35.6$, scanned at $MV_a = 121\,600$, $400\ \mu$ CO_2 , nominal $V_i = 70\ \text{V}$. Galvanometers off at $M/q = 44$ in A and B, A, Metastable suppressor grounded, B, Metastable suppressor at $1.016\ V_a$, C, Metastable suppressor at $1.048\ V_a$.

Table D. 18-I. Fragmentation energy and charge separation in $\text{CO}_2^{++}(\text{m})$.

	MV_a	W Peak width (mass units)	ΔW	Calculated K E (eV)
Mass 11.6	38 000	1.8 ₆	1.6 ₄	1.7 ₂
	11 310	3.5 ₀		
Mass 35.6	121 600	4.1 ₀	2.5 ₀	1.0 ₀
	38 400	6.6 ₀		
Observed total K. E.				2.7 ₂ eV
Calculated total KE				
(1) from O^+ ion = 2.70 eV,				
(2) from CO^+ ion = 2.75 eV.				
Charge separation from KE of fragments = 5.3 Å.				

agreement of the total KE and corresponds to a charge separation of 5.3 Å. This is a reasonable value if the charges at fragmentation are located on the oxygen atoms, since it is only slightly greater than twice the normal bond distance between the oxygen atoms in the carbon dioxide molecule.

Appearance potential (A. P.) curves of CO_2^{++} have been run at various accelerating voltages from 1000 to 3000 volts, in each case comparing them to Kr^{++} standard. The formation of the metastable state could not be detected on the A. P. curves, which appear identical. An A. P. of 38.0 ± 0.2 volts compared to Kr^{++} at 38.56 volts was found.¹

1. F. H. Field and J. L. Franklin, *Electron Impact Phenomena* (Academic Press, Inc., New York, 1957,) p.245.

In the three isotopically labeled species, $\text{C}^{16}\text{O}^{16}\text{O}^{++}$, $\text{C}^{16}\text{O}^{18}\text{O}^{++}$, and $\text{C}^{18}\text{O}^{18}\text{O}^{++}$, the unsymmetrical ion has about 5% lower yield than the doubly charged ion of either of the symmetrical molecules.² The ionization efficiency curves of the doubly charged ions of all three species extrapolate to the same value of the A. P., and the curve for $M/q = 23$ shows no characteristics suggesting the increased dissociation of the unsymmetrical ion. The metastable ions of each isotopic composition all show the same half life and relative initial yield. It is concluded that the isotope effect observed in the unsymmetrical isotopically substituted molecule arises from a state of CO_2^{++} which dissociates by a fast process, and is not connected with the metastable state of CO_2^{++} .

2. A. S. Newton, *J. Chem. Phys.* **20**, 1330 (1952).

19. EXCESS-KINETIC-ENERGY IONS IN ORGANIC MASS SPECTRA*

John A. Olmsted, III, K. Street, Jr., and Amos S. Newton

The characteristics of excess-kinetic-energy ions in mass spectra of organic compounds have been studied with a Dempster-type mass spectrometer (Consolidated 21-103A). The variations of collection efficiencies for ions with

excess kinetic energy were determined as a function of the following operating parameters: accelerating voltage, repeller voltage, and metastable suppressor voltage.

* A summary of work from UCRL-10687, UCRL-10823, UCRL-10823 Rev., and UCRL-10824, to be published, *J. Chem. Phys.*, April 1964.

From a survey of a large number of organic compounds containing many different substituent groups it was found that ion fragments possessing excess energy of between 1 and 3 eV were

formed from virtually all compounds upon impact of 50- to 70-volt electrons. Up to mass 40, the practical resolution limit of the spectrometer for ions with excess kinetic energy, virtually every ion that is formed by the fragmentation of the parent compound into two or more relatively heavy fragments (\geq mass 12) exhibits some excess-kinetic-energy component.

Resolution limitations of the mass spectrometer restricted definitive studies of such excess-kinetic-energy ions to ions of mass 20 or less. Since methyl ions of excess kinetic energy were found in the greatest abundance from most compounds, these were studied in detail.

By use of an improved modification of a method devised previously,^{1, 2} methyl ion kinetic energies were measured to ± 0.02 eV for a large variety of organic compounds. No correlation was found between the magnitudes of these energies and structural parameters, except that the kinetic energies generally decrease with increasing chain length. Virtually all the kinetic energies measured lie in the range of 1.75 to 3.5 eV.

Appearance potential curves obtained for several excess-kinetic-energy ions show a second-power dependence of cross section on electron energy in the threshold region, with threshold values of the order of 30 eV. A typical appearance potential curve, for the excess-kinetic-energy methyl ion from benzene, is shown in Fig. D.19-1. The appearance potentials of excess-kinetic-energy ions from several compounds are given in Table D.19-I.

The methyl ions observed in mass spectra

1. F. L. Mohler, B. H. Dibeler, and R. M. Reese, *J. Chem. Phys.* **22**, 394 (1954).
2. T. Tsuchiya, *Bull. Chem. Soc. Japan* **35**, 1221 (1962).

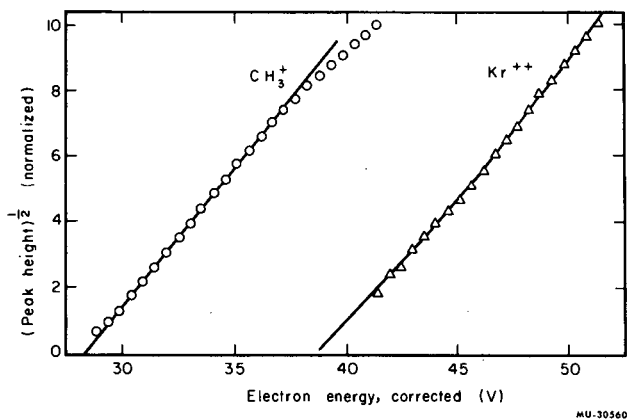


Fig. D.19-1. Ionization efficiency curves for Kr^{++} and excess-kinetic-energy CH_3^+ ions from a krypton-benzene mixture.

of organic compounds under standard spectrometer operating conditions consist of both thermal and high-energy ions. An experimental technique was devised for separating the observed methyl peak into its thermal and high-energy components. An equation, due to Berry,³ giving the discrimination factor of the mass spectrometer toward ions possessing excess kinetic energy was then applied to obtain values for the actual abundances of excess-kinetic-energy methyl ions in the fragmentations of several compounds by 70-V electrons. These actual abundances are shown in Table D.19-II. The extent to which Berry's equation predicts actual discrimination effects on ions of various kinetic energies as a function of mass spectrometer accelerating voltage is shown in Fig. D.19-2.

3. C. E. Berry, *Phys. Rev.* **78**, 597 (1950).

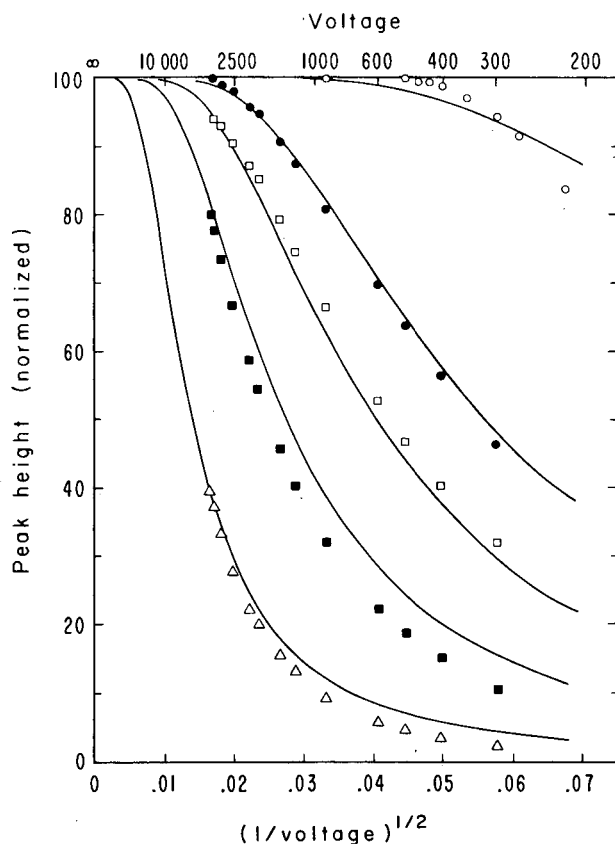


Fig. D.19-2. Comparison of theory with experiment: discrimination of the mass spectrometer against methyl ions of different kinetic energies (in eV), as a function of the accelerating voltage. Points are experimental; smooth curves are theoretical. The source compound for the methyl ions and the kinetic energies of the ions are as follows: O - CH_4 (thermal); ● - CH_3OH (0.14 eV); □ - CH_3Cl (0.27 eV); ■ - CH_3F (0.58 eV); ▲ - C_6H_6 (2.27 eV).

Table D. 19-I. Appearance potentials of excess-kinetic-energy ions

Compound	Ion	A. P.	Reference Ion
benzene	CH_3^+	28.2 ± 0.2	(a)
ethane	CH_3^+	30.3	Ne^+
propane	CH_3^+	30.8	Ne^+
propane	C_2H_3^+	30.8	(b)
n-butane	CH_3^+	29.7	Ne^+
isobutane	CH_3^+	29.4	Ne^+
n-pentane	C_2H_5^+	28.1	Ne^+
neopentane	CH_3^+	29.5	Ne^+
n-heptane	CH_3^+	27.9	Ne^+
n-heptane	C_2H_5^+	24.3	Ne^+
isopropyl chloride	CH_3^+	29.7	Ne^+
isopropyl alcohol	CH_3^+	30.2	Ne^+
benzene	C_2H_3^+	31.1	Ne^+
benzene	C_2H_2^+	32.6	Ne^+
deuterium	D^+	25.3	(c)

^aValue represents the average of four separate determinations using both Ne^+ and Kr^{++} as reference ions.

^bExcess kinetic energy CH_3^+ ion from propane used as a reference.

^cValue obtained from two separate determinations, one using the thermal D^+ ions from D_2 , the other the CH_3^+ ions from benzene, as references.

Table D. 19-II. Percentages of fragment ions of certain masses relative to total ions observed in mass spectra.

Compound	M/q	Thermal ion percentage	Observed excess K. E. ion percentage	Actual excess K. E. ion percentage (calculated) ^a
ethane	15	1.54	1.13	3.34
propane	15	1.10	1.79	5.42
n-butane	15	0.95	1.88	5.94
isobutane	15	1.41	2.39	7.99
n-pentane	15	0.77	1.30	4.47
neopentane	15	0.97	3.17	10.79
n-heptane	15	0.51	0.74	1.94
2, 4-dimethyl pentane	15	0.63	1.95	5.45
n-decane	15	0.22	0.36	0.93
benzene	15	<0.1	0.65	1.98
p-xylene	15	0.11	1.36	4.60
ethyl benzene	15	0.25	1.76	5.32
isopropyl chloride	15	1.30	1.50	5.09
isopropyl alcohol	15	3.66	2.34	7.78
n-heptane	29	8.25	1.08	5.18

^aTotal ion figures were corrected for excess-kinetic-energy ions before percentages were computed.

A more detailed study of the complementary excess-kinetic-energy ion pairs from methyl amine (masses 15 and 16) and propane (masses 15 and 27) was carried out in an attempt to determine the mechanism for excess-kinetic-energy ion formation. For both these compounds, the appearance potentials, momenta, and abundances of the respective complementary ions were the same within experimental error. This agreement indicates that in these two cases the complementary ions come from the same initial state. The data thus support the previous suggestion^{1,4} that excess-kinetic-energy fragment ions from organic compounds are formed by breakdown of doubly charged parent ions into two singly charged fragment ions.

Appearance potentials for excess-kinetic-energy methyl ions from other organic compounds indicate that, for these compounds also, doubly charged ions play a major role in the process of formation. If one assumes that in the higher hydrocarbons as in propane the heavier mass fragment breaks down further by eliminating a hydrogen molecule, then the appearance potentials that one calculates using tabulated appearance potentials for thermal fragment ions,⁵ the ionization potential of the methyl rad-

ical,⁶ and the minimum possible kinetic energy of the fragments agree reasonably with the measured appearance potential values, as is shown in Table D. 19-III.

The data obtained in this study indicate that from many compounds, a significant proportion of the total ions formed under bombardment by 70-V electrons possess excess kinetic energy. This proportion is high enough, we believe, to warrant consideration of the states that give rise to these ions in the breakdown scheme of any comprehensive theory of mass spectra that is based on impact by 70-V electrons.

In the applications of mass spectra to chemical systems undergoing reactions, the abundances of excess-kinetic-energy ions measured in this work may have considerable importance. Inasmuch as recent work of Giese and Maier has shown that ion kinetic energy can be effective in inducing endothermic chemical reactions,⁷ the possibility must be considered that excess-kinetic-energy ions play a significant role, through endothermic processes, in the chemical transformation of organic species under the influence of ionizing radiation.

4. A. Hustrulid, P. Kusch, and J. T. Tate, *Phys. Rev.* **54**, 1037 (1938).

5. F. H. Field and J. L. Franklin, *Electron Impact Phenomena* (Academic Press, New York, 1957), Appendix.

6. F. A. Elder, C. F. Giese, B. Steiner, and M. Inghram, *J. Chem. Phys.* **36**, 3292 (1962).

7. C. F. Giese and W. B. Maier, II, *J. Chem. Phys.* **39**, 197 (1963).

Table D. 19-III. Comparison of calculated with observed excess-kinetic-energy methyl ion appearance potentials.

Compound	A. P. Meas.	Total K. E. (calc.) ^a	A. P. for ^b complementary thermal ion	A. P. ^c calc.
ethane	30.3	4.90	13.95	28.65
propane	30.8	4.02	15.3	29.15
n-butane	29.7	3.35	13.15	26.3
isobutane	29.4	3.59	13.6	27.0
n-pentane	28.1	2.83	14.2	26.85
neopentane	29.5	3.42	14.9	28.1

^a Calculated from measured CH_3^+ ion energies assuming C-C bond cleavage occurs first and little or no kinetic energy is involved in H_2 elimination.

^b i. e. for process $\text{C}_n\text{H}_{2n+2}^{++} \longrightarrow \text{CH}_3^+ + \text{H}_2 + \text{C}_{n-1}\text{H}_{2n-3}^+ + 2e^-$ (values from ref. 15)

^c Assuming overall mechanism is $\text{C}_n\text{H}_{2n+2}^{++} \longrightarrow \text{CH}_3^+ + \text{H}_2 + \text{C}_{n-1}\text{H}_{2n-3}^+ + \text{K. E.}$

20. TRIPLE IONIZATION IN SMALL MOLECULES*

Amos S. Newton

Recently some triply charged ions of large aromatic molecules have been studied,^{1,2} but no triply charged ions of small molecules have previously been reported. The triply charged molecule ion, CS_2^{+++} , is shown to occur in the normal 70-volt mass spectrum of CS_2 with a

* Condensed version of paper in *J. Chem. Phys.* **40**, 607 (1964).

1. S. Meyerson and R. W. Vander Haar, *J. Chem. Phys.* **37**, 2458 (1962).

2. F. H. Dorman and J. D. Morrison, *J. Chem. Phys.* **35**, 575 (1961).

pattern factor of 0.07%. The appearance potentials of the ions CS_2^{++} and CS_2^{+++} were found to be 27.45 ± 0.2 and 53.6 ± 0.5 eV respectively.

Triply charged molecule ions of COS were also observed, but in low yield. No CO_2^{+++} was found. Another small molecule for which the triply charged molecule ion was observed was C_2N_2 . It is concluded that triply charged ions of small molecules can be stable if the molecule has a sufficient number of nonbonding or delocalized electrons. Resonance stabilization of the ion may be a factor in its stability.

21. MOLECULAR BEAM ELECTRIC RESONANCE EXPERIMENTS ON LiF, LiBr, LiI, AND NaF

Alvin J. Hebert, Francis W. Breivogel, Jr.,
Craig D. Hollowell, and Kenneth Street, Jr.

Introduction

The molecular beam electric resonance method has been used to investigate the molecular properties of several dipolar diatomic molecules, as described below. Data are reported for dipole moments μ_v , quadrupole coupling constants, $(eqQ)_v$, and spin rotation interaction constants, c , for molecules in different vibrational states, v , and in low rotational states.

Experimental Procedure

The apparatus and methods used in these investigations, discussed in detail elsewhere,¹ may be briefly described as follows:

The apparatus consists of a consecutive arrangement of four connecting high-vacuum chambers. The source chamber houses a 6-in.-long, 3/8-in.-diam tube of 0.015-in. wall thickness into which has been cut a 0.025×0.004-in. slit that defines the beam. The beam is produced by placing the desired salt in the tube and passing a few hundred amperes of ac current through it,

1. Alvin J. Hebert, *A Molecular Beam Electric Resonance Spectrometer and the Radio-Frequency Spectra of Lithium Fluoride* (Ph. D. Thesis), UCRL-10482, Sept. 1962.

thus heating the salt until vapor effuses through the slit at an adequate rate.

The effusing vapor passes out of the source chamber through a small opening into a buffer or separating chamber and then on through another small opening into the main chamber. The main chamber houses a beam collimator and hot-wire beam ionizer and accelerator as well as two 12-in.-long inhomogeneous electric deflecting fields of the dipole type for quantum state selection. The deflecting fields allow only the desired rotational and electric quantum states to reach the hot-wire ionizer-accelerator.

The main chamber also houses a homogeneous electric field region into which one may introduce radio-frequency or microwave signals to induce the desired electric quantum number or rotational quantum number transitions, respectively. The electric field in this 10-in.-long region is homogeneous to better than 2 parts in 10^5 .

The positive ions generated at the hot wire are accelerated out of the main chamber, through a 5-cm-radius 60° mass-analyzing magnet, and into the electron multiplier chamber,

where a 14-stage electron multiplier amplifies the positive ion current by approximately 10^6 . The electron multiplier output can be fed either into an electrometer with recorder output or into a pulse amplifier and counter with provision for digital recording and graphing.

Results

Lithium Fluoride

The $J = 1$ radio-frequency spectra observed for the three lowest vibrational states of Li^7F^{19} and the four lowest vibrational states of Li^6F^{19} are consistent with the following dipole moment expressions:

$$\text{Li}^6\text{F}^{19}: \mu_v = 6.28396 + 0.08630(v + 1/2) + 0.00054(v + 1/2)^2, \pm 0.001 \text{ Debye};$$

$$\text{Li}^7\text{F}^{19}: \mu_v = 6.28383 + 0.08153(v + 1/2) + 0.00045(v + 1/2)^2, \pm 0.001 \text{ Debye}.$$

The first number in each of the above expressions, and the dipole moments derivable therefrom, are accurate to $\pm 1 \times 10^{-3}$ Debye. This uncertainty is principally due to calibration limitations of present-day voltage standards and resistance bridges. In contrast, the coefficients of $(v + 1/2)$ and $(v + 1/2)^2$ in these expressions are accurate to $\pm 5 \times 10^{-5}$ Debye. This follows from our ability to measure the dipole moments of each of the first three or four vibrational states with a precision of better than 1 part in 10^5 .

Although the dipole moments calculated from the above Li^6F expression are in agreement with previously published values,² (± 0.001 Debye), the corresponding previous coefficient for $(v + 1/2)$ differs from ours by a factor of 3 times the combined experimental errors. Agreement for the coefficient of $(v + 1/2)^2$ is just within the combined errors.

The present results and stated errors are supported by the above experimentally determined expression for the dipole moment of Li^7F , in which the coefficient of $(v + 1/2)$ has the expected isotopic dependence³ well within our stated uncertainties.

Our hyperfine studies are nearing completion for the accurate determinations of $(eqQ)_v$, c_{Li} , and c_{F} for both isotopes and to determine whether or not there is an observable electron coupled spin-spin interaction in addition to the large magnetic spin-spin interaction in Li^7F^{19} .

2. Wharton, Klemperer, Gold, Strauch, Gallagher, and Derr, J. Chem. Phys. 38, 1203 (1963).

3. P. Schlier, Z. Physik 154, 460 (1959).

Lithium Bromide

The observation of $J = 1$ and $J = 2$ spectra for three or more vibrational states resulted in the following molecular constants:

$$\text{Li}^6\text{Br}^{81} \text{ and } \text{Li}^6\text{Br}^{79}:$$

$$\mu_v = 7.22571 + 0.08370(v + 1/2) + 0.00042(v + 1/2)^2, \pm 0.001 \text{ Debye}$$

$$\text{Li}^6\text{Br}^{79}:$$

$$\text{Bromine-79, } eqQ_v = 37.015 + 2.918(v + 1/2) - 0.039(v + 1/2)^2, \pm 0.005 \text{ Mc, } c_{\text{Br}} = 8.7 \pm 0.6 \text{ kc};$$

$$\text{Li}^6\text{Br}^{81}:$$

$$\text{Bromine-81, } eqQ_v = 30.912 + 2.442(v + 1/2) - 0.034(v + 1/2)^2, \pm 0.005 \text{ Mc, } c_{\text{Br}} = 9.5 \pm 0.6 \text{ kc}.$$

The coefficients of $(v + 1/2)$ and $(v + 1/2)^2$ in the expression for μ_v are accurate to ± 0.0001 Debye.

Lithium Iodide

The observation of $\text{Li}^6\text{I}^{127}$ spectra in the $J = 1$ rotational state and the $v = 0$ and $v = 1$ vibrational states give the following molecular constants:

	$v = 0$	$v = 1$
μ (Debye)	7.4286 ± 0.001	7.5131 ± 0.001
Iodine eqQ (Mc)	-198.782 ± 0.005	-207.430 ± 0.010
c_{I} (kc)	7.3 ± 0.6	7.3 ± 0.6

Sodium Fluoride

Observation of the first three vibrational states for the $J = 1$ rotational state of $\text{Na}^{23}\text{F}^{19}$ has yielded the following molecular constants:

$$\mu_v = 8.12282 + 0.06471(v + 1/2) + 0.00025(v + 1/2)^2 \pm 0.001 \text{ Debye,}$$

$$\text{Na}^{23}, eqQ_v = -8.494 + 0.113(v + 1/2) - 0.001(v + 1/2)^2 \pm 0.008 \text{ Mc,}$$

$$c_{\text{Na}} = 1.8 \pm 0.8 \text{ kc,}$$

$$c_{\text{F}} = 1.9 \pm 0.6 \text{ kc.}$$

Here the values for c_{Na} and c_{F} are somewhat preliminary, since further studies are in progress to determine these constants more accurately and also to discover whether an electron-coupled spin-spin interaction may be measurable.

The $J = 1 \rightarrow J = 0$ transition of $\text{Na}^{23}\text{F}^{19}$ has been used to check a recently completed micro-

wave system. The system has yielded approximately 10-kc-wide rotational transition lines at a frequency of approximately 26 kMc. The observed microwave transition frequencies for $v = 0$, $v = 1$, and $v = 2$ are in excellent agree-

ment with recent measurements made by Bauer and Lew.⁴

4. R. K. Bauer and J. Lew, *Can. J. Phys.* **41**, 1461 (1963).

22. ENERGY LEVELS OF AmIV IN LaCl₃ (*)

John G. Conway

To date an analysis of the solid-state spectrum of AmIV (3+ ion) has not been possible with the available absorption and fluorescence data. This is due to several reasons; one is that with a ground state of $J = 0$ and crystal symmetry of C_{3h} it is difficult to determine the J values.¹ A second difficulty is that in the actinide elements the LS coupling scheme is not followed and therefore one must perform rather detailed calculations in the intermediate coupling scheme before much of a guide to the spectrum can be obtained.²

The complete spin orbit matrices have now been calculated by Koster and Nielson;³ earlier incomplete matrices by Ofelt were useful.⁴

There is some question as to the assignments made by Gruber⁵ to the various infrared absorption peaks. A comparison between PuI and AmIV (both 5f⁶) did not give as close an agreement as might be expected.⁶ Furthermore, the selection rule of Ofelt indicates that Gruber should not have seen transitions between $J = 0$ and $J = 3$ or 5 .⁷ The $J = 0$ to $J = 1$ is a magnetic

dipole transition and is expected to be weak.

This work was undertaken in an attempt to better understand some of these discrepancies and if possible assign some of the upper levels of AmIV.

The method chosen to study the low levels of AmIV was that of "selective excitation," where narrow band widths of light are used to excite fluorescence to low levels.⁸ Near-infrared absorption experiments are used to obtain the higher levels of the ground multiplet.

Experimental Procedure

For the selective-excitation experiments a 100-W Hg arc (AH6) was mounted in the source compartment of a Beckman DU monochromator with the output incident on the americium crystal mounted in a quartz Dewar filled with liquid nitrogen. The crystal was imaged on the slit of an $f/6.3$ spectrograph. Exposures from 0.5 hour to several days were taken throughout the photographic range. The crystal is the same one used by Gruber and Conway.⁹

The fluorescence emitted by the crystal brightens as the wave length of the exciting light coincides with the absorption peaks of the americium ion. There is a self-luminescence to the crystal which is excited by the energy of the radioactive decay. Any spectrum, is, therefore, a mixture of both the selectively excited and self-luminescence emissions.

Results

Data may be found in the original article (UCRL-11099). Calculations were made by using the spin orbit matrices of Koster and Nielson.³ The calculations were made with 5f hydrogenic

8. F. Varsanyi and G. H. Dieke, *J. Chem. Phys.* **31**, 1066 (1959).

9. J. B. Gruber and J. G. Conway, *J. Chem. Phys.* **36**, 191 (1962).

* Short version of paper (UCRL-11099, Nov. 1963), submitted to *J. Chem. Phys.*

1. E. V. Sayre and S. Freed, *J. Chem. Phys.* **24**, 1211 (1956).

2. J. B. Gruber and J. G. Conway, *J. Chem. Phys.* **34**, 632 (1961).

3. Dr. C. W. Nielson has kindly sent us a tape containing these matrices, entitled, "Energy Matrices for All Configurations of Equivalent f Electrons," by G. F. Koster and C. W. Nielson, Solid State and Molecular Theory Group, Massachusetts Institute of Technology, Cambridge, Massachusetts.

4. G. S. Ofelt, Ph.D. Thesis, The Johns Hopkins University, 1962.

5. J. B. Gruber, *J. Chem. Phys.* **35**, 2186 (1961).

6. J. Blaise, M. Fred, S. Gerstenkorn, and B. Judd, *Compt. Rend.* **255**, 2403 (1962).

7. G. S. Ofelt, *J. Chem. Phys.* **37**, 511 (1962); B. R. Judd, *Phys. Rev.* **127**, 750 (1962).

wave functions and were carried out using the form E/F_2 instead of energy, and $\chi (= \zeta/F_2)$ instead of ζ . In this form the results are more easily applied to other $5f^6$ cases. Figure D. 22-1 is a plot of these results between χ of 9 and 10. It is possible on a plot of this nature to incorporate the data for PuI and AmIV. These calculations for PuI are an improvement over the previously published values, since the matrices now include singlets. Table III (of the original paper) includes the calculations for energy and g value for PuI. The calculations for AmIV are for values $F_2 = 268 \text{ cm}^{-1}$ and $\zeta = 2605 \text{ cm}^{-1}$; the PuI values are $F_2 = 230.6 \text{ cm}^{-1}$ and $\zeta = 2174.6 \text{ cm}^{-1}$.

Once the fit to hydrogenic values was obtained it was decided to vary the wave-function parameters and to see if it would be possible to obtain a new wave function that would better define the data.

Before undertaking a study of the crystal-field parameters more accurate measurements will be attempted on both the absorption and fluorescence.

ACKNOWLEDGMENTS

I wish to thank Miss Mary Buchley of the Vallejo Junior College (Vallejo, California) for her help with the selective excitation experiments, and Thomas P. Clements for help with the fitting program.

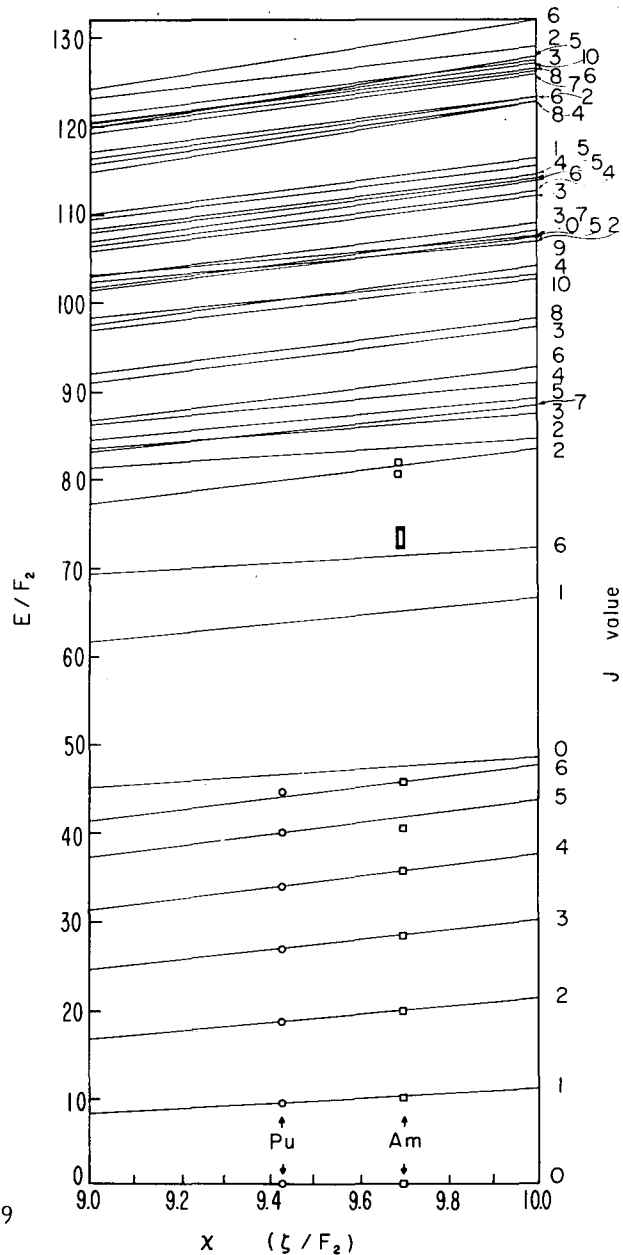


Fig. D. 22-1. Plot of E/F_2 vs χ between $\chi = 9$ and 10. The circles are for PuI and the squares and rectangle for AmIV.

23. SELF-LUMINESCENCE SPECTRUM OF $Bk^{3+}(5f^8)^{(*)}$

Ralph G. Gutmacher, E. Kenneth Hulet, Earl F. Worden, and John G. Conway

The self-luminescence spectrum of $Bk^{3+}(5f^8)$ in $LaCl_3$ has been observed between 3000 and 9000 Å. A crystal containing 5 µg of

^{249}Bk in 3 mg of $LaCl_3$ was used. The experimental details are briefly discussed. Several strong groupings were seen with clearly defined crystal-field splitting. A spin-orbit calculation has been made to determine the location of the low-lying energy levels for the configuration $5f^8$, using 5f hydrogenic wavefunctions. The experimental results are compared with theory.

*Abstract of talk to Optical Society of America; April 1963, abstract appears in J. Opt. Soc. Am. 53, 506 (1963).

24. USE OF ELECTRODELESS DISCHARGE LAMPS IN THE ANALYSIS OF ATOMIC SPECTRA*

John G. Conway, Earl F. Worden, and Ralph G. Gutmacher

Abstract

The use of electrodeless discharge lamps as light sources in the study of atomic spectra of lanthanides and actinides is described, and illustrated with elements ^{96}Cm and ^{64}Gd . It is shown how differentiation of the first and second spectra, self-reversal, and Zeeman-effect observations may be obtained. These methods have been used successfully on a number of lanthanide and actinide elements by ourselves and by other investigators. Although we have confined our discussion to the study of lanthanide and actinide spectra, for which electrodeless discharge lamps are especially advantageous, these procedures should be generally applicable to other elements as well.

spectra. In addition, many of them (particularly the heavier actinides) are either available in limited amounts or highly radioactive or both. For these reasons, an intense source that emits sharp lines and is highly efficient, and in which these elements are completely contained at all times, is preferred. The electrodeless discharge lamp, which meets all these requirements, has become the source of choice for the study of lanthanide and actinide atomic spectra.⁵ The other advantages of these lamps have been comprehensively summarized by Meggers.¹

The great need for increased spectroscopic investigation of the lanthanide and actinide elements has been pointed out by Meggers¹ and Moore²⁻⁴ in their periodic status reports. These elements exhibit exceedingly complex

The essential data needed for the analysis of a complex spectrum, besides an accurate, complete line list, are: (a) classification of the spectral lines as belonging to the neutral or ionized atom; (b) identification of resonance lines and other lines arising from transitions to low-lying levels of the atom, which may be derived from self-reversal; and (c) observations of Zeeman effect to obtain J and Landé g values of the energy levels. Many investigators of atomic spectra have used electrodeless discharge lamps in one or another of these phases of their work (see the compilation of references given by Moore^{3,4}).

Preparation of Electrodeless Discharge Lamps

High-frequency electrodeless discharge lamps containing elements with fairly high vapor

5. F. S. Tompkins and M. Fred, J. Opt. Soc. Am. 47, 1087 (1957).

* Short version of published paper, Appl. Optics 2, 707 (1963).

1. W. F. Meggers, J. Opt. Soc. Am. 50, 405 (1960).

2. C. E. Moore, J. Opt. Soc. Am. 50, 407 (1960).

3. C. E. Moore, J. Opt. Soc. Am. 52, 477 (1962).

4. C. E. Moore, J. Opt. Soc. Am. 52, 583 (1962).

pressures were described by Meggers and Westfall,⁶ Jacobsen and Harrison,⁷ and Zelikoff et al.⁸ Corliss et al.⁹ first constructed lamps containing metal halides. In 1957, Tomkins and Fred⁵ described a method for the preparation of lamps containing about 1 mg of lanthanide or actinide as a pure halide. Bovey and Wise¹⁰ have suggested some changes in their technique. They, like Tomkins and Fred, found that the iodide was preferable to chloride or bromide, since it gave longer-lived lamps.

In the method of Tomkins and Fred,⁵ the lanthanide or actinide iodide is prepared by heating the oxide with anhydrous aluminum iodide at 500° C for 8 h in a sealed tube. The product is then sublimed in vacuo into a carefully outgassed quartz lamp blank. Neon gas is added to a pressure of 2 to 3 mm Hg and the lamp is sealed off.

In the preparation of our lamps we essentially followed the method of Tomkins and Fred. With Cm, however, we desired to work with smaller amounts of material, starting with 100 µg of Cm₂O₃, since only limited quantities were available. The isotopic composition of the curium was 93% Cm²⁴⁴, 3% Cm²⁴⁶, and lesser amounts of other isotopes. It was desirable, in view of the high alpha activity, to conduct the entire preparation in a glove-box enclosure, and slight modifications were made to the procedure to permit this.¹¹

The first lamps we constructed were 100 mm long and had 7-mm i. d. These were found satisfactory for wavelength observations and for separation of the first and second spectra. For Zeeman-effect studies, smaller lamps 15 to 20 mm long with 3-mm i. d. were constructed, to permit operation parallel to the field¹² of a magnet with 2.54 cm gap. Following the work of Davison et al.¹³ with Th, these lamps were made without carrier gas. The short lamps were found to show greater brightness, to work more efficiently with small amounts of material,

6. W. F. Meggers and F. O. Westfall, *J. Res. Natl. Bur. Std.* **44**, 447 (1950).

7. E. Jacobsen and G. R. Harrison, *J. Opt. Soc. Am.* **39**, 1054 (1949).

8. M. Zelikoff, P. H. Wyckoff, L. M. Aschenbrand, and R. S. Loomis, *J. Opt. Soc. Am.* **42**, 818 (1952).

9. C. H. Corliss, W. R. Bozman, and F. O. Westfall, *J. Opt. Soc. Am.* **43**, 398 (1953).

10. L. Bovey and H. Wise, *AERE-R 2976* (1959). *Recent Developments in Light Sources Excited by Microwaves*

11. E. F. Worden (Lawrence Radiation Laboratory), unpublished work.

12. S. P. Davis (Physics Department, University of California), private communication.

13. A. Davison, A. Giacchetti, and R. W. Stanley, *J. Opt. Soc. Am.* **52**, 447 (1962).

and to have an increased lifetime, perhaps due to less cleanup.

Differentiation of First and Second Spectra

The general practice in the past for sorting atomic and ionic lines has been to compare their intensities in two different sources. Commonly, these sources have been conventional dc arcs and high-voltage ac sparks, but hollow cathodes and high-temperature furnaces have also been used to supplement or substitute for dc arc studies. The relatively low first-ionization potentials characteristic of the lanthanides make separation of their first and second spectra difficult. Fassel et al.¹⁴ have suggested that flame spectra may provide for the lanthanides a simple means of identifying lines originating from low-lying states in the neutral atom. Mitchell¹⁵ has described operating conditions by which a hollow cathode may be made to emit predominantly either neutral-atom or first-ion lines. We have produced a similar effect by varying the operating conditions of electrodeless discharge lamps, and have used it to classify first and second spectra.

Electrodeless discharge lamps emit predominantly first-spectrum lines and the strongest lines of the second spectrum. Several authors^{5, 16} have shown that the relative intensities of lines of the first and second spectra vary with the vapor pressure of the element in the lamp. At low vapor pressure lines of the second spectrum are relatively favored, whereas at high vapor pressure, the first spectrum is enhanced.

By varying the operating conditions, using either the director-furnace assembly or the cavity, the vapor pressure of the metal in the lamp can be altered.

In these experiments, we used the parabolic "A" director-furnace assembly with either the long or short lamps. A series of exposures (usually 3 to 5) was taken; for each successive exposure the lamp was operated at a different, consecutively higher furnace temperature (i. e., higher metal vapor pressure). The light output from the lamp should be kept constant during any one exposure. It was found best to precondition a lamp by heating it in operation to the highest temperature to be used, holding it there for 5 to 10 min, and then allowing it to cool well below the lowest furnace temperature to be used, before starting the series of exposures. For long

14. V. A. Fassel, R. H. Curry, and R. N. Kniseley, *Spectrochim. Acta* **18**, 1127 (1962).

15. K. B. Mitchell, *J. Opt. Soc. Am.* **51**, 846 (1961).

16. W. C. Martin and C. H. Corliss, *J. Res. Natl. Bur. Std.* **A64**, 443 (1960).

lamps containing about 100 μg of the triiodide of Cm or Gd, the furnace temperatures ranged from 500° to 750° C; short lamps were operated at 400° to 600° C.

Self-Reversal

Information on lines arising from transitions to the ground state or to low-lying levels of the atom is most useful in the analysis of the spectra of lanthanides and actinides, and of elements generally. Such lines may be recognized by the fact that they are self-reversed when excited by suitable sources. Sugar¹⁷ has reviewed the light sources used for observing reversed lines and has described a high-current arc that may be used to produce self-reversed lines in the spectra of the lanthanides.

It is known that self-absorption and self-reversal occur in the spectra emitted by electrodeless discharge lamps,^{5, 9} and most workers have operated them in such a manner as to avoid this effect. We, on the contrary, have obtained much valuable information by operating the lamps at high temperature in order to produce self-reversed lines. Long lamps with only 100 μg of material could not be used for this purpose (self-reversal has been obtained with long lamps containing 1 mg or more of material), but when the short lamps were operated at high temperature, self-reversal was quite apparent. The short lamps were either run in the cavity, or placed in the field of the parabolic director and heated with a flame.

Self-reversal was first studied with short lamps containing GdI₃. Approximately 200 reversed lines were found. Comparison with Russell's assignments¹⁸ showed that all of these lines involved combinations with low-lying levels (0 to 18 000 cm^{-1}); the majority involved combinations with the ground-term levels (0 to 1719 cm^{-1}). This shows that one obtains about the same information by this technique as by using a King furnace or by using the source described by Sugar,¹⁷ neither of which is applicable for limited samples of radioactive elements.

The technique described here has since been applied successfully by others in extending the analysis of the spectra of Pu,¹⁹ Pa,²⁰ and Np.²¹

17. J. Sugar, J. Res. Natl. Bur. Std. A66, 321 (1962).

18. H. N. Russell, J. Opt. Soc. Am. 40, 550 (1950).

19. J. Blaise, M. Fred, S. Gerstenkorn, and B. R. Judd, Compt. rend. 255, 2403 (1962).

20. A. Giacchetti (Argonne National Laboratory), private communication.

21. M. Fred (Argonne National Laboratory), private communication.

In addition, reversal has been observed with discharge lamps containing the iodides of Ce, Pm, Sm, Eu, Tb, Dy, Ho, and Er.

Zeeman Effect

Electrodeless discharge lamps have been used very successfully by several workers to obtain Zeeman-effect observations.^{18, 19, 22-25} They have employed magnetic fields varying in strength from 24 000 to 80 000 G. In conventional sources, the second spectrum is favored in a magnetic field. If electrodeless lamps are used, the intensities of the first and second spectra are approximately equal.²²

It is convenient to make Zeeman-effect observations by operating the lamp in the cavity. When a cavity is used, the lamp is of course placed perpendicular to the magnetic field. The coupling of microwaves to the lamp is then so efficient that it is necessary to cool the lamp by blowing air through the cavity. Operating a lamp at very high intensity in a magnetic field greatly shortens the useful life of the lamp. High-temperature operation of the lamp yields Zeeman patterns with broadened or self-reversed components. We have observed all variations from complete reversal of all the components to reversal of only the strongest components, the others being normal. Where the line is completely absorbed in the center and only the wings are left, difficulties may arise in the interpretation of the Zeeman patterns. One could interpret the wings as individual lines and thus count more components than are there and miscalculate the J value. To avoid such errors, it is advisable to take a series of exposures at low and medium intensity of the lamp.

Acknowledgments

We are very grateful to Mark Fred for the use of the equipment at Argonne National Laboratory and for much valuable aid and consultation. We are indebted to E. Kenneth Hulet of this laboratory for purification of the Cm and for advice and assistance in handling radioactive material. We wish to thank Frank S. Tomkins and Sumner P. Davis for many helpful discussions.

22. J. W. Lindner and S. P. Davis, J. Opt. Soc. Am. 48, 542 (1958).

23. C. H. Corliss and W. F. Meggers, J. Res. Natl. Bur. Std. 61, 269 (1958).

24. C. C. Kiess and C. H. Corliss, J. Res. Natl. Bur. Std. A63, 1 (1959).

25. L. Bovey and A. Ridgeley, The Zeeman Effect of Plutonium I. Part 1. Apparatus and Some Preliminary Results. AERE-R 3393 (1960); L. Bovey and S. Gerstenkorn, J. Opt. Soc. Am. 51, 522 (1961).

25. CONFIGURATION INTERACTION EFFECTS IN 1^N CONFIGURATIONS

Katheryn E. Rajnak and Brian G. Wybourne*

The diagonalization of the combined electrostatic and spin-orbit interaction energy matrices for a particular electron configuration yields energy levels that deviate by several hundred to a thousand wave-numbers from the observed energy levels, even when the radial integrals are treated as freely variable parameters.¹⁻⁷ These deviations have usually been ascribed to the effects of configuration interaction. The linear theory of configuration interaction has sought to account for these deviations by augmenting the usual Hamiltonian for the N-electron system with additional two-body scalar interaction terms.⁸⁻¹⁵ Associated with each interaction is an adjustable constant which is to be determined from the experimental data. While this theory has had some measure of success, the agreement has not been as good as would be desirable and there has been considerable confusion as to the physical significance of the additional two-body interactions.

In this paper a detailed study of the effects of configuration interactions on the energy levels of configurations of the type 1^N is made using second-order perturbation theory. If we let two particular states, $|a SL\rangle$ and $|a' SL\rangle$, of 1^N

be designated by $|\psi\rangle$ and $|\psi'\rangle$ and consider a perturbing state $|m\rangle$ from a particular excited configuration lying above the center of gravity of 1^N by an energy ΔE_m , the electrostatic matrix element $\langle\psi|G|\psi'\rangle$ is subject to the correction

$$C_m = - \langle\psi|G|m\rangle \langle m|G|\psi'\rangle / \Delta E_m. \quad (1)$$

In most of the cases we shall be considering, the separation, ΔE_m , of the interacting terms is quite large, and it becomes a reasonable approximation to assume the perturbing states degenerate. With this approximation it is possible to sum over the interaction terms of any excited configuration. The correction C then becomes

$$C = - \frac{1}{E_m} \sum_m \langle\psi|G|m\rangle \langle m|G|\psi'\rangle. \quad (2)$$

The only configurations that can interact with a configuration 1^N are those having the same parity and whose individual electron quantum numbers differ for not more than two electrons. Thus there are only five basic types of interacting configurations that can modify the energy level structure of the 1^N configuration:

- (a) $1^{N-2} 1^2$ and $1^N 1''$,
- (b) $1^1 41' + 1^1 N+2$ and $1^1 41' + 1^1 41'' + 1^1 N+2$,
- (c) $1^1 41' + 1^1 N 1''$,
- (d) $1^{N-1} 1'$,
- (e) $1^1 41' + 1^1 N+1$.

The interactions (b), (c), and (e) are core excitations, where an electron is promoted from a closed shell to either an unfilled shell or to the partly filled 1^N shell.

By carrying out explicitly the summation indicated in Eq. (2) it is shown that the two-electron excitations (a), (b), and (c) lead to a scaling of the Slater integrals, a linear shift of the entire configuration, and the additional terms

$$\alpha L(L+1) + \beta G(G_2) + \gamma G(R_7),$$

where α , β , and γ are functions of radial integrals between the two interacting configurations (usually left as parameters to be determined from experimental data); $G(R_7)$ and $G(G_2)$ are eigenvalues of Casimir's operators for the groups R_7 and G_2 respectively. These terms are simply related to the previous parameters of the linear theory. The one-electron excitations (d) and (e) are shown to lead to a scaling of the Slater integrals, to a linear shift of the en-

*Present address: Argonne National Laboratory, Argonne, Illinois.

1. W. A. Runciman and B. G. Wybourne, J. Chem. Phys. **32**, 1149 (1959).
2. B. G. Wybourne, J. Chem. Phys. **32**, 639 (1960).
3. M. H. Crozier and W. A. Runciman, J. Chem. Phys. **35**, 1392 (1961).
4. B. G. Wybourne, J. Chem. Phys. **36**, 2301 (1962).
5. G. S. Ofelt, J. Chem. Phys. **38**, 2171 (1963).
6. W. A. Runciman, J. Chem. Phys. **36**, 1481 (1962).
7. G. Racah and Y. Shadmi, Bull. Research Council, Israel **8F**, 15 (1959).
8. R. I. Bacher and S. Goudsmit, Phys. Rev. **46**, 948 (1934).
9. D. R. Layzer (dissertation), Harvard University, Cambridge, Massachusetts (1950) (unpublished).
10. R. E. Trees, Phys. Rev. **83**, 756 (1951).
11. R. E. Trees, Phys. Rev. **84**, 1089 (1951).
12. R. E. Trees, Phys. Rev. **85**, 382 (1952).
13. G. Racah, Phys. Rev. **85**, 381 (1952).
14. G. Racah, Lunds. Univ. Arsskr. **2** 50, 31 (1954).
15. R. E. Trees and C. K. Jørgensen, Phys. Rev. **123**, 1278 (1961).

tire configuration, and to additional three-body terms proportional to the matrix elements of the triple scalar product

$$\langle \psi | (\{ \underline{U}^{(k)} \underline{U}^{(k'')} \} (k') \underline{U}^{(k')})^{(0)} | \psi' \rangle .$$

The three-body terms arising from the interactions (d) and (e) are of opposite signs and tend to compensate each other when both types of interaction are allowed. There are several ways in which these terms can be parameterized. The choice depends to some extent on the amount of

data available for a particular atom or ion. However, it is shown that with the use of 17 variable parameters (including the three Slater integrals and the spin-orbit coupling constant) it is now possible to include, to second order, all configuration interaction effects on a configuration f^N . It is expected that investigation of particular spectra will show that in practice the number of parameters to be fitted can be somewhat reduced, either by neglecting certain small parameters or by interpolating some of them along the rare earth series.

26. ELECTROSTATICALLY CORRELATED SPIN-ORBIT INTERACTIONS IN l^N -TYPE CONFIGURATIONS

Katheryn E. Rajnak and Brian G. Wybourne*

It is shown that, in second-order perturbation theory, electrostatically correlated spin-orbit interactions give rise to a "screening" of the spin-orbit coupling constant of an l^N -type configuration. In addition to this "screening" effect these interactions also lead to an effective spin-other-orbit interaction which is not included in the usual empirical least-squares determination of the Coulomb and spin-orbit parameters. The consequences of this overt effect are discussed.

It has been a tradition among theoretical spectroscopists to treat the radial integrals that characterize the Coulomb and spin-orbit interactions within a particular configuration as parameters. These parameters have been deduced empirically by making least-squares fits of the calculated energy levels to the corresponding observed energy levels. In general, only the states of the particular configuration under study have been considered in the calculation of the energy matrices. Thus the effects of electrostatically correlated interactions with other configurations have been explicitly ignored. However, in deriving the parameters of a particular configuration by the method of least squares, it cannot be assumed that the parameters have not accommodated a large part of these interactions with other configurations. Furthermore, this implies that the eigenvectors resulting from the diagonalization of the energy matrices do not reflect the composition of the states of only the configuration under study but will also represent contributions from the states of many other configurations. In the empirical treatment only a few specific angle-dependent quantities are con-

sidered; namely, those of the Coulomb repulsion and the spin-orbit interaction within the configuration under study. Electrostatically correlated interactions that give rise to effects having a different angular dependence will not be adequately represented by the parameters of the configuration under study. We shall refer to these effects as "overt," since they may be accommodated only by introducing additional parameters. As part of a continuing study of the empirical calculation of energy levels we have endeavored to determine the angular dependence of these overt effects and to determine what electrostatically correlated interactions are included in the usual least-squares method.

The effects of weak electrostatic configuration interactions on the energy level structure of l^N -type configurations have been considered in an earlier paper¹ (referred to here as I). However, in the heavy elements, especially the actinides, where spin-orbit interactions are appreciable,^{2,3} the combined effects of spin-orbit and electrostatic configuration interactions should also be investigated. Since the spin-orbit interaction may be represented by a one-particle operator that is rigorously diagonal with respect to l but not n ,⁴ it will couple nl^N only with the configurations $nl^{N-1}n'1$, $n'1^{4l'+1}nl^{N+1}$ and $n'1'4l'+1nl^Nn''1'$. Inasmuch as these perturbing configurations will be energetically well separ-

1. K. Rajnak and B. G. Wybourne, *Phys. Rev.* **132**, 280 (1963).

2. B. G. Wybourne, *J. Chem. Phys.* **36**, 2301 (1962).

3. H. Lammernann and J. G. Conway, *J. Chem. Phys.* **38**, 259 (1963).

4. E. U. Condon and G. H. Shortley, *Theory of Atomic Spectra* (Cambridge University Press, New York, 1935).

*Present address: Argonne National Laboratory, Argonne, Illinois. Work done by Dr. Wybourne at Argonne National Laboratory.

ated from the perturbed nl^N configuration, it is a reasonable approximation to apply second-order perturbation theory as in I.

The bulk of these configuration interactions may be taken into account by modifying the energy matrices of nl^N in the same manner as in I. In this paper an attempt is made to determine the angular dependence of these corrections. It is shown that the angular dependence of the correction may be represented by a sum of two

terms, one proportional to the matrix elements of the spin-orbit interaction and the other to the matrix elements of the spin-other-orbit interaction. In the usual determination of the Coulomb and spin-orbit parameters from experimental data by the method of least squares, the first term is absorbed as an effective "screening" of the spin-orbit coupling constant of the nl^N configuration. The second term, being an overt effect, is customarily neglected in the least-squares analysis.

27. QUADRUPOLE ANTISHIELDING IN THE RARE EARTHS

Johan Blok and D. A. Shirley

When an ion is placed in an ionic crystal lattice, the interaction between the ion and the electric crystal field can be described by the Hamiltonian¹

$$\mathcal{H} = V_C + V_Q + \dots \quad (1)$$

In this expression V_C is the interaction energy of the electric crystal field with the orbital electrons, having the leading term $A_2^0 \sum_i (3z_i^2 - r_i^2)$ where the summation is over individual electrons. The term V_Q represents the interaction of the orbital electrons with the nuclear quadrupole moment and is given by

$$\frac{e^2 Q}{2I(2I-1)} \sum_i \left[\frac{I(I+1)}{r_i^3} - \frac{3(\vec{r}_i \cdot \vec{I})^2}{r_i^5} \right]$$

When we consider a closed electron shell such as $5p^6$ in a rare earth ion we have no net angular momentum, hence

$$\langle {}^1S_0 | V_C | {}^1S_0 \rangle = \langle {}^1S_0 | V_Q | {}^1S_0 \rangle = 0.$$

A hyperfine interaction can arise from the off-diagonal terms, however, through a second-order mechanism of the type

$$\frac{\langle 5p^6, {}^1S_0 | V_C | 5p^5 6p, {}^1D_2 \rangle \langle 5p^5 6p, {}^1D_2 | V_Q | 5p^6, {}^1S_0 \rangle}{\Delta E} \quad (2)$$

Terms of this type account for the large negative amplification of the electric field gradient felt at the nucleus, an effect known as antishielding.²

Antishielding interactions such as Eq. (2)

1. R. J. Elliott, Proc. Phys. Soc. (London) B70 119 (1957).

2. R. M. Sternheimer, Phys. Rev. 95, 736 (1954).

have been shown to account for the major part of the quadrupole coupling constant P in the spin Hamiltonian $\mathcal{H} = P(I_z^2 - 1/3I(I+1))$ for Eu^{+3} in europium ethylsulfate.^{3,4}

We have obtained an experimental estimate of the contribution of antishielding to the electric field gradient at the nucleus of the rare earths in the ethylsulfate and the double nitrate lattices, using nuclear orientation techniques. We aligned the closed-shell rare earth ions, $\text{La}^{+3}(4f^0, {}^1S_0)$, $\text{Gd}^{+3}(4f^7, {}^8S_{7/2})$, and $\text{Lu}^{+3}(4f^{14}, {}^1S_0)$, in these lattices. Without antishielding, these ions should have no hyperfine structure and hence should show no alignment. The quadrupole alignment actually observed for a typical case, Gd^{+3} in the ethylsulfate, is shown in Fig. D. 27-1. The angular distribution, $W(\theta)$, of γ radiation emitted from the nuclei in these experiments is given by

$$I(\theta) = 1 + B_2 U_2 F_2 P_2(\cos\theta), \quad (3)$$

where $P_2(\cos\theta)$ is the Legendre polynomial of order 2 and the values of $U_2 F_2$ can be obtained from the angular momentum properties of the nuclear decay; B_2 is related to the quadrupole coupling constant P through the relation⁵

$$B_2 = -\frac{1}{3} \frac{P}{kT} \sqrt{1/5 I(I+1)(2I-1)(2I+3)} \quad (\text{for } kT \gg P). \quad (4)$$

For the closed-shell ions P is directly related to the field gradient at the nucleus through the expression⁴

3. B. R. Judd, C. A. Lovejoy, and D. A. Shirley, Phys. Rev. 128, 1733 (1962).

4. D. T. Edmonds, Phys. Rev. Letters 10, 129 (1963).

5. R. J. Blin-Stoyle and M. A. Grace in *Handbuch der Physik*, edited by S. Flügge (Springer-Verlag, Berlin, 1957), Vol. 42, p. 555.

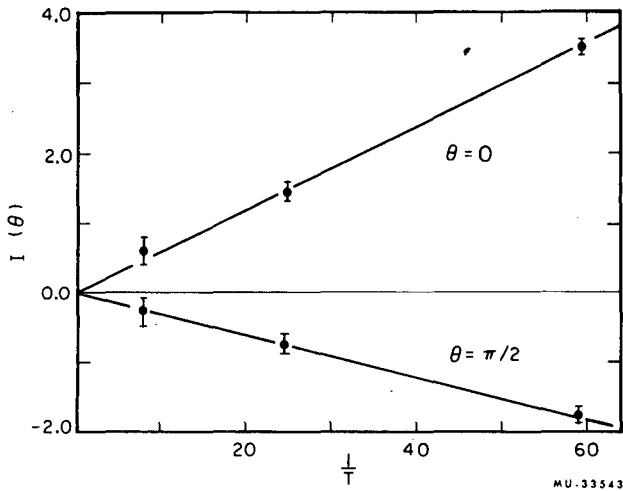


Fig. D. 27-1. Angular distribution function as a function of temperature for the 364-keV γ ray of Tb^{159} following the decay of Gd^{159} oriented in neodymium ethylsulfate. Values of θ refer to the angle between the crystalline axis and the direction of emission of the γ ray.

$$P = \frac{3Q\gamma_N A_2^0}{I(2I-1)} \quad (5)$$

$Eu^{+3}(4f^6, {}^7F_0)$ was also aligned in cerium magnesium nitrate and repeated in neodymium ethylsulfate. For this ion the quadrupole interaction has been analyzed^{1,3} and thus $\gamma_N A_2^0$ can also be found from the measured quadrupole coupling constant. Experimentally determined hyperfine structure constants are given in Table

Table D. 27-1. Hyperfine structure constants

Rare earth ion	$N A_2^0 (10^4 \text{cm}^{-1} a_0^{-2})$		Reference
	Double nitrate	Ethylsulfate	
La^{+3}	1.13	1.22	4
Eu^{+3}	+0.38	-5.2	This work
Gd^{+3}	< 0.07	-3.5	This work
Lu^{+3}	< 0.2 ^a	-4.5	This work

^a It is possible that Lu^{+3} does not substitute isomorphously into the double nitrate lattice.

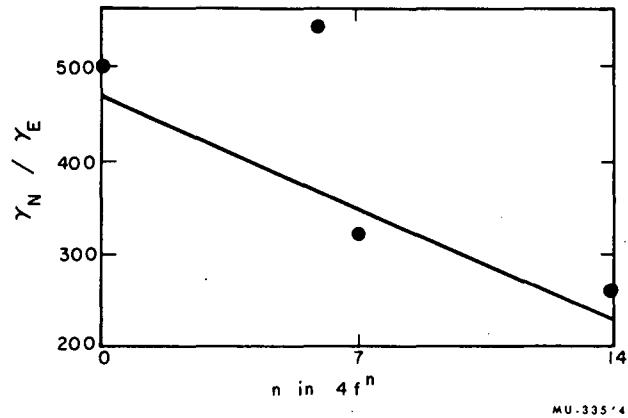


Fig. D. 27-2. The ratio of antishielding to shielding factors for the rare earths in neodymium ethylsulfate as a function of the number of 4f electrons. The curve was drawn with little regard to the point for Eu^{+3} ($n=6$), since the quadrupole coupling constant for this ion is not entirely due to antishielding and had to be corrected.

D. 27-1. In Fig. D. 27-2 we show the ratio γ_N/γ_E . Here γ_E is the factor by which the crystal field is shielded at the 4f orbital owing to the outer electrons. The γ_E has been obtained by interpolation of the crystal field parameters V_2^0 measured for the other rare earths.^{6,7} The relationship between V_2^0 and γ_E is given by

$$V_2^0 = \gamma_E A_2^0 \langle r^2 \rangle$$

Excellent agreement will be noted between Fig. D. 27-2 and the results of Barnes et al.,⁸ who obtained $\gamma_N/\gamma_E = -246$ for Tm^{+3} in thulium ethylsulfate. We also note, in agreement with Wikner and Burns,⁹ that the ratio γ_N/γ_E decreases by about a factor of 2 in passing from La^{+3} to Lu^{+3} .

6. B. R. Judd, Proc. Roy. Soc. (London) A232, 458 (1955).

7. A. J. Freeman and R. E. Watson, Phys. Rev. 127, 2058 (1962).

8. R. G. Barnes, E. Kankeleit, R. L. Mössbauer, and J. M. Poindexter, Phys. Rev. Letters 11, 253 (1963).

9. E. G. Wikner and G. Burns, Phys. Letters 2, 225 (1962).

28. INTERPRETATION OF ISOMER SHIFTS

D. A. Shirley

Since the first paper reporting the discovery of isomer shifts in Mössbauer spectra appeared in 1960,¹ their study has comprised a fast-growing area of modern physics. The attraction of these shifts is that they provide a measurement of a unique product, the differential 2ρ th moment of radial charge for two nuclear isomers and the differential electron density, evaluated at the nucleus, for an atom in two chemical environments.

The theory of isomer shifts is essentially the same as isotope shift theory in atomic spectroscopy. The resulting Doppler-velocity shift is, in perturbation-theory approximation,

$$v = \left(\frac{4\pi Z e^2 R^2 c}{5E_\gamma} \right) \left\{ \frac{30(1+\rho)y_0^{2\rho-2}}{(2\rho+1)(2\rho+3)\Gamma^2(2\rho+1)} \right\} \times \left[\sum_A \psi^2(0) - \sum_S \psi^2(0) \right] \left[\frac{\delta R}{R} \right]$$

The factors on the right-hand side are, from the left,

(a) A "constant factor," containing constants and the nuclear radius. With a radius of $R = 1.20 A^{1/3}$ fermis, and E_γ in keV, this factor is $15.6 \times 10^{-26} ZA^2/3E_\gamma^{-1} \text{ cm}^4/\text{sec}$;

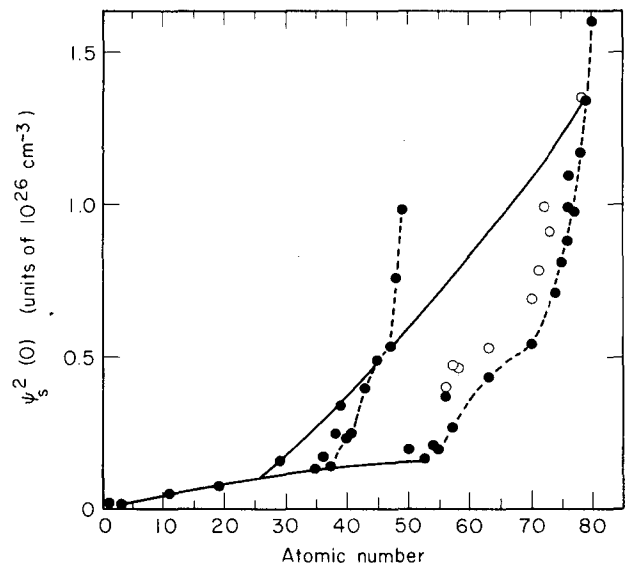
(b) A "relativity factor," which accounts for the fact that electrons in heavy atoms are somewhat relativistic. This factor may be quite large. Several values of the relativity factor, in perturbation theory approximation, are given in Table D. 28-I, along with exact values;

(c) An "electronic factor," the electronic

density difference between source and absorber. This factor contains all the chemical information; and

(d) A dimensionless "nuclear factor" containing the nuclear radius information about the isomeric pair.

The nonrelativistic electron density at the nucleus, $\psi^2(0)$, may be obtained from atomic spectroscopy data. Several electron densities for optical s electrons are shown in Fig. D. 28-1.



MU-31541

Fig. D. 28-1. Nonrelativistic density at the nucleus of valence s electrons in free atoms in the neutral (\bullet) and +1 (\circ) oxidation states. Data are representative rather than complete. In several elements more than one value was obtained for $\psi^2(0)$, using different configurations. In these cases the lowest values are most relevant to isomer shift discussions, as they represent maximum shielding of the valence s electron (thus the configuration $(n-1)d^{x+1}ns$ is preferred over the configuration $(n-1)d^xns np$ or $(n-1)d^xns(n+1)s$ for obtaining the $\psi_{ns}^2(0)$ that is appropriate here). The alkalis are interconnected by a solid curve, as are the IB metals (Cu, Ag, Au). Dotted curves interconnect the 5s and 6s electron series. Decrease of slope through the rare earths may be explained as arising from the more complete shielding of 6s electrons by 4f electrons.

Table D. 28-I. Relativity factors for selected elements.

Atomic number	Relativity factor (perturbation theory factor)	Relativity factor (exact)
26	1.32	1.30
50	2.48	2.31
61	3.71	3.30
66	4.59	4.00
79	8.55	6.84
93	23.6	15.8

1. O. C. Kistner and A. W. Sunyar, Phys. Rev. Letters 4, 412 (1960).

The electronic factor alone may vary for a given isomeric pair. The resultant variation in isomer shift should be correlated with such chemical properties as ligand electronegativity. Such a correlation for the tin tetrahalides is

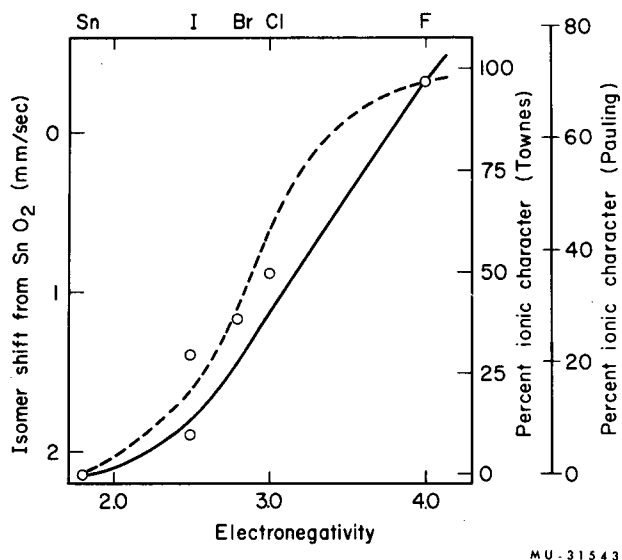


Fig. D. 28-2. Isomer shifts vs electronegativity for stannic halides. The solid (dashed) curves are after those of Pauling (Townes) for diatomic alkali halides. The curves were fitted at gray tin and SnF_4 .

shown in Fig. D. 28-2. We note that the systematic variation of shift with electronegativity, and especially the similarity of this variation with that deduced from quadrupole coupling constants, gives empirical support to the concept of "ionic" character.

Finally in Table D. 28-II we have set out the nuclear factors that may be derived from data available to date. It is interesting to note that these nuclear factors are smaller by about an order of magnitude than those obtained from isotope shifts, which give $\delta R/R$ values of the order of 10^{-2} for the addition of two neutrons.

Table D. 28-II. Nuclear factors.

Isotope	Isomeric energy (keV)	$\delta R/R$
Fe^{57}	14.4	-1.8×10^{-3}
Sn^{119}	23.8	$+1.2 \times 10^{-4}$
Te^{125}	35.5	$\approx +0.7 \times 10^{-4}$
I^{129}	26.8	-1×10^{-4} (or larger)
Eu^{151}	21.7	-5×10^{-4}
Au^{197}	77.5	$(+) 3 \times 10^{-4}$
Hg^{197}	297	$+1.6 \times 10^{-4}$

29. ANGULAR DISTRIBUTION OF CONVERSION ELECTRONS FROM ORIENTED $\text{Ce}^{137\text{m}}$

N. J. Stone, R. B. Frankel, and D. A. Shirley

Conventional nuclear orientation experiments measure the angular distribution of γ radiation emitted in the decay of oriented nuclei. The technique has also been applied to measurement of α -particle emission using semiconductor detecting devices which operate inside the Dewar system at 1°K , but its extension to the study of β decay is complicated by their generally lower total energy and lower energy loss per cm in the detector. Early measurements using anthracene crystals and long light pipes, notably the detection by Wu et al. of parity nonconservation,¹ suffered from low energy resolution and poor thermal characteristics.

This report describes an apparatus using gold-surface germanium counters and its appli-

cation to the measurement of the angular distribution of conversion electrons from $\text{Ce}^{137\text{m}}$ nuclei oriented in the neodymium ethyl sulphate (NES) lattice.

The counters have an active area of about 0.25 cm^2 and were mounted on a molybdenum strip with gold conducting epoxy. The cryogenic system was designed to minimize lead capacitance, and a total of 40 pF for counter and leads was obtained. The counter signals were fed to a charge-sensitive amplifier and pulse-height analyzer. A typical spectrum is shown in Fig. D. 29-1.

The activity was grown onto a small area on the surface of the NES crystal which was mounted in the demagnetization cryostat. Electron counters were placed at 0° and 90° to the crystalline c axis inside the crystal, with scintillation counters in similar positions outside the

1. C. S. Wu, E. Ambler, R. W. Hayward, D. D. Hoppes, and R. P. Hudson, Phys. Rev. 105, 1413 (1957).

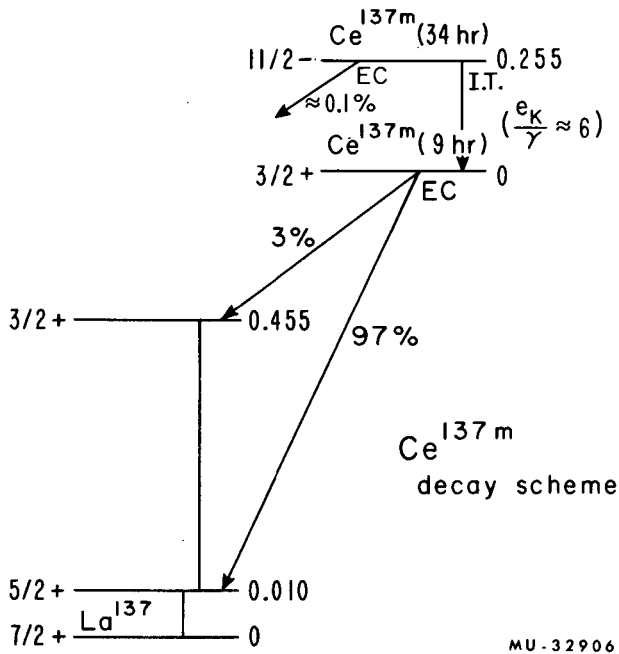


Fig. D. 29-1. Decay scheme of Ce^{137m} . The measurements are made on the 255-keV γ ray and conversion electrons (249 keV and 215 keV).

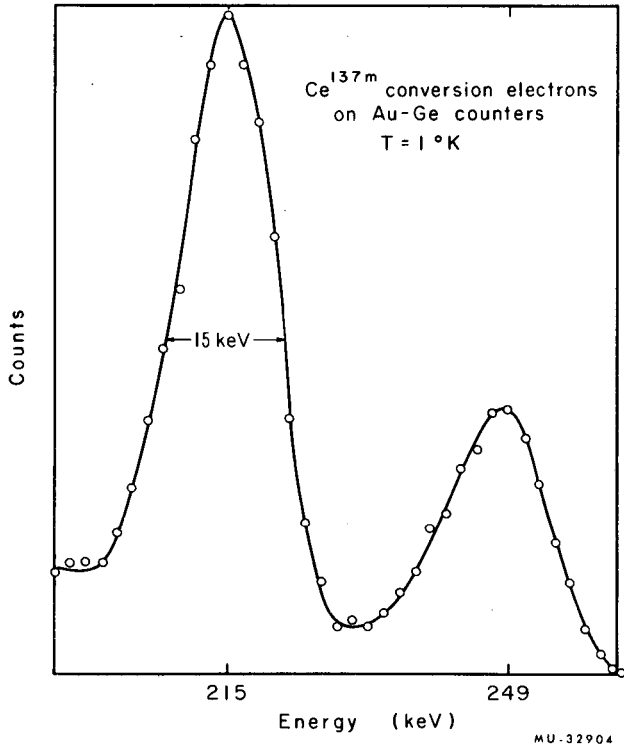


Fig. D. 29-2. Spectrum of Ce^{137m} conversion electrons on an Au-Be counter at $1^\circ K$.

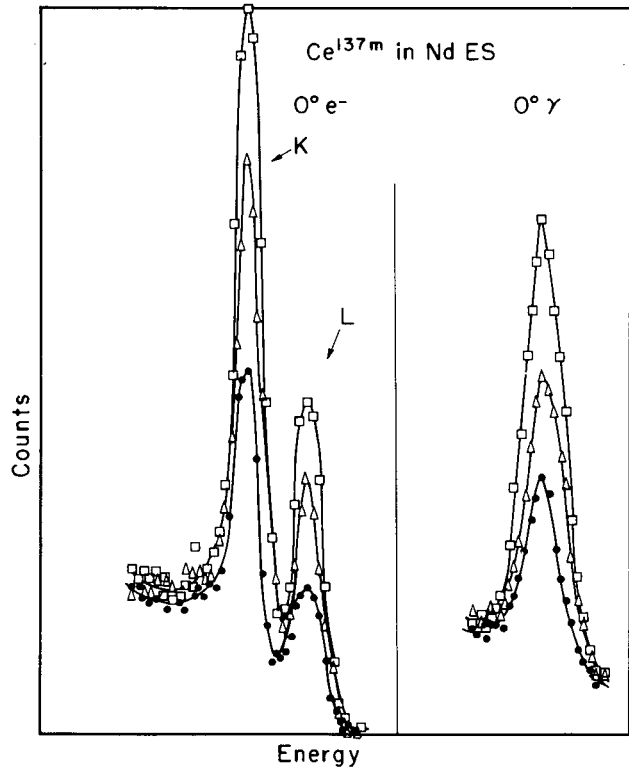


Fig. D. 29-3. Successive 2-min counts of radiation from Ce^{137m} aligned on NES counters at 0° with respect to the crystalline C axis. Counts were half an hour apart. The change in count rate corresponds to a changing degree of alignment as the sample warms up.

apparatus. This allowed comparison of the γ and electron anisotropies.

A decay scheme of Ce^{137m} is shown in Fig. D. 29-1. The γ -ray anisotropy of the 255-keV isomeric transition has been measured by Haag et al.² This nucleus was chosen as it has a large anisotropy, a large conversion coefficient (6), and no electron or positron background under the conversion peaks.

The sample was demagnetized and simultaneous counts were taken on all four counters (Figs. D. 29-3 and D. 29-4).

The theoretical γ -ray angular distribution is given by

$$W(\theta) = 1 + B_2 F_2 P_2(\cos\theta) + B_4 F_4 P_4(\cos\theta),$$

2. J. N. Haag, C. E. Johnson, D. A. Shirley, and D. H. Templeton, Phys. Rev. 121, 591 (1961).

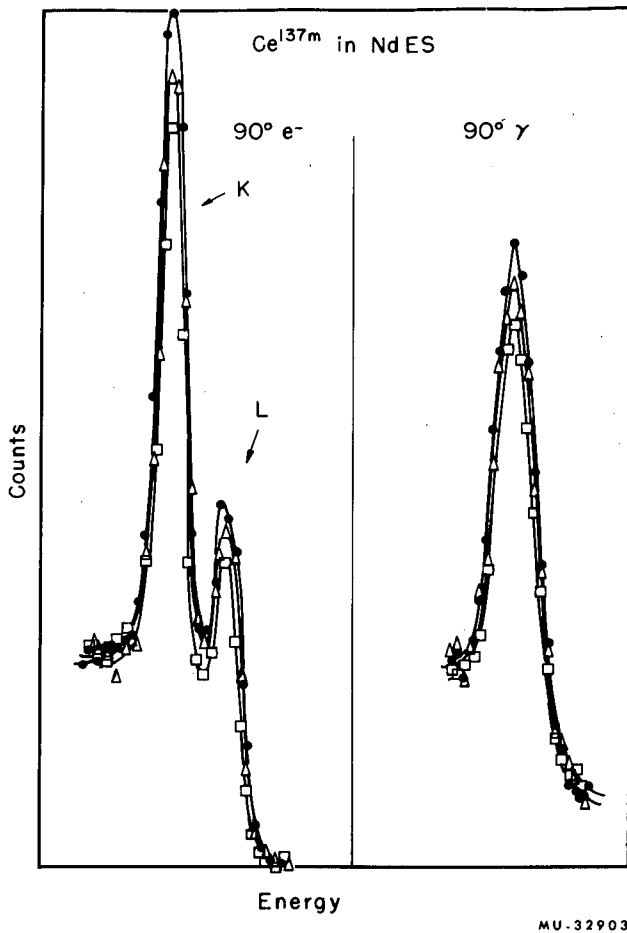


Fig. D. 29-4. Successive 2-min counts of radiation from Ce^{137m} aligned in NES in electron and γ counters at 90° to the crystal C axis. Note that the effect is in the opposite direction to the 0° counts (Fig. D. 29-3) as expected.

where $P_2(\cos\theta)$ and $P_4(\cos\theta)$ are Legendre polynomials, F_2 and F_4 are angular momentum coupling coefficients, and B_2 and B_4 are parameters describing the degree of orientation of the Ce^{137m} nuclei. The electron distribution modifies this only in the introduction of "particle parameters" b_2 and b_4 (Biedenhorn and Rose³), given by

$$W(\theta) = 1 + b_2 B_2 F_2 P_2(\cos\theta) + b_4 B_4 F_4 P_4(\cos\theta).$$

Figure D. 29-5 shows the results for both K and L electrons at 0° plotted as a function of $1/T$. The temperatures are derived from the γ -ray data with the results of reference 2. Also shown is a plot of

3. L. C. Biedenhorn and M. E. Rose, Rev. Mod. Phys. 25, 729 (1953).

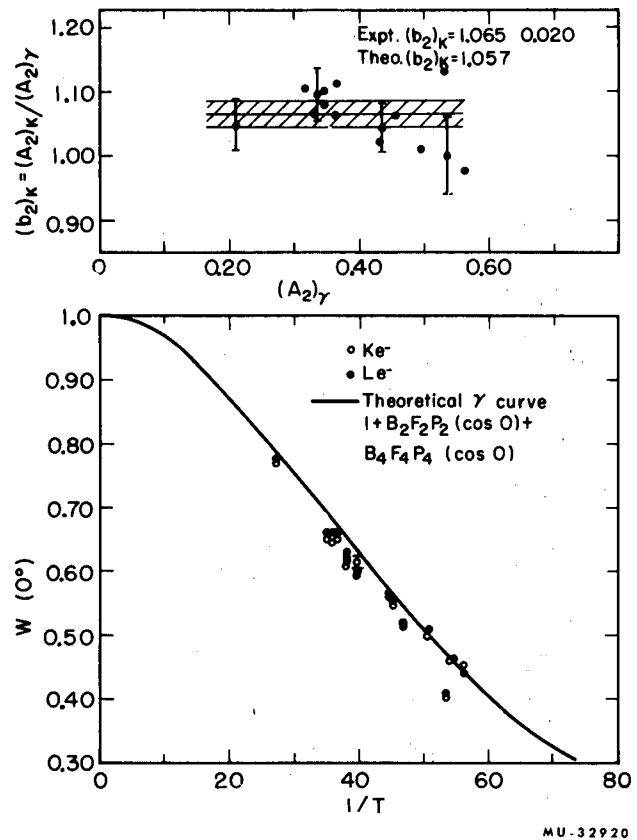


Fig. D. 29-5. Plot of K and L electron anisotropy as a function of temperature. The curve is the theoretical γ anisotropy. The upper part of the figure shows the particle parameter for the K's plotted against the coefficient of the $P_2(\cos\theta)$ term for γ 's.

$$\frac{(b_2 B_2 F_2)_{K \text{ electrons}}}{(B_2 F_2)_{\text{gamma}}} = b_2$$

versus $(B_2 F_2)_{\text{gamma}}$. The P_4 term is neglected in this analysis, as this term is < 0.05 times the P_2 term in the temperature range studied. The resulting value for b_2 is 1.065 ± 0.020 for the K electrons and 1.051 ± 0.020 for the L electrons. The value of b_{2K} has been calculated (reference 3) to be 1.057 for this transition. Particle parameter calculations for L electrons have not been made for M4 transitions.

The agreement between theory and experiment shows that the system operates satisfactorily and should be applicable to measurement of the angular distribution of β particles from oriented nuclei.

30. POLARIZATION OF SILVER NUCLEI IN IRON AND NICKEL

G. A. Westenbarger and D. A. Shirley

Large internal magnetic fields are set up at the nuclei of normally nonmagnetic atoms when these atoms are dissolved in iron. These fields are of considerable practical importance, as they provide a means of applying large magnetic fields (of the order of 10^6 gauss) to these nuclei, and make possible such experiments as nuclear polarization, heat capacity measurement, etc. At the same time the fields are of theoretical interest because they involve some, but not all, of the collective interactions between atoms which are responsible for ferromagnetism.

In order to help elucidate the origins of these induced fields we have compared internal fields at nuclei of the Group IB metals dissolved in Fe, Co, and Ni. For Au in these metals fields were known from Mössbauer spectroscopy measurements (R. W. Grant, et al., Annual Report, UCRL-10624 Jan. 1963, p. 248). Internal fields for Cu became available during this work.¹ We have made measurements on Ag nuclei in Fe and Ni using low-temperature nuclear polarization.

In these experiments a specimen made up of Ag^{110m} and stable silver dissolved in Fe or Ni metal was soldered to a copper "fin" assembly which was in thermal contact with a slurry of chromium potassium sulfate. This salt was then cooled to temperatures in the range 0.01 to 1.0°K and the sample was polarized in a small super-

1. Y. Koi and A. Tsujimura, J. Phys. Soc. Japan 18, 1347 (1963).

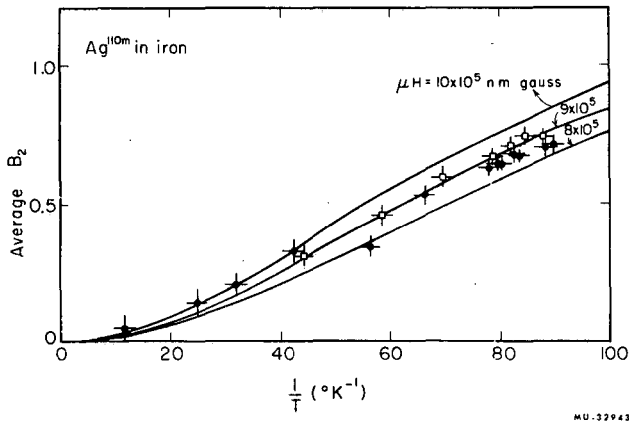


Fig. D. 30-1. B_2 for Ag^{110m} in iron, derived from γ -ray anisotropy measurements. Theoretical curves for several nuclear moment-field values are shown.

conducting magnet. Substantial nuclear orientation was produced and was detected by measuring the spatial anisotropy of β particles and γ rays from the Ag^{110m} . Auxiliary experiments were performed using Ag^{10} made by the reaction $Pd^{104}(p, n)$.

The angular distribution of γ radiation from oriented nuclei is given by

$$I(\theta) = 1 + B_2 U_2 F_2 P_2(\cos\theta) + \dots$$

Here B_2 is an orientation parameter related to the second moment of nuclear spin projected on the quantization axis, and U_2 and F_2 are nuclear parameters. In Fig. D. 30-1, B_2 for Ag^{110m} in iron is plotted against reciprocal absolute temperature. Analysis yields 9×10^5 nm-gauss for the product $|\mu H|$, where μ is the nuclear mo-

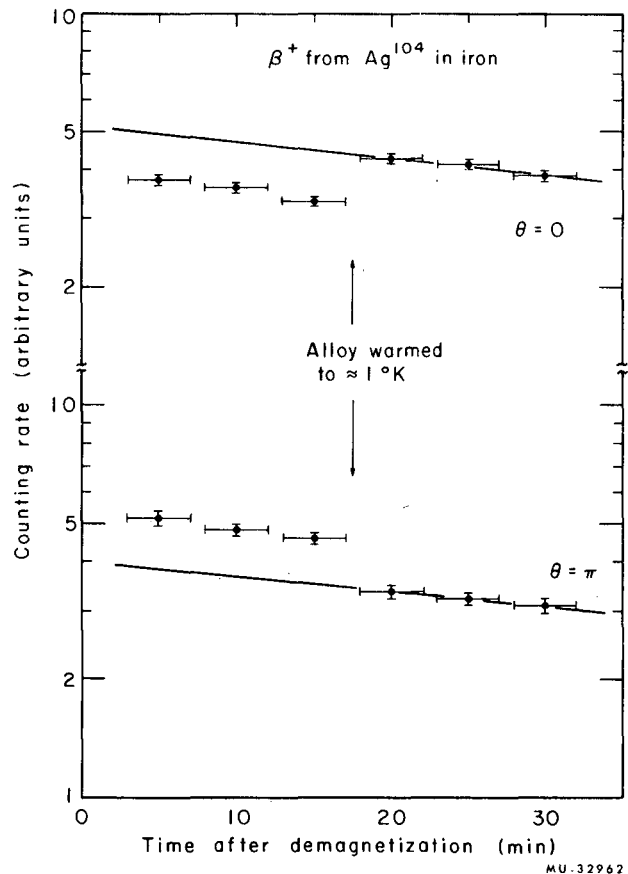


Fig. D. 30-2. Beta intensities along and at 180 deg from the magnetic field direction, for Ag^{104} nuclei polarized in iron. The "cold" temperature is 0.02° K.

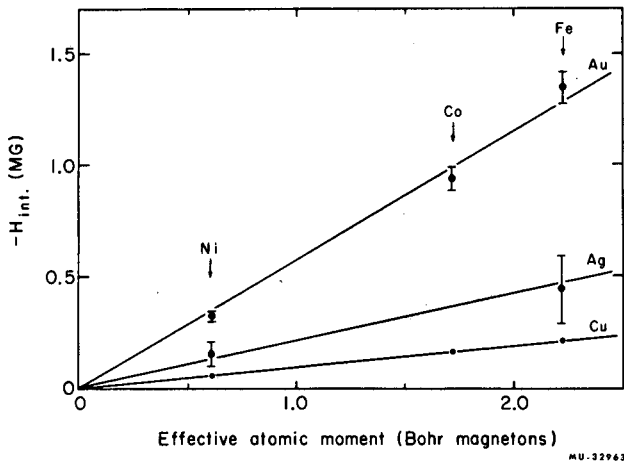


Fig.D. 30-3. Internal fields for the Group IB metals in ferromagnetic hosts, plotted against host moments.

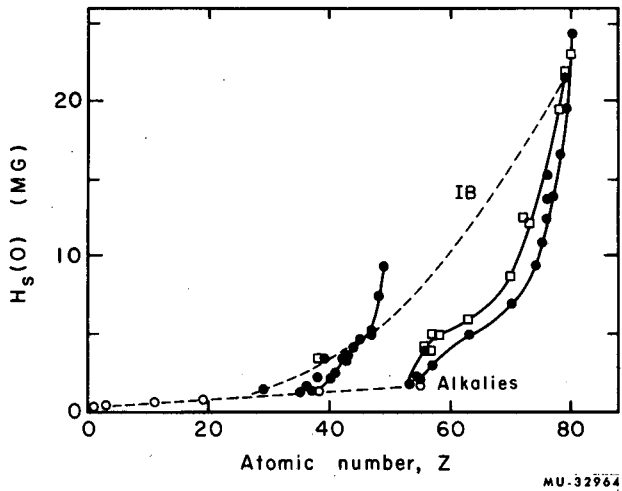


Fig. D. 30-4. Internal fields in atoms with unpaired valence s electrons, calculated from atomic spectroscopy data.

ment and H the internal field. In Fig. D. 30-2 the β^- asymmetry for Ag^{104} in iron is shown. This establishes the sign of the internal field as negative and yields a rough value of 450 ± 150 kgauss for its magnitude.

The internal fields known to date for the IB metals in Fe, Co, and Ni are shown in Fig. D. 30-3. Plotted against the host magnetic moment, they show a roughly linear dependence on the number of unpaired d electrons in the host. This is to be expected if the internal fields arise predominantly by conduction-electron polarization via ferromagnetic exchange polarization, with the polarized conduction electrons (4s in Cu, 5s in Ag, 6s in Au) producing a contact field at the nucleus. To test this mechanism further we have calculated, from atomic spectroscopic data, the internal fields due to unpaired outer s electrons for several elements (Fig. D. 30-4). These fields vary smoothly with atomic number, and we have drawn curves through them. In Fig. D. 30-5 the curves, multiplied by 0.06 (to account for $\approx 6\%$ polarization, which is about what is expected on this model), are displayed together with the internal fields known to date for impurities dissolved in iron. The qualitative agreement of curves and data lend support to the conduction electron mechanism.

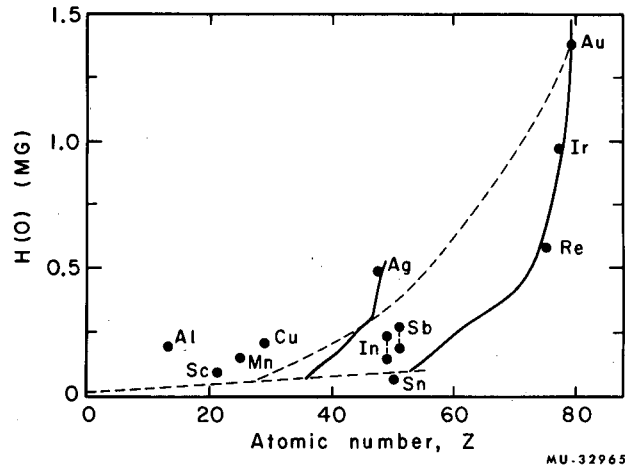


Fig. D. 30-5. Internal fields for several solute atoms in iron, with curves corresponding to 6% of outer s electrons.

31. HYPERFINE STRUCTURE OF ${}_{68}\text{Er}^{171}$

Isaac Maleh

By means of the atomic-beam magnetic resonance flop-in technique the hfs of ${}_{68}\text{Er}^{171}(I=5/2)$ was measured. The results are

$$a = \pm 197.0(2.9) \text{ Mc,}$$

$$b = \pm 3646.0(106.0) \text{ Mc,}$$

$$\frac{b}{a} > 0.$$

With the data published by Doyle and Marrus¹ on Er^{169} , the Fermi-Segrè relation can be used to determine the nuclear magnetic moment, and the $\langle 1/r^3 \rangle$ value can be used to compute the nuclear quadrupole moment. The computations yield

$$\mu_I (\text{corr}) = \pm 0.697 (48) \text{ nm,}$$

1. Walter M. Doyle and Richard Marrus, Direct Measurement of the Magnetic Moment of Erbium-169, UCRL-10484, Nov. 1962.

$$Q (\text{uncorr}) = \mp 2.37 (20) \text{ b.}$$

The μ_I is corrected for diamagnetic shielding while the Q is uncorrected for the Sternheimer core-polarization effect.²

The magnetic moment is less than the collective-model prediction (perhaps because of the uncertainty in g_R) and the quadrupole moment yields a deformation of 0.238(20) which is low compared with those found generally in the rare earth region.

More detailed information on the above isotope, as well as on Tm^{171} and Tb^{161} , can be found in Isaac Maleh, Electronic and Nuclear Properties of Er^{171} , Tm^{171} , and Tb^{161} (Ph.D. thesis), UCRL-10747, March 1963.

2. R. Sternheimer, Phys. Rev. 86, 316 (1952).

32. CHEMICAL EFFECTS FOLLOWING THE ${}^{34}\text{S}(n, \gamma){}^{35}\text{S}$ REACTION IN GASEOUS SULFUR COMPOUNDS*†

M. Lee Hyder† and Samuel S. Markowitz

The chemical behavior of ${}^{35}\text{S}$ formed by the ${}^{34}\text{S}(n, \gamma)$ reaction has been studied in gaseous H_2S , SO_2 , SF_3 , CH_3SH , and thiophene. We obtained the reaction by sealing the gases in quartz ampules and irradiating them with thermal neutrons in the Livermore pool-type reactor (LPTR). Among the effects studied were those of pres-

sure, surface area, and additive gases including argon, nitric oxide, oxygen, and hydrogen. The ${}^{35}\text{S}$ was recovered in gaseous compounds and in deposits on the walls of the ampules; the chemical composition of both portions of activity was determined by aqueous chemistry using carriers. The results are consistent with a model in which the original molecule is broken up in the recoil process and the resulting fragments containing ${}^{35}\text{S}$ react with the surroundings only after they have slowed to thermal energies; in general, the final chemical form of the ${}^{35}\text{S}$ is determined by the chemical environment in which it is produced rather than by its original oxidation state or chemical form. However, irradiations of mixtures of several gases with NO gave results possibly indicating that the chemical form of the ${}^{35}\text{S}$ immediately after molecular disruption may depend upon the nature of the original molecule.

*Full paper in J. Inorg. Nucl. Chem. 26, 257 (1964).

†Submitted by M. Lee Hyder in partial fulfillment of requirements for the degree of Doctor of Philosophy at the Department of Chemistry, University of California, Berkeley, California (UCRL-10360, July 1962).

‡Present address: Chemistry Department, Savannah River Laboratory, E. I. duPont de Nemours and Co., Aiken, South Carolina.

E. INSTRUMENTATION

1. CYCLOTRON DEVELOPMENT EXPERIENCE

Hermann A. Grunder and Frank B. Selph

The Berkeley 88-inch cyclotron is a three-sector AVF variable-energy cyclotron designed to accelerate protons up to 60 MeV, deuterons up to 65 MeV, and heavier ions up to comparable energies per nucleon. The shaping of the magnetic field that is required to ensure isochronous acceleration is accomplished by means of 17 trim coils. For first-harmonic shaping of the field, five sets of valley coils are used. A plan view of the pole face is shown in Fig. E. 1-1, which shows some of the important machine components. Construction details and an account of the early beam-development work were given in several papers presented at the 1962 and 1963 International Conferences on Sector-Focused Cyclotrons.

Internal beams of protons, deuterons, and α particles have been developed, of energies up to and including maximum design energies. The internal beam power is of the order of 4 kW, of which we are able to extract about 1 kW for experimental use. The beams now available for experimental use are 25- to 120-MeV α particles,

12.5- to 60-MeV deuterons, and 10- to 50-MeV protons. In addition, α particles of ≈ 130 MeV and protons of ≈ 60 MeV have been deflected, but difficulties in holding deflector gradient have prevented their use by experimenters. The area of radial phase space occupied by 90% of the deflected 65-MeV α beam is 50 mm mrad, vertically 90 mm mrad. The amount of extracted beam obtainable is being gradually pushed upward as we learn how to make septa that will withstand large beam currents and at the same time permit efficient extraction.

Beam Development

A history of the effort required to obtain a beam of 130-MeV α particles will illustrate the methods employed. The field shaping, which must be done by the trim coils, is most exacting for this case. The first step was the calculation of the optimum main field and trim-coil currents with a linear programming method that minimizes the phase excursions of the particles, consistent with the suitable field gradients re-

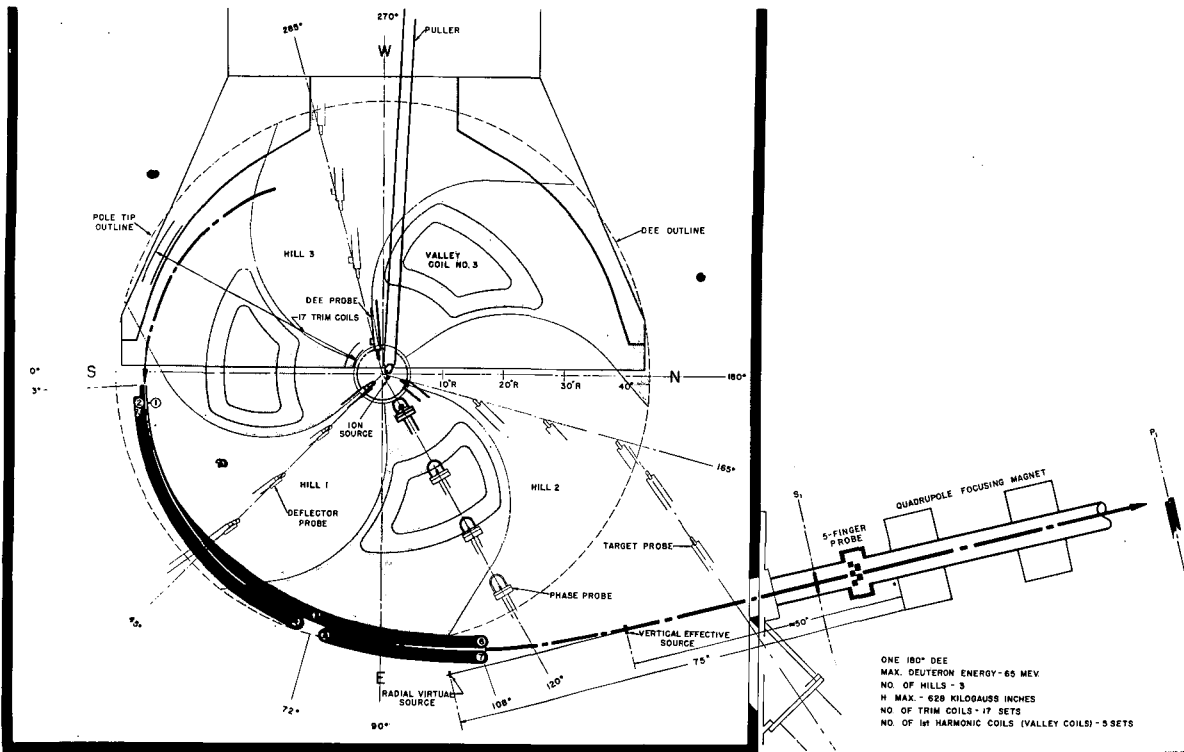


Fig. E. 1-1. Plan view of pole face.

quired for radial and axial stability, and with constraints imposed by trim-coil limitations.

With the currents set according to this calculation, the beam was obtained out to 36.5 in. (Fig. E. 1-2a). We later found a small error in the field data fed to the computer. Without this error the beam would have probably come out somewhat farther. The H_2^+ beam shown was found 89 kc/sec below the α resonance. This beam was from a source that had been running with helium for over 24 hours. To prevent confusion when working with a new beam, we found it a good idea to identify both resonances.

The phase behavior of the α beam was then deduced from records of beam current vs radius for several frequencies above and below the optimum frequency (Figs. E. 1-2b and E. 1-2c), by using a method devised by Garren and Smith. We have concluded from probe measurements that the loss of beam between 35 and 37 in. is due to phase loss; it is clear that the beam particles lag their radio frequency by $\pi/2$ in this region, as a small increase in frequency (causing additional phase lag) results in a large loss of beam at 35 in., while a relatively large decrease in frequency causes only a small loss. These changes locate points 1 and 2 on the phase diagram (Fig. E. 1-3a) as the limit of the beam in

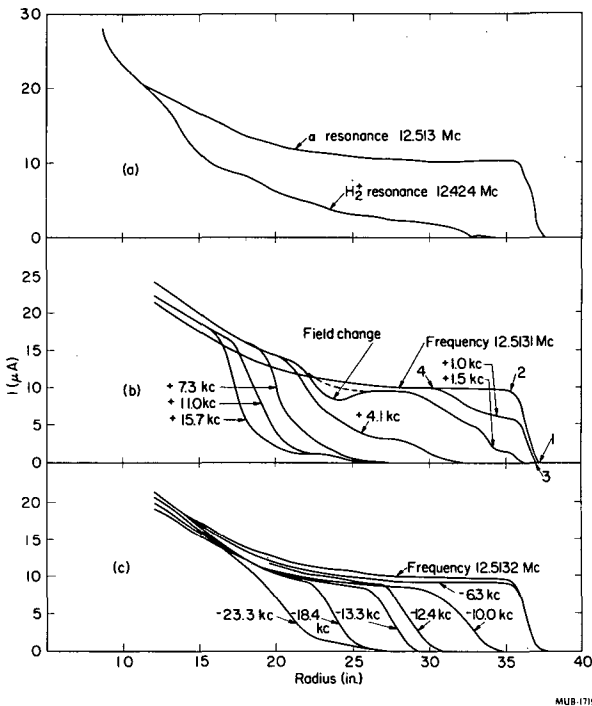


Fig. E. 1-2. Development of the 130-MeV α beam. (a) The first beam obtained with the corresponding H_2^+ beam; (b) and (c) the α beam as a function of frequency.

phase at the optimum frequency of 12.513 Mc/sec. Now when the frequency is shifted an amount Δf , each particle is shifted an additional amount in phase, given approximately by

$$\Delta \sin \phi \approx \frac{2\pi^3 m f R^2}{qV} \Delta f, \quad (1)$$

where m is the mass and q the charge of particle, V the dee voltage, and R the radius. For $\Delta f = +1$ kc/sec, the particles of the beam that are lagging by $\pi/2$ are at points 3 and 4. The position on the phase diagram (Fig. E. 1-3a) is then found by computing $\sin \phi = (1.0 - \Delta \sin \phi)$ for each point. The edges obtained by the other positive frequency shifts are plotted in the same manner. With $\Delta f = -10$ kc/sec and less, the particles are leading the rf by $\pi/2$ when the beam disappears, and the position on the phase plot is found as $\sin \phi = -(1.0 - \Delta \sin \phi)$. In completing the diagram, use is made of the fact that the phase width remains constant with radius as long as the phase is within the $\pm \pi/2$ limits. A check on the accuracy of the data is afforded by the agreement between points obtained from the $+\pi/2$ loss with points obtained from $-\pi/2$ loss. With the phase plot thus obtained as a guide, adjustments were made to the trim-coil currents, which brought the beam to the maximum radius, 40 in. on the target probe (Fig. E. 1-3b).

The large decrease in beam intensity occur-

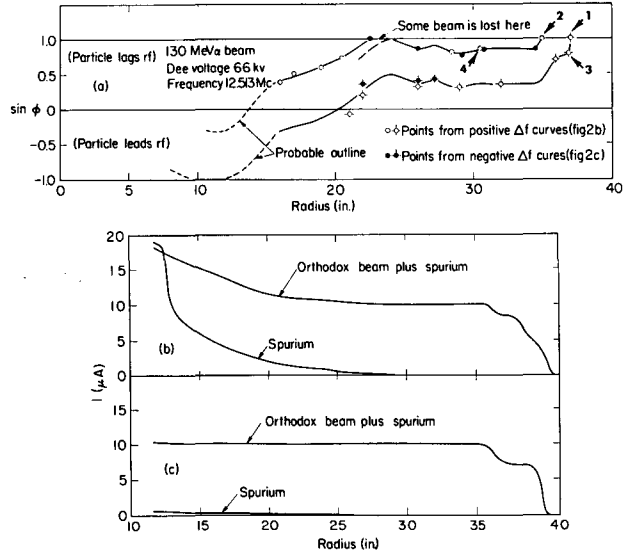


Fig. E. 1-3. Development of the 130-MeV α beam. (a) The phase plot deduced from the curves of Fig. E. 1-2 b and c; (b) the beam obtained after trim-coil adjustments were made (the spurious beam, obtained by blocking the orthodox beam with another probe, is also shown); (c) after center region adjustment was made to eliminate spurious.

ring inside 27 in. is not due to phase loss, however, but apparently to particles following the spiral ridges; hence we call the beam a spurious beam or "spurium." This beam does not disappear when another probe is run into the center of the machine, which of course would stop all of the orthodox beam (Fig. E. 1-3b). The disappearance of this spurious beam beyond 27 in. occurs because the spiral ridge curves away from the probe track in this region. This beam was eliminated by moving the ion source and ion-extraction mechanism (puller), while observing orthodox beam on the dee probe and spurious beam on the target probe, until a position was reached in which the spurious beam largely disappeared and the orthodox beam intensity was unimpaired (Fig. E. 1-3c).

Records made with the three probes in turn showed that the beam was off center about 1 in. toward the target probe. The direction of this off-center displacement could be readily changed to any azimuth by using the valley coils. Centering was tried by repositioning the ion source, but this was not successful. With the valley coils, however, it was possible to obtain a beam that was well centered. The method employed was to position the dee, target, and deflector probes at 20 in., then adjust the currents in valley coils 1 and 2 until all three probes read the same beam current. As the probes are symmetrically located relative to the particle orbits, this should be a good test of centering. The process was repeated by using valley coil 3 with the probe positions at 25 in., valley coil 4 with probe positions at 30 in., and valley coil 5 with probe positions at 37.5 in. The distribution of intensity on the three probes was not very sensitive to frequency when the beam was centered in this fashion.

Operating Stability

An important criterion in constructing the cyclotron was to secure a high degree of stability in operation so that a beam of constant intensity would be available for many hours at a time, with only occasional adjustments necessary by the operator. Of equal importance is the reproducibility of machine settings. Many man-hours of work may be necessary to achieve a particular satisfactory result, and this work can be partly or wholly wasted if the machine conditions are not precisely reproducible. These considerations are familiar to every experimenter, and the following discussion will indicate how they apply to this cyclotron.

The output with a particular beam will depend, among other things, upon the behavior of the beam in phase. Particles that have a phase shift near $\pm \pi/2$ at any radius will not be further accelerated if a frequency or field change causes a shift to a phase greater than $\pi/2$ or less than

$-\pi/2$. The most sensitive region is in the outer few inches, for the phase shift due to such a change is proportional to the square of the radius. In addition, the greatest departure from the isochronous field (and hence the greatest phase shift) is likely to occur at the edge of the magnet, where the trim coils make the greatest contribution.

The experience with the 130-MeV α beam was that to maintain a beam intensity constant within 10% at 39 in. radius the frequency had to be stable to 5 parts in 10^5 (for corresponding stability of the 65-MeV α beam, about 1 part in 10^4 is required). The main coil current requires a corresponding stability, while the trim-coil currents must be held constant to 1 part in 10^3 . For reproducibility of a beam the trim coils require a control and readout of comparable accuracy, whereas the frequency and main coil current can be less by an order of magnitude, since the frequency can be tuned. For beam diagnostics, however, a frequency readout accurate to 100 cycles is essential.

The 88-inch cyclotron does meet the above requirements. The main coil current regulation is about 3 parts in 10^5 , and the frequency regulation is about 5 parts in 10^5 . For short periods of time, under quiet conditions, a more favorable condition can be realized.

The principal object in working with the extracted beam has been to make the extraction efficiency as large as possible. To make this concept precise, we define extraction efficiency as the ratio of the extracted beam intensity--measured external to the cyclotron--to the internal beam intensity measured at 30 in. radius. In working with a beam of 65-MeV α particles, a reproducible extraction efficiency of 53% has been recorded, with a channel transparency of 63%.

The particles that are not extracted can be grouped into three categories: (a) those which acquire vertical amplitudes large enough to strike the inside of the dee, (b) those which lag or lead in phase enough to be decelerated, and (c) those which strike the deflector. With the 65-MeV α beam, about 20% of the beam intensity is lost by the first two mechanisms.

In the beginning, we deflected the beam without using first-harmonic coils. The best beam quality should be expected with a well-centered beam; therefore we tried to center the beam by changing the center region parameters. These center-region parameters are: (a) ion source radial position, (b) ion source azimuthal position, (c) ion source rotation, (d) puller position, north-south, and (e) puller position, east-west. If there are negligible magnetic field distortions it should be possible to center the beam

by varying these center-region parameters and the dee voltage and frequency.

By measuring the deflected beam vs dee voltage, we observed distinct peaks of external beam (Fig. E. 1-4). We suspect that these peaks are connected with the precession of radial betatron oscillations. Whether the beam is centered or merely has a favorable angle for deflection at the peaks has not been shown. However, there are indications that coherent oscillations make the deflection easier, and it seems likely that the peaks correspond to a favorable amount of coherent oscillations.

The number of precessions P required to
EXTERNAL BEAM VS DEE VOLTAGE

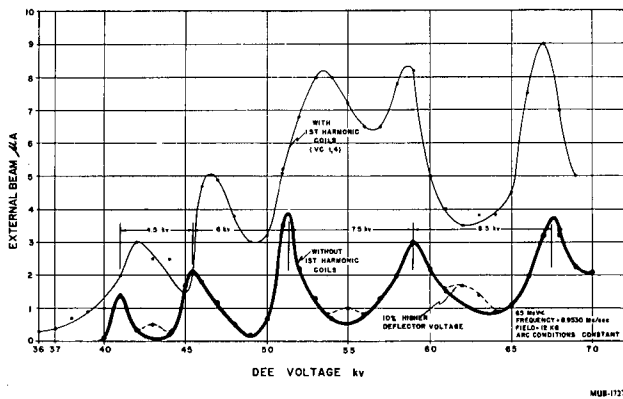


Fig. E. 1-4. External beam vs dee voltage.

achieve full radius is given by

$$P = \frac{E}{\epsilon} (\nu_r - 1), \quad (2)$$

where E is the particle energy, ϵ the average

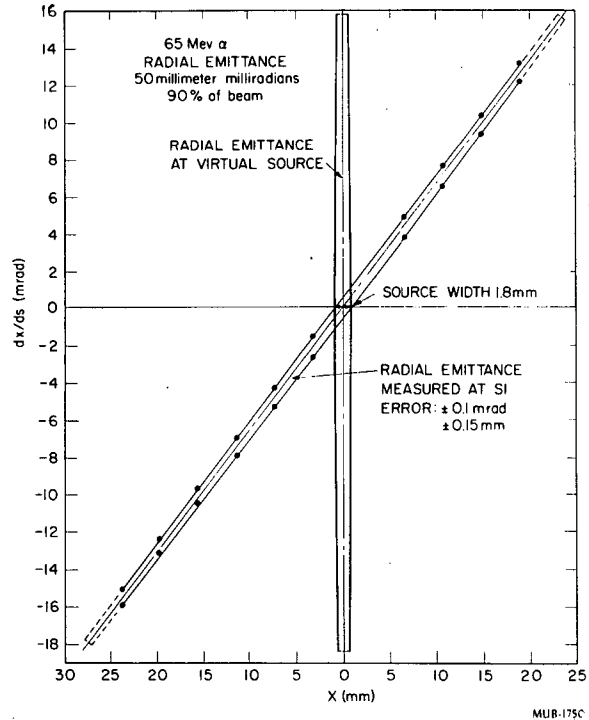


Fig. E. 1-5. Radial emittance.

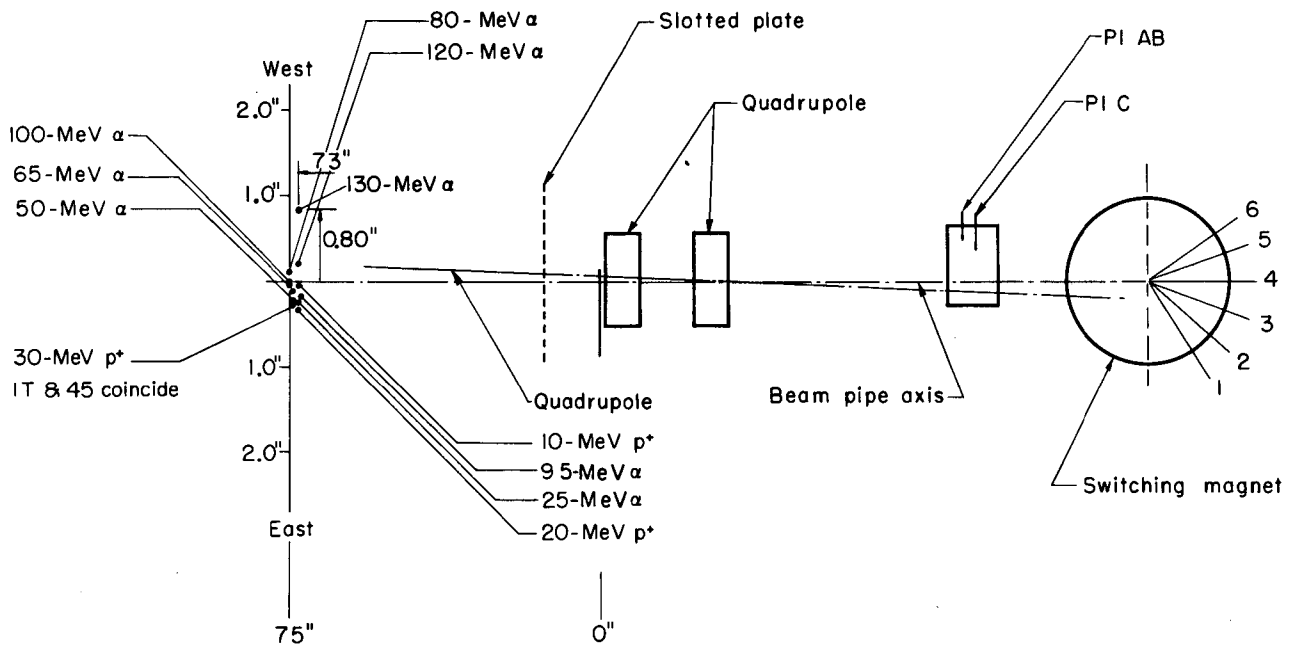


Fig. E. 1-6. Radial-vertical source positions of various beams.

energy gain per turn, and ν_r the average radial betatron frequency. Since ϵ is proportional to dee voltage V , the change in dee voltage ΔV required to increase P by one is seen to be approximately

$$\Delta V \approx -V\epsilon/E(\nu_r - 1). \quad (3)$$

The intervals between the peaks of Fig. E. 1-4 are in good agreement with Eq. (3). The machine was initially tuned for 51.5 kV, which means the external beam had been maximized with center-region parameters and frequency for this dee voltage.

Emittance and Effective Sources

The emittance of the 88-inch cyclotron for 65-MeV α has been measured, radially as well as vertically, for beam currents between 2 and 20 μA continuous beam, and in one case (vertically) for a pulsed beam with a current, during the pulse, of 450 μA internal and 70 μA external. The emittance remained constant radially and vertically. We have measured a radial emittance (Fig. E. 1-5: area of $x, dx/ds$ phase space) for 65-MeV α , of 90% of the beam current contained within 50 mm mrad and a comparable vertical emittance of 90 mm mrad. The accuracy of the measurement is about $\pm 20\%$. This is in good agreement with theoretical calculations made by Dr. Alper A. Garren for the emittance immediately after the deflector channel of 30 mm mrad (radial) and 60 mm mrad (vertical).

These measurements give only the average beam density in phase space, which is probably appreciably lower than that for the most dense spot.

The same measurements yield the virtual source position and source width. Quite consistently we have measured the virtual radial source to be 2 mm wide and 75 ± 1.5 in. upstream of the physical pole edge of the first quadrupole for all energies. In Fig. E. 1-6 several typical measurements of radial virtual source position

are shown in relation to the quadrupole and switching magnet. The slotted plate and probe P1, operated remotely from the control room, are used to make these measurements. It should be noted that these virtual source positions depend upon the trim-coil solution used (i. e., the relation of internal to fringe field level).

The virtual vertical source height has been measured for 65-MeV α as 7 mm, approximately 60 in. upstream of the physical pole edge of the first quadrupole (Fig. E. 1-7). These measurements also agree quite well with the theoretical predictions.

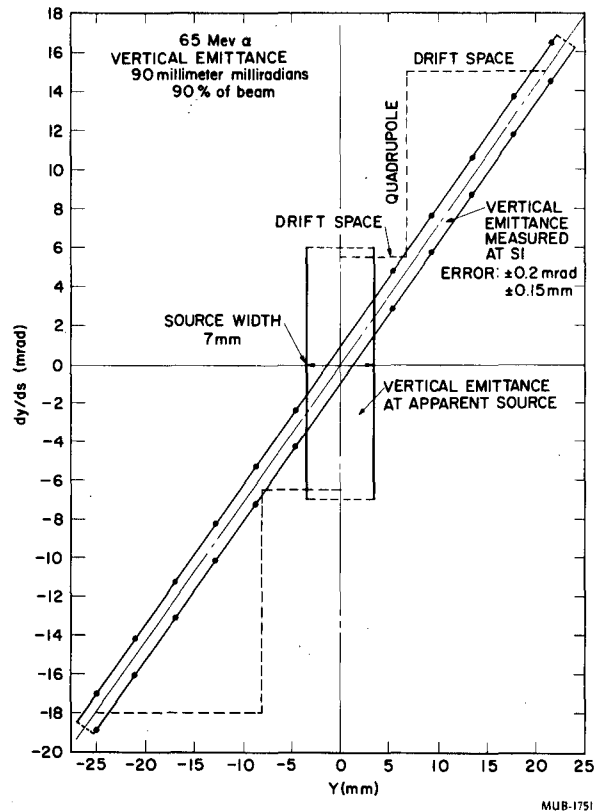


Fig. E. 1-7. Vertical emittance.

2. HIGH-RESOLUTION γ -RAY SPECTROSCOPY WITH LITHIUM-DRIFTED GERMANIUM DETECTORS

D. A. Shirley

Semiconductor Ge(Li) counters¹ are being used to study certain subtle features of several

1. A. J. Tavendale and G. T. Ewan, Nucl. Instr. Methods (to be published).

decay schemes. Some representative spectra are given below (Figs. E. 2-1 to E. 2-3) to illustrate the applications of these high-resolution counters. Their potentials for several counting applications are discussed below.

1. Singles counting

The Ge(Li) counters are particularly useful in resolving high-energy photopeaks. Millicurie sources are required rather than the microcurie sources used with NaI counters, because of the very low photoelectric efficiency of Ge. Most isotopes can be made in mc quantities, however. Accurate determination of relative intensities of high-energy photopeaks is possible with Ge(Li). For low-energy γ rays the Ge(Li) counters can have quite high efficiency and the theoretical resolution is much better than even proportional counters (resolutions of just under 3 keV have

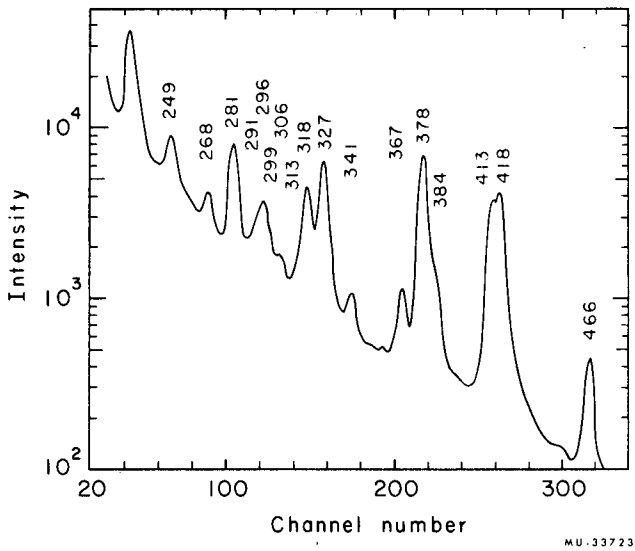


Fig. E. 2-1. Gamma-ray spectrum of $\text{Lu}^{177\text{m}}$, taken with Ge(Li) counters. The energy scale is taken from P. Alexander, F. Boehm, and E. Kankeleit (California Institute of Technology), private communication.

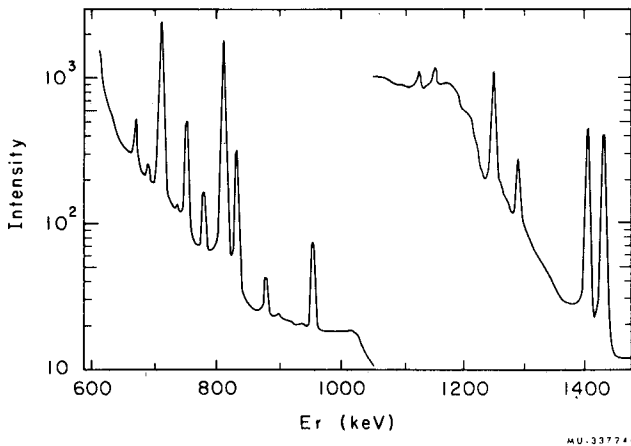


Fig. E. 2-2. Portion of the γ -ray spectrum of $\text{Ho}^{166\text{m}}$, using Ge(Li) counters.

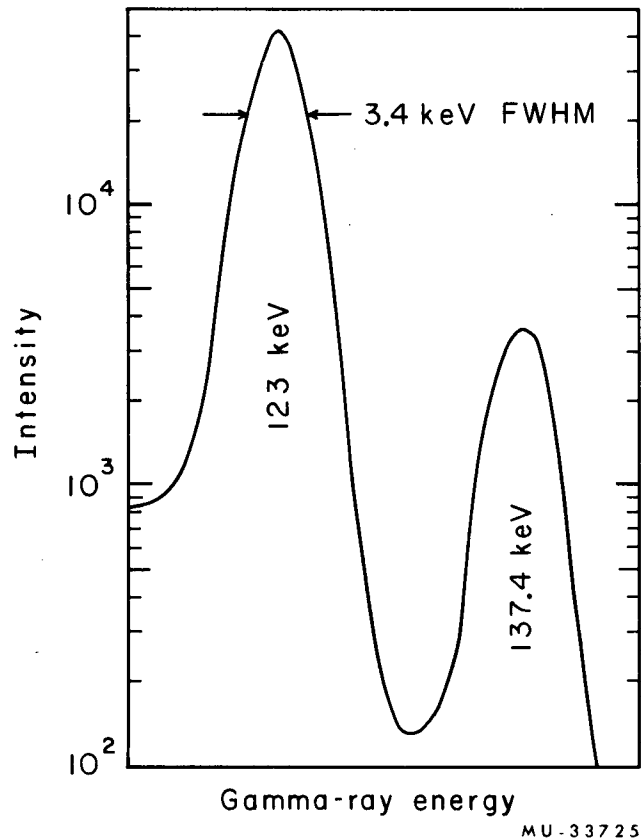


Fig. E. 2-3. The 123-keV and 137.4-keV γ rays following the decay of Co^{57} .

actually been obtained). For applications such as nuclear orientation and Mössbauer spectroscopy, the high signal-to-noise ratio afforded by Ge(Li) counters is very valuable. A particularly obvious case is the decay of Co^{57} , in which the 123-keV and 137-keV γ rays have relative intensities of approximately 9:1. Sodium iodide crystals do not resolve these γ rays, and their anisotropies (following the decay of oriented Co^{57}) just cancel one another. With Ge(Li) counters the resolution is very nearly complete (Fig. E. 2-3).

2. Coincidence work

Here the low photoelectric efficiency makes γ - γ coincidence work with Ge counters very difficult for high-energy gammas. The more common case of high- vs low-energy γ rays is still quite feasible, although the large Compton background underlying low-energy photopeaks will make interpretation difficult.

In both types of application it is clear already that analyzers with many more than the usual 400 channels are needed.

In Fig. E. 2-4 is shown a plot of resolution vs γ -ray energy for Ge(Li) counters. These data are rather preliminary and some improve-

ment is to be expected.

Thanks are due to J. M. Hollander for pointing out the existence of Ge(Li) counters and to W. Hansen, F. Goulding, G. Kilian, and several others for designing and building the counting systems.

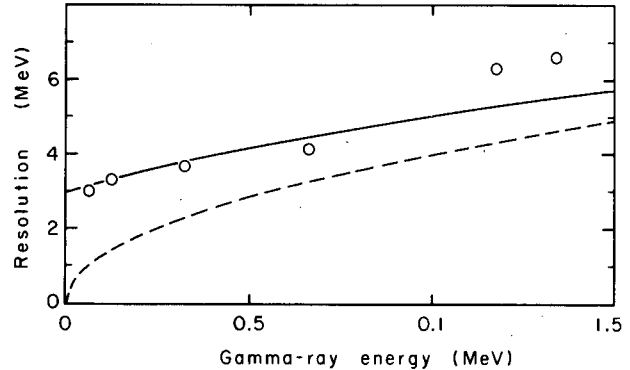


Fig. E. 2-4. Resolution vs energy for γ rays with Ge(Li) counters. Circles are experimental data. Full curve is theoretical resolution with 3-keV contribution from counting system; dashed curve is same with no instrumental contribution.

3. MASS SPECTROSCOPY

F. L. Reynolds

Ion Source for Surface Ionization Studies

An ion source designed for studies of surface ionization and for ionization potential determinations has been constructed. This report covers briefly the source construction details and how the source will be used in experiments in the mass spectrometer.

Figures E. 3-1 and E. 3-2 are schematic drawings of the source, showing two cross-sectional views. Of particular interest is the filament-positioning section, which allows the choice of three different filament surfaces to be studied without changing other experimental conditions. The filament-holding block slides on a supporting way and is operated through a stainless steel bellows from outside the vacuum wall. All filaments present a flat surface nearly normal to the sample beam and normal to the positive ion beam entering the analyzer. These filaments can be viewed at two window positions in the vacuum wall, allowing pyrometer readings of the filament temperature. It will be possible

to study single crystal surfaces of the same element, each filament having different crystal orientation, or to compare three different metals, or to chemically treat one or more surfaces by introducing small gas or solid samples.

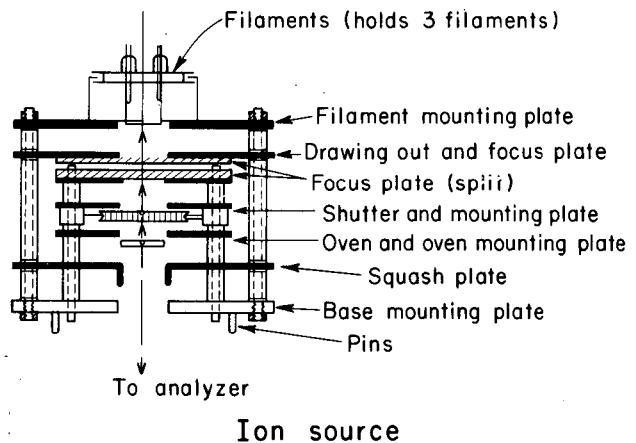


Fig. E. 3-1. Ion source.

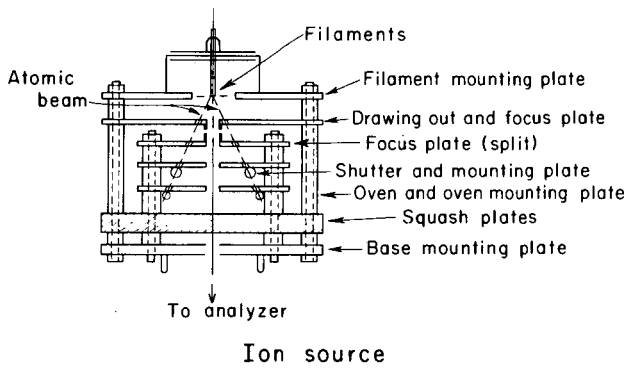


Fig. E. 3-2. Ion source.

MU-33728

The second plate is a drawing-out plate, whose normal potential is only a few volts less positive than the filaments. This plate and the filament-mounting plate are supported by separate insulators from the lower-voltage sections near ground potential. The mounting technique consists of alumina rod and spacers; the rod is threaded on each end for bolting the parts together. The drawing-out plate and the grounded split plate act as a lens system that can be used both for focusing and for slight beam alignment.

The shutter-mounting plate is also at ground potential. The shutter has some unique construction features. It consists of an alumina tube 0.125 in. o. d. by 1.0 in. long and having about a 0.031-in. wall. The outside wall of the tube is ground with a thread cut 32/in. so as to hold a 0.015-in. -diam bare copper wire. The inside bore of the tube holds a nickel tube which is 7/16 in. long and 0.060 in. in diam. This nickel tube can move freely from one end to the other in the alumina tube. Approximately 5/16 in. from one end a 0.020-in. -diam hole was drilled through opposite sides of the alumina tube wall. With the nickel tube at one end, the hole is blocked; when the nickel tube is shifted

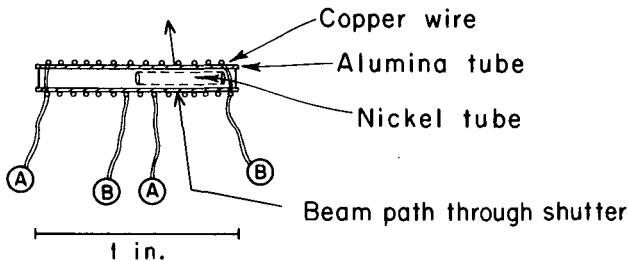


Fig. E. 3-3. Shutter design. Shutter operates by pulse input to (A) (A) to open and to (B) (B) to close.

MU-33729

to the opposite end the sample beam can pass. The nickel slug is operated magnetically. See Fig. E. 3-3 for details.

The following plate holds two oven units which are easily removed from their mounting plate. The ovens are constructed of 0.040-in. tantalum seamless tubing having a 0.001-inch-thick wall. A 0.005- to 0.010-in. beam hole is drilled at the center of this tube. Figure E. 3-4 shows the final oven. These ovens are used once, then discarded.

The last plates are split plates, and are used to squash the ion beam in the "Z" plane to increase total transmission in the mass spectrometer.

In addition to the dual ovens and shutters, there is provision for introducing a directed gas beam so as to impinge on the filament surface under study. This introduced gas sample can be positioned by means outside the vacuum system and its flow controlled to extremely small flow rates. The gas beam is introduced at the same point as one of the hot oven outlets and can thus be controlled by the shutter system. Since this gas beam will have an intensity of from 10^8 to 10^{12} atoms/sec, the pumping system should keep most of the sample from the filaments when the shutter is closed. To stop the flow of gas to the ion-source region an outside valve may be closed and the region from the orifice to the valve can be quickly pumped with an auxiliary system. The gas-handling system is shown as a flow diagram in Fig. E. 3-5. All parts of this system can be baked to 350°C except the manometer. The manometer is valved off after the system is calibrated for a given gas sample.

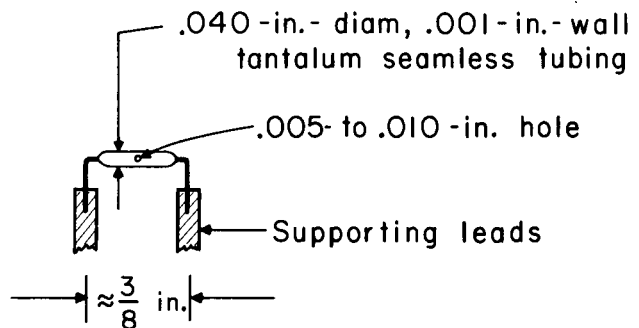
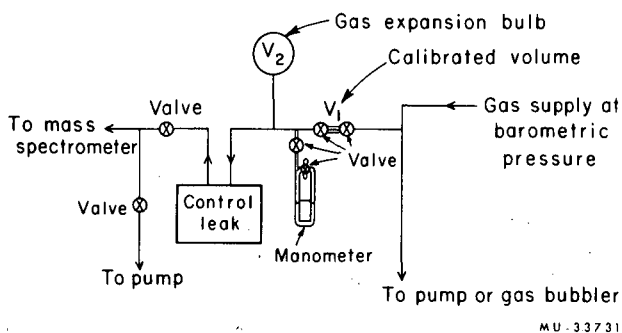


Fig. E. 3-4. Oven design. Seamless tantalum tube ovens are mounted on a removable slide that can be positioned on the oven mounting plate.

MU-33730



MU-33731

Fig. E. 3-5. Gas introduction system.

4. DECAY ENERGY OF U^{235m}

Barbara Bailey and H. P. Robinson

Pu^{239} decays by a emission to an isomeric state of U^{235} with spin = $1/2+$. This isomer then decays to the ground state of U^{235} (spin $7/2-$) by internal conversion with a half-life of 26.6 minutes. The electrons emitted by this decay are of a very low energy; probably less than 100 eV. Conventional means of measuring electron energy (magnetic and electrostatic spectroscopy) are of limited use here, since the energy of the electrons is so low that more than 99% of them are stopped within the sample. To accurately measure the decay energy of this metastable state, a method was devised which would utilize the adsorption of electron energy within the sample. A very sensitive Wheatstone bridge calorimeter has been constructed for this purpose. To keep the heat capacity of the holder as low as possible, one of the pairs of thermistors constituting two arms of the bridge is made to serve both as sample holder and heat detector. The sample of U^{235} , produced by extraction from Pu^{239} , will be placed on the thermistor. The energy released in the isomeric decay is expended within the thermistor, raising its temperature and lowering its resistance in an amount proportional to the power produced by the sample. The resulting unbalance in the bridge is measured by a high-sensitivity mirror-type galvanometer (Leeds and Northrup). Nine feet in front of the galvanometer mirror is a CdSe photo cell connected in series between a 1.5-volt dry cell and the galvanometer terminals. The arrangement is such that whenever the galvanometer beam impinges on the photocell a

small current flows through the galvanometer coil, forcing the mirror back in the opposite direction, thus keeping the galvanometer always in a "null" position. This current is monitored by a VTVM and recorded on a Speedomax recorder.

This arrangement has been found satisfactory, both in stability and sensitivity. To calibrate the calorimeter an rf signal was fed through the sample-holding thermistor. The sensitivity is 4×10^{-10} watt per chart division. The noise level never exceeds one division. Since 10^{-8} watt (approximately) is expected from the U^{235m} , the deflection will be about 25 divisions.

To obtain the sample of U^{235m} an ether extraction is made of Pu^{239} solution saturated with $Al(NO_3)_3$ and containing 7.7 grams of Pu^{239} in the +3 oxidation state. The ether fraction is evaporated down, taken up in an ascorbic acid-HCl mixture, and put through an anion-exchange column. Uranium yields of 60 to 70% are common and the sample is reasonably low in mass. The uranium sample is placed on the thermistor bead from 1λ of HCl solution. It has been found that the additional mass introduced onto the thermistor bead in this way does not adversely affect the performance of the calorimeter.

Special glove boxes are being constructed for the extraction, and an actual experiment will be carried out in the near future.

5. SEMICONDUCTOR RADIATION DETECTORS

Fred S. Goulding and William L. Hansen

During the past year many of the problems in making high-reliability diffused detectors have been resolved. These detectors have a geometry as shown in Fig. E. 5-1. The boron diffusion is done in a reducing atmosphere, with a BI_3 source, and has the function of producing an ohmic back contact. The gallium diffusion is used to compensate for the donor states which will be created by the thermal quartz, and is from an elemental source in a closed box in a reducing atmosphere. Thermal quartz is grown in water vapor at atmospheric pressure at 1000°C . Phosphorus is predeposited in an oxygen atmosphere and diffused in dry nitrogen.

The critical steps in this process that contribute to making it reproducible are: (a) the precise control of the gallium diffusion to exactly compensate for the donors that will appear during growth of the thermal quartz and (b) predepositing the phosphorus under oxidizing conditions to obtain a high surface concentration and diffusing under neutral conditions to obtain a reproducible oxygen concentration. This last step is crucial in that any traces of oxygen during the phosphorus diffusion cause erratic changes in the donor concentration at the SiO_2 -Si interface and negate the effect of the gallium diffusion.

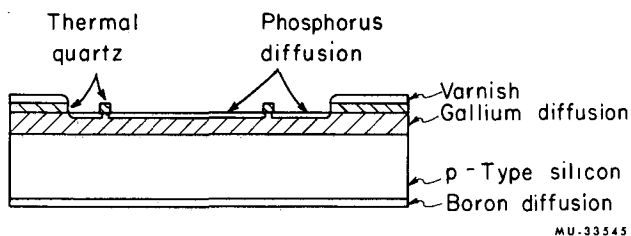


Fig. E. 5-1. Geometry of diffused detector.

As an example of the control possible by this process, 104 detectors were made from $4000\ \Omega\text{-cm}$ silicon in continuous batches with the following specifications and criteria for acceptance: 52 to be 12 mm diam with maximum FWHM for Am^{241} α 's of 18 keV; 52 to be 18 mm diam and to have maximum FWHM for Am^{241} α 's of 30 keV with the guard electrode disconnected. Fifty of each type met the requirements and most were used successfully in experiments.

Several transmission counters were also produced by this process, which had an energy loss equivalent to less than $1\ \mu$ of silicon. It is hoped that, in the future, experience will allow us to adapt these techniques to very high and very low resistivities and to n-type silicon.

Significant progress has also been made in understanding and producing thick lithium-drifted silicon detectors. A simple, completely automatic drifting apparatus has been devised which allows one to drift to any predetermined distance from a back contact without operator attention. It has been found possible, using this apparatus, to produce thin entrance windows without encountering the injection noise that usually results from surface-barrier contacts. An important benefit derived from using this drifting technique is that it allows one to isolate the excess noise produced by the detector to that of the junction intersection with the surface. Some success has been achieved in pacifying this surface.

Gamma detectors with usable efficiency have been made from lithium-drifted germanium used at 77°K . The detectors produced to date have been 2 to $4\ \text{cm}^2$ and 3 mm thick, and give a FWHM for the photopeak from Cs^{137} of 6 keV. It is hoped that much thicker devices can be made in the near future.

6. A LINEAR AMPLIFIER AND GATING SYSTEM

Fred S. Goulding and Donald A. Landis

The design and development of a new transistorized linear amplifier which includes fast coincidence and gating facilities has been completed, and about 20 of the units are in use. The

linear amplifier and associated preamplifiers provide the required flexibility to permit optimization of signal-to-noise ratios for all types of detectors. In semiconductor detectors ex-

hibiting high leakage, for example, very short integrating and differentiating time constants (0.1 μ sec) may be employed to yield the best possible energy resolution. As the available pulse-height analyzers are unable to accept very short pulses the amplifier contains a pulse shaper to produce a suitable signal for analyzers. For many applications delay-line shaping (single or double) is employed, and the design allows for delay lines ranging from 0.1 to 1.5 μ sec.

To supplement the primary function of the unit, the following subunits are also included:

- (a) A single-channel analyzer unit.
- (b) A linear gate unit which produces pedestal and signal breakthrough smaller than 5 mV.
- (c) A biased (or window) amplifier permitting expansion of small parts of a spectrum by factors as high as 20.
- (d) A base-line crossing unit which produces

a timing pulse corresponding to the zero crossing time of a double-delay-line shaped pulse.

(e) A fast coincidence circuit that accepts inputs from the base-line crossing units attached to one, two, or three amplifiers.

These facilities allow two of the units to replace a complete fast-slow coincidence system with improved performance, better reliability, and much smaller size.

A number of these amplifiers are presently used in fission fragment- γ coincidence experiments, making possible an experiment previously impossible. Further amplifiers are used in nuclear reaction experiments at the 88-inch cyclotron, and two are used as part of the particle-identifier system. A number of units are used in miscellaneous applications. Twelve amplifiers have operated for more than 6 months with no failures of any kind.

7. A METHOD FOR PHOTOTUBE NOISE REJECTION IN LOW-ENERGY X-RAY SCINTILLATION SPECTROMETRY*

Donald A. Landis and Fred S. Goulding

A simple method has been devised to reject phototube noise pulses from spectra produced by low-energy x rays in scintillation spectrometers. The method is based on the fact that the x-ray pulses have a slow rise, characteristic of the NaI-Th scintillator, while the phototube noise pulses exhibit a fast rise. With the standard amplifier system described in the previous paper, the timing pulse produced by the base-line crossing provides a sensitive measure of

the pulse rise time. When this time is measured with reference to the start of the pulse, or some other suitable reference time on the pulse, its value can be used to determine whether the pulse was due to an x ray or was a phototube noise pulse.

Together with these investigations, studies of phototubes have shown that the Amperex XP1010 is consistently an excellent phototube for low-energy x-ray work. Using this type of tube and the noise-rejection system, 48% resolution (FWHM) is obtained on a 5.9-keV x ray (Fe⁵⁵), and noise counts above a 2-keV level amount to less than 1 count per minute.

*To be described in detail at the Scintillation and Semi-Conductor Detector Symposium, Washington, February 1964.

8. AN IMPROVED PARTICLE IDENTIFIER TECHNIQUE

Fred S. Goulding and Joseph Cerny

Studies of nuclear structure involving the bombardment of nuclei by beams of energetic particles (e. g., p' s) require the identification of the reaction products and a determination of their energies. In general, the reaction products of interest may consist of a mixture of protons,

deuterons, tritons, helium-3, and alpha particles. Previous work on particle identifiers has been based on the use of a transmission (ΔE) counter in front of a thick (E) counter which completely stops the particle and measures its remaining energy. The ΔE counter signal in

principle allows the determination of the differential energy loss (dE/dX) of the particle and, since the particle energy is also determined, the type of particle is easily identified. In applying this technique, it has been common to calculate the quantity $\Delta E(E + k\Delta E + E_0)$, where E_0 and k are empirical factors that may be adjusted by the experimenter. Despite the use of these adjustments, this technique for particle identification has proved quite limited and difficult to use.

The new identifier is based on the fact that the range-energy relationship for the range 10 to 200 MeV (which encompasses the complete energy range of the 88-inch cyclotron) can be empirically expressed in the form

$$\text{Range } R = aE^b,$$

where R = range,

a = constant that depends upon the type of particle and upon the absorbing material,

b = constant, with a value of about 1.75.

Using a ΔE counter in front of an E counter, we find:

$$R_1 = aE_1^b,$$

where R_1 = total range,

E_1 = total energy of particle,

and

$$R_2 = aE_2^b,$$

where R_2 = range after ΔE counter,

E_2 = energy after particle passage through ΔE counter;

$$\therefore R_1 - R_2 = a(E_1^b - E_2^b) = \Delta E \text{ counter thickness } T,$$

$$\text{i. e., } \frac{T}{a} = (E_1^b - E_2^b) \\ = (E + \Delta E)^b - E^b,$$

where

$E = E_2$ = energy in E counter,

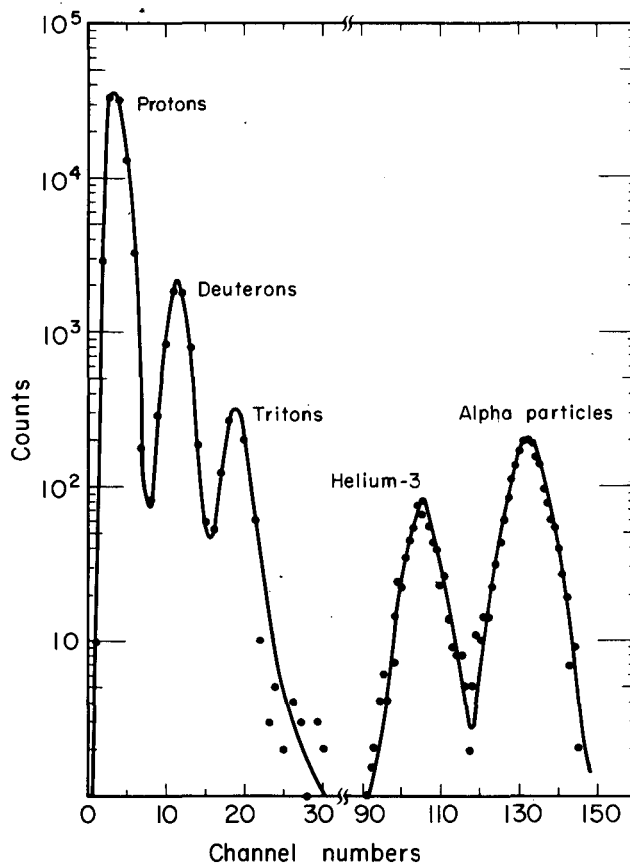
and

ΔE = energy in ΔE counter.

Semiconductor detectors are used for E and ΔE counters to provide electrical signals proportional to E and ΔE . These signals are amplified and fed to the identifier unit, provided that they are in coincidence and that they fall within a selected amplitude range. The most important circuit in the identifier is a function generator which calculates E_{in}^b (where E_{in} is the input to it). Calculation of E_{in}^b is performed in about 1 μ sec by taking the logarithm of E_{in} , multiplying it by b , and determining the antilogarithm of the result. The E signal feeds this function generator and, after 1.5 μ sec, the ΔE signal is added to the E signal at the input of the function generator. The resulting step in the function-generator output is then proportional to $(E + \Delta E)^b - E^b$.

Determination of this step amplitude provides a signal which, in principle, has a fixed value for each type of particle. Because of noise in the detectors and amplifiers some modulation of the identifier signal occurs, but in practice this is insufficient to cause ambiguity in the identification of particles. A preset control allows adjustment of the constant b , but a fixed value of about 1.75 has been found quite satisfactory. Therefore, no adjustments are required before the instrument is used, and the time previously devoted to identifier adjustments is saved. The major advantage accrues, however, from the fact that the calculations performed involve only total energies and not dE/dx . Thus, the identifier can handle simultaneously all five kinds of particle, each over a wide energy range.

Experimental work so far has used the particle identifier for separating reactor products from motor pickup reactions. Figure E. 8-1 shows a typical identifier spectrum obtained by using a 40-mg/cm² phosphorus-diffused Si ΔE detector and a 240-mg/cm² lithium-diffused Si E detector. It should be noted that this spectrum was optimized for separation of charge-2 reaction products, by using this ΔE detector.



MU-33319

Fig. E. 8-1. Particle-identifier spectrum from the reaction of 40-MeV protons on O^{16} at 28° (lab).

Much better separation of the charge-1 reaction products can be obtained by increasing the thickness of the ΔE counter. This excellent separation of the charge-2 reaction products greatly

exceeds that previously obtainable with the old "multiplier" type of particle identifier, and, as noted earlier, is accomplished without any tedious adjustments of parameters.

9. AUTOMATIC RECORDING OF INFORMATION FROM SPECTROGRAMS

Francisco O. de Haro, Michiyuki Nakamura, and Kenneth C. Ward

An electronic system to rapidly record measurements of wavelength from a spectrum line comparator directly on magnetic tape is being assembled in the Laboratory. The system comprises a Grant Instrument Spectrum Line Measuring Comparator, data-handling electronics, and a Precision Instrument Incremental Tape Recorder. The technique employed is a development of previous automatic spectrum line comparators.^{1,2}

On the comparator the spectrogram is moved at constant speed under a projection lens. A digital signal continuously represents the spectrogram's relative position, accurate to within a micron. A photomultiplier behind a

1. G. R. Harrison, Automatic Measurement, Reduction and Recording of Wavelengths from Spectrograms, *J. Opt. Soc. Am.* 25, 169 (1935).

2. G. R. Harrison and J. P. Molnar, Photoelectric Measurement of Scale Marks and Spectrum Lines, *J. Opt. Soc. Am.* 30, 343 (1940).

slit at the lens's focal plane generates a signal proportional to the light transmission through the spectrum line as it passes under the lens. This signal is used to determine the center, width, and relative intensity of the spectrum line. The resulting information is then printed in IBM format on magnetic tape. Spectrogram identification information set into panel switches is recorded on the tape.

The system has the advantages that (a) it makes feasible the recording and subsequent reduction of nearly all the information on a spectrogram; (b) the spectrum lines are read at a rate of 1000 lines per minute; (c) measurement is uniformly accurate; (d) automatic sequence of operations reduces operator errors; (e) the intermediate step involving IBM punch cards or punched paper tape is eliminated; (f) information is recorded compactly on magnetic tape in form ready for computer ingestion; and (g) the system may be operated by a relatively inexperienced person.

10. IRON-FREE SPECTROMETER POWER SUPPLY AND CURRENT-STEPPING SYSTEM

Paul Salz, Donald E. McClure, and J. M. Hollander

During the past year the power supply and automatic current-stepping system of the iron-free beta spectrometer have been brought into routine operation, and the performance of all parts of the system now approaches closely or exceeds the design specifications.

At present the maximum current variation (measured over a period of several hours) is $\approx 3:10^5$. This variation is caused mainly by the cycling of temperature in the spectrometer cooling system ($\pm 0.4^\circ\text{C}$), in which the sensing resistors in the current-control feedback system are located. Because the short-term current stabil-

ity is now better than $1:10^5$, it is expected that the overall stability will equal $1:10^5$ when the temperature fluctuation of the cooling system is reduced to $\pm 0.2^\circ\text{C}$. To achieve this reduction, a modification of the coolant temperature regulator has been designed; installation will be made during the coming months.

A high degree of current stability is desirable in an instrument of this type, for in combination with the automatic scanning feature it allows full use to be made of its capabilities for precision measurement. Figure A. 5-1 in this report illustrates this capability. It would have

been difficult to collect data with comparable statistical accuracy by manual operation because of the prohibitive amount of effort required.

The current-measuring system has been completed by the recent installation of a Guildline Model 9144 precision potentiometer. This potentiometer is a four-dial, six-figure instrument with a linearity of better than 2 ppm and a stability of 1.5 ppm per year. Relative spec-

trometer currents are measured with this instrument by reading the IR drop across a thermostated 0.01- Ω precision resistor. Current measurements can be made with an accuracy of 0.001 to 0.002% with this potentiometer. The null detector in use is a Guildline Type SR-21 Galvanometer and No. 5214 Galvanometer Amplifier.

A full report on the system is in preparation.

11. A DIGITAL GAIN-STABILIZATION SYSTEM

Michiyuki Nakamura and Richard L. LaPierre

A method for stabilizing semiconductor-detector systems, and hence realizing the full resolution of the detector, has been developed.

The basic system concepts, as well as a mathematical analysis of the stabilizer's properties, have been issued by Ladd and Kennedy.¹ The digital stabilizer divides the region of any selected peak of a multichannel analyzer spectrum into two segments. Counts occurring in the lower segment of the selected peak add counts to the contents of a reversible scaler, whereas counts occurring in the upper segment subtract counts from the scaler's content. As the position of the peak shifts owing to gain changes, the relative counting rates of the two segments change, thus producing a net increase or decrease of the reversible scaler's contents. A digital-to-analog converter generates a control voltage which is proportional to the contents of the reversible scaler.

We have used this control voltage to operate a variable-gain amplifier² inserted between the

preamplifier and the main linear amplifier of our stabilized system.

The unique feature of this system lies in the achievement of simplicity in operational setup without any sacrifice of system flexibility. This is accomplished by routing the digitized pulse height of the analyzer to a binary coded decimal subtract scaler which has been preset to the channel location of the peak to be used for stabilization. The null-detection approach employed here simplifies the problem of determining whether the count occurred in the lower or upper segment of the peak. Appropriate gating is then used to add or subtract counts from a reversible scaler, the contents of which are used to produce a control voltage.

Only two sets of decimal switches are needed when the digitized pulse is handled by a null-detection scheme. One switch permits the operator to select the desired peak; the other enables him to select the maximum number of adjacent channels to be used for stabilization.

1. J. A. Ladd and J. M. Kennedy, A Digital Spectrum Stabilizer for Pulse Analyzing Systems, CREL-1063, Dec. 1961, Chalk River, Ontario, Canada.

2. Michiyuki Nakamura and James E. Ream, Use of a Variable-Gain Amplifier for System Stabilization, in Chemistry Division Annual Report, UCRL-10624, Jan. 1963, p. 283.

12. MÖSSBAUER EFFECT INSTRUMENTATION

Ronald Zane

Mössbauer effect experiments performed with a sine-wave drive result in a cosecant display on the pulse-height analyzer spectrum display. The nonlinearity of the display reduces the ease of data acquisition. R. L. Cohen, P. G. McMullin, and G. K. Wertheim of Bell Telephone Laboratories (Rev. Sci. Instr. 34, No. 6, 1963) have described a linear velocity drive system for Mössbauer effect experimentation. The necessary condition for a linear display on the pulse-height analyzer in Mössbauer experiments is that the sum of the absolute values of the derivatives of the velocity wave forms for alternate half cycles of the velocity wave form be equal to a constant throughout the cycle. A linear triangular wave shape meets this condi-

tion, as does an alternating exponential wave shape. A drive system modeled after the Bell Laboratories system is being developed here.

It is possible to produce a linear Mössbauer spectrum by subtracting the effect of the drive wave shape from the spectrum curve. Mössbauer effect pulses fed through the velocity wave form modulator may be fed into the analyzer in the "add" mode of operation. Random pulses, of the same average frequency as the Mössbauer pulses, may be fed through the same modulator and fed into the analyzer in the "subtract" mode. The results should be a straight-line spectrum on the analyzer with well-defined absorption lines.

13. ANALOG GAIN STABILIZER

Francisco O. de Haro

An instrument suitable for stabilizing nuclear spectra recording systems was developed. The circuit is in principle similar to the one described by DeWaard,¹ with the exception that a variable-gain amplifier is used to correct for the fluctuations in gain, instead of controlling the voltage supplied to the detector.² This

1. D. DeWaard, Stabilizing Scintillation Spectrometers with Counting Rate Difference Feedback, *Nucleonics* 13, 36 (1955).

2. Michiyuki Nakamura and James E. Ream, Use of a Variable-Gain Amplifier for System Gain Stabilization, UCRL-10624, Jan. 1963, 283.

makes the instrument useful with either scintillators or solid-state detectors, as long as a well-defined peak is provided for control purposes. If this peak does not exist in the spectrum to be recorded, an auxiliary radioactive source or a light pulser can be used; for this case an "external trigger" feature is included, which prevents the pulses from the recorded spectrum from getting into the controller circuit.

The stability factor (change in relative gain of the system when the AGS is excluded, compared with the change in relative gain when it is included), is larger than 100.

E.14. HILAC OPERATIONS AND IMPROVEMENTS

Albert Ghiorso and Robert M. Main

This material is covered in an article appearing on page 52.

F. CHEMICAL ENGINEERING

1. SULFATE REDUCTION BY BACTERIA.

Mark Leban and Charles R. Wilke

Bacteria of the genus *Desulfovibrio* use sulfate instead of oxygen as the oxidizing agent in their metabolism, expiring sulfide. A number of uses exist for a means of converting sulfate to sulfide cheaply, indicating a possible use for these bacteria. Another possible application would take advantage of their ability to achieve partial fractionation of sulfur isotopes. They are already of considerable importance as geochemical agents and as irritants because of the corrosive and noxious nature of hydrogen sulfide.

A comprehensive survey of the literature supplied ample data on the ecology, isolation, metabolism, and cultivation of *Desulfovibrio*, but virtually no quantitative data on their rate of sulfate reduction. Such data are not only of scientific interest, they are also required for evaluation of any scheme using the bacteria.

The necessary data could be obtained only with a pure culture of the bacteria. A halophilic strain was sought because sulfate is an undesirable impurity in many commercial salt brines. No such strain was available from culture collections; a direct isolation was necessary. A pure strain, *Desulfovibrio aestaurii*, was eventually isolated from the mud of a marine saltern. The isolation proved difficult. Conventional methods--including enrichment culture techniques, streak plate and pour plate methods, the dilution shake culture technique, micromanipulation, and the use of certain inhibitors--were generally unsuccessful, principally because of the bacteria's sensitivity to oxygen, their distaste for solid media, and the presence of a vig-

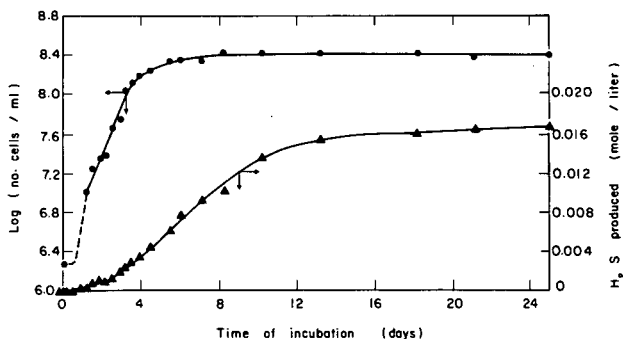


Fig. F. 1-1. Growth curve of *Desulfovibrio* in complex lactate medium at 30° C. Experiment No. 1.

orous contaminant. Isolation was finally achieved independently with two methods, a dilution method and a method that discriminated on the basis of motility. A set of standard tests showed conclusively that the isolated organism was *Desulfovibrio aestaurii*.

Batch experiments were conducted with the isolated strain in which cell and sulfide concentrations were measured periodically throughout the life of the culture. The effects of sodium chloride, sulfate, and yeast extract on the sulfate reduction rate were determined in the experiments. Typical results are shown in Fig. F.1-1.

The bacteria could be grown in salt concentrations greater than 12% only by gradual adaptation, indicating that the strain was tolerant of high salt concentrations, but not halophilic. Figure F. 1-2 shows how changing the sodium chloride concentration changed the rate of sul-

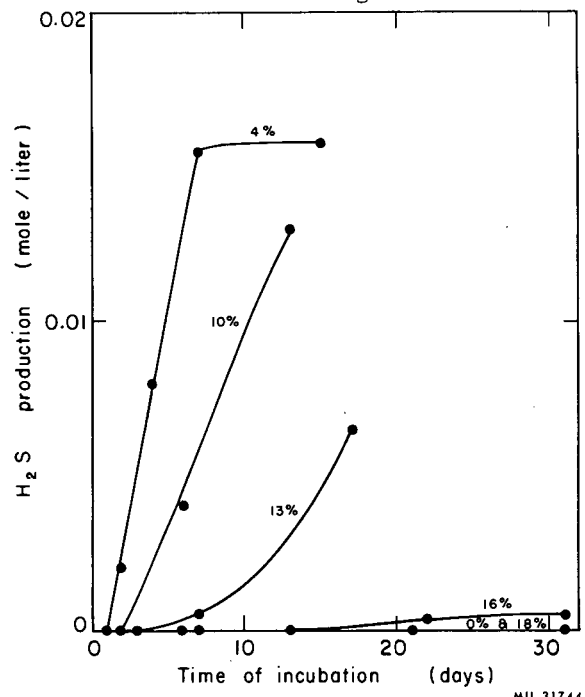


Fig. F. 1-2. Sulfide production by a pure culture of *Desulfovibrio* at different salinities. (The curves correspond to various wt percentages of NaCl in the medium.)

fate reduction. Rates at high salt concentrations were increased considerably by adaptation, ultimately leading to a significant growth in 16% salt solutions. Adaptation to higher salt concentrations should be possible.

Figure F.1-3 shows sulfate concentration as a function of time for different initial sulfate concentrations. The initial lactate concentration was changed in proportion to changes in the initial sulfate concentration, but the initial concentrations of all other nutrients were kept constant.

Lactate was the carbon source in all the rate experiments, but the addition of yeast extract greatly enhanced growth. Correlations for the rate of sulfate reduction per bacterium were developed from the experimental data. The possible performance of a continuous reactor was examined on the basis of the correlations.

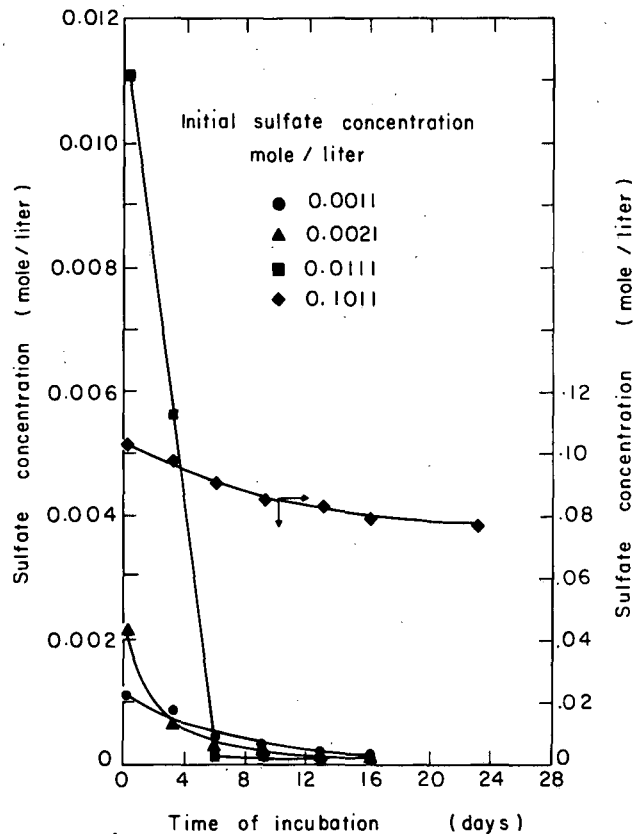


Fig. F.1-3. Sulfate reduction at various initial sulfate concentrations.

2. TURBULENT EXCHANGE OF MOMENTUM, MASS, AND HEAT BETWEEN FLUID STREAMS AND PIPE WALL*

D. T. Wasan and C. R. Wilke

The turbulent exchange of momentum, mass, and heat in the vicinity of a boundary is encountered in many engineering processes. It is well established that in the vicinity of a boundary the turbulent exchange of momentum, mass, and heat is governed not only by molecular motion but also by an eddy motion. In the past a number of empirical expressions have been proposed for eddy viscosity variation near a wall.¹ It is noted that the success of any analysis in predicting rates of mass and heat transfer depends to a considerable extent on how the eddy variation near the wall is chosen.

* Summary of the paper to appear in the International Journal of Heat and Mass Transfer (Mollier Commemoration Issue) (1963).

1. T. K. Sherwood, Chem. Eng. Progr. Symp. Ser. 55, 71 (1959).

In this investigation it is considered that the choice of the assumed eddy distribution is justified only if (a) it satisfies the equations of mean motion; (b) it is continuous with respect to that obtained from Von Karman distribution in the turbulent core region; (c) it is compatible with the mean velocity distribution expression and gives no discontinuity in the velocity distribution function over the region from the wall to the axis of the pipe; and (d) it agrees with the experimental mass- and heat-transfer data.

Recently Wasan, Tien, and Wilke² have presented theoretical expressions for the continuous variation of velocity and eddy viscosity for the wall region of pipe flow. In this paper

2. D. T. Wasan, C. L. Tien, and C. R. Wilke, A. I. Ch. E. J. 9, 567 (1963).

we present new correlations relating the fluid friction and turbulent exchange rates of mass and heat over a wide range of Schmidt and Prandtl numbers based on these distributions. The corresponding concentration and temperature distributions for the wall region of pipe flow are also presented.

Mass transfer correlation in the form of Stanton number is given for dilute solutions by

$$St_m = \frac{k_c}{U_{av}} = \frac{f/2}{1 + \sqrt{f/2}[F(Sc, 20) - 13.0]}, \quad (1)$$

where f = friction factor,
 k_c = mass transfer coefficient,
 U_{av} = time-average velocity,
 St_m = Stanton number for mass transfer,
 and Sc = Schmidt number for mass transfer.

The function $F(Sc, 20)$ can be approximated by the following equations:

$$F(Sc, 20) = 13.0 (Sc)^{0.8}, \text{ for } 0.2 \leq Sc \leq 2, \quad (2)$$

$$F(Sc, 20) = 13.8 (Sc)^{0.71}, \text{ for } 2 \leq Sc \leq 100, \quad (3)$$

$$\text{and } F(Sc, 20) = 17.25 (Sc)^{0.66}, \text{ for } 100 \leq Sc \leq 10000. \quad (4)$$

Similar expressions for the heat-transfer

Stanton number can be obtained by replacing function $F(Sc, 20)$ by $F(Pr, 20)$, where Pr is the Prandtl number. Again equations (2) and (4) can be used to approximate the function F .

In Fig. F.2-1 the proposed mass- and heat-transfer Stanton number relationship [Eq. (1)] is compared with heat- and mass-transfer data of many workers at Reynolds number of 10 000.

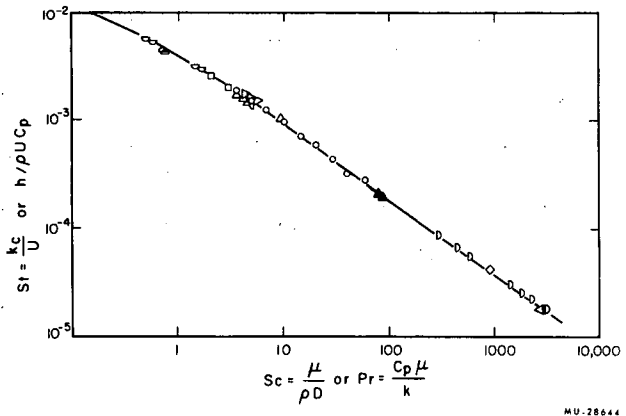


Fig. F.2-1. Comparison of present theory with experimental data at a Reynolds number of 10 000.

3. THE ADDITION OF INDIVIDUAL PHASE RESISTANCES IN MASS-TRANSFER PROCESSES

C. Judson King

The design and analysis of apparatus for mass transfer between two fluid phases is commonly based upon the two-film addition-of-resistances equation,

$$\frac{1}{K_1 a} = \frac{1}{k_1^* a} + \frac{m}{k_2^* a}, \quad (1)$$

where $K_1 a$ represents the volumetric overall mass transfer coefficient for a process with significant resistance afforded by both phases, $k_1^* a$ represents the coefficient for Phase 1 measured in the absence or suppression of resistance in Phase 2, $k_2^* a$ represents the coefficient for Phase 2 measured in the absence or suppression of resistance in Phase 1, and m is an equilibrium partition coefficient representing the slope of the equilibrium curve, dC_1/dC_2 .

Among the criteria necessary for this equation to hold true are the following:¹

(a) k_1 at any point must not depend upon the value of k_2 , and vice versa; the two resistances must not interact with each other,

(b) the ratio mk_1/k_2 must be constant at all points of interface between the fluids.

These conditions are not met in most practical mass-transfer devices, but have rarely been recognized as necessary criteria for Eq. (1) to be valid.

Numerical solutions, employing the 7094 digital computer, have been carried out for two simple models of countercurrent mass transfer.² Model 1 pictures two phases in countercurrent flow across a short interface, each obeying the simple penetration theory. The fluids are hypothesized to be "perfect," i. e., there is complete slip at the interface and there is a flat velocity profile within both phases. Model 2

1. C. J. King, The Additivity of Individual Phase Resistances in Mass Transfer Operations, paper to be presented at Pittsburgh, Pa., meeting of Am. Inst. of Chem. Engrs., May 1964;

Submitted to A. I. Ch. E. J.

2. C. J. King, Mass Transfer During Short Surface Exposures in Countercurrent Flow, UCRL-11196, Jan. 1964.

depicts a more realistic situation corresponding to countercurrent contacting of a gas and a liquid over a short exposure interval. The liquid phase is again described by a simple penetration model, but the gas-phase velocity profile is given by a boundary-layer approximation. The total rates of mass transfer for both models are compared with the rates predicted by simple addition of resistances [Eq. (1)] in Fig. F.3-1. K_1/K_{F1} represents the ratio of the actual effective overall mass-transfer coefficient to that predicted by Eq. (1); R represents the group mk_1^*/k_2^* , which is the ratio of the two individual phase coefficients in Eq. (1). The rates are always higher than predicted by Eq. (1), by a maximum of 20% for Model 1 and 14% for Model 2. Model 3 on the figure refers to the case of a penetration model in Phase 1 coupled with a simple film model for Phase 2.

Large-scale equipment, such as packed and plate towers, may be considered to be made up of many short fluid surface exposures of the sort considered in the above numerical solu-

tions.¹ Although the rate of mass transfer in any one exposure interval should be greater than that predicted by Eq. (1), there will be an additional effect when the rates for all exposure intervals are compounded into a single gross observation of mass-transfer rate. To the extent that the group mk_1^*/k_2^* varies markedly from one exposure interval to another, the observed mass transfer coefficient will tend to be less than that predicted by Eq. (1) when applied to the entire apparatus. This is a necessary result of the violation of Criterion 2 above. In packed and plate columns this effect is apparently sufficiently great to cause mass-transfer coefficients for the absorption of ammonia, methanol, acetone, etc., from air into water to be less than those predicted by Eq. (1) from vaporization and oxygen-desorption data. Often the reduction is by a factor of 100% or more. Another interesting consequence of this concept is that the "effective" interfacial area for absorption, currently employed for design, should vary with changes in solubility of the gas being absorbed. Present data are inadequate to test this prediction.

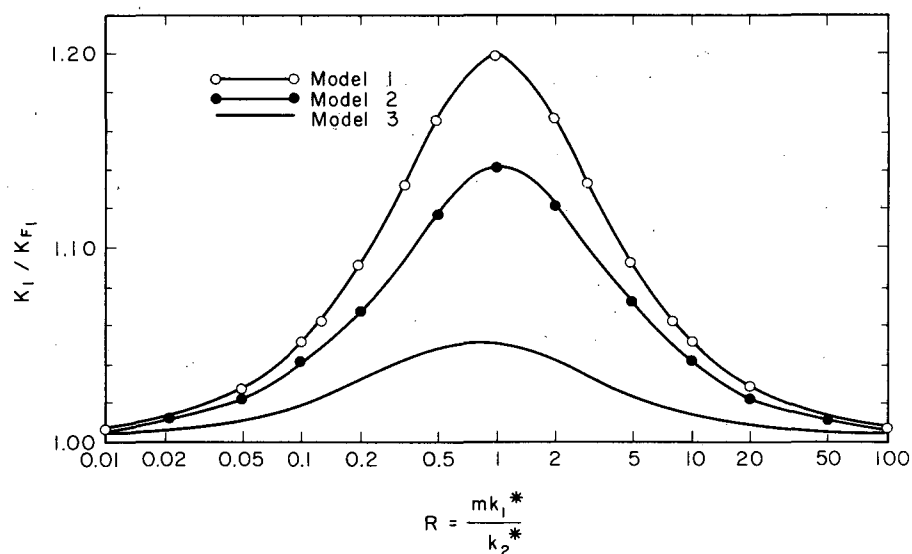


Fig. F.3-1. Overall mass-transfer coefficients--deviation from Eq. (1).

MU-33223

4. MECHANICAL AND CHEMICAL PROPERTIES OF NONEQUILIBRIUM LIQUID-LIQUID INTERFACES--STUDIES WITH THE OSCILLATING JET

Alfred E. Vandegrift and T. Vermeulen

The oscillating jet formed by flow through an elliptical nozzle or orifice has been investigated as a means of measuring dynamic interfacial tension in the 0.01-to-0.1-second time range. The interfacial tension varies with interface concentration of a transferring solute; the

variation can be calibrated in separate equilibrium experiments. During mass transfer from the jet liquid to the surrounding liquid, or vice versa, a change in interfacial tension is indicated by a variation in the wave length between successive nodes of the jet. An initial phase of

the study has just been completed,¹ and a second phase will be started soon with the aim of improving the precision of the experimental technique.

In the initial stage, the mathematical behavior of the liquid-liquid system has been solved for the first time, with the aid of computer calculations; the exact solution previously available, developed by Niels Bohr in 1909, applies only to liquid-gas systems. A parametric solution of the simultaneous differential equations indicates that the dimensionless groups involved are the interior Reynolds number $a_i w_i / \nu$, the "wave number" $2\pi a_0 / \lambda$, the viscosity ratio μ_e / μ_i , the density ratio ρ_e / ρ_i , and the Weber number $\sigma / \rho_i w_0^2$. The relation between these groups, for a representative set of values of the parameters, is shown in Fig. F. 4-1. It was also necessary to solve for the radial velocity distribution within the jet, treating it approximately as being circular in cross section. These calculations are now undergoing further refinement preparatory to publication.

On the experimental side, about six satisfactory nozzles have been found (in the 1-to-2-mm size range, from capillary glass tubing) out of more than 200 made and tested. The apparatus that has been constructed and operated has been found relatively satisfactory for equilibrium measurements, but gives jets too short to be suitable for the dynamic studies. In this apparatus, the jet is injected into a stationary

1. Alfred E. Vandegrift, Peter N. Tenney, and Theodore Vermeulen, Liquid-Liquid Interfacial-Tension Measurement with an Oscillating Jet, UCRL-10717, March 1963.

second phase. In future studies it is planned to have the outside phase moving in streamline flow at essentially the same velocity as the jet.

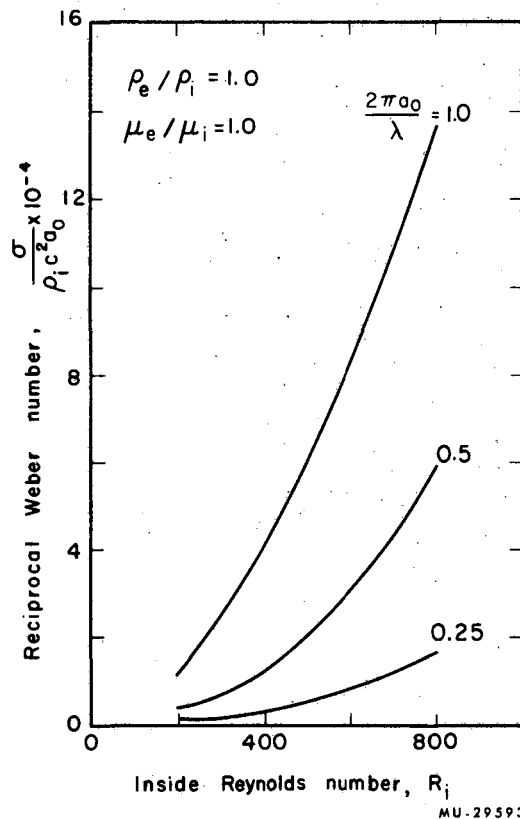


Fig. F.4-1. Relation between dimensionless parameters defining oscillating-jet behavior.

5. KINETIC STUDIES OF SUPER-ACID CATALYSIS

John I. Gmitro, Reid C. Miller, and T. Vermeulen

This study has two longer-term objectives: to determine the catalytic properties of near-anhydrous sulfuric, perchloric, phosphoric, acetic, nitric, and similar acids; and to develop the interrelations between mass transfer and chemical kinetics that apply in different contacting arrangements where acid catalysis is used. An intermediate objective is the development and analysis of a vapor-phase apparatus for nitration of aromatic hydrocarbons.

As a basic step toward the thermodynamic description of mixed-acid systems, the vapor-pressure behavior of aqueous sulfuric acid solu-

tions (in terms of water, H_2SO_4 , and SO_3 as the vapor constituents) has been evaluated from 0 to 100% H_2SO_4 and from -50° to $+400^\circ$ C.¹ The contributions of the different partial pressures, at 25° C, are shown in Fig. F.5-1.

In aromatic nitration, the active intermediate species is believed to be the nitronium (NO_2^+) ion, whose concentration depends upon the relative thermodynamic activity of free pro-

1. John I. Gmitro and Theodore Vermeulen, Vapor-Liquid Equilibria for Aqueous Sulfuric Acid, UCRL-10886, June 1963.

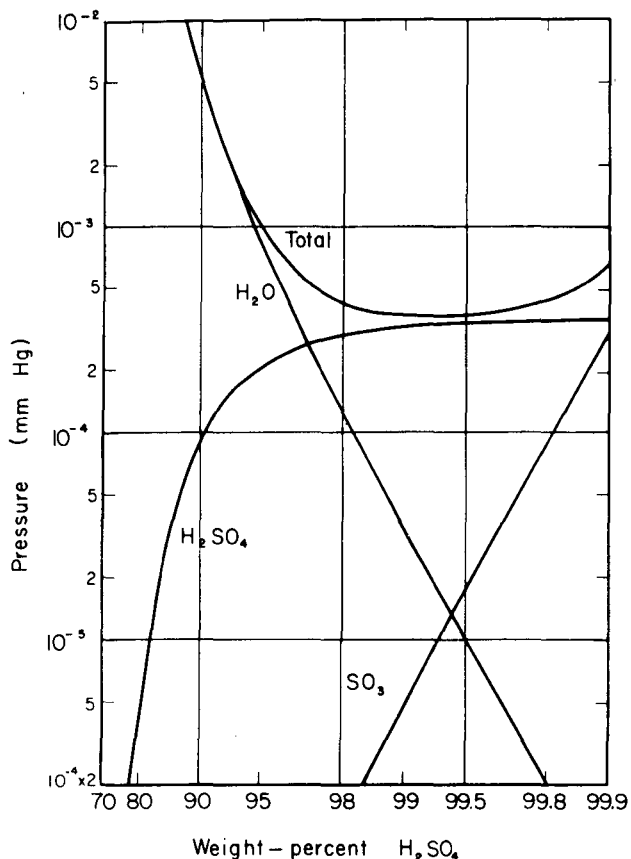


Fig. F.5-1. The sulfuric acid azeotrope at 25°C.

tons (H^+) in the system. The relative rates of nitration have been determined by others for a limited range of HNO_3 and H_2SO_4 mole-fractions. Heterogeneous nitration rates of the aromatic organic compound 1, 3-bis(trifluoromethyl)benzene have now been measured in an extensive range of very concentrated mixed acids (aqueous HNO_3 and H_2SO_4), with each run at essentially constant acid composition.²

2. Reid C. Miller and Theodore Vermeulen, Kinetics of Aromatic Nitration, UCRL-11069, October 1963.

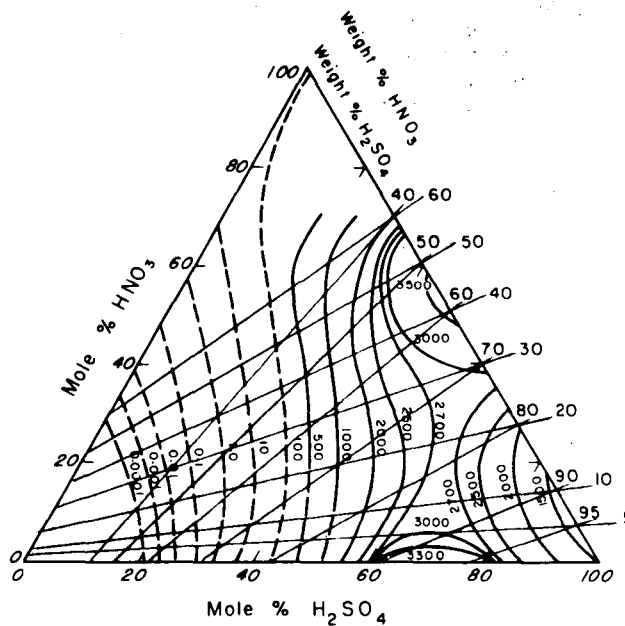


Fig. F.5-2. Values of the apparent rate coefficient k_0 for the rate equation $R = k_0 (HNO_3)_a (ArH)_a$.

The new nitration-rate data are correlated in a manner that indicates, at any given mixed-acid composition, (a) the nonideality of the reaction medium expressed by the activity-coefficient behavior; and (b) the ability of the medium to convert HNO_3 to NO_2^+ , the attacking species in the nitration sequence. To apply this correlation to aromatics having varying resistance to nitration, the correlation has been extended to the dilute mixed-acid region, using equilibrium equations based on the nitronium-ion mechanism. This correlation is generally applicable, except for effects that are not a direct result of the state of the acid medium. One form of plot for the correlation is given in Fig. F.5-2, with the contours representing values of the rate coefficient for nitration relative to 1,3-bis(trifluoromethyl)benzene at 50°C.

6. LIQUID-LIQUID AND GAS-LIQUID AGITATION

Michael W. Clark, T. D. Coughlen, and T. Vermeulen

Power requirements have been measured in the turbulent-flow region for a series of rectangularly shaped vessels. The power-number val-

ues for these experiments proved to lie between the baffled and unbaffled values for a cylindrical tank using the impeller.

The power requirements of agitated liquid-gas systems using both four-bladed flat-paddle impellers and a four-bladed turbine in a baffled cylindrical tank have been investigated and reported.¹ The power-number reduction has been

1. Michael Wayne Clark and Theodore Vermeulen, Power Requirements for Mixing of Liquid-Gas Systems, UCRL-10996, August 1963.

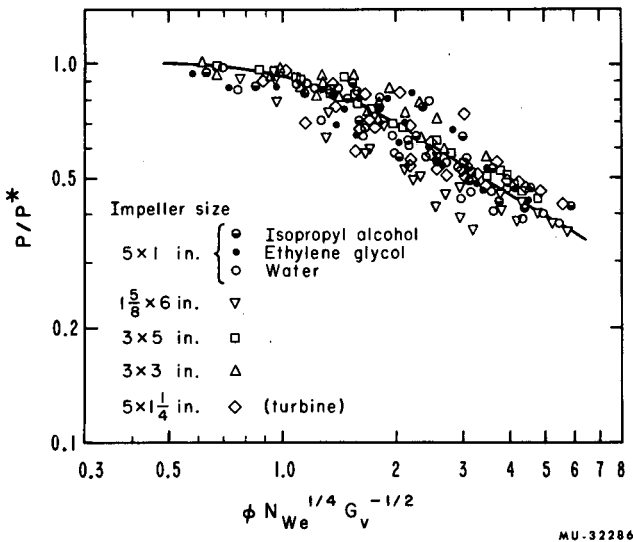


Fig. F.6-1. Correlation of two-phase-to-single-phase power ratio, based on gas holdup, Weber number, and a geometrical factor.

related qualitatively to cavitation, and is correlated as a function of Weber number, geometrical factors, and the volumetric gas holdup, as given in Fig. F. 6-1. The gas holdup has been found to vary with impeller speed and impeller dimensions, as well as with gas flow rate and liquid properties.

Incipient vortex formation, whereby air is introduced downward into an agitated liquid, was encountered and investigated. A correlation involving geometrical factors and the Froude number, shown in Fig. F.6-2, was developed to predict the onset of this phenomenon and the subsequent power-number behavior.

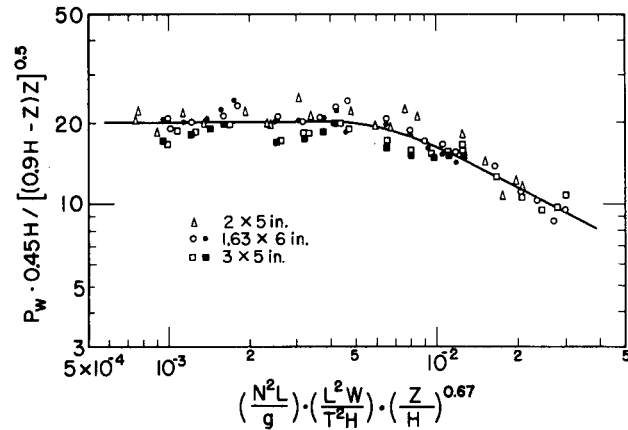


Fig. F. 6-2. Correlation of power number for various impeller sizes and positions.

7. AXIAL MIXING (LONGITUDINAL DISPERSION) IN PACKED EXTRACTION AND ABSORPTION COLUMNS

Alphonse N. Hennico, Joon S. Moon, and T. Vermeulen

Major progress has been made on this long-term problem during 1963. Theoretical results obtained about four years ago, by Miyauchi and Vermeulen, have reached the stage of publication in two articles in Industrial and Engineering Chemistry Fundamentals, in the May and the November issues. A new theoretical analysis of laminar-flow longitudinal dispersion, and its comparison with the longer-established theoretical treatments, are given in a paper by Hennico¹ together with the results of extensive experimen-

tal work. A continuation of this project, by Moon,² has led to refinements in measurement and correlation, and has explored the closely related problem of column behavior under pulsed conditions.

Laboratory studies of liquid-phase dispersion have been continued, both in single-phase flow and in countercurrent operation. The extension to pulsed operation is a means of gaining insight into the fluid-mechanical characteristics

1. Alphonse Hennico, Gabriel Jacques, and Theodore Vermeulen, Longitudinal Dispersion in Packed Extraction Columns, UCRL-10696, March 1963.

2. Joon S. Moon, Alphonse Hennico, and Theodore Vermeulen, Longitudinal Dispersion in Packed Extraction Columns With and Without Pulsation, UCRL-10928, October 1963.

of dispersion, and also allows the evaluation of pulsing as a possible means of improving packed-column performance.

Both the unpulsed and the pulsed single-phase measurements confirm previous observations of a transition between "laminar" and "turbulent" regions, the Péclet number for axial dispersion increasing sharply from the former to the latter. Figure F. 7-1 shows a theoretical interpretation of the difference between the currently observed results for the liquid phase and previous values for the vapor phase³ under laminar-flow conditions; the rise at extremely low Reynolds number, for a liquid, has not been confirmed experimentally but may have been counterbalanced by "channeling" in the 0.0058-in. - particle bed used.

The observed variation in Péclet number (relative to unpulsed operation) as the amplitude and frequency of pulsing increase has been correlated by a combined Reynolds number as indicated in Fig. F. 7-2.

In an extension of the work of Jacques and

3. K. W. McHenry and R. H. Wilhelm, A. I. Ch. E. J. 3, 83 (1957).

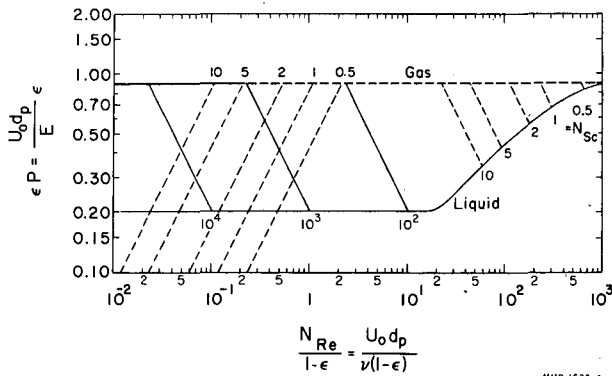


Fig. F. 7-1. Relation between liquid and gas phase dispersion coefficients.

Cotter in this Laboratory, the continuous-phase dispersion behavior has been found to correlate as a function of continuous-phase Reynolds number, packing-particle sphericity, and ratio of dispersed-phase to continuous-phase superficial velocity; the Péclet number may fall to one-tenth, or less, of the single-phase value at high values of the velocity ratio. By contrast, relatively high (and nearly constant) values are obtained for the dispersed-phase Péclet numbers, whether or not the dispersed phase wets the packing. For both phases, pulsed operation gives a higher Péclet number than unpulsed, but general correlations are still lacking.

A series of actual extraction runs has been made in the experimental columns, using diisobutyl ketone and water with acetic acid as solute; and isododecane-water with crotonic acid. The latter system has also been run with pulsing. Analysis of these runs confirms the dispersion-coefficient values measured in unsteady-state runs, along with the method of analysis.

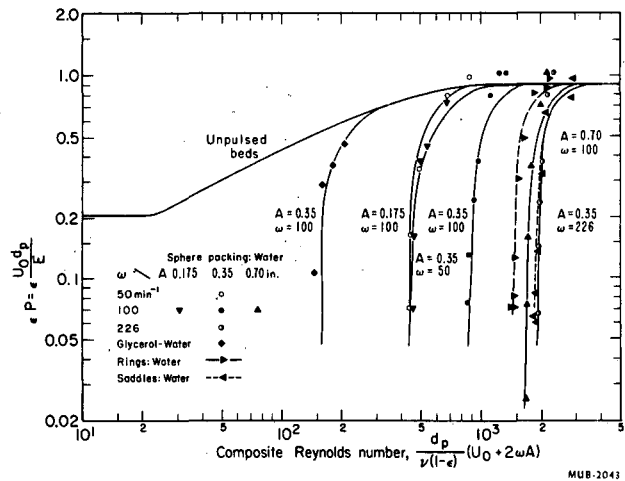


Fig. F. 7-2. Péclet number vs composite Reynolds number for pulsed packed columns.

G. THESIS ABSTRACTS

On the following pages the abstracts of theses issued in 1963 are reproduced from the original documents.

Papers elsewhere in this report cover work described in theses by

Donald S. Burnett (Ph. D.)	Paper B. 4
Michael W. Clark (Ph. D.)	Paper F. 6
John I. Gmitro (M. S.)	Paper F. 5
Alphonse Hennico (Ph. D.)	Paper F. 7
Mark Leban (M. S.)	Paper F. 1
Reid C. Miller (M. S.)	Paper F. 5
John A. Olmsted (Ph. D.)	Paper D. 19
Richard H. Pehl (Ph. D.)	Paper C. 3
Joon S. Moon (Ph. D.)	Paper F. 7
Mannque Rho (Ph. D.)	Paper A. 21
Alfred E. Vandegrift (Ph. D.)	Paper F. 4

(from UCRL-10798
Ph. D. Thesis)

1. EVIDENCE FOR A NEW REGION OF DEFORMATION
WITH LESS THAN EIGHTY-TWO NEUTRONS

Richard N. Chanda
Lawrence Radiation Laboratory
University of California
Berkeley, California

April 29, 1963

ABSTRACT

Experimental evidence for a new region of nuclear deformation in the neutron-deficient rare earths has been obtained through the use of reactions of the type (heavy ion, xn) leading to several new neutron-deficient lanthanum isotopes. Three previously unreported lanthanum isotopes have been identified: La^{126} , La^{128} , and La^{130} , with half-lives of 1.0 ± 0.3 , 6.1 ± 0.6 and 9.0 ± 1.0 min respectively.

The decays of these odd-odd lanthanum isotopes have been investigated using γ - γ coincidence spectroscopy and partial-level schemes are proposed for the respective even-even daughter barium isotopes. Observed energy levels (in keV) with their proposed spins and parities are:

Ba^{126}	256(2+)	716(4+)	1341(6+)
Ba^{128}	279(2+)	764(4+)	\approx 1385(6+)
Ba^{130}	360(2+)	900(1-, 2+)	

Systematics of deformed nuclei are discussed in general and the barium nuclei compared with other deformed nuclei from other regions of deformation. Evidence for the existence of deformation is derived both from the energies of the first excited states and from the ratios of energies expected and observed in rotational bands in even-even nuclei.

(No UCRL number,
Ph.D. Thesis)

2. THE EFFECT OF VARIABLE PROPERTIES ON LIQUID PHASE, LAMINAR FLOW MASS TRANSFER

Alan Emanuel

Lawrence Radiation Laboratory and
Department of Chemical Engineering
University of California
Berkeley, California

September, 1962

ABSTRACT

Mass transfer from a rotating disk has been investigated for liquid systems in which the density, diffusivity, and viscosity are concentration dependent and in which the diffusing species leaves the surface with a velocity large enough to have a significant effect on the transfer rate.

It is assumed that the logarithm of the density is a linear function of the mass fraction of solute, that the velocity profile can be corrected for a variable viscosity by the dimensionless factor $(\mu_{\infty}\rho_{\infty}/\mu_0\rho_0)^{1/2}$, and that the interfacial velocity can simply be treated as an additive term in the velocity expression.

For a number of systems, the diffusion equation is solved numerically with the exact relation between the diffusivity and solute concentration and by an approximate integral method assuming the diffusivity to be a quadratic function of the concentration. Experimental measurements were made for mass transfer of benzoic acid, sucrose, copper sulfate, and potassium bromide into water. It was found that the simplifying assumptions were valid over a wide range of property variations and that the integral and numerical solutions agreed to within 10%.

The observed and calculated results agreed within the experimental error except in those cases in which the viscosity change was greater than a factor of 10. This discrepancy was caused by the breakdown of the variable viscosity correction applied to the velocity gradient. More accurate methods are presented for correcting the velocity in the case of large viscosity changes.

(from UCRL-10649;
Ph. D. Thesis)

3. STUDY OF THE NUCLEAR ZEEMAN EFFECT IN Au¹⁹⁷

Ronald W. Grant

Department of Chemistry and
Lawrence Radiation Laboratory
University of California
Berkeley, California

January 29, 1963

ABSTRACT

Mössbauer experiments have been performed in external magnetic fields up to 86 kG with Pt¹⁹⁷ dissolved in Fe, Co, and Ni sources, and Au absorbers. The magnetic moment of the 77-keV isomeric state of Au¹⁹⁷ was measured as $\mu = +0.37 \pm 0.05$ nm. The hyperfine fields at Au nuclei dissolved in Fe, hex. Co, cubic Co, and Ni were found to be -1420 ± 220 , -980 ± 150 , -990 ± 150 and -340 ± 70 kG, respectively. The magnitude of the hyperfine field was found to be nearly proportional to the effective atomic magnetic moment of the host ferromagnetic material. Experiments were performed in an external magnetic field with sources of Pt¹⁹⁷ dissolved in Be and Pt in an attempt to measure μ directly; however, complicated behavior was observed which is explicable in terms of mixed magnetic dipole and electric quadrupole interactions. The effect of magnetostriction has been observed in ferromagnetic sources which makes sign determinations of internal fields in ferromagnets, using the Mössbauer effect, less straightforward than is usually assumed.

(No UCRL number,
Ph. D. Thesis)

4. DYNAMIC ANALYSIS OF A ONE DIMENSIONAL POROUS ELECTRODE MODEL

Edward Anthony Grens II

Department of Chemical Engineering
University of California, Berkeley, California

ABSTRACT

A one dimensional model is developed to represent flooded porous electrodes in which there is no bulk flow of electrolyte in the pores. In this representation the pore configuration is ignored and the entire electrode treated as a homogeneous macroscopic region of electrolyte with distributed current and species sources. Mass transport in the electrolyte by diffusion and migration is considered. No assumptions of uniformity of electrolyte conductivity or composition are made. The model is capable of incorporating electrode reaction overpotential expressions of quite arbitrary nature.

Analysis of the model is conducted by numerical techniques to furnish descriptions of electrode behavior for both steady state and transient operation. Performance characterization includes electrode overpotential and current and concentration distributions as functions of current drain and system parameters. The computational procedure is implemented on digital computing machinery.

Examples based on the cadmium anode in 5N KOH and on the ferri-ferrocyanide electrode in 2N NaOH are investigated. In these examples overpotential relationships incorporating both forward and reverse reaction terms are used and the inadequacies of approximations to these relationships are demonstrated.

(No UCRL number,
Ph. D. Thesis)

5. The Effect of Buoyancy Forces
on Forced Convection Ionic Mass Transfer
at Horizontal Planar Electrodes

by

Robert Gordon Hickman

ABSTRACT

The effect of buoyancy forces on ionic mass transfer to electrodes in a horizontal flat duct were studied experimentally with both laminar and turbulent bulk flow. Copper electrodes and an acidified cupric sulfate electrolyte were used in obtaining mass transfer data by the technique of limiting currents. The ranges of the significant dimensionless groups covered in the experiments were as follows:

$$10^5 < Gr \text{ (Grashof number)} < 10^{12}$$

$$75 < Re \text{ (Reynolds number)} < 7000$$

$$600 < Sc \text{ (Schmidt number)} < 12,000$$

$$0.05 < \frac{d}{L} \left(\frac{\text{duct diameter}}{\text{electrode length}} \right) < 20$$

With turbulent bulk flow, buoyancy forces were found to have a negligible effect on the mass transfer process in the range of variables covered.

With laminar bulk flow, buoyancy forces can induce secondary flows near the electrode interface in the form of roll cells or even turbulence if the Grashof number is sufficiently high. Either of these free convective secondary flows can dominate the mass transfer process. Average mass transfer coefficients for laminar bulk flow may be predicted by estimating which of the two convective modes (forced or free) controls the mass transfer process and then using the

existing correlating equation appropriate to the controlling mode. If

$$\log(\text{Gr}) \geq 2.964 + \log(\text{Re})$$

the process is dominated by free convection; otherwise forced convection dominates.

The data were compared with either the equation of Norris and Streid:

$$\text{Nu}' = 1.85 (\text{Re Sc } d/L)^{1/3}$$

for forced convection dominated systems, or that proposed by Fenech and Tobias

$$\text{Nu}' = 0.19 (\text{Gr Sc})^{1/3}$$

for free convection dominated systems, where Nu' is the mass transfer Nusselt number. The average deviation of all the data from the appropriate correlating equation when so treated was seven percent.

Other experiments were performed to obtain local mass transfer rates. These showed the transition in the direction of flow from forced convection control to free convection control as a function of the Reynolds and Grashof numbers. The influence of the secondary convective flows on the deposition profiles transverse to the direction of flow was also investigated.

(from UCRL-11049,
Ph. D. Thesis)

6. THE ISOMER RATIO OF Ce^{137m} - Ce^{137g} PRODUCED
IN SEVERAL CHARGED-PARTICLE REACTIONS

Richard Leslie Kiefer

Lawrence Radiation Laboratory
University of California
Berkeley, California

October 17, 1963

ABSTRACT

The isomer ratio of Ce^{137m} - Ce^{137g} is studied to obtain information on the effect of angular momentum in the de-excitation of a compound nucleus. The ratio of the formation cross section of the high-spin isomer to that of the low-spin isomer is measured as a function of energy for reactions induced by He^3 , He^4 , Li^7 , and C^{12} . The ratio is seen to increase with increasing projectile energy. This increase is shown to correspond to an increase in the average angular momentum. The ratio at the peak of the excitation function is found to increase linearly from reaction to reaction with increasing $\langle l \rangle$. Above the peak of the excitation function, the ratio is observed to increase more rapidly. This is considered to be due to the competition of neutron and γ - ray emission that causes the product to be formed from states of high angular momentum.

The cross sections are also measured for the four reactions. Those induced by Li^7 and C^{12} peak 5 to 6 MeV above the cross sections induced by He^3 and He^4 .

The results are compared with calculations based on the Huizenga-Vandenbosch theory. When we calculated the nuclear temperature based on the Fermi gas model and used 0.7 of the rigid-body value of the moment of inertia, the calculated results showed good agreement with the experimental results. Calculations employing a simple pairing model and a superconductor model are also shown.

from UCRL-11028,
Ph.D. Thesis)

7. THE STRUCTURE OF HEAVY NUCLEI:
A STUDY OF VERY WEAK ALPHA BRANCHING

Charles Michael Lederer

Lawrence Radiation Laboratory
University of California
Berkeley, California

September 27, 1963

ABSTRACT

Very weak alpha branching in heavy elements was studied by a recently developed coincidence technique. This technique makes it possible to measure the energies and intensities of both α -particle groups and de-exciting radiation, even when the transition intensities are as low as 10^{-8} relative to the most intense alpha group. Twenty α -particle emitters from Po^{214} to Fm^{254} have been examined.

$00+$ states ("beta vibrations") were observed in six even-even nuclei, and analogous states were found in three odd-mass nuclei. They are in general characterized by low alpha-decay hindrance factors and roughly equal de-excitation by electric monopole and quadrupole transitions. However, the de-excitation of these states is in disagreement with vibrational model predictions in certain cases; more important, the de-excitation and other properties of the states exhibit some irregular variations from nucleus to nucleus which are evidence for some particle character in the states.

Information was also obtained about some other types of levels. A number of $1-$ states ("octupole vibrations") were observed, and a possible $2-$ state was observed in U^{236} . A state that appears to be analogous to the 1 -octupole states of even-even nuclei was observed in U^{235} . In Pu^{239} , a $K = 3/2+ [631]$ band was identified with reasonable certainty, and numerous particle states were observed in Bk^{249} , although it was not possible to classify them. No $22+$ states ("gamma vibrations") were observed, and it appears that the alpha transitions to these states are rather highly retarded.

(from UCRL-10673,
Ph. D. Thesis)

8. MASS-SPECTROMETRIC STUDY OF FISSION FROM THE U^{236}
COMPOUND NUCLEUS AT MODERATE EXCITATIONS

James Anthony McHugh, Jr.

Lawrence Radiation Laboratory and Department of Chemistry
University of California
Berkeley, California

February 12, 1963

ABSTRACT

The helium-ion-induced fission of Th^{232} (U^{236*}) has been investigated by using high-sensitivity mass-spectrometric techniques. The nuclear-charge-distribution function was measured directly for one isobaric sequence and indirectly in another; it was found to be Gaussian and independent of the excitation in U^{236*} . An empirical Z_p function was derived from 12 measured fractional independent yields, and compared with the Z_p function from $U^{235}(n_{th}, F)$. The various postulates of nuclear charge division were discussed. The total number of neutrons emitted per fission as a function of mass ratio was determined from the Z_p function, the neutron yields being found to depend strongly on the asymmetry of the fission mode.

The relative cumulative yields for the majority of isotopes in the mass 131 to 154 range have been determined. The xenon cumulative yields show no structure at these excitations. Information concerning the distribution of independent yields within an element and the formation of the Kr^{85} isomeric states has been obtained for the helium-ion-induced fission of Th^{232} and U^{235} .

(from UCRL-10850,
Ph. D. Thesis)

9. THE EFFECT OF ANGULAR MOMENTUM OF THE COMPOUND NUCLEUS
ON THE RATIO OF THE ISOMERS Te^{119} AND Te^{119m}
PRODUCED IN LOW-ENERGY BOMBARDMENTS

David W. Seegmiller

Lawrence Radiation Laboratory and Department of Chemistry
University of California
Berkeley, California

August 1963

ABSTRACT

The effect of angular momentum on compound nucleus reactions was investigated by measuring the formation cross-section ratios of a pair of isomers produced through compound nuclei- xn reactions.

Five different projectiles were used to produce the compound nucleus Te^{122*} , which yielded the isomers of tellurium-119 through a $3n$ reaction. The projectiles ranged in size from He^3 to O^{18} .

The same isomers were also produced through $2n$ and $4n$ reactions by bombardment of the appropriate tin isotopes with He^3 and He^4 .

A method involving separation of the antimony daughter was devised for determining the isomer ratios. This method was completely independent of any decay scheme.

The experimentally determined ratios (upper-state to lower-state isomer) varied from a low of about 0.75 to a high of about 25. The expected increase of ratio with energy and projectile size was verified. An apparent direct interaction of Li^7 projectiles was observed.

Excitation functions were obtained for the reactions proceeding through the Te^{122*} compound nucleus. The expected shift in peak position with projectile size was clearly demonstrated.

Compound-nucleus calculations were performed by assuming a rounded nuclear potential approximated by a parabola (Bunthorne). Good agreement was obtained between experimentally determined isomer ratios and predictions based upon the calculated average angular momentum of the compound nucleus.

Reasonable estimates of the isomer ratios were obtained by assuming that all compound nuclei with a spin greater than 8 populate the high-spin isomer, while those with a spin of 8 or less yield the low-spin isomer.

Calculations of the Vandenbosch-Huizenga type were performed for the various reactions. Different combinations of input parameters were investigated and the best results were obtained by assuming a spin cut-off parameter of $0.5 \sigma_{\text{rigid}}$ and equal energy, dipole gamma rays of multiplicity defined by

$$\bar{N}_{\gamma} = (\sqrt{\underline{a} E_c}) / 2 ,$$

where $\underline{a} = A/8 \text{ MeV}^{-1}$ and E_c is the nuclear excitation. σ_{rigid} represents the spin-cutoff parameter calculated by assuming that the nucleus has a moment of inertia equivalent to that of a rigid sphere.

(from UCRL-10783,
Ph.D. Thesis)

10. TOTAL-REACTION CROSS-SECTION MEASUREMENTS FOR CHARGED PARTICLES

Bruce D. Wilkins

Lawrence Radiation Laboratory and Department of Chemistry
University of California
Berkeley, California

May 9, 1963

ABSTRACT

Total reaction cross sections have been measured for 10-MeV protons, 22.4-MeV deuterons, and 40-MeV alpha particles on Be, C, Al, Ti, V, Fe, Ni, Cu, Zn, Zr, Nb, Mo, Rh, Ag, Sn, Ta, Au, Pb, Bi, and Th. A beam attenuation method that utilized millimicrosecond electronic techniques was used; these techniques made possible 3% counting statistics to be obtained in 20 minutes. The total reaction cross section σ_R shows structure as a function of A in the vicinity of Ni for proton and alpha-particle bombardments.

The results of an optical-model analysis for 10-MeV protons on Cu, Ni, Al, and Ag indicate that good fits to σ_R and the elastic-scattering angular distributions could only be obtained by using a Gaussian form factor, located on the nuclear surface, for the imaginary optical potential. Furthermore, an optical-model analysis of 48-MeV alpha particles on C^{12} indicates that the addition of total reaction cross-section data places a powerful constraint on the shape of the imaginary potential at the extreme surface of the nucleus.

The experimental techniques used in these measurements are discussed in detail. Improvements in technique for future measurement of σ_R are suggested.

(from UCRL-10625,
M. S. Thesis)

11. MECHANISM OF LIQUID-LIQUID SETTLING

Albert D. Epstein

Lawrence Radiation Laboratory
University of California
Berkeley, California

January 14, 1963

ABSTRACT

The separation of two immiscible liquids in a gravity settler was studied in a program to learn more about the mechanism of the settling process. The liquids used were water and Aroclor 1248 (sp gr 1.36). A mixture of the two liquids was fed into one end of a long horizontal tank in which the two phases were separated by gravity and were drawn off at the top and bottom of the opposite end. The liquids were introduced through a pipe narrow enough to assure a high degree of turbulent mixing. The effectiveness of the settling process was determined by measuring the concentration of water in the Aroclor phase resulting from (a) water dispersed during the initial mixing of the two phases and (b) water showered down into the Aroclor during the coalescence of the droplets into their respective phases from an emulsion layer at the settler interface. This emulsion layer moved toward the settler outlet at two to three times the velocity of the Aroclor phase. For the system investigated, the depth and length of the emulsion layer were found to depend upon the Reynolds number in the mixing section.

The settler flow patterns were also drawn for the cases in which the emulsion layer ended in the settler and those in which it extended the entire length of the section.

(No UCRL number
M. S. Thesis)

12. PREPARATION OF METALLIC TITANIUM BY FILM BOILING

Alfred William Petersen

Radiation Laboratory and
Department of Chemistry and Chemical Engineering

April, 1954

I. ABSTRACT

The Van Arkel-deBoer method for producing ductile titanium by thermal decomposition of TiI_4 vapor and deposition on an electrically heated filament is modified by film boiling TiI_4 liquid on a heated filament, resulting in similar titanium deposition on the filament and liberation of iodine to the gaseous phase. The increase of deposition rate from 10-100 mg/cm^2 -hr for the Van Arkel process to 1000-10,000 mg/cm^2 -hr decreases the energy input from 40-90 Kw-hr/lb Ti^8 for the Van Arkel process to 2-20 Kw-hr/lb Ti by the film boiling method.

(from UCRL-10527,
M.S. Thesis)

13. DOWNFLOW BOILING OF n-BUTANOL
IN A UNIFORMLY HEATED TUBE

Graham F. Somerville

Lawrence Radiation Laboratory
University of California
Berkeley, California

October 29, 1962

ABSTRACT

Local heat-transfer coefficients and two-phase total-pressure drops were measured for the forced-convection boiling of n-butanol in electrically heated tubes having an inside diameter of 0.4670 in. and heated lengths of 5.69 and 4.10 ft respectively. Heat fluxes ranged from $2.8 \cdot 10^4$ to $6.6 \cdot 10^4$ Btu/h-ft² and mass fluxes from 136 to 440 lbm/sec ft². Exit qualities up to 31% were obtained at pressures between 16.9 and 50.0 psia. Measured heat-transfer coefficients ranged between 2,000 and 10,000 Btu/h-ft²-°F.

The boiling heat-transfer data were compared with previous correlations that had been based on the water-steam system. A new boiling heat-transfer correlation was derived having the form

$$St = 0.9005 Re_l^{-0.286} X_{tt}^{-0.292} Bo^{0.191} Pr_l^{-0.233};$$

it was successful in correlating data for both water and n-butanol to within $\pm 30\%$.

Local two-phase total-pressure gradients which ranged up to 8 psi/ft, have been successfully correlated by the method of Schrock and Grossman. Local two-phase frictional-pressure gradients have been obtained and compared with previous results for the water-steam system.

H. AUTHOR INDEX

1. PAPERS PUBLISHED AND UCRL REPORTS ISSUED, 1963

- Agarwal, B. R., and R. M. Diamond
 The Extraction of Tetraalkyl Ammonium Hydroxides and the Solvation of the Hydroxide Ion
 UCRL-10893, July 1963 J. Phys. Chem.
- Alexander, J. M., and G. N. Simonoff
 The Average Energy and Angular Momentum Removed from Dy Compound Nuclei by Neutrons and Photons
 UCRL-10541, January 1963 Phys. Rev.
- Alexander, J. M. (see J. Gilat, UCRL-10774 Abstract)
- Alexander, J. M. (see G. N. Simonoff, UCRL-10679 Abstract)
- Alexander, J. M. (see L. Yaffe)
- Asaro, F., S. Björnholm, and I. Perlman
 The Decay Scheme of Fm^{255}
 UCRL-10635, July 1963 Phys. Rev.
- Asaro, F., and K. Siegbahn
 L = 2, 4 Mixing Ratios in Am^{243} α -Decay and Magnetic Perturbation Effects
 UCRL-11024, September 1963 For Proc. Uppsala Angular Correlation Conf. Uppsala, Sweden, May 1963
- Asaro, F. (see P. Thoresen, UCRL-11148)
- Asaro, F. (see P. Thoresen, UCRL-11035 Abstract)
- Asaro, F. (see R. W. Hoff, UCRL-7211)
- Barrett, P. H., R. W. Grant, M. Kaplan, D. A. Keller, and D. A. Shirley
 Electron Transfer in Dilute Gold Alloys
 UCRL-10608, February 1963 J. Chem. Phys. 39, 1035 (1963).
- Barrett, P. H., and D. A. Shirley
 Hyperfine Structure in Europium Metal
 UCRL-10583, January 1963 Phys. Rev. 131, 123 (1963).
- Björnholm, S. (see F. Asaro, UCRL-10635)
- Blok, Johan (see D. A. Shirley, UCRL-10844)
- Brandt, R., S. G. Thompson, R. C. Gatti, L. Phillips
 Mass and Energy Distributions in the Spontaneous Fission of Some Heavy Isotopes
 UCRL-10506, January 1963 Phys. Rev. 131, 2617 (1963).

- Burnett, D. S.
Kinetic Energy and Mass Distributions for Nuclear Fission at Moderate
Excitation Energy
UCRL-11006, October 1963 Ph.D. Thesis
- Burnett, D. S., R. C. Gatti, F. Plasil, P. B. Price, W. J. Swiatecki, and
S. G. Thompson
Fission Barrier of Thallium-201
UCRL-11079, November 1963 Phys. Rev.
- Cerny, J., R. Pehl, E. Rivet, and B. G. Harvey
Investigation of Isobaric-Spin Conservation in the $O^{16}(d, \alpha)N^{14}$ Reaction Using
a High Resolution Semi-Conductor E - dE/dx System
UCRL-10911, July 1963 Physics Letters
- Cerny, J., M. S. Kirshenbaum, and R. C. Nichols
Range-Energy Relations for Protons and Alpha Particles in Various Explosives
Nature 198, (1963)
- Chanda, R. N.
Evidence for a New Region of Deformation with Less than 82 Neutrons
UCRL-10798, April 1963 Ph.D. Thesis
- Clark, M. W.
Power Requirements for Mixing of Liquid Gas Systems
UCRL-10996, August 1963 M. S. Thesis
- Conocchioli, T.
Extraction of Strong Acids into Tri-N-Octyl Phosphine Oxide
UCRL-10971, September 1963 M. S. Thesis
- Conway, J. G.
The Energy Levels of AmIV in $LaCl_3$
UCRL-11099, November 1963 J. Chem. Phys.
- Conzett, H. E., A. Isoya, and E. Hadjimichael
Phase Shift Analysis of Heavy Ion Scattering
UCRL-10694, February 1963 Abstract for 3rd Conf. on
Reactions Between Complex
Nuclei, Asilomar, Calif.
April 1963
- Conzett, H. E. (see A. Isoya, UCRL-10691 Abstract)
- Cunningham, B. B. (see J. Burnett, UCRL-11126)
- Cunningham, B. B. (see J. Fuger, UCRL-10722)
- Darriulat, P., J. H. Elliott, B. G. Harvey, W. B. Jones, J. R. Meriwether,
E. J. Rivet, and A. Springer
Scattering of 65-MeV Helium Ions from O^{16}
UCRL-10727, March 1963 Nucl. Phys.

- Darriulat, P., G. Igo, H. G. Pugh, J. M. Meriwether, and S. Yamabe
The Scattering of 64.3-MeV Alpha Particles
UCRL-11054, October 1963 Phys. Rev.
- Darriulat, P., G. Igo, and H. G. Pugh
Analysis of Scattering of 63.7-MeV Alpha Particles from Ni⁵⁸ and Fe⁵⁸
UCRL-11059, October 1963 Abstract for APS Meeting,
Pasadena
- Darriulat, P. (see B. G. Harvey, UCRL-10727-Rev.)
- Darriulat, P. (see H. G. Pugh, UCRL-11060 Abstract)
- Demildt, A. C.
Range Energy Relations of He³ Calculated for Several Elements
UCRL-10647, February 1963 Anal. Chem.
- Demildt, A. C.
Microactivation Analysis for Oxygen in the Actinide Metals
UCRL-10324-Rev., February 1963 Anal. Chem.
- Diamond, R. M.
The Aqueous Solution Behavior of Large Univalent Ions: A New Type of Ion
Pairing
UCRL-10909, July 1963 J. Phys. Chem.
- Diamond, R. M. (see D. C. Whitney, UCRL-10602)
- Diamond, R. M. (see D. C. Whitney, UCRL-10604)
- Diamond, R. M. (see D. C. Whitney, UCRL-10984)
- Diamond, R. M. (see D. C. Whitney, UCRL-10912)
- Diamond, R. M. (see B. R. Agarwal, UCRL-10893)
- Diamond, R. M., and F. S. Stephens
Isomeric Levels in the Light Thallium Isotopes
UCRL-10603, February 1963 Nucl. Phys.
- Diamond, R. M., and F. S. Stephens
Metastable States in the Light Thallium Isotopes Produced in Heavy-Ion
Reactions
UCRL-10699, February 1963 Abstract for 3rd Conf. on Reactions
Between Complex Nuclei, Asilomar,
Calif., April 1963
- Dietrich, K., H. J. Mang, and J. H. Pradal
Conservation of Particle Number in the Nuclear Model
UCRL-11083, November 1963 Phys. Rev.
- Elliott, J. H. (see P. Darriulat, UCRL-10727)
- Elliott, J. H. (see B. G. Harvey, UCRL-10727-Rev.)
- Epstein, A.
Mechanism of Liquid-Liquid Settling
UCRL-10625, January 1963 M. S. Thesis

- Forrester, J. D., A. Zalkin, and D. H. Templeton
Crystal and Molecular Structure of In_2I_6 ¹
UCRL-10941, July 1963 J. Inorg. Chem.
- Forrester, J. D., A. Zalkin, D. H. Templeton, and J. C. Wallmann
Crystal Structure of Terbium Trichloride
UCRL-10910, July 1963 J. Inorg. Chem.
- Forrester, J. D. (see D. H. Templeton, UCRL-10804)
- Forrester, J. D. (see D. H. Templeton, UCRL-10803)
- Forrester, J. D. (see D. H. Templeton, UCRL-10661)
- Forrester, J. D. (see A. Zalkin, UCRL-10962)
- Forrester, J. D. (see A. Zalkin, UCRL-10902)
- Forrester, J. D. (see A. Zalkin, UCRL-11130)
- Forrester, J. D. (see A. Zalkin, UCRL-11085)
- Forrester, J. D. (see A. Zalkin, UCRL-11010)
- Frankel, R. D., D. A. Shirley, and N. J. Stone
The Angular Distributions of Conversion Electrons from Oriented $\text{Ce}^{137\text{m}}$
Nuclei
UCRL-11063, October 1963 Abstract for APS meeting,
Pasadena, Dec. 1963
- Frankel, R. D. (see D. A. Shirley, UCRL-10945 Abstract)
- Fritsch, A. R. (see G. T. Seaborg)
- Fuger, J., and B. B. Cunningham
Heats of Formation of Pu^{+3} (aq), PuCl_3 (c), PuOCl (c), Am^{+3} (aq), AmCl_3 (c),
and AmOCl (c)
UCRL-10722, March 1963 J. Inorg. and Nucl. Chem.
- Garrison, W. M.
Actions of Ionizing Radiations on Nitrogen Compounds in Aqueous Media
UCRL-10827, May 1963 Academic Press
- Gatti, R. C. (see R. Brandt, UCRL-10506)
- Gatti, R. C. (see D. S. Burnett, UCRL-11079)
- Getzinger, R. W., and C. R. Wilke
An Experimental Test of the Stefan-Maxwell Equations
UCRL-9987-Rev., September 1963 A. I. Ch. E.
- Gilat, J., and J. M. Alexander
Recoil Range Straggling of Heavy Ion Reaction Products in Helium
UCRL-10774, May 1963 Abstract for 3rd Conf. on
Reactions Between Complex
Nuclei, Asilomar, Calif.
April 1963

Gmitro, J. I.

Vapor Liquid Equilibria for Aqueous Sulfuric Acid
UCRL-10886, July 1963 M. S. Thesis

Graham, R. L., J. M. Hollander, and P. Kleinheinz

Properties of the 57- and 351-keV Excited States in $^{59}\text{Pr}^{143}$
UCRL-10792, June 1963 Nucl. Phys.

Graham, R. L. (see T. Novakov, UCRL-11101 Abstract)

Graham, R. L. (see T. Novakov, UCRL-10875).

Grant, R. W.

Study of the Nuclear Zeeman Effect in Au^{197}
UCRL-10649, January 1963 Ph. D. Thesis

Grant, R. W., D. A. Keller, and D. A. Shirley

The Nuclear Zeeman Effect in Gold Atoms Dissolved in Iron, Cobalt, and
Nickel
UCRL-10847, July 1963 Phys. Rev.

Grant, R. W. (see P. H. Barrett, UCRL-10608)

Grant, R. W. (see D. A. Shirley, UCRL-10944 Abstract)

Grant, R. W. (see D. A. Shirley, UCRL-10946 Abstract)

Griffioen, R. D., and R. D. Macfarlane

Alpha Decay Properties of Some Francium Isotopes Near the 126-Neutron
Closed Shell
UCRL-10930, July 1963 Phys. Rev.

Griffioen, R. D. (see R. D. Macfarlane, UCRL-10937)

Griffioen, R. D. (see R. D. Macfarlane, UCRL-10952)

Haag, J. N.

Measurement of the Plane Polarization of Gamma Radiation
UCRL-10880, June 1963 Phys. Rev.

Hadjimichael, E. (see H. E. Conzett, UCRL-10694 Abstract)

Hadjimichael, E. (see A. Isoya, UCRL-10691 Abstract)

Haines, E. L., and S. G. Thompson

Mass-Energy Relations in the Fission of Highly Excited Heavy Nuclei
UCRL-10342-Rev., February 1963 Phys. Rev.

Harvey, B. G., J. R. Meriwether, and D. J. Horen

Excitation of Collective Levels in Cu^{63} by 50-MeV Alpha Scattering
UCRL-11036, October 1963 Abstract for APS meeting,
Pasadena, Calif, Dec. 1963

Harvey, B. G., E. J. Rivet, A. Springer, J. R. Meriwether, W. B. Jones,
J. H. Elliott, and P. Darriulat

Scattering of 65-MeV Helium Ions from O^{16}
UCRL-10727-Rev., August 1963 Nucl. Phys.

Harvey, B. G. (see P. Darriulat, UCRL-10727)

Harvey, B. G. (see J. Cerny, UCRL-10911)

Heinzelmann, F. J., D. T. Wasan, and C. R. Wilke

Concentration and Velocity Profiles in a Stefan Diffusion Tube
UCRL-10421-Rev., August 1963 Ind. Eng. and Chem.

Hennico, A.

Longitudinal Dispersion in Packed Extraction Columns
UCRL-10696, March 1963 Ph.D. Thesis

Hoff, R. W., F. Asaro, and I. Perlman

Alpha Decay of Neutron Deficient Astatine Isotopes
UCRL-7211, January 1963 J. Inorg. and Nucl. Chem.

Hollander, J. M. (see R. L. Graham, UCRL-10792)

Hollander, J. M. (see T. Novakov, UCRL-10875)

Hollander, J. M. (see T. Novakov, UCRL-11101 Abstract)

Holmgren, H. D. (see H. G. Pugh, UCRL-11060 Abstract)

Horen, D. J. (see B. G. Harvey, UCRL-11036 Abstract)

Hyde, E. K.

Nuclear Models and Their Application to the Heavy Elements
UCRL-8783-Rev., April 1963

Hyde, E. K.

Natural Radioactivity of the Heavy Elements: A Comprehensive Review
UCRL-10612, February 1963

Hyde, E. K. (see L. Yaffe)

Igo, G., and B. D. Wilkins

Alpha Particle Reaction Cross Sections at 40 MeV
UCRL-10568-Rev., April 1963 Phys. Rev. 131, 1251 (1963)

Igo, G., and B. D. Wilkins

The Role of Compound Elastic Scattering in Reaction Cross Section
Measurements
UCRL-10994, September 1963 Abstract for Topical Conf.,
Gatlinburg, Tenn. Oct. 1963

Igo, G. (see P. Darriulat, UCRL-11059 Abstract)

Igo, G. (see P. Darriulat, UCRL-11054)

Igo, G. (see B. D. Wilkins, UCRL-10692 Abstract)

Igo, G. (see H. G. Pugh, UCRL-11060 Abstract)

Isoya, A., H. E. Conzett, E. Hadjimichael, and E. Shield

Inelastic Scattering of 166-MeV O^{16} Ions by Ta^{181}
UCRL-10691, February 1963 Abstract for 3rd Conf. on
Reactions Between Complex
Nuclei, Asilomar, Calif.
April 1963

Isoya, A. (see H. E. Conzett, UCRL-10694 Abstract)

- Jones, W. B.
New Isomers of Astatine-212
UCRL-10645, January 1963 Phys. Rev. 130, 2042 (1963)
- Jones, W. B. (see P. Darriulat, UCRL-10727)
- Jones, W. B. (see B. G. Harvey, UCRL-10727-Rev.)
- Jura, G. (see J. A. Stone, UCRL-10630-Rev.)
- Kaplan, M. (see P. H. Barrett, UCRL-10608)
- Keller, D. A. (see R. W. Grant, UCRL-10847)
- Keller, D. A. (see P. H. Barrett, UCRL-10608)
- Keller, D. A. (see D. A. Shirley, UCRL-10944 Abstract)
- Kiefer, R. L.
The Isomer Ratio of Ce^{137m} - Ce^{137g} Produced in Several Charged-Particle Reactions
UCRL-11049, October 1963 Ph. D. Thesis
- Kim, Y. E.
I. Tensor-Force Effects in the Nuclear Shell Theory. II. Nuclear Spectroscopic Studies of Isomeric States in Odd-Odd Yttrium Nuclei
UCRL-10865, June 1963 Ph. D. Thesis
- Kim, Y. E.
The Low-Energy States in Y^{90}
UCRL-10329, February 1963 Phys. Rev. 131, 1712 (1963)
- Kim, Y. E., and J. O. Rasmussen
Energy Levels of Bi^{210} and Po^{210} and the Shell-Model Residual Force
UCRL-10707, March 1963 Nucl. Phys. 47, 184 (1963)
- Kirshenbaum, M. S. (see J. Cerny)
- Kleinheinz, P. (see R. L. Graham, UCRL-10792)
- Koch, C. W. (see A. Zalkin, UCRL-11010)
- Leban, M.
Sulfur Reduction by Bacteria
UCRL-10966, August 1963 Ph. D. Thesis
- Lederer, C. M.
The Structure of Heavy Nuclei: A Study of Very Weak Alpha Branching
UCRL-11028, September 1963 Ph. D. Thesis
- McHugh, J. A., Jr.
Mass-Spectrometric Study of Fission from the U^{236} Compound Nucleus at Moderate Excitation
UCRL-10673, February 1963 Ph. D. Thesis
- Macfarlane, R. D., and R. D. Griffioen
Alpha Decay Properties of Some Erbium Isotopes Near the 82-Neutron Closed Shell
UCRL-10937, July 1963 Phys. Rev. 131, 2176 (1963).

- Macfarlane, R. D., and R. D. Griffioen
A System for Studying Accelerator-Produced Short-Lived Alpha Emitters
UCRL-10952, August 1963 Nucl. Inst. and Methods
- Mang, H. J., J. O. Rasmussen, and J. K. Poggenburg
Some Shell Model Calculations of Alpha Decay Rates of Odd-Mass
Spheroidal Nuclei
UCRL-10648, February 1963 Abstract for APS meeting,
Washington, D. C., April 1963
- Margulis, T. N. (see D. H. Templeton, UCRL-10923)
- Markowitz, S. S. (see P. L. Reeder, UCRL-10924)
- Marshalek, E. R., and J. O. Rasmussen
Collective Vibrations of Spheroidal Even Nuclei
Nucl. Phys. 43, 438 (1963)
- Meriwether, J. R. (see B. G. Harvey, UCRL-10727-Rev.)
- Meriwether, J. R. (see B. G. Harvey, UCRL-11036 Abstract)
- Meriwether, J. R. (see P. Darriulat, UCRL-11054)
- Meriwether, J. R. (see P. Darriulat, UCRL-10727)
- Miller, R. C.
Kinetics of Aromatic Nitration
UCRL-11069, October 1963 M. S. Thesis
- Miyauichi, T. (see T. Vermeulen, UCRL-11016)
- Moon, J. S.
Longitudinal Dispersion in Packed Extraction Column with and without
Pulsation
UCRL-10928, November 1963 Ph. D. Thesis
- Nagarajan, M. A.
On the Enhancement of Single Particle Transition Rates in C^{13}
UCRL-10982, August 1963 Nucl. Phys.
- Newton, A. S., and A. F. Sciamanna
A Metastable State of the Doubly Charged Carbon Dioxide Ion
UCRL-10639, January 1963 Abstract for 11th Ann. Conf.
Amer. Soc. Testing Materials
Comm., San Francisco, Calif.,
May 1963
- Newton, A. S., and A. F. Sciamanna
A Metastable State of the Doubly Charged Carbon Dioxide Ion
UCRL-10922, July 1963 J. Chem. Phys.
- Newton, A. S.
Triple Ionization in Small Molecules
UCRL-10936, July 1963 J. Chem. Phys.

- Newton, A. S.
The Combined Use of Gas Chromatography and Mass Spectrometry for the
Identification of Minor Components
UCRL-11092
Abstract for 4th Meeting in
Miniature of the Calif. Section
of the ACS, Dec. 1963
- Newton, A. S. (see J. A. Olmsted, UCRL-10824)
- Newton, A. S. (see J. A. Olmsted, UCRL-10823)
- Newton, A. S. (see J. A. Olmsted, UCRL-10823-Rev.)
- Nichol, M. (see J. A. Stone, UCRL-10630-Rev.)
- Nichols, R. C. (see J. Cerny)
- Novakov, T., J. M. Hollander, and R. L. Graham
An Electrostatic Method for the Recoil Measurement of Sub-Nanosecond
Nuclear Lifetimes
UCRL-10875, July 1963
Nucl. Inst. and Methods
- Novakov, T., J. M. Hollander, and R. L. Graham
An Electrostatic Method for the Recoil Measurement of Sub-Nanosecond
Nuclear Lifetimes
UCRL-11101, October 1963
Abstract for APS meeting,
New York, Jan. 1964
- Olmsted, J. A., K. Street, and A. S. Newton
Excess-Kinetic-Energy Ions in Organic Mass Spectra
UCRL-10823-Rev., November 1963
J. Chem. Phys.
- Olmsted, J. A.
Formation of Energetic Fragment Ions by Bombardment of Organic
Molecules with Slow Electrons
UCRL-10687, February 1963
Ph. D. Thesis
- Olmsted, J. A., K. Street, and A. S. Newton
Excess-Kinetic-Energy Ions in Organic Mass Spectra: I. Kinetic Energies,
Appearance Potentials, and the Mechanism of Formation
UCRL-10823, May 1963
J. Chem. Phys.
- Olmsted, J. A., K. Street, and A. S. Newton
Excess-Kinetic-Energy Ions in Organic Mass Spectra: II. Abundances and
Implication for the Quasi-Equilibrium Theory of Mass Spectra
UCRL-10824, May 1963
J. Chem. Phys.
- Pehl, R. H.
Studies in Nuclear Spectroscopy by Two-Nucleon Transfer Reactions
UCRL-10993, August 1963
Ph. D. Thesis
- Pehl, R. H. (see J. Cerny, UCRL-10911)
- Perlman, I. (see R. W. Hoff, UCRL-7211)
- Perlman, I. (see F. Asaro, UCRL-10635)
- Perlman, I. (see J. O. Rasmussen, UCRL-10669)
- Perlman, I. (see P. Thoresen, UCRL-11035 Abstract)

- Perlman, I. (see P. Thoresen, UCRL-11148)
- Petersen, R.
Purification Message Used for the Mass-Spectrometric Study of Fission of
U-235 and U-238 at Moderate Energies
UCRL-11074, October 1963 M. S. Thesis
- Phillips, L. (see R. Brandt, UCRL-10506)
- Plasil, F. (see D. S. Burnett, UCRL-11079)
- Poggenburg, J. K. (see H. J. Mang, UCRL-10648 Abstract)
- Price, P. B. (see D. S. Burnett, UCRL-11079)
- Pugh, H. G., P. Darriulat, H. D. Holmgren, and G. Igo
Elastic Scattering of Alpha Particles from Helium at Energies Between
52 MeV and 120 MeV
UCRL-11060, October 1963 Abstract for APS Meeting,
Pasadena, Dec. 1963
- Pugh, H. G. (see P. Darriulat, UCRL-11054)
- Pugh, H. G. (see P. Darriulat, UCRL-11059 Abstract)
- Rajnak, K. (see B. G. Wybourne, UCRL-10742)
- Rasmussen, J. O., and I. Perlman
Alpha Decay: A Survey
UCRL-10669, February 1963 Chapter in Siegbahn book
- Rasmussen, J. O. (see J. A. Stone, UCRL-10630-Rev.)
- Rasmussen, J. O. (see Y. E. Kim, UCRL-10707)
- Rasmussen, J. O. (see H. J. Mang, UCRL-10648 Abstract)
- Rasmussen, J. O. (see E. R. Marshalek)
- Reeder, P. L., and S. S. Markowitz
Excitation Function for the $C^{12}(\pi^-, \pi^-n)C^{11}$ Reaction
UCRL-10924, July 1963 Phys. Rev.
- Reynolds F. L.
Surface Ionization on Tungsten Single-Crystal Filaments
UCRL-10710, February 1963 Abstract for Am. Soc. for
Testing Material, May 1963
- Reynolds, F. L.
Ionization on Tungsten Single-Crystal Filaments
UCRL-10618, February 1963 J. Chem. Phys. 39, 1107 (1963)
- Rho, Mannque
On the Quasi-Particle Interaction in Spherical Nuclei
UCRL-11080, October 1963 Ph. D. Thesis
- Rivet, E. J. (see B. G. Harvey, UCRL-10727-Rev.)
- Rivet, E. J. (see P. Darriulat, UCRL-10727)

- Rivet, E. (see J. Cerny, UCRL-10911)
- Ruben, H. (see A. Zalkin, UCRL-10832)
- Sciamanna, A. F. (see A. S. Newton, UCRL-10922)
- Sciamanna, A. F. (see A. S. Newton, UCRL-10639 Abstract)
- Seaborg, G. T., and A. R. Fritsch
 The Synthetic Elements: III
 1963
 Scientific American
- Seegmiller D. W.
 The Effect of Angular Momentum of the Compound Nucleus on the Ratio of
 the Isomers Te^{119} and Te^{119m} Produced in Low-Energy Bombardments
 UCRL-10850, August 1963
 Ph. D. Thesis
- Shield, E. (see A. Isoya, UCRL-10691 Abstract)
- Shirley, D. A., R. W. Grant, and D. A. Keller
 Quadrupole Splitting in Aurous Halides
 UCRL-10944, August 1963
 Abstract for 3rd Intn'l Conf. on
 the Mössbauer Effect, Ithaca,
 N. Y. Sept. 1963
- Shirley, D. A., R. W. Grant, and G. A. Westenbarger
 Systematics of Conduction-Electron Polarization of Impurity Atoms
 UCRL-10946, August 1963
 Abstract for 3rd Intn'l Conf. on
 the Mössbauer Effect, Ithaca,
 N. Y. Sept. 1963
- Shirley, D. A., R. B. Frankel, and H. H. Wickman
 Resonant Absorption Studies with Eu^{151}
 UCRL-10945, August 1963
 Abstract for 3rd Intn'l Conf. on
 the Mössbauer Effect, Ithaca,
 N. Y. Sept. 1963
- Shirley, D. A. (see R. W. Grant, UCRL-10847)
- Shirley, D. A. (see R. B. Frankel, UCRL-11063 Abstract)
- Shirley, D. A. (see P. H. Barrett, UCRL-10608)
- Shirley, D. A. (see P. H. Barrett, UCRL-10583)
- Shirley, D. A., and J. Blok
 Quadrupole Antishielding in the Rare Earths
 UCRL-10844, June 1963
 J. Chem. Phys. 39, 1128 (1963)
- Siegbahn, K. (see F. Asaro, UCRL-11024)
- Simonoff, G. N., and J. M. Alexander
 Effect of Angular Momentum on Neutron Emission from Tb and Dy
 Compound Nuclei
 UCRL-10679, February 1963
 Abstract for 3rd Conf. on
 Reactions Between Complex
 Nuclei, Asilomar, Calif.,
 April 1963
- Simonoff, G. N. (see J. M. Alexander, UCRL-10541)

- Sommerville, Graham
Downflow Boiling of n-Butanol in a Uniformly Heated Tube
UCRL-10527, January 1963 M. S. Thesis
- Springer, A. (see B. G. Harvey, UCRL-10727-Rev.)
- Springer, A. (see P. Darriulat, UCRL-10727)
- Steiger, N. H.
Equilibrium Distributions of Effective Charges of Products of Heavy-Ion-Induced Spallation
UCRL-10806, May 1963 Phys. Rev.
- Steiger, N. H.
Internal Ionization That Follows a Reaction Between Complex Nuclei
UCRL-10888, July 1963
- Stephens, F. S. (see R. M. Diamond, UCRL-10699 Abstract)
- Stephens, F. S. (see R. M. Diamond, UCRL-10603)
- Stone, J. A.
The Influence of High Pressures on the Mössbauer Effect in Dy¹⁶¹
UCRL-10630, January 1963 Ph. D. Thesis
- Stone, J. A., M. Nichol, G. Jura, and J. O. Rasmussen
The Influence of High Pressures on the Mössbauer Effect in Dy¹⁶¹
UCRL-10630-Rev., April 1963 Phys. Rev.
- Stone, N. J. (see R. B. Frankel, UCRL-11063 Abstract)
- Street, K. (see J. A. Olmsted, UCRL-10823)
- Street, K. (see J. A. Olmsted, UCRL-10823-Rev.)
- Street, K. (see J. A. Olmsted, UCRL-10824)
- Subrahmanyam, V. B.
Alpha-Decay Studies of Protactinium Isotopes
UCRL-11082, October 1963 Ph. D. Thesis
- Swiatecki, W. J. (see D. S. Burnett, UCRL-11079)
- Templeton, D. H., A. Zalkin, J. D. Forrester, and S. M. Williamson
Crystal and Molecular Structure of Xenon Trioxide
UCRL-10661, January 1963 J. Am. Chem. Soc. 85, 817 (1963)
- Templeton, D. H., A. Zalkin, J. D. Forrester, and S. M. Williamson
Determination of the Crystal Structure of Xenon Trioxide
UCRL-10803, April 1963 Conf. Book "Noble Gas Compound,"
Univ. of Chicago Press
- Templeton, D. H., A. Zalkin, J. D. Forrester, and S. M. Williamson
A Determination of the Crystal Structure of Xenon Tetrafluoride
UCRL-10804, April 1963 Conf. Book "Noble Gas
Compound," Univ. of Chicago
Press

- Templeton, D. H., A. Zalkin, and T. N. Margulis
Comments on the Orientation of the Proton-Proton Vectors of Water in
Tutton's Salts
UCRL-10923, July 1963 J. Chem. Phys.
- Templeton, D. H. (see L. K. Templeton, UCRL-10969)
- Templeton, D. H. (see A. Zalkin, UCRL-10832)
- Templeton, D. H. (see A. Zalkin, UCRL-10901)
- Templeton, D. H. (see A. Zalkin, UCRL-10962)
- Templeton, D. H. (see A. Zalkin, UCRL-11085)
- Templeton, D. H. (see A. Zalkin, UCRL-11010)
- Templeton, D. H. (see A. Zalkin, UCRL-11130)
- Templeton, D. H. (see A. Zalkin, UCRL-10902)
- Templeton, D. H. (see J. D. Forrester, UCRL-10910)
- Templeton, D. H. (see J. D. Forrester, UCRL-10941)
- Templeton, L. K., D. H. Templeton, and A. Zalkin
Refinement of the Crystal Structure of Mercuric Sulfate Monohydrate
UCRL-10969, August 1963 Acta Cryst.
- Thompson, S. G. (see E. L. Haines, UCRL-10342-Rev.)
- Thompson, S. G. (see R. Brandt, UCRL-10506)
- Thompson, S. G. (see D. S. Burnett, UCRL-11079)
- Thoresen, P., F. Asaro, and I. Perlman
Concerning Isomers of At²⁰⁸, At²⁰⁶, and At²⁰⁴
UCRL-11148, September 1963 J. Inorg. Nucl. Chem.
- Thoresen, P., F. Asaro, and I. Perlman
Investigation of Isomers of At²⁰⁸, At²⁰⁶, and At²⁰⁴
UCRL-11035, August 1963 Abstract for Gordon Conf.
Canada, August 1963
- Vandegrift, A. E.
Liquid-Liquid Interfacial Tensions Measurement with an Oscillating Jet
UCRL-10717, March 1963 Ph. D. Thesis
- Vermeulen, T., and T. Miyauichi
Diffusion and Back Flow Models for 2 Phase Axial Dispersion
UCRL-11016, 1963 Indr. Engr. Chem., Fund.
- Wallmann, J. C. (see J. D. Forrester, UCRL-10910)
- Wasan, D. T., and C. R. Wilke
Turbulent Exchange of Momentum, Mass, and Heat Between Fluid Streams
and Pipe Wall
UCRL-10556, March 1963 Inst. of Chem. Engr. J.
- Wasan, D. T. (see F. J. Heinzelmann, UCRL-10421-Rev.)

- Weidenmuller, H. A.
Studies of Many-Channel Scattering
UCRL-11040, October 1963
Annals of Physics
- Westenbarger, G. A.
Polarization of Silver Nuclei in Ferromagnets and the Internal Magnetic Field
UCRL-11143, November 1963
Ph.D. Thesis
- Westenbarger, G. A. (see D. A. Shirley, UCRL-10946 Abstract)
- Whitney, D. A., and R. M. Diamond
Ion Exchange Studies in Concentrated Solutions, II. The Alkali Cations
with a Carboxylic Acid Resin
UCRL-10602, January 1963
Inorg. Chem.
- Whitney, D. C., and R. M. Diamond
The Extraction of Acids by Basic Organic Solvents. IV. Tributyl Phosphate
and Trioctyl Phosphine Oxide - HAuCl_4 and HAuBr_4
UCRL-10912, August 1963
J. Phys. Chem.
- Whitney, D. C., and R. M. Diamond
Ion Exchange Studies in Concentrated Solutions. III. The Alkaline Earth
Cations with a Sulfonic Acid Resin
UCRL-10984, October 1963
Inorg. Chem.
- Whitney, D. C., and R. M. Diamond
The Extraction of Acids by Basic Organic Solvents
UCRL-10604, February 1963
J. Phys. Chem.
- Wickman, H. H. (see D. A. Shirley, UCRL-10945 Abstract)
- Wilke, C. R. (see F. J. Heinzelmann, UCRL-10421-Rev.)
- Wilke, C. R. (see R. W. Getzinger, UCRL-9987-Rev.)
- Wilke, C. R. (see D. T. Wasan, UCRL-10556)
- Wilkins, B. D.
Total-Reaction Cross Section Measurements for Charged Particles
UCRL-10783, May 1963
Ph. D. Thesis
- Wilkins, B. D., and G. Igo
Total Reaction Cross Sections for Heavy Ions
UCRL-10692, February 1963
Abstract for 3rd Conf. on
Reactions Between Complex
Nuclei, Asilomar, Calif.,
April 1963
- Wilkins, B. D. (see G. Igo, UCRL-10568-Rev.)
- Wilkins, B. D. (see G. Igo, UCRL-10994 Abstract)
- Williamson, S. M. (see D. H. Templeton, UCRL-10661)
- Williamson, S. M. (see D. H. Templeton, UCRL-10803)
- Williamson, S. M. (see D. H. Templeton, UCRL-10804)
- Williamson, S. M. (see A. Zalkin, UCRL-11010)

- Wybourne, B. G., and K. Rajnak
Configuration Interaction Effects in 1^N Configurations
UCRL-10742, April 1963 Phys. Rev.
- Yaffe, L., J. M. Alexander, and E. K. Hyde
Neutron-Deficient Isotopes of Lanthanum-La¹²⁷, La¹²⁸, La¹²⁹, and La¹³¹
1963 Can. J. Chem.
- Yamabe, S. (see P. Darriulat, UCRL-11054)
- Zalkin, A., H. Ruben, and D. H. Templeton
The Crystal Structure and Hydrogen Bonding of Magnesium Sulfate
Hexahydrate
UCRL-10832, May 1963 Acta. Cryst.
- Zalkin, A., and D. H. Templeton
x-Ray Diffraction Refinement of the Calcium Tungstate Structure
UCRL-10901, July 1963 J. Chem. Phys.
- Zalkin, A., J. D. Forrester, and D. H. Templeton
The Crystal Structure of Thorium Tetraiodide
UCRL-10962, August 1963 J. Inorg. Chem.
- Zalkin, A., J. D. Forrester, and D. H. Templeton
The Crystal Structure of Sodium Fluosilicate
UCRL-11130, November 1963 Acta Cryst.
- Zalkin, A., J. D. Forrester, and D. H. Templeton
The Crystal Structure of Manganese Dichloride Tetrahydrate
UCRL-11085, October 1963 Inorg. Chem.
- Zalkin, A., J. D. Forrester, D. H. Templeton, S. M. Williamson,
and C. W. Koch
Sodium Perxenate Hexahydrate
UCRL-11010, September 1963 Science 142, 3591 (1963)
- Zalkin, A., J. D. Forrester, and D. H. Templeton
Crystal Structure of Cerium Magnesium Nitrate Hydrate
UCRL-10902, July 1963 J. Chem. Phys.
- Zalkin, A. (see J. D. Forrester, UCRL-10941)
- Zalkin, A. (see J. D. Forrester, UCRL-10910)
- Zalkin, A. (see D. H. Templeton, UCRL-10661)
- Zalkin, A. (see D. H. Templeton, UCRL-10803)
- Zalkin, A. (see D. H. Templeton, UCRL-10804)
- Zalkin, A. (see D. H. Templeton, UCRL-10923)
- Zalkin, A. (see L. K. Templeton, UCRL-10969)

2. CONTRIBUTORS TO THIS REPORT

Agarwal, B.: D.14
Alexander, J. M.: C.9, C.10
Ali, D.: A.13
Asaro, F.: A.8, A.9, A.10, A.11, A.12
Baer, R. M.: A.24
Bailey, B.: E.4
Bennett, W.: D.16
Björnholm, S.: A.10
Blok, J.: D.27
Bowman, H. R.: B.1
Breivogel, F. W., Jr.: D.21
Burnett, D. S.: B.4, B.6
Cerny, J.: C.3, C.5, E.8
Chanda, R. N.: G.1
Choppin, G.: B.3
Clark, M. W.: F.6
Cole, S.: D.17
Conway, J. G.: D.22, D.23, D.24
Conzett, H. E.: C.1, C.11, C.12
Cooper, J. A.: A.14
Coughlen, T. D.: F.6
Cunningham, B. B.: D.2
Darriulat, P.: C.4, C.7
de Haro, F. O.: E.9, E.13
Diamond, R. M.: A.1, D.12, D.13, D.14, D.15
Dietrich, K.: A.22, A.23
Elliott, J. H.: C.4
Emanuel, A.: G.2
Epstein, A. D.: G.11
Forrester, J. D.: D.3, D.4, D.6, D.7, D.8
Frankel, R. B.: D.29
Gatti, R.: A.14, B.6, B.7
Garrison, W. M.: D.16, D.17
Ghiorso, A.: B.2
Gilat, J.: C.9, C.10
Gillet, V.: C.6
Gmitro, J. I.: F.5
Goulding, F. S.: E.5, E.6, E.7, E.8
Graham, R. L.: A.2, A.3, A.4, A.6, A.7
Grant, R. W.: G.3
Grens, E. A.: G.4
Grunder, H. A.: E.1
Gutmacher, R. G.: D.23, D.24
Haag, J.: C.5
Hadjimichael, E.: C.11, C.12
Hansen, W. L.: E.5
Harada, K.: A.25
Harvey, B. G.: C.4, C.5, C.8
Hebert, A. J.: D.21
Hennico, A. N.: F.7
Hickman, R. G.: G.5
Hollander, J. M.: A.2, A.3, A.4, A.5, A.6,
A.7, E.10
Hollowell, C. D.: D.21
Holtz, M.: A.3, A.4
Horen, D. J.: A.6, C.8
Hulet, E. K.: D.23
Hyder, M. L.: D.32
Igo, G.: C.1, C.7
Isoya, A.: C.11, C.12
Jenkins, D.: C.6
Jones, W. B.: C.4
Khodai-Joopary, A.: B.7
Kiefer, R. L.: G.6
Kim, Y. E.: A.16, A.17
King, C. J.: F.3
Kleinheinz, P.: A.7
Knox, W. J.: C.1
Koch, C. W.: D.8, D.9, D.10, D.11
Landis, D. A.: E.6, E.7
LaPierre, R. L.: E.11
Lark, N.: A.1
Leban, M.: F.1
Lederer, C. M.: G.7
Macfarlane, R. D.: A.20
Mahony, J. D.: D.1

Main, R. : B.2
Maleh, I. : D.31
Mang, H. J. : A.15, A.22, A.23
Markowitz, S. S. : C.13, C.14, D.1, D.32
Marrus, R. : A.13
McClure, D. E. : E.10
McHarris, W. : A.8
McHugh, J. A. : G.8
Meriwether, J. R. : C.4, C.7, C.8
Miller, R. C. : F.5
Moon, J. S. : F.7
Mosier, D. F. : A.12
Nakamura, M. : E.9, E.11
Newton, A. S. : D.18, D.19, D.20
Novakov, T. : A.2, A.3, A.4, A.5
Olmsted, J. A., Jr. : D.19
Pape, A. : C.13
Parsa, Bahman: D.1
Pehl, R. H. : C.2, C.3, C.5
Perlman, I. : A.8, A.9, A.10, A.11, A.12
Petersen, A. W. : G.12
Plasil, F. : B.5, B.6
Poggenburg, J. K. : A.15
Pradal, J. : A.22, A.23
Price, P. B. : B.6
Pugh, H. G. : C.7
Rajnak, K. E. : D.25, D.26
Rasmussen, J. O. : A.14, A.15, A.16, A.17,
A.18, A.19, A.20, B.1
Radlich, M. : A.24
Reeder, P. L. : C.14
Reynolds, F. L. : E.3
Rho, M. : A.18, A.19, A.20, A.21
Rivet, E. : C.4, C.5
Robinson, H. P. : E.4
Salz, P. : E.10
Sciamanna, A. F. : D.18
Seegmiller, D. W. : G.9
Selph, F. B. : E.1
Shield, E. : C.11
Shirley, D. A. : D.27, D.28, D.29, D.30, E.2
Sikkeland, T. : B.3
Sisson, D. H. : C.9
Sokol, H. A. : D.16
Somerville, G. F. : G.13
Springer, A. : C.4
Stephens, F. S. : A.1, A.8
Stone, N. J. : D.29
Street, K., Jr. : D.19, D.21
Subrahmanyam, V. B. : A.11, A.12
Swiatecki, W. J. : B.6
Templeton, D. H. : D.3, D.4, D.5, D.6, D.7,
D.8
Templeton, L. K. : D.5
Thompson, S. G. : A.14, B.1, B.4, B.5, B.6
B.7
Thoresen, P. E. : A.9
Tocher, M. I. : D.13
Vandergrift, A. E. : F.4
Vermeulen, T. : F.4, F.5, F.6, F.7
Wallmann, J. C. : D.2, D.4
Ward, K. C. : E.9
Wasan, D. T. : F.2
Weeks, B. M. : D.17
Westenbarger, G. A. : D.30
Whitney, D. C. : D.12, D.13
Wilke, C. R. : F.1, F.2
Wilkins, B. D. : C.2, G.10
Williamson, S. M. : D.7, D.8, D.9, D.10,
D.11
Worden, E. F. : D.23, D.24
Wybourne, B. G. : D.25, D.26
Yamabe, S. : C.7
Zalkin, A. : D.3, D.4, D.5, D.6, D.7, D.8
Zane, R. : E.12

This report was prepared as an account of Government sponsored work. Neither the United States, nor the Commission, nor any person acting on behalf of the Commission:

- A. Makes any warranty or representation, expressed or implied, with respect to the accuracy, completeness, or usefulness of the information contained in this report, or that the use of any information, apparatus, method, or process disclosed in this report may not infringe privately owned rights; or
- B. Assumes any liabilities with respect to the use of, or for damages resulting from the use of any information, apparatus, method, or process disclosed in this report.

As used in the above, "person acting on behalf of the Commission" includes any employee or contractor of the Commission, or employee of such contractor, to the extent that such employee or contractor of the Commission, or employee of such contractor prepares, disseminates, or provides access to, any information pursuant to his employment or contract with the Commission, or his employment with such contractor.

